Diss. 2006 - 07
August

Studies and Measurements of Linear Coupling and Nonlinearities in Hadron Circular Accelerators

A. Franchi

(Dissertation Johann Wolfgang Goethe-Universität Frankfurt am Main)

Gesellschaft für Schwerionenforschung mbH
Planckstraße 1 · D-64291 Darmstadt · Germany
Postfach 11 05 52 · D-64220 Darmstadt · Germany

Studies and Measurements of Linear Coupling and Nonlinearities in Hadron Circular Accelerators

Dissertation
zur Erlangung des Doktorgrades
der Naturwissenschaften

vorgelegt beim Fachbereich Physik
der Johann Wolfgang Goethe-Universität
in Frankfurt am Main

von
Andrea Franchi
aus Teramo (Italien)

Frankfurt am Main 2006

vom Fachbereich Physik der Johann Wolfgang Goethe-Universität als Dissertation angenommen.

Dekan:	Prof. Dr. Wolf Assmus
Erster Gutachter:	Prof. Dr. Ingo Hofmann
Zweiter Gutachter:	Prof. Dr. Ulrich Ratzinger
Datum der Disputation:	

La brevità, gran pregio!

La Bohème, Atto 1

Contents

Chapter 1

Introduction

The future hadron circular accelerators SIS-100/SIS-300 of the FAIR complex of GSI are superconducting machines and shall accelerate high-intensity beams. Superconducting magnets are known to drive nonlinear fields usually up to one order of magnitude higher than room-temperature magnets. This is due to a limited accuracy in cabling the coils and to persistent currents after each energy ramp. Magnet nonlinearities are of main concern because particles having large oscillations or moving close to the pipe are subject to chaotic motion resulting in unstable trajectories and eventually in beam loss. In high energy proton colliders the beam size is usually small compared to the dimensions of the pipe. The region of stability (dynamic aperture) is also large enough to contain the entire beam. This is not the case for the heavy ion synchrotron SIS-100 where the beam occupies transversely a large fraction of the pipe and the dynamic aperture is close to both the beam contour and the wall. A continuous monitoring of the "nonlinearity budget" is mandatory not only to reach the expected beam quality, but also to avoid radiation and quenching damages driven by losses of high energy particles at the dipole walls.

The commissioning of new large accelerators, as well as of existing machines after the periodic maintenance, might become a tedious task in presence of uncorrected magnet polarities or problems in the power supply connections. While for dipoles and quadrupoles established beam-based methods for detecting wrong magnet strengths already exist (closed orbit and linear optics), state-of-art techniques for skew quadrupoles and sextupoles are either time consuming or limited to the measurement of global quantities (amplitude dependent detuning, minimization of tune split and nonlinear chromaticity). A beam-based method to infer on-line both the strength and the polarity of corrector magnets in few machine cycles is therefore desirable especially in machines with a large number of correctors.

Furthermore, high-gradient superconducting quadrupoles induce linear coupling between the transverse planes because of both skew quadrupole field errors and limited accuracy installing the magnets in the beam line (tilting angle). Betatron coupling is of concern because it makes the beam rotate in the $x - y$ plane. In high-intensity heavy ion synchrotrons any rotation would lead to beam scraping, as the beam fills almost entirely the elliptical pipe at injection energy. On the other hand, it is under consideration to operate the existing SIS-18 as booster for the SIS-100 with equal transverse emittances at flat top. During multi-turn injection a partial exchange of the beam emittance from the horizontal plane to the vertical is also foreseen to protect the injection septum in high-intensity operations. Both manipulations can be obtained with controlled betatron coupling to be artificially driven by external skew quadrupoles.

Both the heavy ions synchrotrons SIS-100 and SIS-300 shall operate in a regime of beam current and energy where the repulsive space-charge force F_s is not negligible. The latter one scales with the beam parameters according to

$$F_s \propto \frac{ZI}{A(\gamma\beta)^3} \ ,$$

where Z is the charge state, A is the mass number, I the averaged beam current, γ and β are the relativistic factors. Machines like RHIC and LHC operate or shall operate either at much higher energies or at lower beam current such that F_s plays a negligible role in the beam dynamics. Space-charge effects are known to drive halo formation (with consequent risk of beam loss), the *Montague resonance* and the consequent spontaneous emittance exchange if the transverse tunes are close to each other, $Q_x \simeq Q_y$. As these resonances are excited in machines with unsplit tunes only, i.e. Q_x and Q_y have the same integer part, it is of no concern for machines like the SIS-18 ($Q_x = 4.29$, $Q_y = 3.28$), whereas it must be cured or avoided in the SIS-100/SIS-300.

The aim of this thesis is threefold:

- to develop a beam-based method to measure lattice nonlinearities and betatron coupling;
- to study the emittance exchange driven by betatron coupling and space charge;
- to develop fast techniques to correct betatron coupling and to control the emittance exchange between the transverse planes.

The proposed technique to measure lattice nonlinearities is an extension of the method proposed by Tomás [1] of measuring the resonance driving terms (RDT) using beam position monitor (BPM) data. Once the beam is transversally displaced (either by fast kicker magnets or ac exciters), it experiences coherent oscillations that can be turn by turn recorded by all the BPMs in the ring. The spectrum of these oscillations can be inferred via FFT. From the difference between the spectral line amplitudes between two consecutive BPMs nonlinearities are localized. This technique was already applied to SPS in 2002, when strong extraction sextupoles were powered and then localized using BPM data. In this thesis the same approach is used and extended not only to localize nonlinearities but also to infer their strengths and polarities.

Presently, the SIS-18 is not equipped with turn-by-turn multi-BPM acquisition system necessary to perform this analysis. In this thesis it is shown how powerful this tool can be to improve the knowledge of the bare machine and to cure the most harmful lattice errors. Therefore, the machine optimization for any SIS-18 high current operations would profit from the implementation of such a system in the next future.

The emittance exchange driven by betatron coupling is also studied by using the resonance driving terms formalism. Here the goal is to improve existing formulae to describe some counter-intuitive features, like the emittance variation along the ring observed in multi-particle simulations. A systematic numerical study is also performed in order to derive heuristic scaling laws for the stop band widths of space-charge resonances in the region $Q_x \simeq Q_y$. Multi-particle simulations are also run to study possible strategies to control or to avoid the exchange.

The same mathematical formalism is eventually applied to betatron coupling and its equivalence with the traditional matrix formalism is proven. Here the goal is to use the same turn-by-turn harmonic analysis to provide a fast method for measuring and correcting linear coupling using BPM data, without the traditional time-consuming scan of the skew quadrupole families.

The proposed technique to measure lattice nonlinearities has been experimentally tested using existing BPM data from SPS at CERN, since no turn-by-turn multi-BPM acquisition is presently available in the SIS-18. For the same reason BPM data from RHIC have been used for testing the new algorithm to measure and correct betatron coupling in a single machine cycle. Emittance exchange is experimentally observed in the SIS-18 using rest gas monitor (RGM) data. As far as the Montague resonance is concerned, since the SIS-18 is a machine with split tunes, it was not possible to carry out any new measurements. The proposed scheme to avoid the emittance exchange is therefore noly numerically tested, running multi-particle simulations with particle-in-cell (PIC) space-charge solver.

In this thesis only the 4D betatronic motion is studied. Synchrotron motion, as well as dispersive and chromatic effects, are not taken into account when deriving new formulae. However BPM data from SPS and RHIC used to validate the theory were acquired using bunched beams. Emittance measurements in the SIS-18 were carried out with a coasting beam at injection plateau (11.4 MeV/u).

The new theoretical findings on the turn-by-turn harmonic analysis are the result of a collaboration with R. Tomás (CERN) and R. Calaga (BNL). Both provided the BPM data for testing the new algorithms.

Experimental studies carried out at GSI have profited from the new RGM designed and installed in the SIS-18 during 2004 by T. Giacomini and P. Forck. Despite the lack of a turn-by-turn BPM acquisition system, linear optics measurements in the SIS-18 have been carried out making use of a unconventional acquisition system developed for this purpose by P. Moritz.

From the computational point of view, single- and multi-particle simulations have been run making use of the MICROMAP libraries developed by G. Franchetti (GSI) and the group of Bologna lead by prof. G. Turchetti.

This thesis is structured as follows.

In Chapter 2 an overview of the GSI complex of accelerators and a brief description of the SIS-18 instrumentation related to this study are given. The expected performances in view of the SIS-18 upgrade for FAIR are also outlined together with the main beam dynamics issues that are at the basis to this work.

In Chapter 3 the mathematical formalism is presented. The resonance driving terms (RDT) are defined and their relations with the BPM spectral lines and the magnet strengths are derived using the Lie algebra. The main results already derived in the literature are reviewed here and presented in a unified formalism to be used as basis for the new derivations of the next chapters.

In Chapter 4 a new algorithm to infer the magnet strengths from BPM data is derived and applied to existing SPS data. In the first order approximation the RDT (to be measured by using BPM data) are related to the magnet strengths through a linear system whose analytical solution is derived here. Countermeasures for some of the most important experimental limitations, such as BPM calibration errors, are also outlined.

In Chapters 5 and 6 the RDT formalism is used to derive new formulae describing the betatronic motion close to the difference resonance (1,-1). Expressions for the single particle and RMS emittances in terms of the RDT f_{1001} and the distance from the resonance $\Delta = Q_x - Q_y$ are derived here. The use of the Lie algebra leads to explicit relations for the single particle invariants and for decoupling the equations of motion. The equivalence with the traditional matrix approach is proven. The counter-intuitive emittance variation along the ring is shown to be consistent with the variation along the ring of f_{1001}. The emittance exchange curves observed in multi-particle simulations when approaching the resonance, in the static as well as in the dynamic case, are eventually compared with new and existing formulae.

Chapter 7 is devoted to the experimental results obtained in the SIS-18. Measurement and localization of nonlinearities require the use of several BPMs distributed along the ring. Presently only one BPM is equipped with the necessary turn-by-turn acquisition system and only standard optics measurement could be performed. In the first part of this chapter this acquisition system is described and the results measuring the SIS-18 tunes and chromaticity are discussed. The second part focuses on the emittance measurement. Emittances are inferred from the beam profiles measured by the recently installed rest gas monitor (RGM). A short description of this device is therefore given before presenting the main results in manipulating the beam emittances (exchange and equilibration).

In Chapter 8 a new algorithm for a fast measurement and the correction of betatron coupling is derived making use of the RDT formalism. It is shown how from BPM data it is possible to measure not only the resonance stop band width $|C|$, but also its phase Θ. This leads to an immediate definition of the best setting of the corrector skew quadrupoles, without need of any scan. The method is described here, applied to RHIC BPM data and compared with standard techniques.

In Chapter 9 the emittance exchange driven by space charge is numerically investigated. Multi-particle simulations for different beam parameters (initial emittances and currents) and different working points (unsplit and split tunes) are run. From the exchange curve scaling laws for the resonance stop band width and the shift of the resonance center are derived. It is also proven why the Montague resonance cannot be excited in machines with split tunes. Eventually, a possible strategy to *suppress* the effects of the Montague resonance in machines with unsplit tunes by using a normal quadrupole is illustrated.

Chapter 2

Motivations

2.1 The heavy ion synchrotron SIS-18 at GSI

The heavy ion synchrotron SIS-18 is a part of the complex of accelerators at GSI, composed of the linear accelerator UNILAC, the synchrotron SIS-18 and the storage ring ESR. The layout of the complex is sketched in the upper picture of Fig. 2.1. The ions (partially or fully stripped) out of UNILAC are injected in the SIS-18 at energy of 11.4 MeV/u, with a multi-turn injection scheme.

After acceleration the beam is extracted at different energies according to the ion species: up to 2 GeV/u for light ions, 1 GeV/u for heavy ions. After either a *fast* or a *slow* extraction the beam is delivered to experimental targets, as well as to the cancer therapy station, to ESR and the fragment separator FRS.

The ESR can store stable beam coming from the SIS-18 as well as radioactive beam generated by the primary beam hitting a thick target. During the storage of unstable beam mass measurements are performed. Stable beam instead can be cooled down and re-injected and accumulated in the SIS-18. Both SIS-18 and ESR are equipped with electron coolers. In the storage ring stochastic cooling can be also performed.

In the framework of the new facility for antiproton and ion research (FAIR) the SIS-18 shall also operate as booster for the new heavy ion synchrotron SIS-100 and accelerate protons coming out from the new high-intensity proton linac. The layout of the planned facility is sketched in the bottom picture of Fig. 2.1.

General description

The SIS-18 is a normal-conducting machine able to accelerate beam species from proton up to Uranium. The main design parameters are listed in Tab. 2.1.

The focusing system consists of 12 periods, each one containing at injection energy a quadrupole triplet FDF. During ramp and at flat top the quadrupoles of the third family are turned off and the lattice switches to a duplet FD. At injection the phase advance per cell is almost 129^o horizontally and 99^o vertically.

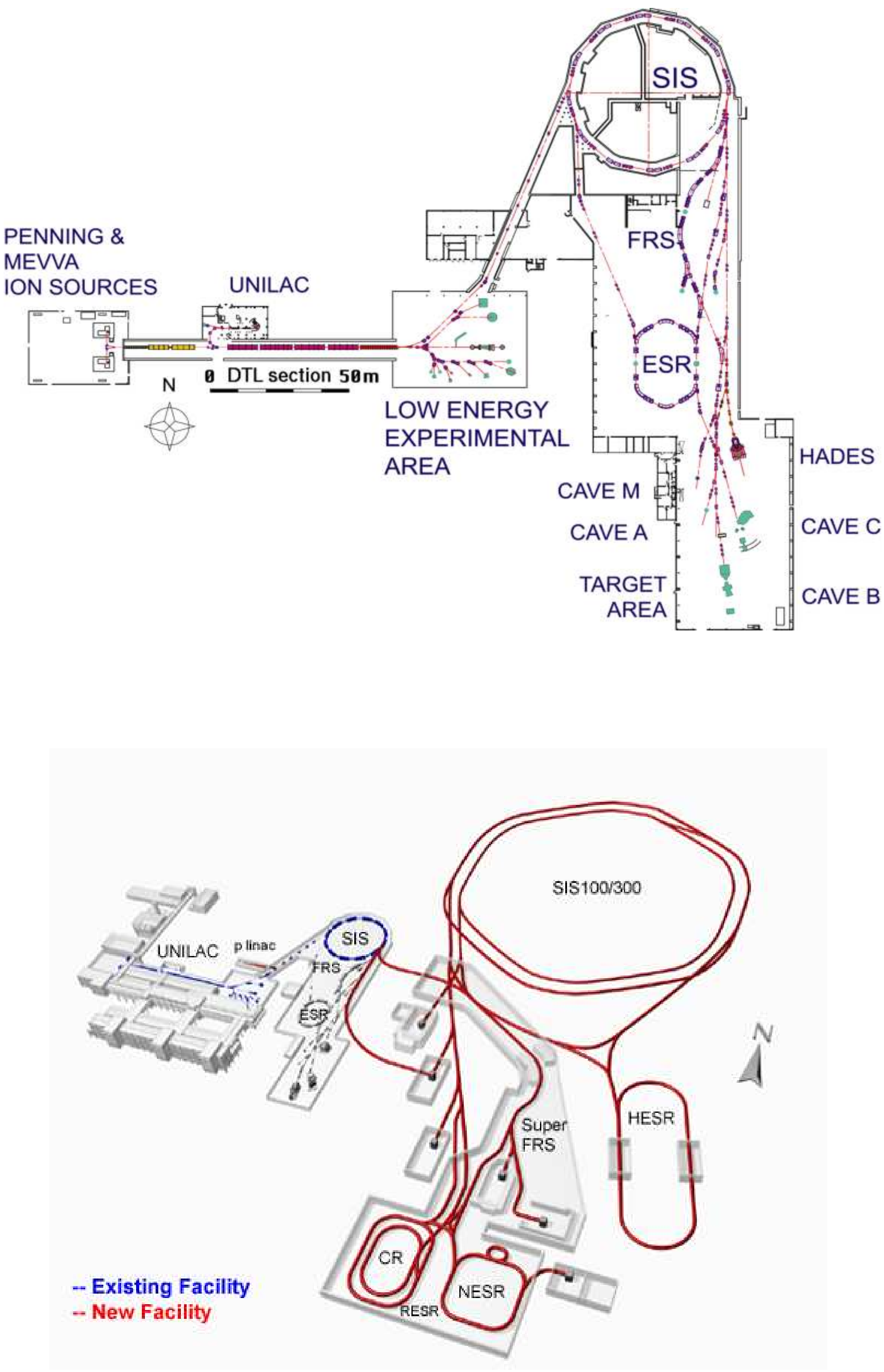

Figure 2.1: View of the actual complex of accelerators and the planned complex for the FAIR project at GSI.

Ion species:	p to ^{238}U^{73+}
Final energies:	4.5 GeV (p), 2 GeV/u (Ne^{10+}), 1 Gev/u (U^{73+})
Circumference:	216.72 m
Magnetic rigidity:	18 Tm
# of periods:	12
Bending radius:	10 m
Injection scheme:	horizontal multi-turn-injection
Injection energy:	11.4 MeV/u
Acceptance:	200 (horizontal) 50 (vertical) mm mrad
Momentum spread:	$\pm 1 \times 10^{-3}$ (FWHM) without cooling
Working point:	4.29, 3.29
RF frequency range:	0.85 - 6.02 MHz
Harmonic number:	4
Extraction scheme:	fast, slow ($\Delta T \leq 8$ s)
Resid. gas pressure:	4×10^{-11} mbar

Table 2.1: Main parameter list of the SIS-18

SIS-18 instrumentation

The SIS-18 is equipped with a large collection of instruments used to control the beam and measure its parameters. In this section a brief description of those instruments of interest in the context of the present work is given.

The beam positioning system consists of 12 dual-plane BPMs located at the end of the 12 focusing periods. Two additional phase pick-ups are available and used for the transverse feedback system. A resonant pick-up is also installed for Schottky measurement (tunes and momentum spread). A turn-by-turn multi-BPM acquisition system is under development. Presently a 20 MHz 4-channel 12 bits PCI card with a resolution of $\delta x/x \simeq 10^{-3}$ is available for turn-by-turn sampling of a single BPM [2, 3]. A new 500 MHz single-BPM acquisition system has been recently installed and tested [4].

Transverse beam profiles are measured by a recently developed residual gas monitor. A detailed description of this hardware is given in Sec. 7.4.

Transverse betatron oscillations can be driven either by a transverse kicker magnet used for tune measurement (Q-kicker), or by a horizontal noise shaker originally developed for knock-out extraction. A vertical shaker is also installed but not in use.

Resonant extraction and chromaticity correction are performed by means of 12 normal sextupoles independently powered. 8 independent skew quadrupoles have been recently installed for linear coupling resonance correction and optimization of multi-turn-injection. An additional normal quadrupole is also installed for correction of the half-integer resonance.

2.2 Motivations in view of the SIS-18 upgrade and FAIR

The SIS-18 top intensity reached so far with $^{238}\text{U}^{+73}$ is of $4 \div 5 \times 10^9$ particles at 0.5 Hz extracted at 1 GeV/u. The SIS-18 upgrade program [5] in the framework of the FAIR project foresees an increase of the extracted beam intensity staged in to phases. In the first one, the SIS-18 shall be upgraded to deliver 2×10^{10} particles ($^{238}\text{U}^{+73}$) at 1 Hz to the new Super Fragment Separator (SFR). In the second phase it shall operate as booster of the SIS-100 with a nominal intensity of 10^{11} particles ($^{238}\text{U}^{+28}$) at 2.6 Hz. Both stages, among other aspects, require a precise control and manipulation of the beam parameters at injection as well as at extraction and a continuous monitoring of lattice coupling and nonlinearities.

The SIS-18 shall also accelerate protons out of the new high-intensity proton linac [6]. Improving the injection scheme at low energy would result in a more compact and convenient linac design.

In this section the main motivations of the present study are outlined. Most of the new algorithm and schemes discussed in this work could not be tested and applied directly to the SIS-18, as the needed turn-by-turn acquisition of beam position monitors (BPM) is still under development. BPM data from the Super Proton Synchrotron (SPS) of CERN and the Relativistic Heavy Ion Collider (RHIC) of BNL were used. Both machines are also briefly described.

2.2.1 Measurement of nonlinearities

Nonlinearities in circular hadron accelerators are closely related to the shrinking of the dynamic aperture (stable region in phase phase) and to the deterioration of the beam quality. For high-intensity beams occupying almost the entire pipe aperture, among other effects, uncontrolled nonlinearities drive unstable motion for particles close to the beam pipe, resulting in particles hitting the vacuum chamber, electron clouds, vacuum break-down and eventually unacceptable beam loss.

The SIS-18 is a normal-conducting machine operating with transverse tunes separated by one integer (split tunes). The tune separation mitigates the strengths of the most dangerous resonances and the nonlinear field errors in the room-temperature magnets are usually one order of magnitude lower than the one driven by superconducting magnets. The monitoring the eddy currents during ramp is anyway of help preventing emittance blow-up.

A continuous monitoring of both the strength and polarities of extraction sextupoles will be also of help improving the spill structure during slow extraction over several seconds [7].

Both the SIS-100 and SIS-300 are super-conducting machines with tunes having the same integer part (unsplit tunes). Control and correction of nonlinearities in the magnet fields are therefore mandatory at any stage of the machine cycle.

2.2.2 Linear coupling studies

Natural lattice linear coupling is driven by errors and tilted installations of the focusing quadrupoles and is usually compensated or controlled by means of skew quadrupoles (i.e. normal quadrupoles rotated of 45^o).

The most critical stage as far as linear coupling is concerned is the injection phase, where the working point is usually chosen to be close to the difference resonance, namely with almost equal fractional part of the tunes. In this region linear coupling drives a fast emittance transfer between the two transverse planes. With the horizontal emittance usually larger than the vertical acceptance (i.e. the maximum acceptable emittance) this exchange might drive losses due to a vertical beam scraping. Correcting linear coupling after injection is therefore beneficial preventing such losses.

On the other hand a controlled linear coupling can be of help during multi-turn-injection. The beamlets out of the injector have a vertical emittance lower than the vertical acceptance. Multi-turn-injection is performed horizontally and a fast emittance transfer to the vertical plane can increase the injection efficiency. Such a scheme was proposed and successfully applied for the first time at the PS-booster [8] and has been proposed for the SIS-18 [9].

Increasing the injection efficiency at low energy will be beneficial also for the proton linac under design at the IAP [6], lowering its final energy and, in turn, its cost.

for the SIS-18 operations as booster of the SIS-100 it might be advantageous to have equal emittances at extraction. In this work a scheme to achieve such equilibration via linear coupling is presented.

2.2.3 Analysis of RHIC and SPS data

Both the algorithm and the software written to measure sextupolar nonlinearities from BPM data have been tested using data acquired in 2002 in the Super Proton Synchrotron (SPS) of CERN [1, 10, 11]. The SPS turn-by-turn multi-BPM acquisition [12] and the presence of eight strong sextupoles for resonant extraction offered a unique opportunity for this purpose and a proof that such measurements will be possible also in the SIS-18 as soon as an analogous acquisition system will be ready.

Since the SPS is a machine operating with unsplit tunes linear coupling correction requires one family of skew quadrupoles only, whereas in machines with split tunes like the SIS-18 at least two families are necessary requiring a different correction strategy (See discussion in Sec. 8.1). The same software for BPM data analysis has been therefore updated for linear coupling studies and tested using data of the super-conducting Relativistic Heavy Ion Collider (RHIC) of the Brookhaven National Laboratories, whose nominal working point is $Q_x = 28.28$, $Q_y = 29.29$. Most of the RHIC BPM data were acquired after exciting the beam with an AC dipole [13], whose advantage with respect to the traditional Q-kicker is that neither decoherence nor emittance blow up is induced, preserving the beam quality and increasing the experimental resolution. This makes possible to perform measurement in parasitic without deteriorating the beam before extraction, and, more important, to monitor the beam optics during ramp. The success of this technique in RHIC has a direct impact on the SIS-18, where a similar AC shaker was originally installed for knock-out extraction and is suitable for these type of measurement.

Chapter 3

Resonance driving terms (RDT): theoretical basis

The new theoretical findings on lattice nonlinear beam dynamics and betatron linear coupling presented in the next chapters are based on the description in normal forms of the betatronic motion. In this chapter the theoretical background of this formalism is outlined, reviewing the main results derived in Refs. [1, 15]. The intent is here also of introducing a unified formalism to be used as basis for the new derivations of Chapter 4, since in the literature slightly different notations and resonance classifications exist.

The normal form approach has been independently proposed and developed in the 90's by the Bologna group [16, 17, 18, 19] and E. Forest [20, 21, 22] for a detailed description of the betatron motion driven by nonlinearities. The application of this complex mathematical tool in the realm of particle accelerators is justified by two main aspects: the beam dynamics is dominated by linear potentials and nonlinearities are described with polynomial terms (multipolar expansion) whose effects are usually small perturbations making the motion quasi-periodic.

Once the beam is transversely displaced (either by fast kicker magnets or AC exciters), it experiences coherent oscillations that can be recorded turn by turn by beam position monitors (BPM). The spectrum of these oscillations can be inferred via FFT. If the lattice is free from nonlinearities the spectrum contains the betatron tune line only, whereas introducing nonlinearities secondary spectral lines appear.

Bartolini and Schmidt [15], constructing the normal form of the one-turn map, already clarified the connection between the spectrum of the complex variable $x-ip_x$ and the resonances excited by sextupoles, i.e. between the secondary lines and the sextupolar resonance driving terms (RDTs).

In the following sections the map approach to describe the betatron motion in circular accelerators is outlined together with the nonresonant normal form transformation. The corresponding RDTs are then defined and explicited in terms of the observable BPM spectral lines.

3.1 Physics assumptions and hypothesis

The approach we present is based on a first order nonresonant normal form.

The following analysis is limited up to the sextupoles. Higher multipoles, such as octupoles, can still be studied with a first order normal form, but only in absence of sextupoles, whose second order terms are of the same order of magnitude as the octupolar first order terms.

Effects due to chromaticity and dispersion are not taken into account.

Dealing with the complex variable $x - ip_x$, also the momentum p_x must be inferred from BPM data. It is well-known [25] how to derive p_x at one BPM looking at the position of the next BPM provided that the region between the two probes is free from nonlinearities. So far no analogous relations have been derived without this assumption. In this chapter we refer to “BPM” as a pair (or two pairs if they are single-plane monitors) of pick-ups whose region in between is free of nonlinearities, namely a location were both x and p_x can be inferred exactly. If this condition is not satisfied, a more subtle approach using either one or three BPMs should be used (see Chapter 4).

In the derivation of our algorithm we make use of the optical functions at the magnets and BPM locations. Effects due to lattice errors, such as beta beating, are not taken into account.

3.2 One-turn map, Hamiltonian coefficients and nonlinearities

Following the approach given in [15] and [1], the beam centroid at a certain position b (BPM) is modeled as a single particle whose transport after one turn is described by the one-turn (symplectic) map acting on the 4D vector $\mathbf{X_b} = (x, p_x, y, p_y)|_b$

$$\mathbf{X_{b,i}} = \mathcal{M}_b \mathbf{X_{b,i-1}}, \qquad \mathcal{M}_b = M_{W+1} \prod_{w=1}^{W} e^{:H_w:} M_w, \tag{3.1}$$

where W is the number of nonlinear multipoles. According to fig. 3.1, M_w is the linear map describing the linear elements (dipole, drift or quadrupole) between the nonlinear magnets $w-1$ and w. The latter ones are described by the Hamiltonian H_w and $e^{:H_w:}$ is the Lie operator. The linear map M_{W+1} is introduced to take into account the linear section between the last multipole and the position b. It can been shown [1] that moving to the complex Courant-Snyder coordinates

$$\begin{pmatrix} \hat{x} \\ \hat{p}_x \end{pmatrix} = \begin{pmatrix} (\beta_x)^{-1/2} & 0 \\ \alpha_x (\beta_x)^{-1/2} & (\beta_x)^{1/2} \end{pmatrix} \begin{pmatrix} x \\ p_x \end{pmatrix},$$

$$h_{x,\pm} = \hat{x} \pm i\hat{p}_x = \sqrt{2J_x} e^{\mp i(\phi_x + \phi_{x,0})} \quad , \tag{3.2}$$

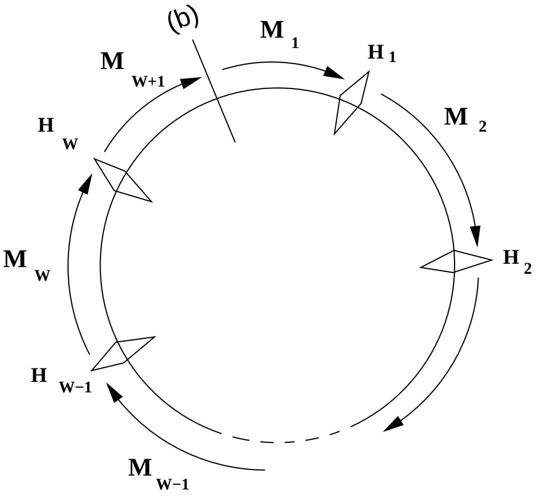

Figure 3.1: Schematic view of a ring and its transfer maps, M_w refer to sections free of nonlinearities, H_w represent the nonlinear kicks.

the one-turn map simplifies to

$$\mathcal{M}_b = \prod_{w=1}^{W} e^{:\tilde{H}_{bw}:} R \quad , \tag{3.3}$$

where R is the rotation matrix describing the linear motion (its angles are 2π times the betatron *linear* tunes) and $\tilde{H}_{bw}$ is the Hamiltonian expressed in the new coordinates *propagated* by the map describing the linear lattice between the observation point b and the w-th multipole. Defining the coordinate 4D vector

$$\mathbf{h_w} \quad = \quad (h_{w,x,+} \,, h_{w,x,-} \,, h_{w,y,+} \,, h_{w,y,-}) \quad , \tag{3.4}$$

the propagation is defined as

$$\mathbf{h_{bw}} \quad = \quad M_b \cdot M_{b+1} \cdots M_w \mathbf{h_w} \quad . \tag{3.5}$$

In the complex Courant-Snyder coordinate the above relation is a rotation whose angle is the phase advance between the points w and b (as the propagation is a linear map composition the actions $J_{x,y}$ do not change)

$$h_{bw,q,\pm} = h_{w,q,\pm} \; e^{\mp i \Delta\phi^b_{w,q}} \tag{3.6}$$

and $\tilde{H}_{bw}$ becomes

$$\tilde{H}_{bw} = H_w(\mathbf{h_{bw}}) \quad . \tag{3.7}$$

Applying the properties of the Lie operator and using the Campbell-Backer-Hausdorf theorem up to the first order the product in Eq. (3.3) reads

$$\prod_{w=1}^{W} e^{:\tilde{H}_{bw}:} \simeq e^{:\tilde{H}_{b}:}, \quad \tilde{H}_b = \tilde{H}_b(J_x, J_y, \phi_x, \phi_y) = \sum_{w=1}^{W} \tilde{H}_{bw} \quad . \tag{3.8}$$

According to Eqs. (3.3) and (3.8), in the complex Courant-Snyder coordinates, up to the first order, the one-turn map is factorized in a rotation and a Lie operator containing the sum of all the nonlinear contributes properly propagated.

We derive now an explicit expression for the Hamiltonians H_w introduced in (3.1). Dealing with the Lie operator, H_w are integrated Hamiltonians and all the nonlinear elements are modeled as thin kicks. The starting point is the multipolar expansion

$$H_w = -\Re\left[\sum_{n\geq 2}(K_{n-1} + iJ_{n-1})\frac{(x+iy)^n}{n!}\right]_w = \sum_{n\geq 2} H_w^{(n)} \quad . \tag{3.9}$$

According to this nomenclature, the skew quadrupole ($n = 2$) coefficient is J_1 [m^{-1}], the normal sextupole ($n = 3$) coefficient is K_2 [m^{-2}] whereas J_2 [m^{-2}] refers to the skew sextupole ($n = 3$). In the complex Courant-Snyder coordinates $H_w^{(n)}$ reads

$$\begin{aligned}\tilde{H}_w^{(n)} &= \sum_{jklm}^{n=j+k+l+m} h_{w,jklm} h^j_{w,x,-} h^k_{w,x,+} h^l_{w,y,-} h^m_{w,y,+} \\ &= \sum_{jklm}^{n=j+k+l+m} h_{w,jklm} (2J_x)^{\frac{j+k}{2}} (2J_y)^{\frac{l+m}{2}} e^{i[(j-k)(\phi_x+\phi_{x,0})+(l-m)(\phi_y+\phi_{y,0})]} \quad .\end{aligned} \tag{3.10}$$

The coefficients $h_{w,jklm}$ are real and proportional to the multipole strengths via (see APPENDIX A for the derivation)

$$\begin{aligned} h_{w,jklm} &= -\frac{\left[K_{w,n-1}\Omega(l+m) + iJ_{w,n-1}\Omega(l+m+1)\right]}{j!\ \ k!\ \ l!\ \ m!\ \ 2^{j+k+l+m}} i^{l+m}\left(\beta_{w,x}\right)^{\frac{j+k}{2}}\left(\beta_{w,y}\right)^{\frac{l+m}{2}}, \\ \Omega\ \ &(i) = 1 \text{ if } i \text{ is even}, \quad \Omega(i) = 0 \text{ if } i \text{ is odd} \quad . \end{aligned} \tag{3.11}$$

$\Omega(i)$ is introduced to select either the normal or the skew multipoles. According to the above relation the dimensions of $h_{w,jklm}$ are

$$\begin{array}{ccccccc} [h_{w,jklm}] & = & \mathrm{m}^{-(n-1)} & \cdot\ \mathrm{m}^{\frac{j+k}{2}} & \cdot\ \mathrm{m}^{\frac{l+m}{2}} & = \mathrm{m}^{1-\frac{j+k+l+m}{2}} \\ & & \Uparrow & \Uparrow & \Uparrow & \\ & & K_{n-1}, J_{n-1} & \left(\beta_{w,x}\right)^{\frac{j+k}{2}} & \left(\beta_{w,y}\right)^{\frac{l+m}{2}} & \end{array}$$

From Eqs. (3.6)-(3.7) $\tilde{H}_{bw}$ eventually reads

$$\tilde{H}_{bw} = \sum_{jklm}^{n=j+k+l+m} h_{w,jklm} e^{i[(j-k)\Delta\phi^b_{w,x}+(l-m)\Delta\phi^b_{w,y}]} h^j_{w,x,-} h^k_{w,x,+} h^l_{w,y,-} h^m_{w,y,+} \quad , \tag{3.12}$$

where $\Delta\phi^b_w$ is the phase advance between the locations b and w.

3.3 Normal form, resonance driving terms and BPM spectrum

The Hamiltonian $\tilde{H}_b$ defined in Eq. (3.8) depends on both the actions J_x, J_y and the phases $\phi_{b,x}$, $\phi_{b,y}$. Nonresonant normal form coordinates can be introduced to obtain a Hamiltonian (i.e. a one-turn map) depending on the action variables only, e.g. $\mathsf{H}_b(I_x, I_y)$. The transformation is performed by a generating function F

$$\begin{aligned} F &= \sum_{jklm}^{n=j+k+l+m} f_{jklm} \zeta_{x,-}^{j} \zeta_{x,+}^{k} \zeta_{y,-}^{l} \zeta_{y,+}^{m} \qquad (3.13) \\ &= \sum_{jklm}^{n=j+k+l+m} f_{jklm} (2I_x)^{\frac{j+k}{2}} (2I_y)^{\frac{l+m}{2}} e^{i[(j-k)(\psi_x+\psi_{x,0})+(l-m)(\psi_y+\psi_{y,0})]} \quad , \end{aligned}$$

where $\zeta_{q,\pm} = \sqrt{2I_q} e^{\mp i(\psi_q+\psi_{q,0})}$. $I_{x,y}$, $\psi_{x,y}$ and $\psi_{x,y,0}$ are the new actions, phases and arbitrary initial conditions respectively. The symbolic expression for the transformation is

$$e^{:-F:} e^{:\tilde{H}:} R e^{:F:} = e^{:\mathsf{H}(I_x,I_y):} R \quad . \qquad (3.14)$$

It can be shown [24] that, making again use of the CBH theorem up to the first order, the generating function terms $f_{jklm}^{(b)}$ at a certain location b are related to the Hamiltonian coefficients $h_{w,jklm}$ via

$$f_{jklm}^{(b)} = \frac{h_{jklm}^{(b)}}{1 - e^{2\pi i[(j-k)Q_x+(l-m)Q_y]}} = \frac{\sum_w h_{w,jklm} e^{i[(j-k)\Delta\phi_{w,x}^{b}+(l-m)\Delta\phi_{w,y}^{b}]}}{1 - e^{2\pi i[(j-k)Q_x+(l-m)Q_y]}} \quad , \qquad (3.15)$$

where the sum is over all the nonlinear elements and $\Delta\phi_w^b$ is the phase advance between the w^{th} multipole and the location b. The resonance driving terms (RDTs) f_{jklm} (at any location) diverge when a resonance occurs, i. e. when

$$(j-k)Q_x + (l-m)Q_y = p \qquad p \in \mathbf{N} \quad . \qquad (3.16)$$

From the inverse transformation truncated to the first order

$$h(N) = e^{:F(N):} \zeta(N) \simeq h(N) + [F(N), \zeta(N)] \qquad (3.17)$$

it is possible to explicit turn by turn the Fourier components of the complex Courant-Snyder variables at location b:

$$\begin{aligned} h_{x,-}(b,N) &= \sqrt{2I_x} e^{i(2\pi\nu_x N+\psi_{b,x,0})} - \qquad (3.18) \\ & 2i \sum_{jklm} j f_{jklm}^{(b)} (2I_x)^{\frac{j+k-1}{2}} (2I_y)^{\frac{l+m}{2}} e^{i[(1-j+k)(2\pi\nu_x N+\psi_{b,x,0})+(m-l)(2\pi\nu_y N+\psi_{b,y,0})]} \end{aligned}$$

and

$$\begin{aligned} h_{y,-}(b,N) &= \sqrt{2I_y}e^{i(2\pi\nu_y N+\psi_{b,y,0})} - \\ & 2i\sum_{jklm} l f^{(b)}_{jklm}(2I_x)^{\frac{j+k}{2}}(2I_y)^{\frac{l+m-1}{2}}e^{i[(k-j)(2\pi\nu_x N+\psi_{b,x,0})+(1-l+m)(2\pi\nu_y N+\psi_{b,y,0})]} \ . \end{aligned} \tag{3.19}$$

The nonlinear tunes $\nu_{x,y}$ appear in the above expression instead of $Q_{x,y}$ introduced in (3.15), since this approach takes into account possible detuning due to either linear coupling or amplitude dependent effects.

Expressions (3.18) and (3.19) have the following form:

$$h_{q,-}(b,N) = a^{(b)}_{q,0}e^{i2\pi N\nu_q} + \sum_{jklm} a^{(b)}_{jklm}e^{i2\pi N(\theta_{j,k}\nu_x+\omega_{l,m}\nu_y)}$$

$$a^{(b)}_{q,0}, a^{(b)}_{jklm} \in \mathbf{C} \ , \qquad \theta_{j,k}, \omega_{l,m} \in \mathbf{N} \ .$$

The first term on the r.h.s. is the ***fundamental*** or ***tune*** line. Its position in the spectrum provides the fractional part of the tune ν. The ***secondary*** lines contained in the summation are instead generated by the nonlinear magnets as well as by skew quadrupoles and depend on the RDTs f_{jklm}. Their amplitude and phase in the horizontal spectrum are given by

$$H(1-j+k, l-m) = 2\cdot j|f^{(b)}_{jklm}|(2I_x)^{\frac{j+k-1}{2}}(2I_y)^{\frac{l+m}{2}} \tag{3.20}$$

$$\phi_{(1-j+k,l-m)} = \phi^f_{b,jklm} + (1-j+k)\psi_{b,x,0} + (m-l)\psi_{b,y,0} - \frac{\pi}{2} \ , \tag{3.21}$$

whereas in the vertical plane

$$V(k-j, 1+m-l) = 2\cdot l|f^{(b)}_{jklm}|(2I_x)^{\frac{j+k}{2}}(2I_y)^{\frac{l+m-1}{2}} \tag{3.22}$$

$$\phi_{(k-j,1+m-l)} = \phi^f_{b,jklm} + (k-j)\psi_{b,x,0} + (1-l+m)\psi_{b,y,0} - \frac{\pi}{2} \ . \tag{3.23}$$

$\phi^{f^{(b)}}_{jklm}$ denotes the phase of the RDTs f_{jklm}. The horizontal and vertical tune lines are represented by $H(1,0)$ and $V(0,1)$ respectively. Their amplitudes and phases are

$$H(1,0) = \sqrt{2I_x}, \qquad \phi_{H(1,0)} = \psi_{b,x,0} \ , \tag{3.24}$$

$$V(0,1) = \sqrt{2I_y}, \qquad \phi_{V(0,1)} = \psi_{b,y,0} \ . \tag{3.25}$$

Note that from equations (3.16)-(3.19), the spectral lines $H(1-j+k, l-m)$ and $V(k-j, 1-m+l)$ appear only if $j \neq 0$ and $l \neq 0$ respectively. In Sec. 3.4 the correspondences between excited spectral lines and RDTs are listed. Note that the analogous classification given in [15] is incorrect for those entries concerning the vertical plane [1]. In Fig. 3.2 some typical BPM spectra obtained by single particle tracking are also shown.

---

[1] The sign of the horizontal component of the vertical spectral lines has to be inverted. One of the Author (FS) recognized the error.

multipole kind	n	potential term	index relations	
norm. quad. x	2	x^2	$j+k=2$	$m+l=0$
norm. quad. y	2	y^2	$j+k=0$	$m+l=2$
skew quad.	2	xy	$j+k=1$	$m+l=1$
norm. sext. 1	3	x^3	$j+k=3$	$m+l=0$
norm. sext. 2	3	xy^2	$j+k=1$	$m+l=2$
skew sext. 1	3	y^3	$j+k=0$	$m+l=3$
skew sext. 2	3	x^2y	$j+k=2$	$m+l=1$

Table 3.1: Selection of index relative to skew quadrupole, normal and skew sextupole.

3.4 Resonance classification and nomenclature

The starting point for a complete classification (up to the first order) of RDTs, spectral lines and excited resonances are the following relations:

$$(j-k)Q_x + (l-m)Q_y = p \in \mathbf{N} \quad \text{excited resonance} \tag{3.26}$$

$$H(1-j+k, m-l) \quad \text{horizontal line, if } j \neq 0 \tag{3.27}$$

$$V(k-j, 1-l+m) \quad \text{vertical line, if } l \neq 0 \tag{3.28}$$

Not all the coefficients f_{jklm} are of interest to us, since only some of them are related to the multipoles. The generic potential $x^s y^q$ selects the index $j+k=s$ and $m+l=q$, as shown in table 3.1.

The indexes select in turn the driven resonances and the relative spectral lines. The latter are explicitly related to the RDTs in tab 3.2, where the line amplitudes $|a_{jklm}|$ and the phases ϕ^a_{jklm} are derived from equations (3.20)-(3.23).

Since the line $H(0,0)$ is driven by two RDTs (f_{2100} and f_{1011}) it is not considered an observable. Table 3.3 shows eventually how to compute the RDTs from the spectral lines, i.e. how to remove the dependences from $I_{x,y}$ and $\phi_{x,y,0}$. Note that these relations apply only to properly calibrated BPMs and turn-by-turn oscillations without decoherence.

QUADRUPOLE TERM $\propto x^2$, y^2

n	$jklm$	resonance	horiz. line	V-line	$\lvert a_{jklm}\rvert$	ϕ^a_{jklm}
2	1100	$(2,0)$	$(1,0)$ F		$(2I_x)^{1/2}$	$\psi_{x,0}$
2	0011	$(0,2)$		$(0,1)$ F	$(2I_y)^{1/2}$	$\psi_{y,0}$

SKEW QUADRUPOLE TERM $\propto xy$

n	$jklm$	resonance	H-line	V-line	$\|a_{jklm}\|$	ϕ^a_{jklm}
2	0110	(1,-1)		$(1,0)$	$2\|f_{0110}\|(2I_x)^{1/2}$	$\phi^f_{0110}+\psi_{x,0}-\frac{\pi}{2}$
2	1001	(1,-1)	$(0,1)$		$2\|f_{1001}\|(2I_y)^{1/2}$	$\phi^f_{1001}+\psi_{y,0}-\frac{\pi}{2}$
2	1010	(1,1)	$(0,-1)$	$(-1,0)$	H: $2\|f_{1010}\|(2I_y)^{1/2}$ V: $2\|f_{1010}\|(2I_x)^{1/2}$	H: $\phi^f_{1010}-\psi_{y,0}-\frac{\pi}{2}$ V: $\phi^f_{1010}-\psi_{x,0}-\frac{\pi}{2}$

NORMAL SEXTUPOLE TERM $\propto x^3$

n	$jklm$	resonance	H-line	V-line	$\|a_{jklm}\|$	ϕ^a_{jklm}
3	1200	(1,0)	$(2,0)$		$2\|f_{1200}\|(2I_x)$	$\phi^f_{1200}+2\psi_{x,0}-\frac{\pi}{2}$
3	2100	(1,0)	$(0,0)$		$4\|f_{2100}\|(2I_x)$	$\phi^f_{2100}-\frac{\pi}{2}$
3	3000	(3,0)	$(-2,0)$		$6\|f_{3000}\|(2I_x)$	$\phi^f_{3000}-2\psi_{x,0}-\frac{\pi}{2}$

NORMAL SEXTUPOLE TERM $\propto xy^2$

n	$jklm$	resonance	H-line	V-line	$\|a_{jklm}\|$	ϕ^a_{jklm}
3	0111	(1,0)		$(1,1)$	$2\|f_{0111}\|(2I_x 2I_y)^{1/2}$	$\phi^f_{0111}+\psi_{x,0}+\psi_{y,0}-\frac{\pi}{2}$
3	0120	(1,-2)		$(1,-1)$	$4\|f_{0120}\|(2I_x 2I_y)^{1/2}$	$\phi^f_{0120}+\psi_{x,0}-\psi_{y,0}-\frac{\pi}{2}$
3	1002	(1,-2)	$(0,2)$		$2\|f_{1002}\|(2I_y)$	$\phi^f_{1002}+2\psi_{y,0}-\frac{\pi}{2}$
3	1011	(1,0)	$(0,0)$	$(-1,1)$	H: $2\|f_{1011}\|(2I_y)$ V: $2\|f_{1011}\|(2I_x 2I_y)^{1/2}$	H: $\phi^f_{1011}-\frac{\pi}{2}$ V: $\phi^f_{1011}-\psi_{x,0}+\psi_{y,0}-\frac{\pi}{2}$
3	1020	(1,2)	$(0,-2)$	$(-1,-1)$	H: $2\|f_{1020}\|(2I_y)$ V: $4\|f_{1020}\|(2I_x 2I_y)^{1/2}$	H: $\phi^f_{1020}-2\psi_{y,0}-\frac{\pi}{2}$ V: $\phi^f_{1020}-\psi_{x,0}-\psi_{y,0}-\frac{\pi}{2}$

SKEW SEXTUPOLE TERM $\propto y^3$

n	$jklm$	resonance	H-line	V-line	$\|a_{jklm}\|$	ϕ^a_{jklm}
3	0012	(0,1)		$(0,2)$	$2\|f_{0012}\|(2I_y)$	$\phi^f_{0012}+2\psi_{y,0}-\frac{\pi}{2}$
3	0021	(0,1)		$(0,0)$	$4\|f_{0021}\|(2I_y)$	$\phi^f_{0021}-\frac{\pi}{2}$
3	0030	(0,3)		$(0,-2)$	$6\|f_{0030}\|(2I_y)$	$\phi^f_{0030}-2\psi_{y,0}-\frac{\pi}{2}$

SKEW SEXTUPOLE TERM $\propto x^2y$

n	$jklm$	resonance	H-line	V-line	$\|a_{jklm}\|$	ϕ^a_{jklm}
3	1101	(0,1)	$(1,1)$		$2\|f_{1101}\|(2I_x 2I_y)^{1/2}$	$\phi^f_{1101}+\psi_{x,0}+\psi_{y,0}-\frac{\pi}{2}$
3	2001	(2,-1)	$(-1,1)$		$4\|f_{2001}\|(2I_x 2I_y)^{1/2}$	$\phi^f_{2001}-\psi_{x,0}+\psi_{y,0}-\frac{\pi}{2}$
3	0210	(2,-1)		$(2,0)$	$2\|f_{0210}\|(2I_x)$	$\phi^f_{0210}+2\psi_{x,0}-\frac{\pi}{2}$
3	1110	(0,1)	$(1,-1)$	$(0,0)$	H: $2\|f_{1110}\|(2I_x 2I_y)^{1/2}$ V: $2\|f_{1110}\|(2I_x)$	H: $\phi^f_{1110}+\psi_{x,0}-\psi_{y,0}-\frac{\pi}{2}$ V: $\phi^f_{1110}-\frac{\pi}{2}$
3	2010	(2,1)	$(-1,-1)$	$(-2,0)$	H: $4\|f_{2010}\|(2I_x 2I_y)^{1/2}$ V: $2\|f_{2010}\|(2I_x)$	H: $\phi^f_{2010}-\psi_{x,0}-\psi_{y,0}-\frac{\pi}{2}$ V: $\phi^f_{2010}-2\psi_{x,0}-\frac{\pi}{2}$

Table 3.2: List of spectral lines driven by resonances and corresponding RDTs. ”F” means that the line is the fundamental one. Note that the half-integer resonance driven by normal quadrupoles is not derived from Eq. (3.26), because the latter one refers to the perturbative terms only.

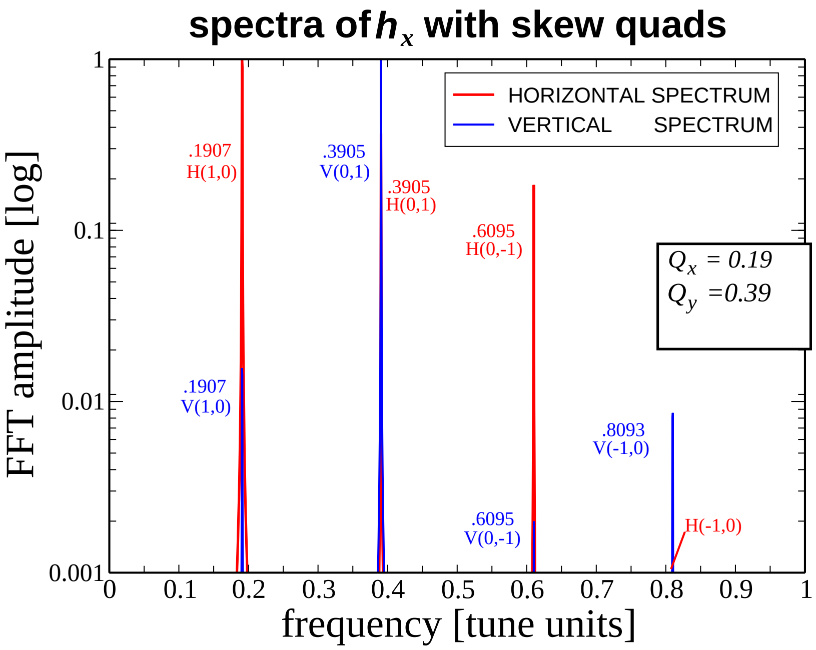

Figure 3.2: Examples of BPM spectra from single particle tracking simulation with betatron linear coupling driven by skew quadrupoles.

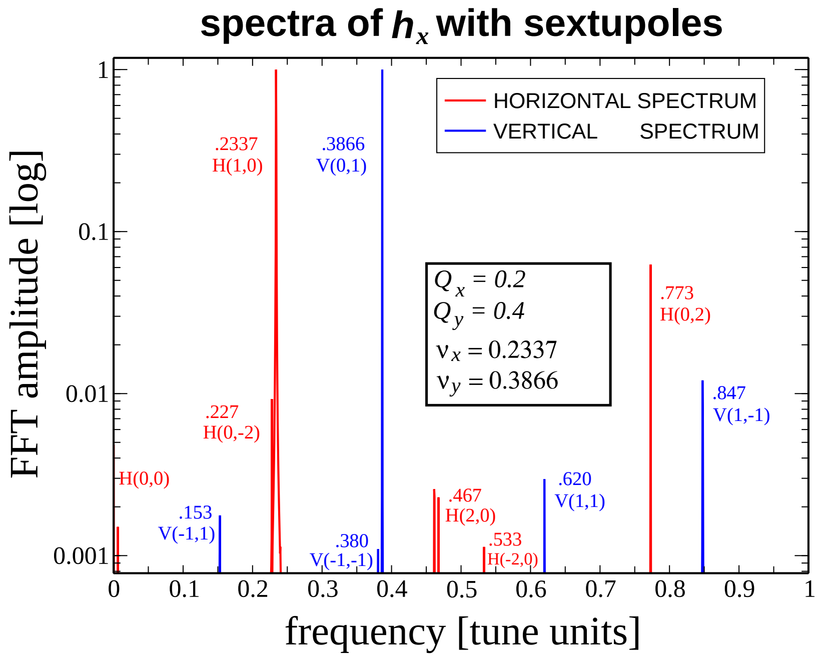

Figure 3.3: Examples of BPM spectra from single particle tracking simulation with non-linearities driven by normal sextupoles.

RDT f_{jklm}	amplitude $\lvert f_{jklm}\rvert$	phase ϕ^{f}_{jklm}
f_{0110}	$\frac{V(1{,}0)}{2H(1{,}0)}$	$\phi_{V(1,0)} - \phi_{H(1,0)} + \frac{\pi}{2}$
f_{1001}	$\frac{H0{,}1()}{2V(0{,}1)}$	$\phi_{H(0,1)} - \phi_{V(0,1)} + \frac{\pi}{2}$
f^{H}_{1010}	$\frac{H(0{,}-1)}{2V(0{,}1)}$	$\phi_{H(0,-1)} + \phi_{V(0,1)} + \frac{\pi}{2}$
f^{V}_{1010}	$\frac{V(-1{,}0)}{2H(1{,}0)}$	$\phi_{V(-1,0)} + \phi_{H(1,0)} + \frac{\pi}{2}$
f_{0111}	$\frac{V(1{,}1)}{2H(1{,}0)V(0{,}1)}$	$\phi_{V(1,1)} - \phi_{H(1,0)} - \phi_{V(0,1)} + \frac{\pi}{2}$
f_{0120}	$\frac{V(1{,}-1)}{4H(1{,}0)V(0{,}1)}$	$\phi_{V(1,-1)} - \phi_{H(1,0)} + \phi_{V(0,1)} + \frac{\pi}{2}$
f_{1002}	$\frac{H(0{,}2)}{2V(0{,}1)^2}$	$\phi_{H(0,2)} - 2\phi_{V(0,1)} + \frac{\pi}{2}$
f_{1011}	$\frac{V(-1{,}1)}{2H(1{,}0)V(0{,}1)}$	$\phi_{V(-1,1)} + \phi_{H(1,0)} - \phi_{V(0,1)} + \frac{\pi}{2}$
f^{H}_{1020}	$\frac{H(0{,}-2)}{2V(0{,}1)^2}$	$\phi_{H(0,-2)} + 2\phi_{V(0,1)} + \frac{\pi}{2}$
f^{V}_{1020}	$\frac{V(-{,}1-1)}{4H(1{,}0)V(0{,}1)}$	$\phi_{V(-1,-1)} + \phi_{H(1,0)} + \phi_{V(0,1)} + \frac{\pi}{2}$
f_{1200}	$\frac{H(2{,}0)}{2H(1{,}0)^2}$	$\phi_{H(2,0)} - 2\phi_{H(1,0)} + \frac{\pi}{2}$
f_{3000}	$\frac{H(-2{,}0)}{6H(1{,}0)^2}$	$\phi_{H(-2,0)} + 2\phi_{H(1,0)} + \frac{\pi}{2}$
f_{1101}	$\frac{H(1{,}1)}{2H(1{,}0)V(0{,}1)}$	$\phi_{H(1,1)} - \phi_{H(1,0)} - \phi_{V(0,1)} + \frac{\pi}{2}$
f_{2001}	$\frac{H(-1{,}1)}{4H(1{,}0)V(0{,}1)}$	$\phi_{H(-1,1)} + \phi_{H(1,0)} - \phi_{V(0,1)} + \frac{\pi}{2}$
f_{0210}	$\frac{V(2{,}0)}{2H(1{,}0)^2}$	$\phi_{V(2,0)} - 2\phi_{H(1,0)} + \frac{\pi}{2}$
f_{1110}	$\frac{H(1{,}-1)}{2H(1{,}0)V(0{,}1)}$	$\phi_{H(1,-1)} - \phi_{H(1,0)} + \phi_{V(0,1)} + \frac{\pi}{2}$
f^{H}_{2010}	$\frac{H(-1{,}-1)}{4H(0{,}1)V(0{,}1)}$	$\phi_{H(-1,-1)} + \phi_{H(1,0)} + \phi_{V(0,1)} + \frac{\pi}{2}$
f^{V}_{2010}	$\frac{V(-2{,}0)}{2H(1{,}0)^2}$	$\phi_{V(-2,0)} + 2\phi_{H(1,0)} + \frac{\pi}{2}$
f_{0012}	$\frac{V(0{,}2)}{2V(0{,}1)^2}$	$\phi_{V(0,2)} - 2\phi_{V(0,1)} + \frac{\pi}{2}$
f_{0030}	$\frac{V(0{,}-2)}{6V(0{,}1)^2}$	$\phi_{V(0,-2)} + 2\phi_{V(0,1)} + \frac{\pi}{2}$

Table 3.3: Formulae to infer f_{jklm} from the secondary lines assuming properly calibrated BPMs and turn-by-turn oscillations without decoherence.

Chapter 4

Magnet strength measurement from BPM data

The possibility of reconstructing the magnetic potential experienced by the beam in particle accelerators can be of great help during the machine commissioning and the routine maintenance. Once the corrector magnets such as skew quadrupoles and sextupoles are installed in the beam line, it is important to check that the power supplies generate the requested magnetic strengths and polarities. Field errors in dipoles and focusing quadrupoles, especially if superconducting, are also important to be continuously monitored to avoid dynamic aperture reductions.

If several BPMs are available, it is possible to localize the nonlinearities [1] from the variation along the ring of the RDTs. This method was successfully applied to the CERN SPS [10] where the RDTs were measured and polarity errors were detected and corrected. The minimization of the RDT f_{1001} was also used to correct betatron linear coupling in the SPS providing an alternative method to the minimization of the tune split ΔQ_{min}.

So far no explicit relations have been established between the spectral lines, or the RDTs, and the magnet strengths [1]. Making use of the formalism outlined in the Chapter 3, such new relations are derived here and applied to the same SPS data of [1], after some considerations on experimental issues.

4.1 From BPM spectrum to magnet strength

Nonzero multipole strengths, for example a skew quadrupole gradient $J_1 \neq 0$, as well as a sextupolar gradient $K_2 \neq 0$, result in a perturbing Hamiltonian via Eq. (3.11) and (3.12).

If the beam is transversely displaced it experiences coherent oscillations driven by both the (linear) focusing lattice and the coupling and/or nonlinear forces. The complex variable $h_{q,\pm}$ is constructed from the recorded oscillations via Eq. (3.2) and described as superposition of several harmonics whose amplitudes are proportional

---

[1] In the following the general expression “magnet strength” is used referring to both the corrector magnet strength and the field error

to the RDTs according to (3.18) and (3.19).
The fundamental lines provides the fractional parts of the tunes $\nu_{x,y}$ and the factors $\sqrt{2I_{x,y}}$ and $\psi_{x,y,0}$ necessary to infer the RDTs using Eq. (3.20)-(3.24).
If detuning effects are negligible, the measured tune $\nu_{x,y}$ corresponds to the linear one, $Q_{x,y}$, which can be directly used to infer the Hamiltonian coefficients $h_{w,jklm}$ via

$$f^{(b)}_{jklm} = \frac{h_{w,jklm} e^{i[(j-k)\Delta\phi^{b}_{w,x}+(l-m)\Delta\phi^{b}_{w,y}]}}{1 - e^{2\pi i[(j-k)Q_x+(l-m)Q_y]}} \ , \tag{4.1}$$

corresponding to Eq. (3.15) for $W = 1$. Inverting Eq. (3.11), the magnet strength is eventually inferred.

4.2 Magnet strengths from RDT variation along the ring

The direct relation $K_{w,n-1}, J_{w,n-1} \leftrightarrow h_{w,jklm} \leftrightarrow f^{(b)}_{jklm}$ is valid under the condition that a single multipole drives the h_{jklm} terms along the machine. If many multipoles of the same kind (i.e. described by the same set of index $jklm$) are present, Eq. (4.1) does not hold anymore. The summation over all multipoles and the availability of several BPMs lead to the linear system (3.15) whose analytic solution is derived in APPENDIX B.

The difference of the resonance driving terms at two observation locations (BPMs) of the ring, w and $w-1$, depends only on the multipoles placed between these two locations

$$\hat{h}_{w,jklm} = f^{(w)}_{jklm} e^{-i[(j-k)\Delta\phi_x^{w,w-1}+(l-m)\Delta\phi_y^{w,w-1}]} - f^{(w-1)}_{jklm} \ , \tag{4.2}$$

where $\Delta\phi_q^{w,w-1}$ are the phase advances between the two locations and $f^{(w)}_{jklm}$ are the RDTs measured at the w-th BPM. The l.s.h. of the above equation is therefore an observable given by

$$\hat{h}_{w,jklm} = \sum_{\tau} h_{\tau,jklm} e^{i[(j-k)\Delta\phi^{w-1}_{\tau,x}+(l-m)\Delta\phi^{w-1}_{\tau,y}]} \ . \tag{4.3}$$

The sum runs over all the multipoles between the $(w-1)$-th and the w-th BPMs, and $\Delta\phi^{w-1}_{\tau,q}$ are the phase advances between those multipoles and the $(w-1)$-th BPM. $h_{\tau,jklm}$ are the Hamiltonian coefficients defined in Eq. (3.11).
Eq. (4.2) reveals the most important feature of this approach: from the variation of the RDT f_{jklm} between two locations the total strength of the multipoles in between $\hat{h}_{w,jklm}$ is inferred.

In Fig. 4.1 the variation along the SIS-18 ring of $|f_{1001}|$ is plotted showing abrupt jumps corresponding to skew quadrupoles (single particle tracking simulation).

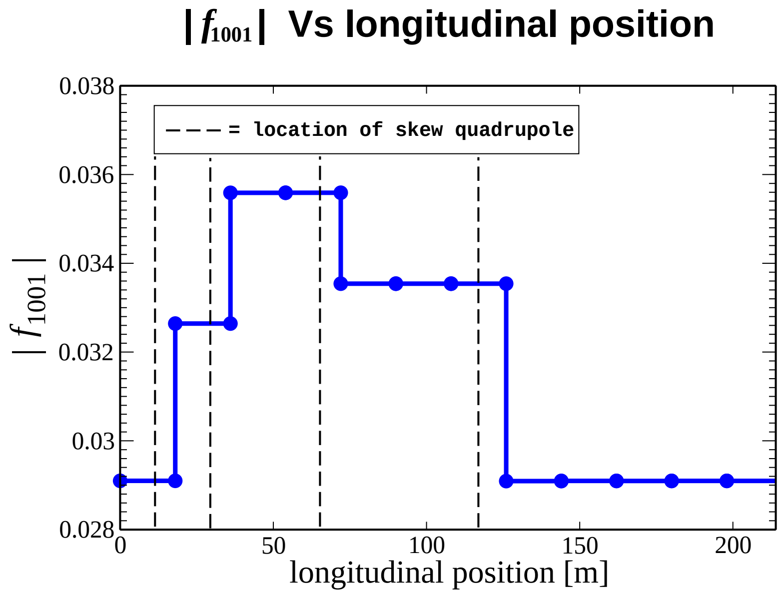

Figure 4.1: .Variation of $|f_{1001}|$ along the SIS-18 ring together with the locations of the simulated skew quadrupoles.

As shown in [1, 26] and reported in Sec. B.2 the variation along the ring of the RDT becomes weaker approaching a resonance, where f_{jklm} is invariant.

In general it is not possible to extract from $\hat{h}_{w,jklm}$ directly the strengths K and J. Nevertheless, in the case of only one multipole between two consecutive BPMs, Eq. (4.2) simplifies to

$$h_{w,jklm}e^{-i[(j-k)\Delta\phi_x^w+(l-m)\Delta\phi_y^w]} = f_{jklm}^{(w)}e^{-i[(j-k)\Delta\phi_x^{w,w-1}+(l-m)\Delta\phi_y^{w,w-1}]} - f^{(w-1)}. \tag{4.4}$$

If the betatron phase and the beta functions at the multipole are known, from the l.s.h. of the above equation and Eq. (3.11), the strength $K_{w,n-1}$ or $J_{w,n-1}$ is inferred.

Even if the amplitudes of the RDTs change ***only*** in presence of nonlinear magnets switched on, it is not true that the latter ones make ***always*** the RDTs change. Indeed, particular lattice configurations exist, which can make the method fail, as shown in Sec. B.1.

4.3 Experimental aspects

In the previous chapter we assumed ideal BPMs with calibration factors $\eta_{x,y} = 1$. This assumption might not hold in a real accelerator due to calibration errors and pick-up tilting. Misalignment error are less severe, since they produce an off-center signal whose only effect is to drive a zero-frequency line that we are not interested in.

Wrong momentum reconstruction from two consecutive BPMs due to nonlinearities placed in between introduces another error when computing the complex Courant-Snyder variable $h_{q,-}$.

The computation of $h_{q,-}$, as well as Eq. (4.2), makes also use of the Twiss parameters $\Delta\phi$ and β at the BPM location. Deviation from the model of the real linear optics is another source of error when inferring the magnet strength $\hat{h}_{jklm}$.

These experimental aspects are addressed in this section, together with some strategies aimed to reduce the sources of errors.

4.3.1 BPM calibration factor

Calibration errors result in a wrong BPM signal and a scaled complex Courant-Snyder variable according to

$$h_{x,-} = \eta_x(\hat{x} - i\hat{p}_x), \qquad h_{y,-} = \eta_y(\hat{y} - i\hat{p}_y) \ , \tag{4.5}$$

where it is assumed that the calibration factors of the two consecutive pick-ups are the same. The normalizations listed in table 3.3 were introduced to remove the dependence of the secondary spectral lines on the actions and phases and infer the RDTs. If calibration factors need to be taken into account, that normalization introduces a dependence on $\eta_{x,y}$. From Eqs. (3.20) and (3.22)

$$\begin{aligned} |f^H_{jklm}| &\propto \frac{1}{\eta_x^{j+k-2}\eta_y^{l+m}} && \text{horizontal spectrum,} \\ |f^V_{jklm}| &\propto \frac{1}{\eta_x^{j+k}\eta_y^{l+m-2}} && \text{vertical spectrum.} \end{aligned} \tag{4.6}$$

As shown in [1, 10] for the RDTs excited by skew quadrupoles, a solution is provided combining the spectral line amplitudes in such a way to cancel out both η_x and η_y. Since $f_{0110} = f^*_{1001}$ and f_{1010} is visible in both the horizontal and vertical spectra,

$$|f_{1001}| = \sqrt{f^V_{0110} \cdot f^H_{1001}} = \frac{1}{2}\sqrt{\frac{V(1,0)H(0,1)}{H(1,0)V(0,1)}} \ , \tag{4.7}$$

$$|f_{1010}| = \sqrt{f^V_{1010} \cdot f^H_{1010}} = \frac{1}{2}\sqrt{\frac{V(-1,0)H(0,-1)}{H(1,0)V(0,1)}} \ , \tag{4.8}$$

do not depend anymore on the calibration factor.

This approach does not work for higher multipoles. A way to remove this dependence and infer f_{3000}, for example, is first to divide the line amplitude for the amplitude of the tune line

$$\tilde{H}(-2,0) = \frac{H(-2,0)}{H(1,0)} = 6|f_{3000}|\sqrt{2I_x} \quad , \tag{4.9}$$

and repeat the measurement for different kick amplitude ($\propto \sqrt{2I_x}$). From the slope of the linear fit f_{3000} is eventually inferred [10].

4.3.2 Do we really need to reconstruct the momentum?

The momentum reconstruction from two consecutive BPMs in the Courant-Snyder coordinates reads [25]

$$\hat{p}_{i,x} = (\hat{x}_{i+1} - \hat{x}_i \cos\Delta\phi_x)/\sin\Delta\phi_x \quad , \tag{4.10}$$

or, equivalently, if an up-stream BPM is used,

$$\hat{p}_{i,x} = (-\hat{x}_{i-1} + \hat{x}_i \cos\Delta\phi_x)/\sin\Delta\phi_x \quad , \tag{4.11}$$

where $\Delta\phi_x$ is the phase advance between the two BPMs. These relations hold only in absence of nonlinearities in between. If this condition is not satisfied a systematic error is introduced. In [27] a new (real) observable has been introduced from the turn-by-turn signals of three BPMs

$$\chi(N) = \frac{\tilde{x}_1}{\cos\delta_{x,1}} + \tilde{x}_2(\tan\delta_{x,1} + \tan\delta_{x,2}) + \frac{\tilde{x}_3}{\cos\delta_{x,2}} \quad , \tag{4.12}$$

where $\tilde{x}$ is the Courant-Snyder variable normalized to the amplitude of the foundamental betatron oscillation $\tilde{x} = \hat{x}/H(1,0)$, $\delta_{x,1} = \Delta\phi_{x,1} - \pi/2$, and $\delta_{x,2} = \Delta\phi_{x,2} - \pi/2$. $\Delta\phi_{x,1}$ and $\Delta\phi_{x,2}$ are the phase advances between the first and the second BPM and between the second and the third respectively. The construction of χ does not require any momentum reconstruction, and its FFT depends on the local nonlinearities, namely

$$\chi_{jklm} = \sum_q e^{i[(1-j+k)\phi_{xq}+(m-l)\phi_{yq}]} SEN(\phi_{xq}) h_{q,jklm} \ . \tag{4.13}$$

The above summation extends over the multipoles in between the three BPMs, $h_{q,jklm}$ are the coefficient defined in (3.11) of the q-th multipole, ϕ_{xq} and ϕ_{yq} are the phase advances between the first BPM and the q-th multipole, and $SEN(\phi_{xq})$ is defined as

$$\begin{cases} \sin\phi_{xq}\sqrt{1+\tan^2\delta_{x,1}} & \text{if } \phi_{xq} < \Delta\phi_{x,1} \\ \sin(\phi_{xq} - \delta_{x,1} - \delta_{x,2})\sqrt{1+\tan^2\delta_{x,2}} & \text{if } \phi_{xq} > \Delta\phi_{x,1} \end{cases}$$

If one multipole is placed in between the three BPMs, its strength and polarity can be unambiguously inferred, provided that the phase advance between the multipole and the first BPM is known. The analytical proof of these statements and expressions is given in [27].

If only one multipole is placed between the BPMs even one BPM is enough to measure its strength, despite the fact that the RDTs are not anymore observable. According to eq.(3.18) the turn-by-turn observable $\hat{x} = \Re\{h_{x,-}\}$ reads

$$\begin{aligned}\hat{x}(b,N) = \frac{\sqrt{2I_x}}{2}&[e^{i(2\pi\nu_x N+\psi_{b,x,0})} + c.c.] \;-\\ &2\Re\{i\sum_{jklm} j f^{(b)}_{jklm}(2I_x)^{\frac{j+k-1}{2}}(2I_y)^{\frac{l+m}{2}} \;\times\\ &\quad e^{i[(1-j+k)(2\pi\nu_x N+\psi_{b,x,0})+(m-l)(2\pi\nu_y N+\psi_{b,y,0})]}\}\;.\end{aligned}$$

For any complex number z, $\Re\{iz\} = -\Im\{z\}$ and the above summation simplifies in

$$\sum_{jklm} 2j(2I_x)^{\frac{j+k-1}{2}}(2I_y)^{\frac{l+m}{2}}\Im\{f^{(b)}_{jklm}e^{i[(1-j+k)(2\pi\nu_x N+\psi_{x,b,0})+(m-l)(2\pi\nu_y N+\psi_{b,y,0})]}\}\;.$$

For the sake of clarity we limit our analysis to the sextupolar terms $f^{(b)}_{3000}$ and $f^{(b)}_{1200}$. After some algebra, the above expression reads

$$(2I_x)e^{i\frac{\pi}{2}}\left[(3f^{*(b)}_{3000} - f^{(b)}_{1200}\,)\cdot e^{i2(2\pi\nu_x N+\psi_{b,x,0})} - (3f^{(b)}_{3000} - f^{*(b)}_{1200}\,)\cdot e^{-i2(2\pi\nu_x N+\psi_{b,x,0})}\right]$$

The first and second terms are complex conjugate and correspond to the $H(2,0)$ and $H(-2,0)$ lines respectively. The amplitude and the phase of the tune line can still be used to remove the dependence on I_x and $\psi_{b,x,0}$. A linear fit can also be used in the case the calibration factors must be taken into account. The complex quantity $3f^{(b)}_{3000} - f^{*(b)}_{1200}$ is therefore observable. From eq. (3.15)

$$3f^{(b)}_{3000} - f^{*(b)}_{1200} = 3\frac{\sum_w h_{w,3000}e^{-3i\Delta\phi_{x,bw}}}{1-e^{i6\pi Q_x}} - \frac{\sum_w h^{*}_{w,1200}e^{i\Delta\phi_{x,bw}}}{1-e^{i2\pi Q_x}}\;, \tag{4.14}$$

with $h_{w,1200} = 3h_{w,3000} = K_{w,2}\beta^{3/2}_{w,x}/16$, some algebra yields the linear system

$$3f^{(b)}_{3000} - f^{*(b)}_{1200} = \sum_w h_{w,1200}\left[\frac{e^{-3i\Delta\phi_{x,bw}}}{1-e^{i6\pi Q_x}} - \frac{e^{i\Delta\phi_{x,bw}}}{1-e^{i2\pi Q_x}}\right]\;, \tag{4.15}$$

where $\Delta\phi_{x,bw}$ is the horizontal phase advance between the b-th BPM and the w-th multipole and the summation extends over all the multipoles. The above linear system can be numerically inverted providing the strengths $h_{w,1200}$.

4.3.3 Upon the dependence on the model

According to eq. (3.2) the optical functions at the BPMs location are needed to construct the complex signal $h_{x,-}$. Nevertheless for practical uses we are interested only to its spectrum, i.e its Fourier Transform $\mathcal{F}\{\hat{x}_i - i\hat{p}_{i,x}\}$. As this is a linear operator, the computation can be split in two steps.
With $\hat{x}_i = x/\sqrt{\beta_{i,x}}$, $\mathcal{F}\{\hat{x}_i\} = \eta_x/\sqrt{\beta_{i,x}}\mathcal{F}\{x_i\}$, the constant $1/\sqrt{\beta_{i,x}}$ can be included in the calibration factor providing

$$\mathcal{F}\{\hat{x}_i\} = \eta_x^* \mathcal{F}\{x_i\} \quad . \tag{4.16}$$

According to eq. (4.10), we have

$$\mathcal{F}\{\hat{p}_{i,x}\} = \frac{\eta_{i+1,x}}{\sin\Delta\phi_{i,i+1}}\mathcal{F}\{\hat{x}_{i+1}\} - \eta_{i,x}\cot\Delta\phi_{i,i+1}\mathcal{F}\{\hat{x}_i\} \ .$$

Assuming that the calibration factor is the same for the two consecutive BPMs, i.e. $\eta_{i,x} = \eta_{i+1,x} = \eta_x$, and extracting $\eta_x^* = \eta_x/\sqrt{\beta_{i,x}}$, the above equation reads

$$\mathcal{F}\{\hat{p}_{i,x}\} = \eta_x^* \left[\frac{\sqrt{\beta_{i,x}}}{\sqrt{\beta_{i+1,x}}} \frac{1}{\sin\Delta\phi_{i,i+1}} \mathcal{F}\{x_{i+1}\} - \cot\Delta\phi_{i,i+1}\mathcal{F}\{x_i\} \ \right] \quad . \tag{4.17}$$

The ratio $\sqrt{\beta_{i,x}}/\sqrt{\beta_{i+1,x}}$ is equal to the ratio between the amplitudes of the i-th and the $(i+1)$-th tune lines. It is therefore observable and measured from $\mathcal{F}\{x_i\}$ and $\mathcal{F}\{x_{i+1}\}$. The same holds for $\Delta\phi_{i,i+1}$, which is the difference between the phases of the i-th and the $(i+1)$-th tune lines.

Eqs. (4.17) and (4.16) show that $\mathcal{F}\{\hat{x}_i - i\hat{p}_{i,x}\}$, and hence the RDTs, can be inferred in a model-independent way from the FFT of the pure BPM data x_i and x_{i+1}, without moving to the complex Courant-Snyder coordinates. The dependence on the calibration factor η_x^* can be removed according to Sec. 4.3.1. The same applies to the vertical signal.

4.4 Analysis of existing SPS data

During 2002 a measurement campaign aimed to measure the RDTs was carried out in the Super Proton Synchrotron (SPS) of CERN [1, 10, 11]. Seven strong sextupoles were connected to introduce large non-linearities. Their locations and the model parameters are listed in Tab. 4.1. Other 108 sextupoles used for the chromaticity correction where also turned on. These sextupoles are grouped in four families, whose parameters are listed in Tab. 4.2.

The new software application **bpm2rdt** has been developed for the analysis of BPM data and is documented in APPENDIX E. The code reads in input the

name	location [m]	K_2 [m^{-1}]	β_x [m]	h_{3000} [m$^{-1/2}$]
LSE.1060	766.2	0.44629	96.335	8.7913
LSE.1240	1342.2	0.44629	92.238	8.2365
LSE.2060	1918.2	0.44629	100.542	9.3734
LSE.2240	3646.1	-0.44629	100.210	-9.3271
LSE.4060	4222.0	-0.44629	90.488	-8.0032
LSEN.424	4798.0	-0.44629	97.020	-8.8852
LSE.5240	5373.9	-0.44629	94.413	-8.5300

Table 4.1: List and parameters of the excited normal sextupoles.

BPM turn-by-turn data and the Twiss parameters to construct $h_{q,-}(N)$ and $\chi(N)$ introduced in Sec. 4.3.2. Then it performs the FFT of these variables, finds the peaks of the Fourier spectra and infers the RDTs f_{jklm}, the strengths $\hat{h}_{jklm}$ and the local terms χ_{jklm}. All these observables are printed out together with the corresponding values of the model, computed from the nominal values of strengths and the Twiss parameters.

In Fig. 4.2 an example of turn-by-turn BPM data is shown together with the computed spectrum of $h_{x,-}(N)$. The tune line $H(1,0)$ is the largest peak at 0.1758, whereas the secondary line $H(-2,0)$ driven by f_{3000} is visible at 0.6484.

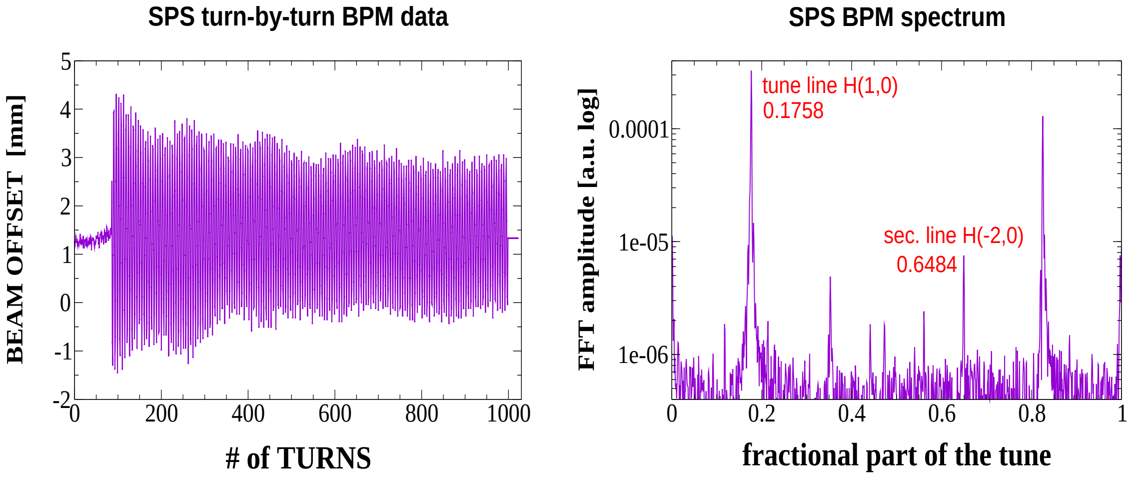

Figure 4.2: . Example of SPS turn-by-turn BPM data $x(N)$ (left) and BPM spectrum $\mathcal{F}\{\hat{x}_i - i\hat{p}_{i,x}\}$ (right). Note the tune line $H(1,0)$ at 0.1758 and the secondary line $H(-2,0)$ driven by f_{3000} at 0.6484. (SPS BPM data 2002, courtesy of R. Tomás and F. Schmidt)

family name	#	K_2 [m^{-1}]	β_x [m]
LSFA	36	-0.02245	∼100
LSFB	18	-0.04496	∼100
LSDA	18	0.08417	∼22
LSDB	36	0.06641	∼22

Table 4.2: Strengths of the sextupole families used for chromaticity correction.

Note that the relations listed in Tab. 3.2 are derived assuming turn-by-turn oscillations without decoherence and properly calibrated BPM. To take into account the decoherence of the SPS data the measured f_{3000} and χ_{3000} were multiplied by 2 according to Ref. [1].

BPM noise has been found to introduce large fluctuations when averaging several data sets. In Ref. [1] a BPM pre-analysis was carried out to detect and remove all the BPM producing a background noise higher than a certain threshold. The strategy adopted here does not include any data pre-processing: noisy BPMs are rejected *a posteriori* when the statistical fluctuations in the measured quantities are higher than 20%.

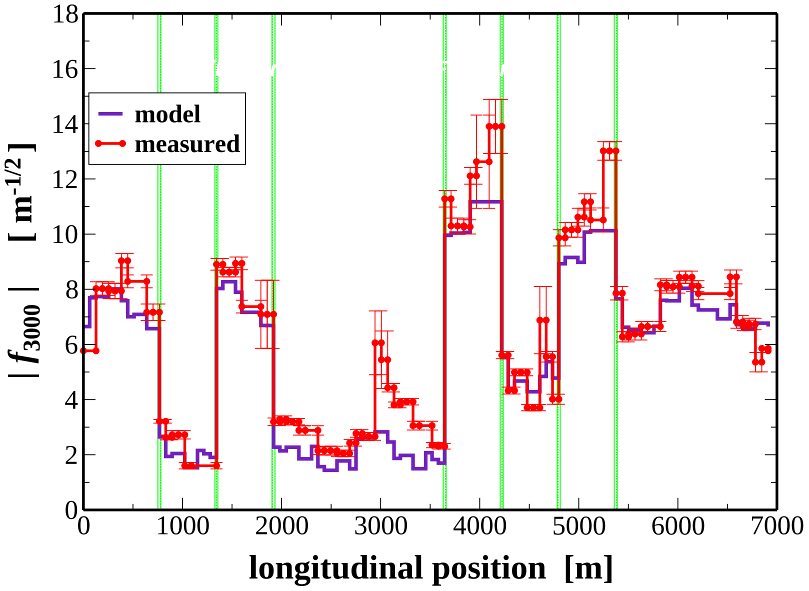

Figure 4.3: RDT f_{3000} along the ring. Error bars correspond to 1σ. Only the values from BPMs providing fluctuations smaller than 20% are shown (SPS BPM data 2002, courtesy of R. Tomás and F. Schmidt).

In Fig. 4.3 the measured f_{3000} is plotted around the ring together with the prediction from the model. Model and measurement are in good agreement as in [10, 11]. However the measured f_{3000} shows visible jumps at locations where they were not expected. This is due to a wrong momentum reconstruction and can be proven by measuring the local resonance term χ_{3000}, which does not need of any momentum reconstruction, see Fig 4.4. These local resonance terms are similar to the $\hat{h}_{3000}$ but are computed from three BPMs and are strictly local. Their value only depends on the sources placed between the three BPMs. Therefore, from the figure we conclude that there are only seven dominating sextupolar sources placed at the location of the strong sextupoles.

Due to the BPM distribution, LSE.1240, LSE.2240 and LSEN.424 fulfill the condition of being the only source of nonlinearities between the two adjacent BPMs. The other four extraction sextupoles have at least another chromaticity sextupole in between the two adjacent BPMs. However the extraction sextupoles are much stronger than the chromaticity sextupoles and as first approximation the latter ones might be neglected. Therefore the Hamiltonian terms $\hat{h}_{3000}$ at the location of the BPM next to the seven extraction sextupoles s_i read

$$|\hat{h}^{(s_i)}_{3000}| \simeq \frac{K_{s_i,2}\beta^{3/2}_{s_i,x}}{48} \tag{4.18}$$

In Fig. 4.5 the measured $\hat{h}_{3000}$ are plotted together with the predictions from the

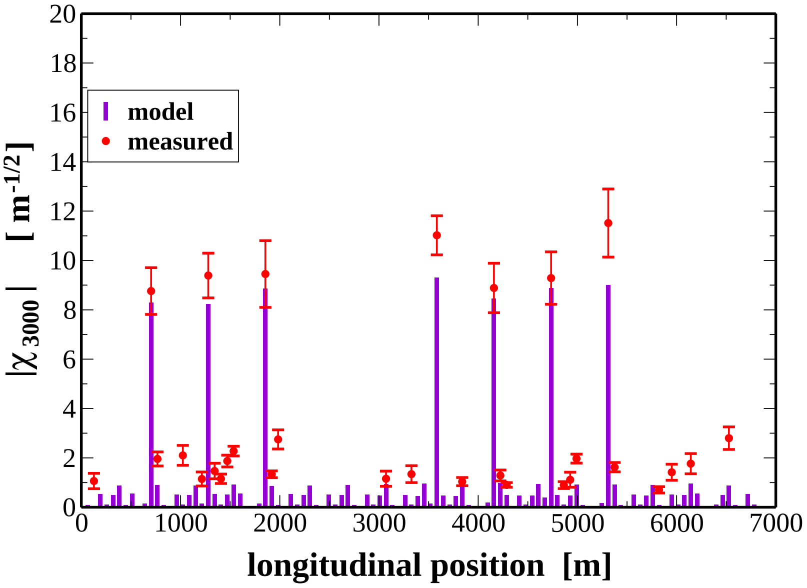

Figure 4.4: Measured and expected absolute value of χ_{3000}. Error bars correspond to 3σ. Only the values providing fluctuations smaller than 20% are shown (SPS BPM data 2002, courtesy of R. Tomás and F. Schmidt).

model. The agreement for $|\hat{h}_{3000}|$ varies from 3% (LSEN.424) to 28% (LSE.4060). Error in the phases is of about 10%, confirming the correct setting of the polarities. Due to the lattice configuration of the SPS the phases of $\hat{h}_{3000}$ provide a direct measurement of their polarities as shown in the figure.

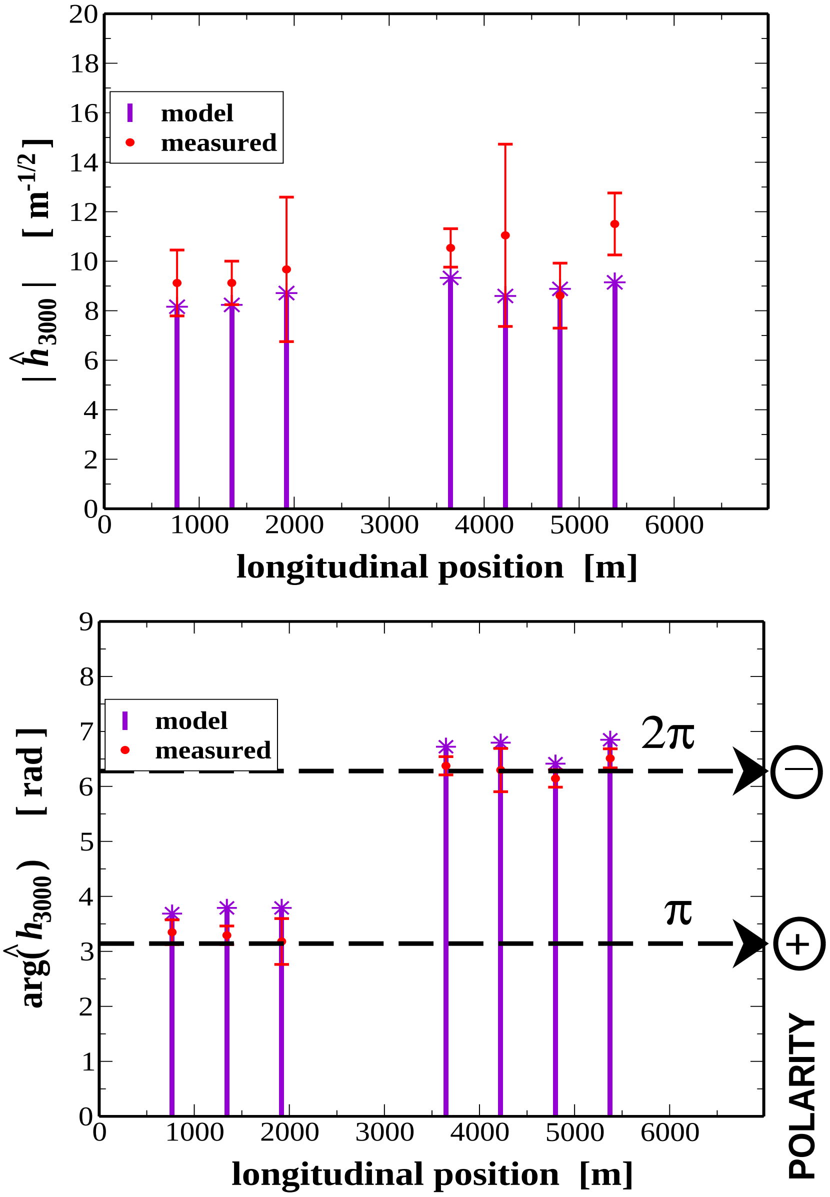

Figure 4.5: Measured and expected absolute value and phase of $\hat{h}_{3000}$ corresponding to the seven excited extraction sextupoles. Error bars correspond to 3σ (SPS BPM data 2002, courtesy of R. Tomás and F. Schmidt).

Chapter 5

Betatron coupling and emittance transfer: static case

Emittance transfer between planes has been widely studied in the framework of betatron linear coupling [8, 28, 29, 30]. The understanding of this mechanism is of help in both optimizing the multi-turn injection, distributing horizontal emittance in the vertical plane, and preventing beam losses when the emittance in one plane is larger than the acceptance in the other one.

Equations governing this process have been already derived from the equation of motion of a single particle. This results in coupled differential equations whose explicit solutions have been found in the smooth approximation only and assuming a uniformly distributed skew quadrupole representing the global betatron coupling. A more general treatment has been also derived in the **C** matrix notation [31], leading to relations straightforward to implement numerically, but difficult to explicit in terms of observables.

Emittance transfer has been studied mainly in two different processes, namely the *static approaching to the resonance* [8, 28] driving an emittance sharing, and the recently developed *dynamical resonance crossing* [29, 30], which lead to a complete emittance exchange between the two planes.

In this chapter we use the RDT formalism illustrated in Chapter 3 to derive analogous equations describing the emittance sharing in terms of f_{1001}. The new relations are able to describe the emittance transfer , turn by turn as well as averaged in time, to higher accuracy than the existing formulae. The advantage of this approach is that no differential equations need to be solved and the assumption of having a smooth lattice is removed. With respect to the **C** matrix approach, the dynamics is now parameterized by one complex number f_{1001}, instead of four real matrix elements. Explicit relations connecting the matrix and the RDT approaches are given in APPENDIX D.

In the following analysis betatron coupling is assumed to be weak enough and the dynamic crossing slow enough to make the particle distribution be always matched. This condition is essential for the derivation of the new formulae when computing the RMS emittance ϵ_x from the single particle emittance E_x. Longitudinal coupling is not take into account, as well as chromaticity, dispersion and tune modulation driven by synchrotron motion, as the beam under study is assumed to be coasting.

5.1 Short review of previous theory

Static approaching to the resonance refers to the exploration of the resonance stop band in several machine cycles. From cycle to cycle the tune in one plane is usually varied, keeping the other fixed. Both tunes are anyway fixed during each cycle. Close to the resonance, the transverse planes share their RMS emittances. The amount of sharing depends on the strength of the coupling and the distance from the resonance condition. On the resonance the two emittances (averaged over several turns) are equal, i.e. $\epsilon_x = \epsilon_y$. Analytic formulae were previously derived [8, 28] for a constant focusing lattice with uniform betatron coupling whose integrated strength is given by [32]

$$C = -\frac{1}{2\pi} \oint ds \; j(s) \sqrt{\beta_x(s)\beta_y(s)} e^{-i(\phi_x(s)-\phi_y(s))+is/R\Delta} \; , \tag{5.1}$$

where R is the machine radius, $j(s)$ the smoothly distributed skew quadrupole strength and Δ the distance from the resonance of the bare tunes (fractional part):

$$\Delta = Q_x - Q_y \; . \tag{5.2}$$

C is also known as the “tune difference on the coupling resonance”, ΔQ_{min}. The transverse RMS emittances, averaged over a time $T >> 1/|C|$, are coupled according to

$$\epsilon_x = \epsilon_{x0} + \frac{|C|^2}{\Delta^2 + |C|^2} \frac{\epsilon_{y0} - \epsilon_{x0}}{2} \tag{5.3}$$

$$\epsilon_y = \epsilon_{y0} - \frac{|C|^2}{\Delta^2 + |C|^2} \frac{\epsilon_{y0} - \epsilon_{x0}}{2} \tag{5.4}$$

In Fig. 5.1 RMS emittances from multi-particle simulations are plotted versus Δ and compared with Eqs. (5.3)-(5.4) for two different amounts of coupling, $|C| = 1\%$ and $|C| = 0.2\%$ respectively. In the latter case the RMS curves show an asymmetry not foreseen by the existing formulae (5.3)-(5.4). In the simulation, the realistic SIS-18 lattice was used and betatron coupling was generated by random skew quadrupolar components at the end of each focusing quadrupole.

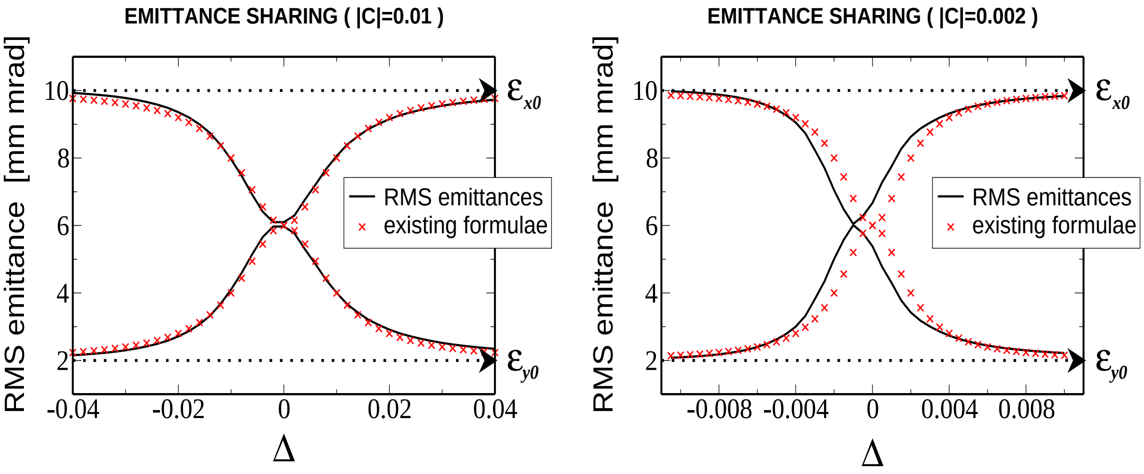

Figure 5.1: RMS emittances against $\Delta = Q_x - Q_y$ from multi-particle simulations compared with Eqs. (5.3)-(5.4) for $|C| = 1\%$ (left) and $|C| = 0.2\%$ (right) generated by distributed random skew quadrupole components in the focusing quadrupoles of the SIS-18.

5.2 Betatron motion close to the (1,-1) resonance

Close to the difference resonance (1,-1) a complete Lie expansion (i.e. including all orders) of the turn-by-turn BPM signal defined in Eq. (3.2) is derivable in terms of the RDT f_{1001}, namely

$$h_x(N) = \cos 2f\sqrt{2I_x}e^{i(2\pi NQ_h+\psi_{x0})} - ie^{iq}\sin 2f\sqrt{2I_y}e^{i(2\pi NQ_v+\psi_{y0})} \tag{5.5}$$

$$h_y(N) = \cos 2f\sqrt{2I_y}e^{i(2\pi NQ_v+\psi_{y0})} - ie^{-iq}\sin 2f\sqrt{2I_x}e^{i(2\pi NQ_h+\psi_{x0})} \ , \tag{5.6}$$

where N is the turn number, $I_{x,y}$ and $\psi_{x0,y0}$ are the normal form single particle invariants and phases respectively. f and q are the amplitude and phase of f_{1001} defined by

$$f_{1001} = fe^{iq} \ . \tag{5.7}$$

An expression of f_{1001}, approximated up to first order, reads

$$\bar{f}_{1001} = \frac{\sum_w J_{w,1}\sqrt{\beta_x^w\beta_y^w}e^{i(\Delta\phi_{w,x}-\Delta\phi_{w,y})}}{4(1-e^{2\pi i(Q_h-Q_v)})} \ . \tag{5.8}$$

The difference between the above definition and the one given in Eq. (3.15) is in that here the eigen tunes Q_h, Q_v appear instead of the bare tunes Q_x, Q_y. The substitution makes the quasiresonant f_{1001} not to diverge for $\Delta \rightarrow 0$. Outside the resonance stop band the two expressions are equivalent.

The derivation of Eqs. (5.5)-(5.6) is given in APPENDIX C. In matrix notation the above system reads

$$\begin{pmatrix} h_x(N) \\ h_y(N) \end{pmatrix} = \begin{pmatrix} \cos 2f & -ie^{iq}\sin 2f \\ -ie^{-iq}\sin 2f & \cos 2f \end{pmatrix} \begin{pmatrix} e^{i2\pi NQ_h} & 0 \\ 0 & e^{i2\pi NQ_v} \end{pmatrix} \begin{pmatrix} \sqrt{2I_x}e^{i\psi_{x0}} \\ \sqrt{2I_y}e^{i\psi_{y0}} \end{pmatrix} \tag{5.9}$$

The system evaluated at $N = 0$ and inverted reads

$$\begin{pmatrix} \sqrt{2I_x}e^{i\psi_{x0}} \\ \sqrt{2I_y}e^{i\psi_{y0}} \end{pmatrix} = \begin{pmatrix} \cos 2f & ie^{iq}\sin 2f \\ ie^{-iq}\sin 2f & \cos 2f \end{pmatrix} \begin{pmatrix} \sqrt{E_{x0}}e^{i\phi_{x0}} \\ \sqrt{E_{y0}}e^{i\phi_{y0}} \end{pmatrix}, \tag{5.10}$$

where we explicited $h_q(0) = \sqrt{E_{q0}}e^{i\phi_{q0}}$, with E_{q0} and ϕ_{q0} the initial single particle emittance and phase in the Cartesian coordinates respectively.

5.3 Single particle emittances

Single particle emittances $E_{x,y}$ can be described in terms of the normal form invariants according to

$$E_{x,y}(N) = |h_{x,y}(N)|^2 \ . \tag{5.11}$$

Eqs. (5.5) and (5.6) yield

$$\begin{aligned} E_x(N) &= \cos^2 2f\ (2I_x) + \sin^2 2f\ (2I_y) + \Phi & (5.12) \\ E_y(N) &= \cos^2 2f\ (2I_y) + \sin^2 2f\ (2I_x) - \Phi & (5.13) \\ \Phi &= 2\sqrt{2I_x 2I_y}\cos 2f \sin 2f \sin\left[q - (\psi_{x0} - \psi_{y0}) - 2\pi N(Q_h - Q_v)\right] , \end{aligned}$$

where q and f are the phase and the amplitude of f_{1001} defined in Eq (5.7). The sum of the two emittances reads

$$E_x(N) + E_y(N) = 2I_x + 2I_y = E_{x0} + E_{y0} \tag{5.14}$$

and is constant in time, where $I_{x,y}$ are invariants.

In order to remove the dependence of $E_{x,y}$ on $I_{x,y}$ and to make explicit the dependence on the initial emittances, we substitute Eq. (5.10) in Eq. (5.9). The complex Courant-Synder variables are therefore given by

$$\begin{aligned}
h_x(N) &= \sqrt{E_{x0}}e^{i(2\pi N Q_h+\phi_{x0})}\left[\cos^2 2f + e^{-i2\pi N\Delta_e}\sin^2 2f\right] + \\
&\quad i\sqrt{E_{y0}}e^{i(2\pi N Q_v+\phi_{y0}+q)}\cos 2f\sin 2f\left[e^{i2\pi N\Delta_e}-1\right] \qquad (5.15)\\
h_y(N) &= \sqrt{E_{y0}}e^{i(2\pi N Q_v+\phi_{y0})}\left[\cos^2 2f + e^{i2\pi N\Delta_e}\sin^2 2f\right] + \\
&\quad i\sqrt{E_{x0}}e^{i(2\pi N Q_h+\phi_{x0}-q)}\cos 2f\sin 2f\left[1-e^{-i2\pi N\Delta_e}\right]\ , \qquad (5.16)
\end{aligned}$$

where $\Delta_e = Q_h - Q_v$ is the distance from the resonance of the eigen-tunes. The single particle emittances $E_{x,y} = |h_{x,y}|^2$ are obtained

$$\begin{aligned}
E_x(N) &= E_{x0} + \sin^2 4f\ \left[1-\cos\left(2\pi N\Delta_e\right)\right]\frac{E_{y0}-E_{x0}}{2} + \mathbf{R}(\phi_{x0},\phi_{y0}) \qquad (5.17)\\
E_y(N) &= E_{y0} - \sin^2 4f\ \left[1-\cos\left(2\pi N\Delta_e\right)\right]\frac{E_{y0}-E_{x0}}{2} - \mathbf{R}(\phi_{x0},\phi_{y0})\ , \qquad (5.18)
\end{aligned}$$

where $\mathbf{R}(\phi_{x0},\phi_{y0})$ is a linear combination of $\sin\left(\phi_{x0}-\phi_{y0}\right)$ and $\cos\left(\phi_{x0}-\phi_{y0}\right)$.

5.4 RMS emittances

Turn-by-turn RMS emittances are computed by averaging over the particle distribution the single particle emittances given in Eqs. (5.17)-(5.18). The matching condition results in a particle distribution which is independent on the phases $\phi_{x,y}$. Therefore the average cancels out $\mathbf{R}(\phi_x,\phi_y)$, yielding

$$\epsilon_x(N) = \epsilon_{x0} + \sin^2\left(4|f_{1001}|\right)\left\{1-\cos\left(2\pi N\Delta_e\right)\right\}\frac{\epsilon_{y0}-\epsilon_{x0}}{2} \qquad (5.19)$$

$$\epsilon_y(N) = \epsilon_{y0} - \sin^2\left(4|f_{1001}|\right)\left\{1-\cos\left(2\pi N\Delta_e\right)\right\}\frac{\epsilon_{y0}-\epsilon_{x0}}{2}\ , \qquad (5.20)$$

where we have substituted $f = |f_{1001}|$. The two emittances oscillate in time (e.g. in N) with frequency $\omega_N = 2\pi\Delta_e$. On the resonance the frequency is $\omega_0 = 2\pi|C|$, with $|C|$ the tune separation at $\Delta = 0$. Unless betatron coupling is extremely low and $\Delta \simeq 0$, or a turn-by-turn emittance monitor is available, these oscillations cannot be detected by any hardware integrating the signal over many turns. A further averaging over $N >> 1/|C|$ is therefore required to derive an *averaged* RMS emittance. The time integration removes the oscillating term, with Δ_e independent on time, yielding

$$\begin{aligned}
\epsilon_x &= \epsilon_{x0} + \sin^2\left(4|f_{1001}|\right)\frac{\epsilon_{y0}-\epsilon_{x0}}{2} \qquad (5.21)\\
\epsilon_y &= \epsilon_{y0} - \sin^2\left(4|f_{1001}|\right)\frac{\epsilon_{y0}-\epsilon_{x0}}{2} \qquad (5.22)
\end{aligned}$$

In Fig. 5.2 the turn-by-turn RMS emittances from SIS-18 multi-particle simulation are plotted for $|C| = 0.128$ and three different working points. The closer Δ is to 0 (resonance condition) the larger is the amount of shared emittance and the slower is the exchange frequency. In the same pictures the horizontal lines correspond to the *averaged* RMS emittance.

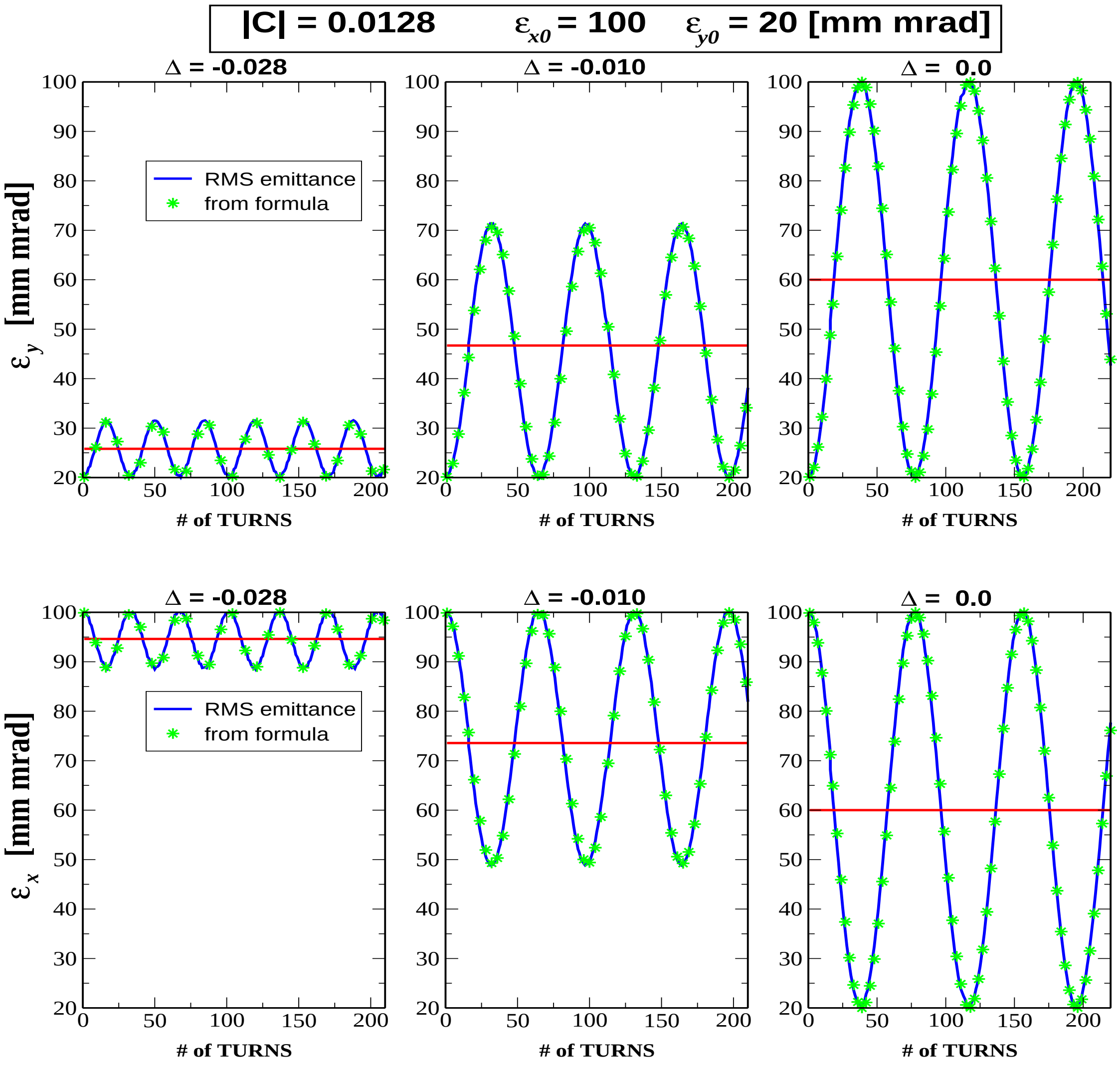

Figure 5.2: vertical (top) and horizontal (bottom) turn-by-turn RMS emittance from SIS-18 multi-particle simulation. Betatron coupling of $|C| = 0.0128$ is introduce by random skew quadrupolar components at the end of each focusing quadrupoles. Simulations are repeated for three working points $\Delta = 0.028, 0.01, 0.0$. Horizontal lines correspond to the integrated RMS emittance. Stars are derived from Eqs. (5.19)-(5.20).

5.5 From f_{1001} to formulae in the literature

Previously derived formulae (5.3)-(5.4) are obtained from the above relations under several approximations. Assuming the observation point at the origin, i.e. $s = 0$, from Eq. (5.8) we obtain

$$\begin{aligned} |\bar{f}_{1001}| &\simeq \frac{1}{8|\sin(\pi\Delta_e)|}\left|\sum_w J_{w,l}\sqrt{\beta_x^w\beta_y^w}e^{i(\Delta\phi_{w,x}-\Delta\phi_{w,y})}\right| \\ &\simeq \frac{1}{8\pi|\Delta_e|}\left|\sum_w J_{w,1}\sqrt{\beta_x^w\beta_y^w}e^{i(\phi_{w,x}-\phi_{w,y})}\right| , \end{aligned} \tag{5.23}$$

with $\Delta_e << 1$ and $\sin(\pi\Delta_e) \simeq \pi\Delta_e$. The above summation is closely related to the integral $|C_0|$ defined as follow

$$C_0 = -\frac{1}{2\pi}\oint ds\ j(s)\sqrt{\beta_x(s)\beta_y(s)}e^{-i(\phi_x(s)-\phi_y(s))} , \tag{5.24}$$

with

$$\begin{aligned} |C_0| &= \frac{1}{2\pi}\left|\oint ds\sum_w J_{w,1}\delta(s-s_w)\sqrt{\beta_x(s)\beta_y(s)}e^{-i(\phi_x(s)-\phi_y(s))}\right| \\ &= \frac{1}{2\pi}\left|\sum_w J_{w,1}\sqrt{\beta_x^w\beta_y^w}e^{i(\phi_{w,x}-\phi_{w,y})}\right| . \end{aligned} \tag{5.25}$$

Expanding the sine up to the first order $\sin x \simeq x$ and replacing $f_{1001} \simeq \bar{f}_{1001}$,

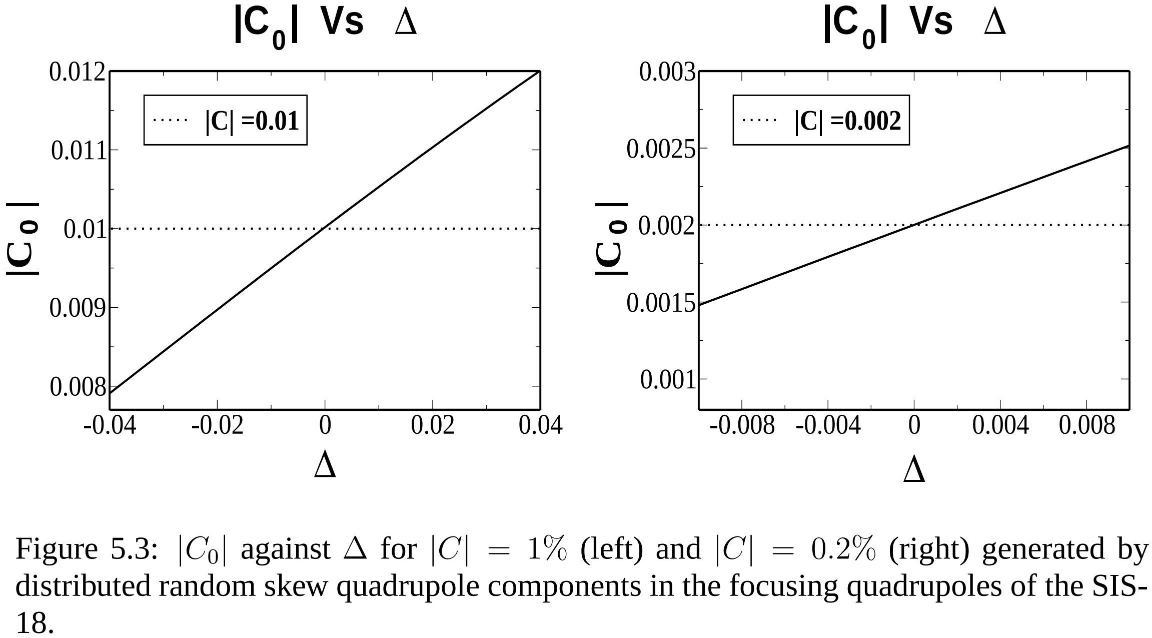

Figure 5.3: $|C_0|$ against Δ for $|C| = 1\%$ (left) and $|C| = 0.2\%$ (right) generated by distributed random skew quadrupole components in the focusing quadrupoles of the SIS-18.

the latter defined in Eq. (5.8), we obtain

$$\sin^2(4|f_{1001}|) \simeq 16|\bar{f}_{1001}|^2 \simeq \frac{C_0^2}{\Delta_e^2} \ . \tag{5.26}$$

After substituting $\Delta_e^2 = \Delta^2 + |C_0|^2$ [16], Eqs. (5.21)-(5.22) eventually read

$$\epsilon_x = \epsilon_{x0} + \frac{1}{2}\frac{|C_0|^2}{\Delta^2 + |C_0|^2}(\epsilon_{y0} - \epsilon_{x0}) \tag{5.27}$$

$$\epsilon_y = \epsilon_{y0} - \frac{1}{2}\frac{|C_0|^2}{\Delta^2 + |C_0|^2}(\epsilon_{y0} - \epsilon_{x0}) \ . \tag{5.28}$$

Eqs. (5.3)-(5.4) are obtained expanding $|C_0|^2$ as Taylor series around $\Delta = 0$, namely $|C_0|^2 \simeq |C|^2 + O(\Delta)$. Note that the approximation made in Eq. (5.26) provides a way to compute the maximum error $|f_{1001}| - |\bar{f}_{1001}|$: for $\Delta \to 0$, $|C_0| \to \Delta_e$ and $|f_{1001}| \to \frac{\pi}{8}$, whereas $|\bar{f}_{1001}| \to 1/4$.

The phase $e^{is/R\Delta}$ inside the integral (absent in C_0) makes $|C|$ independent of Δ. In case of a single skew quadrupole driving betatron coupling, as well as in the smooth approximation, $|C_0| = |C|$. In case instead of several localized skew quadrupoles $|C_0|$ exhibits a dependence on Δ. For $\Delta << 1$ this dependence appears to be linear as shown in Fig. 5.3. Related to this dependence is the asymmetry of $\sin(4|f_{1001}|)$ inside the stop band as shown in Fig. 5.4, as well as the asymmetry in the emittance sharing.

In Fig. 5.5 our new formulae (5.21)-(5.22) are compared with the simulated RMS emittances and the predictions from the previous model, Eqs. (5.3)-(5.4): for a coupling $|C| = 1\%$ both formulae follow the RMS values, whereas for $|C| = 0.2\%$ only the new formulae describe properly the sharing curve.

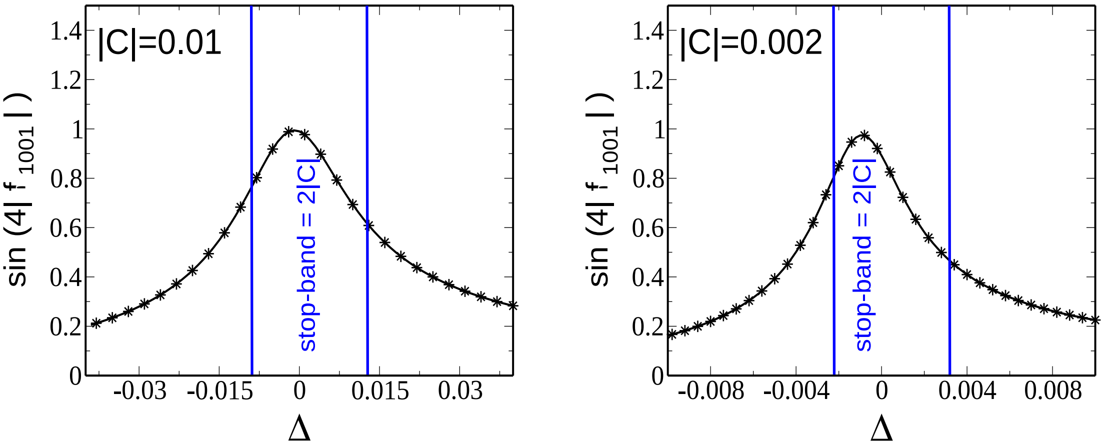

Figure 5.4: $\sin(4|f_{1001}|)$ against Δ for $|C| = 1\%$ (left) and $|C| = 0.2\%$ (right) generated by distributed random skew quadrupole components in the focusing quadrupoles of the SIS-18.

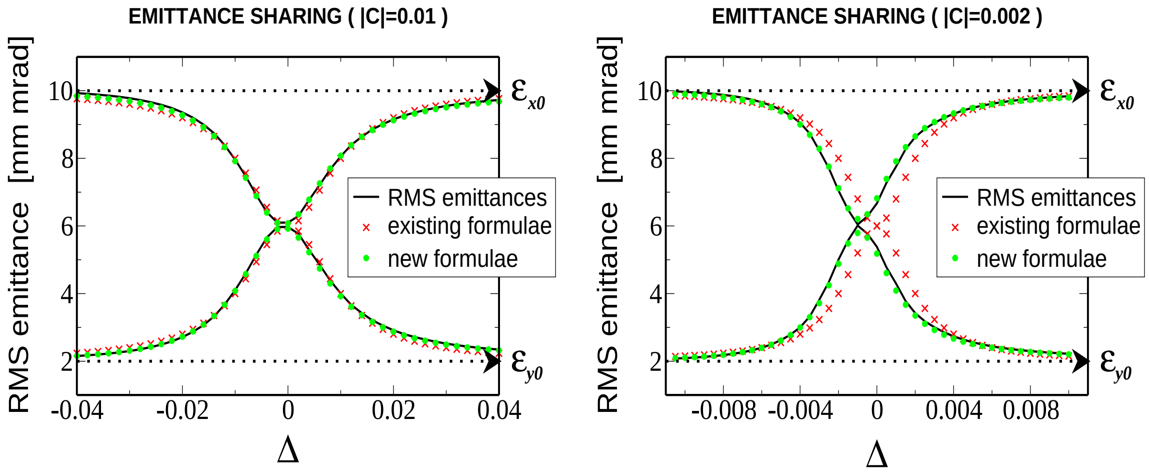

Figure 5.5: The same RMS emittances of Fig. 5.1 compared with previous formulae Eqs. (5.3)-(5.4) and the new formulae Eqs. (5.21)-(5.22) for $|C| = 1\%$ (left) and $|C| = 0.2\%$ (right).

5.6 Computing and measuring f_{1001}

The approximate expression of f_{1001} given in Eq. (5.8) might not be enough accurate close to the resonance. This relation is indeed derived from a first order normal form, and higher order contributions need to be taken into account. Nevertheless Eqs. (5.5)-(5.6) provide a direct way to compute (and measure) $f_{1001} = fe^{iq}$: the spectrum of turn-by-turn oscillations of a test particle contains two peaks, namely

$$H(1,0) = \cos 2f\sqrt{2I_x}e^{i\psi_{x0}} \qquad H(0,1) = -ie^{iq}\sin 2f\sqrt{2I_y}e^{i\psi_{y0}} \tag{5.29}$$

$$V(0,1) = \cos 2f\sqrt{2I_y}e^{i\psi_{y0}} \qquad V(1,0) = -ie^{-iq}\sin 2f\sqrt{2I_x}e^{i\psi_{x0}} \tag{5.30}$$

It is easy to prove that

$$\cos 2f = \frac{|H(1,0)|}{\sqrt{|H(1,0)|^2+|V(1,0)|^2}} = \frac{|V(0,1)|}{\sqrt{|V(0,1)|^2+|H(0,1)|^2}} \tag{5.31}$$

$$\sin 2f = \frac{|H(0,1)|}{\sqrt{|V(0,1)|^2+|H(0,1)|^2}} = \frac{|V(1,0)|}{\sqrt{|H(1,0)|^2+|V(0,1)|^2}} \tag{5.32}$$

$$q = \phi_{H(0,1)} - \phi_{V(0,1)} + \frac{\pi}{2} = \phi_{H(1,0)} - \phi_{V(1,0)} - \frac{\pi}{2}\ , \tag{5.33}$$

where $\phi_{V(m,n)}$ and $\phi_{H(m,n)}$ are the phases of the spectral peaks $V(m,n)$ and $H(m,n)$ respectively. f_{1001} can be therefore inferred numerically from $h_{x,y}(N)$ (as well as measured using a kicked beam) inverting the above relations. In Fig. 5.6 the exact

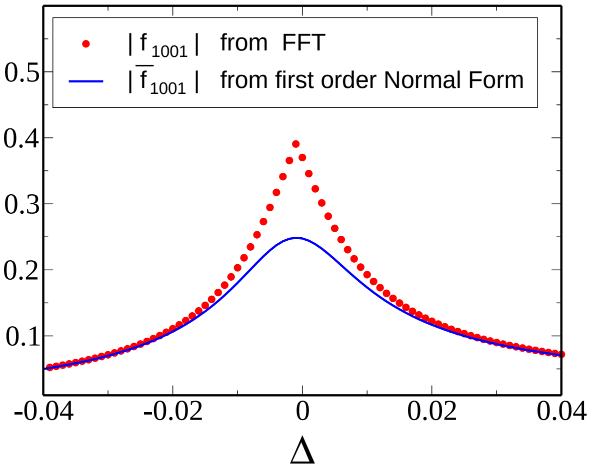

Figure 5.6: $|\bar{f}_{1001}|$ from Eq. (5.8) (blue line) compared with $|f_{1001}|$ from Eq. (5.31) against Δ. Note how on the resonance, $\Delta = 0$, $|\bar{f}_{1001}| = 1/4$ whereas $|f_{1001}| = \pi/8$.

$|f_{1001}|$ as computed from the above relations is plotted against Δ and compared with the approximate expression $|\bar{f}_{1001}|$ given in Eq. (5.8). Note that for $\Delta > |C|$ the above formulae and the one given in Tab. 3.3 to infer f_{1001} are equivalent.

If a fast emittance monitor is available, fitting the turn-by-turn oscillations of RMS emittances with Eqs. (5.19)-(5.20) provides an alternative way to infer both Δ_e and $|f_{1001}|$ for any working point. In Tab. 5.1 the fit results are listed at $s = 0$ together with the values computed from Eq.(5.8) and the FFT of a test particle. The fit is performed on the data corresponding to Fig. 5.2.

	$\Delta = -0.028$	$\Delta = -0.010$	$\Delta = -0.005$
$\lvert f_{1001}\rvert^2$	0.0101 (0.0104)	0.0352 (0.0355)	0.0501 (0.0505)
Δ_e	0.0324 (0.0320)	0.0173 (0.0171)	0.0143 (0.0143)

Table 5.1: Fitted values obtained from the turn-by-turn emittance oscillations according to Eqs. (5.19)-(5.20) for different working points. The data correspond to the bottom plots of Fig. 5.2. In parenthesis the values from the model.

If no turn-by-turn emittance monitor is available, Δ_e is no longer observable, the time integration removing the oscillating term. Nevertheless $|f_{1001}|$ is still measurable from Eqs. (5.21)-(5.22).

5.7 Generalized coordinates and decoupled motion

In this section we provide a way to decouple the equations of motion alternative to the one given in [31]. In the decoupled planes the motion is a pure rotation whose frequencies are given by the eigen-tunes $Q_{h,v}$. Explicit expressions for the single particle invariants are also derived.

Defining

$$\mathbf{h} \;=\; \begin{pmatrix} h_x \\ h_y \end{pmatrix} \qquad\qquad \mathbf{F} = \begin{pmatrix} \cos 2f & -ie^{iq}\sin 2f \\ -ie^{-iq}\sin 2f & \cos 2f \end{pmatrix} \tag{5.34}$$

$$\mathbf{a} \;=\; \begin{pmatrix} \sqrt{2I_x}e^{i\psi_{x0}} \\ \sqrt{2I_x}e^{i\psi_{x0}} \end{pmatrix} \qquad \mathbf{Q} = \begin{pmatrix} e^{i2\pi Q_h} & 0 \\ 0 & e^{i2\pi Q_v} \end{pmatrix}, \tag{5.35}$$

system (5.9) can be written in a more compact notation

$$\mathbf{h}(N) = \mathbf{F}\mathbf{Q}^N\mathbf{a} \quad \Rightarrow \quad \mathbf{h}(N) = \mathbf{F}\mathbf{Q}^N(\mathbf{F}^{-1}\mathbf{F})\mathbf{a}\ . \tag{5.36}$$

with $\mathbf{F}\mathbf{a} = \mathbf{h}(0)$,

$$\mathbf{h}(N) = \mathbf{F}\mathbf{Q}^N\mathbf{F}^{-1}\mathbf{h}(0)\ , \tag{5.37}$$

or equivalently

$$\mathbf{h}(N) = \mathbf{F}\mathbf{Q}(\mathbf{F}^{-1}\mathbf{F})\mathbf{Q}^{N-1}\mathbf{F}^{-1}\mathbf{h}(0)\ . \tag{5.38}$$

Eq. (5.37) applied to the $(N-1)^{th}$ turn reads

$$\mathbf{h}(N-1) = \mathbf{F}\mathbf{Q}^{N-1}\mathbf{F}^{-1}\mathbf{h}(0)\ , \tag{5.39}$$

providing the recursive turn-by-turn relation

$$\mathbf{h}(N) = \mathbf{F}\mathbf{Q}\mathbf{F}^{-1}\mathbf{h}(N-1)\ . \tag{5.40}$$

New generalized coordinates can be defined as

$$\tilde{\mathbf{h}}(N) = \mathbf{F}^{-1}\mathbf{h}(N)\ , \tag{5.41}$$

where $\mathbf{F}^{-1}$ is the matrix of Eq. (5.10). In the new variables system (5.40) is decoupled

$$\tilde{\mathbf{h}}(N) = \mathbf{Q}\tilde{\mathbf{h}}(N-1)\ . \tag{5.42}$$

The solution is a pure rotation, and $\tilde{E}_q = |\tilde{h}_q(N)|^2 = |\tilde{h}_q(0)|^2 = 2I_q$ are the invariants (see Eq. (5.10)). Note that for an uncoupled lattice $f_{1001} \to 0$ and $\mathbf{F} \to \mathbf{I}$, where $\mathbf{I}$ is the identity matrix, $\tilde{h}_q(N) \to h_q(N)$ and $2I_q \to E_{q0}$. Eq. (5.10) provides

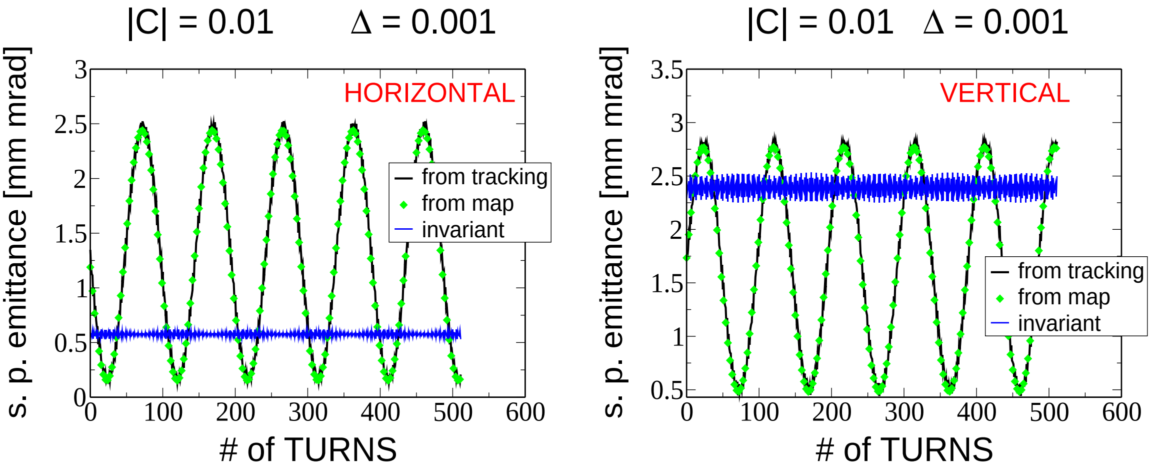

Figure 5.7: Turn-by-turn single particle emittances (left horizontal, right vertical) from tracking (Black curve) compared with the one obtained from Eq. (5.37) (Green diamonds) and $|\tilde{h}(N)|^2$ (blue curve) introduced in Eq. (5.41).

also the dependence of the invariants on the initial emittances and f_{1001}

$$\sqrt{2I_x} = |\sqrt{E_{x0}}e^{i\phi_{x0}}\cos 2f + i\sqrt{E_{y0}}e^{i\phi_{y0}+q}\sin 2f| \tag{5.43}$$

$$\sqrt{2I_y} = |\sqrt{E_{y0}}e^{i\phi_{y0}}\cos 2f + i\sqrt{E_{x0}}e^{i\phi_{x0}-q}\sin 2f| \; . \tag{5.44}$$

The turn-by-turn evolution of the generalized (decoupled) coordinates is given by

$$\tilde{h}_x(N) = |\sqrt{E_{x0}}e^{i\phi_{x0}}\cos 2f + i\sqrt{E_{y0}}e^{i\phi_{y0}+q}\sin 2f| \; e^{i2\pi NQ_h} \tag{5.45}$$

$$\tilde{h}_y(N) = |\sqrt{E_{y0}}e^{i\phi_{y0}}\cos 2f + i\sqrt{E_{x0}}e^{i\phi_{x0}-q}\sin 2f| \; e^{i2\pi NQ_v} \; . \tag{5.46}$$

In presence of betatron coupling $\tilde{E}_q = |\tilde{h}_q|^2$ replaces the single particle emittance E_q as adiabatic invariant. As E_q is invariant for slow tune modulations in an uncoupled lattice, $\tilde{E}_q$ is constant for a slow tune variation in a coupled lattice.

In Fig. 5.7 the turn-by-turn single particle emittances computed from tracking is compared with the ones obtained propagating the initial condition via Eq. (5.37), revealing an excellent agreement. It is also confirmed that $|\tilde{h}_{x,y}(N)|^2$ remain invariant, up to some fast oscillations, whose origin might be numerical.

5.8 Emittance variation along the ring

Eqs. (5.19)-(5.20) reveal a counterintuitive aspect of the emittance behavior along the ring: in Chapter 3 it was shown how $|f_{1001}|$ remains constant in regions free of betatron coupling, whereas it exhibits abrupt jumps after a localized source of coupling (see Fig. 4.1). Approaching the resonance conditions these jumps become less visible, and $|f_{1001}|$ tends to remain constant along the ring as shown in [1, 26] and reported in APPENDIX B. Jumps of $|f_{1001}|$ result in variations of the amount of shared emittance along the ring, according to Eqs. (5.19)-(5.20).

This is indeed confirmed by multi-particle simulations shown in Fig. 5.8: the vertical RMS emittance is plotted turn by turn at three different locations of the SIS-18, for different Δ and for two different amounts of coupling. ϵ_y (as well as ϵ_x), at any locations, oscillates with frequency $\omega_N = 2\pi\Delta_e$, which is invariant. The minimum of the oscillations is also invariant, $\epsilon_{y0} = 20$ mm mrad: this occurs when $\cos(2\pi N\Delta_e) = 1$ in Eqs. (5.19)-(5.20), regardless on the local value of $|f_{1001}|$. On the other hand the upper crest occurs when $\cos(2\pi N\Delta_e) = 0$ and its value depends on the local value of $|f_{1001}|$; the relative difference tends to zero approaching the resonance, as $|f_{1001}|$ remains constant along the ring.

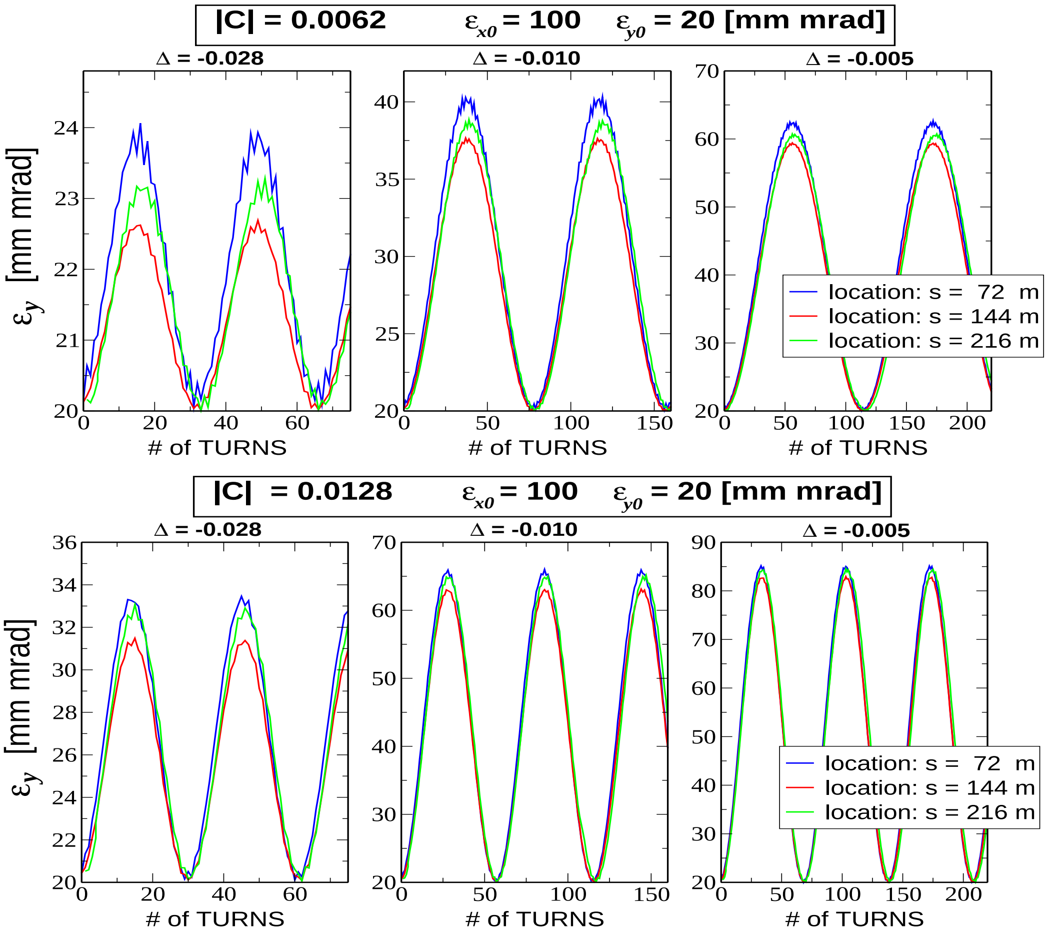

Figure 5.8: Multi-particle simulations of the turn-by-turn RMS emittance oscillations for two different amounts of coupling and three working points. The three lines correspond to different locations where the emittances were computed.

Chapter 6

Betatron coupling and emittance transfer: dynamic case

One of the constraints imposed in Chapter 5 was the invariance of the bare tunes $Q_{x,y}$ within the machine cycle. Explicit expressions for the single particle invariants $I_{x,y}$ were derived and the connection between single particle emittance $E_{x,y}$ and I_{xy} was established. This resulted in a fast emittance exchange between the two transverse planes and an averaged emittance sharing depending on the amount of betatron coupling and the distance from the resonance.

In this chapter we discuss the effect of a slow tune variation and the dynamical crossing of the resonance stop band. As for the static case, new formulae containing f_{1001} are derived and the connection with previous analogous relations is discussed.

6.1 Short review of previous theory

Dynamical resonance crossing refers to the exploration of the resonance stop band in a single machine cycle by slowly sweeping one or both bare tunes, i.e. introducing a time dependence (usually linear) in Δ. The two emittances become equal on the resonance and completely exchange at the end of the crossing, assuming that both the starting point Δ_{in} and the final one Δ_{out} are large enough compared with the resonance stop band $|C|$ defined in Eq. (5.1). Analytic formulae were derived in [29] for a constant focusing lattice with a uniformly distributed betatron coupling. The two *averaged* emittances are in this case coupled according to

$$\epsilon_x = \epsilon_{x0} + \frac{|C|^2}{\Delta^2 + |C|^2 \pm \Delta\sqrt{\Delta^2 + |C|^2}} \frac{\epsilon_{y0} - \epsilon_{x0}}{2} \tag{6.1}$$

$$\epsilon_y = \epsilon_{y0} - \frac{|C|^2}{\Delta^2 + |C|^2 \pm \Delta\sqrt{\Delta^2 + |C|^2}} \frac{\epsilon_{y0} - \epsilon_{x0}}{2} , \tag{6.2}$$

where $\Delta = Q_x - Q_y$, $Q_{x,y}$ the (fractional part of the) bare tunes. The factor $\Delta\sqrt{\Delta^2 + |C|^2}$ makes possible the exchange, and ± depends on the crossing direction.

The adiabatic condition in this case refers to a tune variation slow enough to keep the particle distribution always matched with the lattice. As for the static case, we make use of the matching condition when computing the RMS emittances $\epsilon_{x,y}$ for the single particle emittances $E_{x,y}$.

Another assumption is that the tune variation is performed over a number of turns $N_t >> 1/|C|$, with N_t the integration time of the emittance monitor. Within N_t both the tunes and f_{1001} are assumed to be almost constant.

6.2 Single particle emittances

As the single particle emittance $E_{x,y}$ is invariant for slow tune modulations in an uncoupled lattice, $\tilde{E}_{x,y} = |\tilde{h}_{x,y}|^2 = 2I_{x,y}$ remains constant for a slow tune variation in a coupled lattice. On the resonance $\Delta = 0$ the two invariants exchange abruptly. This exchange is related to the change in the phase q of f_{1001} by π as shown in Fig. 6.1.

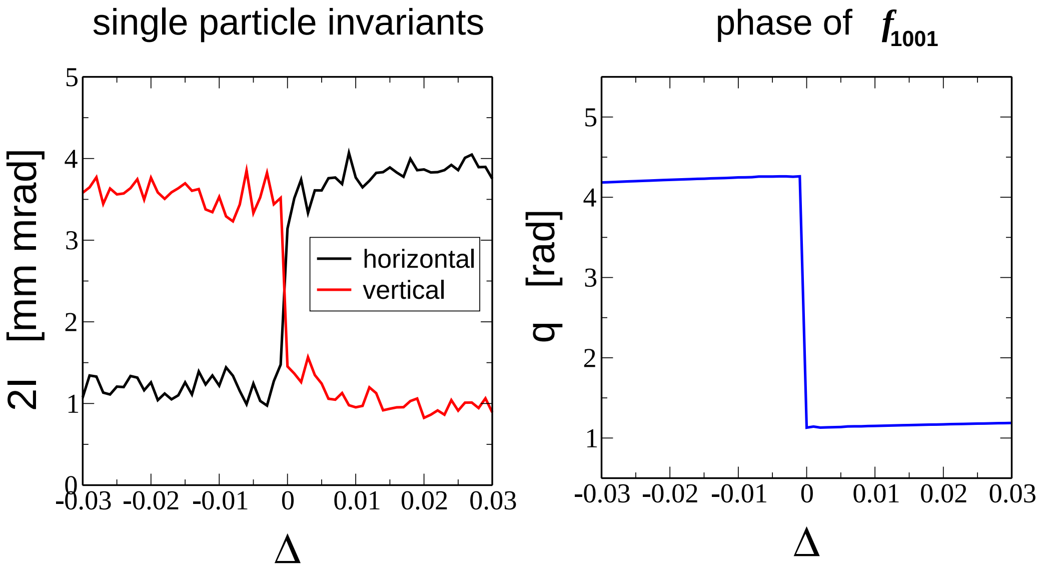

Figure 6.1: $2I_{x,y}$ (left) and q (right) against the distance from the resonance Δ.

To show how this abrupt exchange occurs we compute $2I_{x,y}$ from Eqs. (5.43)-(5.44)

$$2I_x = \cos^2 2f\ E_x + \sin^2 2f\ E_y - \sqrt{E_x E_y}\sin 4f\ \sin(\phi_x - \phi_y - q) \tag{6.3}$$

$$2I_y = \cos^2 2f\ E_y + \sin^2 2f\ E_x + \sqrt{E_x E_y}\sin 4f\ \sin(\phi_x - \phi_y - q)\ , \tag{6.4}$$

where as usual $f_{1001} = fe^{iq}$. Sum and difference read respectively

$$2I_x + 2I_y = E_x + E_y = E_{x0} + E_{y0} \tag{6.5}$$

$$2I_x - 2I_y = \cos 4f\ (E_x - E_y) - 2\sqrt{E_x E_y}\sin 4f\ \sin(\phi_x - \phi_y - q)\ . \tag{6.6}$$

For a given particle close to the resonance, i.e. $\Delta \simeq 0$ and $f \simeq \pi/8$, the tune working point $\Delta = \pm\delta$, where $\delta \simeq 0$, are not equivalent since

$$(2I_x - 2I_y)\Big|_{-\delta} = -2\sqrt{E_x E_y}\sin\left(\phi_x - \phi_y - q\right) \tag{6.7}$$

$$(2I_x - 2I_y)\Big|_{\delta} = +2\sqrt{E_x E_y}\sin\left(\phi_x - \phi_y - q\right)\ . \tag{6.8}$$

Indeed $q(\delta) = q(-\delta) - \pi$ and $\phi_{x,y}(\delta) \simeq \phi_{x,y}(-\delta)$. The crossing therefore makes the difference change sign, while the sum remains constant. This is equivalent to say that the crossing makes $2I_x$ and $2I_y$ exchange while crossing the ***discontinuity*** $\Delta = 0$. The two invariants C_1 and C_2 and Eqs. (5.12)-(5.13) therefore read

$$\begin{aligned}
C_1 &= 2I_x \qquad C_2 = 2I_y \qquad \text{before crossing} && (6.9)\\
C_1 &= 2I_y \qquad C_2 = 2I_x \qquad \text{after crossing} && (6.10)\\
E_x(N) &= \cos^2 2f\ C_1 + \sin^2 2f\ C_2 + \Phi && (6.11)\\
E_y(N) &= \cos^2 2f\ C_2 + \sin^2 2f\ C_1 - \Phi && (6.12)\\
\Phi &= \sqrt{C_1 C_2}\cos 4f\ \ \sin\left[q - (\psi_{x0} - \psi_{y0}) - 2\pi N \Delta_e\right] && (6.13)
\end{aligned}$$

6.3 RMS emittances

The computation of the RMS emittances requires the knowledge of the RMS values of $C_{1,2}$. The adiabatic condition can be invoked to keep the particle distribution always matched and therefore independent of the betatron phases. As for the static case, when the RMS values are computed, terms proportional to $\sin\left(\phi_{x0} - \phi_{y0}\right)$ and $\cos\left(\phi_{x0} - \phi_{y0}\right)$ cancel out. Eqs. (6.3)-(6.4) evaluated at $N = 0$ yield

$$\begin{cases} c_1 = \cos^2 2f_0\ \epsilon_{x0} + \sin^2 2f_0\ \epsilon_{y0} \\ c_2 = \cos^2 2f_0\ \epsilon_{y0} + \sin^2 2f_0\ \epsilon_{x0} \end{cases} \quad \text{before crossing} \tag{6.14}$$

$$\begin{cases} c_1 = \cos^2 2f_0\ \epsilon_{y0} + \sin^2 2f_0\ \epsilon_{x0} \\ c_2 = \cos^2 2f_0\ \epsilon_{x0} + \sin^2 2f_0\ \epsilon_{y0} \end{cases} \quad \text{after crossing}\ , \tag{6.15}$$

where f_0, ϵ_{x0} and ϵ_{y0} are the initial absolute value of f_{1001} and RMS emittances respectively. The average over $N >> 1/|C|$ cancels out Φ and the RMS ***averaged*** emittances eventually read

$$\begin{aligned}
\epsilon_x &= c_1 + \sin^2 2|f_{1001}|(c_2 - c_1) \\
\epsilon_y &= c_2 - \sin^2 2|f_{1001}|(c_2 - c_1)\ .
\end{aligned}$$

It can be shown that the above relations are equivalent to

$$\begin{aligned}
\epsilon_x &= c_h + T_f\ (c_v - c_h) && (6.16)\\
\epsilon_y &= c_v - T_f\ (c_v - c_h)\ , && (6.17)
\end{aligned}$$

where

$$c_h = \cos^2 2f_0\ \epsilon_{x0} + \sin^2 2f_0\ \epsilon_{y0} \tag{6.18}$$

$$c_v = \cos^2 2f_0\ \epsilon_{y0} + \sin^2 2f_0\ \epsilon_{x0} \tag{6.19}$$

$$T_f = \begin{cases} \sin^2(2|f_{1001}|) & \text{before crossing} \\ \cos^2(2|f_{1001}|) & \text{after crossing} \end{cases} . \tag{6.20}$$

With this notation the exchange of the invariants is implicit in T_f whereas c_h and c_v remain constant. Note that the above relations hold for a starting point not necessarily far from the resonance, mandatory condition for the existing formulae Eqs. (6.1)-(6.2). As shown in Fig. 6.2 the agreement between the RMS emittances computed from multi-particle simulations and new formulae remains excellent for any starting points, whereas discrepancies appear with the existing formulae.

In order to re-derive previous formulae we assume a starting point far enough from the resonance stop band, such that $f_0 \simeq 0$, $c_h \simeq \epsilon_{x0}$ and $c_v \simeq \epsilon_{y0}$. We also rewrite T_f as

$$\sin^2 2f = \frac{1-\cos 4f}{2} = \frac{1-\sqrt{1-\sin^2 4f}}{2} \tag{6.21}$$

$$\cos^2 2f = \frac{1+\cos 4f}{2} = \frac{1+\sqrt{1-\sin^2 4f}}{2} . \tag{6.22}$$

Substituting $\sin^2 4f \simeq 16\bar{f}$ as done in Eq. (5.26), after some algebra we obtain

$$\sin^2 2f \simeq \frac{1}{2}\frac{|C_0|^2}{\Delta^2+|C_0|^2+|\Delta|\sqrt{\Delta^2+|C_0|^2}} \tag{6.23}$$

$$\cos^2 2f \simeq \frac{1}{2}\frac{|C_0|^2}{\Delta^2+|C_0|^2-|\Delta|\sqrt{\Delta^2+|C_0|^2}} , \tag{6.24}$$

with C_0 defined in Eq. (5.24). Under these assumptions Eqs. (6.16)-(6.17) read

$$\epsilon_x = \epsilon_{x0} + \frac{|C_0|^2}{\Delta^2+|C_0|^2 \pm \Delta\sqrt{\Delta^2+|C_0|^2}}\frac{\epsilon_{y0}-\epsilon_{x0}}{2} \tag{6.25}$$

$$\epsilon_y = \epsilon_{y0} - \frac{|C_0|^2}{\Delta^2+|C_0|^2 \pm \Delta\sqrt{\Delta^2+|C_0|^2}}\frac{\epsilon_{y0}-\epsilon_{x0}}{2} . \tag{6.26}$$

The sign in the denominator depends on the crossing direction. Eqs. (6.1)-(6.2) are eventually obtained expanding $|C_0|^2 \simeq |C|^2$ as done for the static case.

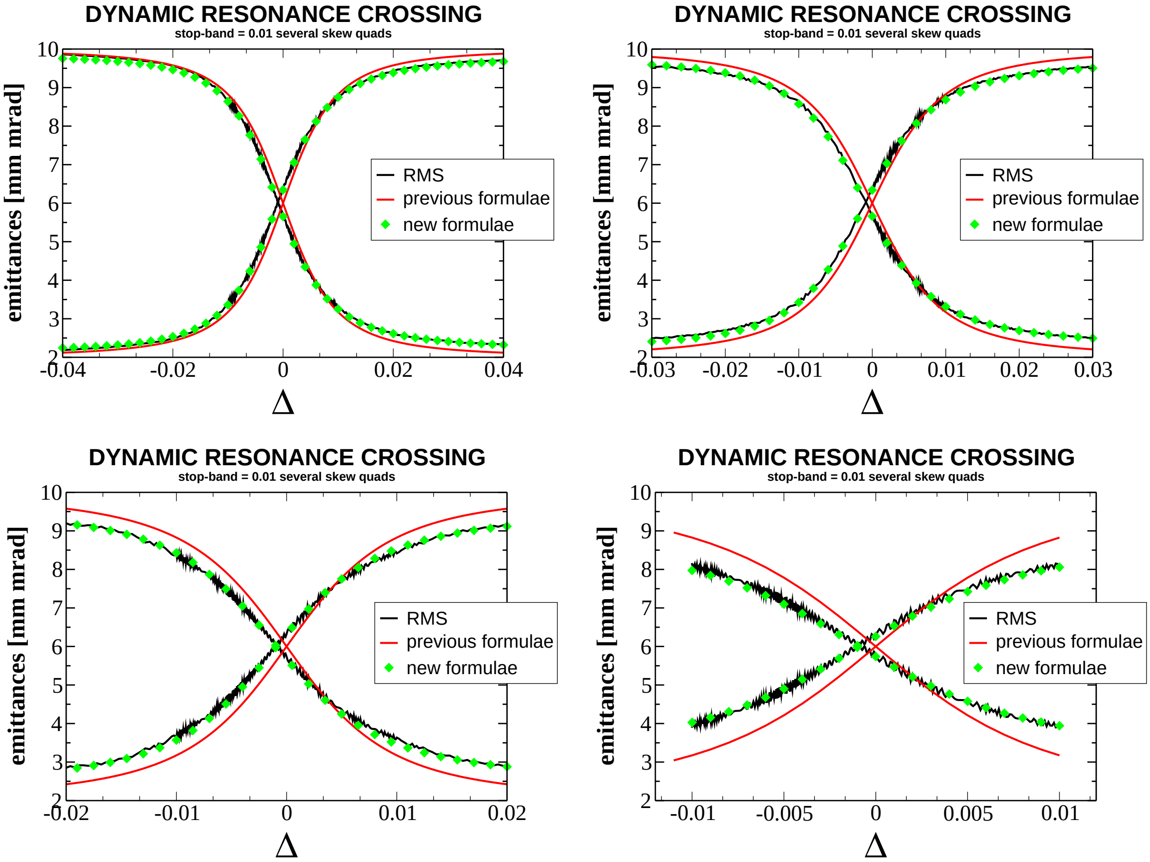

Figure 6.2: Dynamical crossing from multi-particle simulations: the RMS emittances are plotted together with Eqs. (6.16)-(6.16) and Eqs. (6.1)-(6.2) for several starting points. A betatron coupling of $|C| = 1\%$ was introduced with random errors in the normal quadrupoles of the SIS-18 lattice.

Chapter 7

Optics and emittance measurements in the SIS-18

The SIS-18 is presently not equipped with a turn-by-turn multi-BPM acquisition system. Its implementation is still in the prototyping phase. In order to investigate the feasibility and the effectiveness of RDT measurement in the SIS-18, a preliminary turn-by-turn acquisition system over two BPMs was developed during 2003 and 2004 making use of a more cost-effective hardware. Despite the fact that the turn-by-turn sampling was working properly at the front-end of each one of the two pick-ups, problems in synchronizing the two systems prevented any RDT measurement.

In the SIS-18 it has been always observed that a shift exists between the set Q-values and the measured ones. The turn-by-turn analysis provides a method for a fast machine tuning alternative to the Schottky analysis. Single BPM data were therefore used for tune and nonlinear chromaticity measurements, the latter one providing informations on the global lattice nonlinearities. Both the hardware and the measurement results are described in the first part of this chapter.

At the end of 2004 a new residual gas monitor (RGM) was commissioned in the SIS-18, allowing the measurement of the transverse emittances. The emittance curves were used to infer both $|C|$ and the $|f_{1001}|$, providing an alternative technique to the harmonic analysis of BPM data. First evidences of emittance equilibration were also observed. For the first time, two skew quadrupoles have been used to compensate betatron coupling. Both the hardware and the measurement results obtained during 2005 are described in the second part of this chapter.

7.1 SIS-18 turn-by-turn BPM acquisition system

From the experimental point of view, the crucial issue for the measurement of the RDT is the correct turn-by-turn construction of the complex signal $\tilde{x} - i\tilde{p}_x$ defined in Eq. (3.2), which means:

1 correct triggering and BPM turn-by-turn synchronization

2 Correct p_x reconstruction

3 Correct transformation to the normalized coordinates

Point 2. requires that the region between two consecutive pick-ups be free from nonlinearities. In this case the momentum can be inferred from the data of the neighbor BPMs [25]. Since the real linear optics not always corresponds to the model, the optical functions needed in point 3. are derived directly from the spectrum of x and y at each BPM [33]. Both points 2. and 3. depend anyway on the proper BPM data acquisition: not synchronized data would produce uncorrelated time series x_N and p_{xN} and wrong optical functions.

A new PC data acquisition system has been developed during 2003 and 2004 by Peter Moritz. The analog signals (Σ and Δ) from a pick-up are digitized by means of a 20 MHz 4-channel PCI card installed on a PC. As trigger the event generator (Q-kicker signal) is used, whereas the sampling (turn-by-turn) clock is provided by the RF master signal (divided by the harmonic number $h = 4$). The data are stored in 12-bits integer words, providing a resolution $\delta\Sigma/\Sigma = \delta\Delta/\Delta \simeq 5 \times 10^{-4}$ and $\delta x/x \simeq 10^{-3}$. A post-processing software was developed to convert these numbers in mm and perform the FFT of the time series (speeded up by a peak-search routine [34]).

This approach differs from the one used, for example, at the CERN PS [35] where the sampling is performed in continuous mode with a fast digitizer at high frequency (500 MHz). The beam position at each turn is then obtained from the full data stream with a peak-search algorithm. The advantages of our PCI card system are the lower hardware costs (a factor ten with respect to the fast digitizer) and smaller storage memory requirements and output files, already suitable for post-processing. The drawback is that the synchronization must be guaranteed during the acquisition since a wrong setting would compromise the entire acquisition, the full data being nonrecoverable. With a continuous fast sampling (each 2 ns) this risk is automatically avoided.

A first test using one BPM was performed in 2003 when the betatron tunes were measured with an accuracy of 0.3%. In the first half of 2004 a second PCI card was installed and a second BPM connected. To synchronize the two acquisitions both the trigger and the sampling clock of the second card have been delayed by the time-distance between the two BPMs. The SIS-18 has a strictly 12-fold superperiodicity and the 12 available BPMs are placed at the end of each period, hence this distance corresponds to 1/12 of the revolution time (4.689 μs). All tests were performed at the injection energy (11.4 MeV/u). To check the synchronization of the two cards we compared the phase advances between the two BPMs from the model with the ones obtained from the measured spectra $\psi_{x,y,0}^{BPM2} - \psi_{x,y,0}^{BPM1}$. In Fig. 7.1 the result of this test is plotted, showing a poor agreement made worse by the proximity of the vertical phase advance to 90^o, which makes the optical functions reconstruction problematic using the algorithm described in [33]. The use of SVD methods would prevent such a problem.

The reason for this bad synchronization is not yet well understood and requires more dedicated tests. One reason might be the 32-bit bus of the PCI card, which might have prevented the simultaneous storage of all the 4 channels.

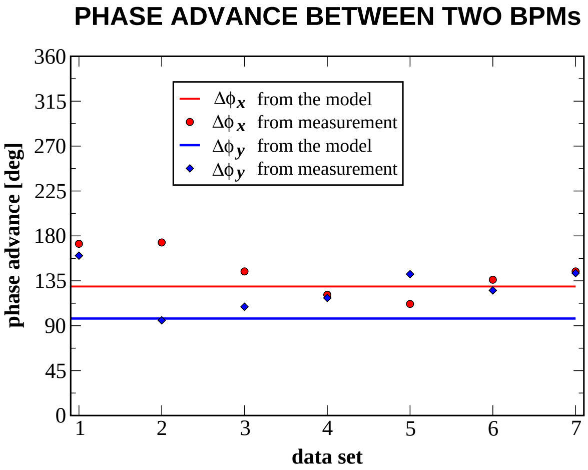

Figure 7.1: measured phase advance between the two BPMs with respect to the model.

7.2 Tune measurement

On October 23 2004 turn-by-turn BPM data were acquired after displacing transversely a low intensity beam by means of 45^o-rotated fast dipole magnet (Q-kicker). The phase-pickup (originally meant for Schottky analysis) was used instead of one of the twelve BPMs at the end of each focusing period because of the higher resolution. The machine and beam parameters are listed in Tab. 7.1. The measurement was carried out in parasitic and the electron cooler used for the main beam was kept on during our acquisition. Two sets of data were acquired for two different tune working points.

Beam:	^{124}Xe^{47+}
injected current:	$\sim 1\ \mu$A
injected # of particles:	$\sim 6 \times 10^6$
energy:	11.27 MeV/u
RF Voltage:	0 kV
Q_x	4.29; 4.21
Q_y	3.31; 3.20
tune shift at injection:	$\Delta Q_x, \Delta Q_y < 10^{-4}$

Table 7.1: Beam parameters during tune measurement of October 23 2004.

The phase-pickup showed a noise whose frequency of 87.43 kHz was such to produce in the FFT diagram a line at 0.41, as illustrated in Fig. 7.2. As this line was far enough from the expected tune lines, this was of no concern for the measurement.

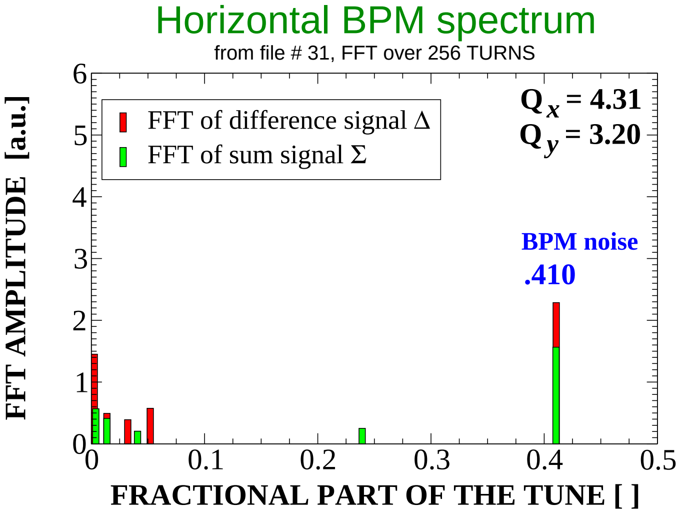

Figure 7.2: FFT of the sum and difference BPM signals for a bunched on-axis beam: “fake” oscillations driven by electric noise are observed. The frequency corresponding to the .410 peak is $f_n = .410 \cdot f_{rev} \simeq .410 \cdot 2.13 = 87.43$ kHz. This peak was always present during our measurement.

The measured betatron tunes (fractional part) are shifted with respect to the input values given in the control room software `SISMODI` :

$$Q_x^{mea} = 0.3189 \pm 0.0002 \qquad Q_x^{input} = 0.2900 \tag{7.1}$$

$$Q_y^{mea} = 0.1971 \pm 0.0005 \qquad Q_y^{input} = 0.2100 \tag{7.2}$$

$$Q_x^{mea} = 0.3379 \pm 0.0002 \qquad Q_x^{input} = 0.3100 \tag{7.3}$$

$$Q_y^{mea} = 0.1875 \pm 0.0001 \qquad Q_y^{input} = 0.2000 \tag{7.4}$$

$$Q_x^{mea} - Q_x^{input} \simeq 0.028 \qquad Q_y^{mea} - Q_y^{input} \simeq 0.013 \tag{7.5}$$

Comparisons between older and more recent tune measurements reveal that these shifts are rather cycle-dependent. Nevertheless the measured tunes are well reproducible for each kind of cycle. The performed FFT using N =256 turns ensures an error $\propto 1/N^2 \approx 10^{-5}$. The maximum measured fluctuation is within 0.3%. An example of recorded (vertical) data and corresponding FFT is shown in Fig. 7.3.

The solenoidal field from the the electron cooler introduces linear coupling between the two planes. The presence of the horizontal tune line in the vertical spectrum $V(1, 0)$, absent when the cooler was turned off, is a proof of this.

One of the effects of a non-zero chromaticity is to add sidebands to the spectral lines at distance $\pm qQ_s$, where Q_s is the synchrotron tune and q is an integer. From the spacing between the sidebands Q_s can be inferred. Such “satellite” lines have been observed during our measurement (one example is shown in the right plot of

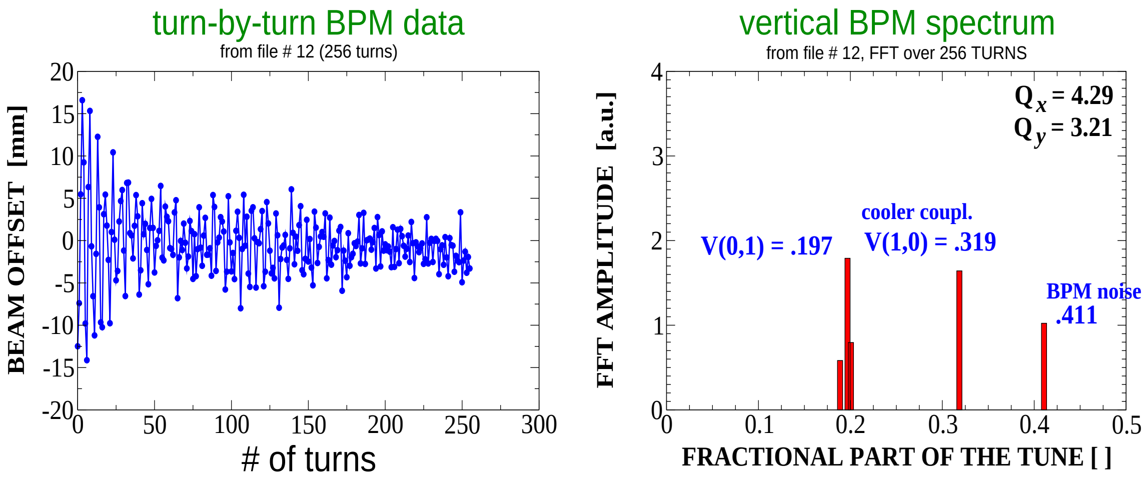

Figure 7.3: Vertical turn-by-turn data and corresponding FFT (Q-kicker voltage =34 kV).

fig. 7.4), providing the following value for the synchrotron tune

$$Q_s = 0.0038 \pm 0.0012 \ , \tag{7.6}$$

compatible (despite the large uncertainty of $\sim 30\%$) with the nominal value[1]

$$Q_s = \sqrt{\frac{|\eta| e h \hat{V} Z}{2\pi m_p \gamma \beta^2 c^2 A}} \simeq 0.0045 \tag{7.7}$$

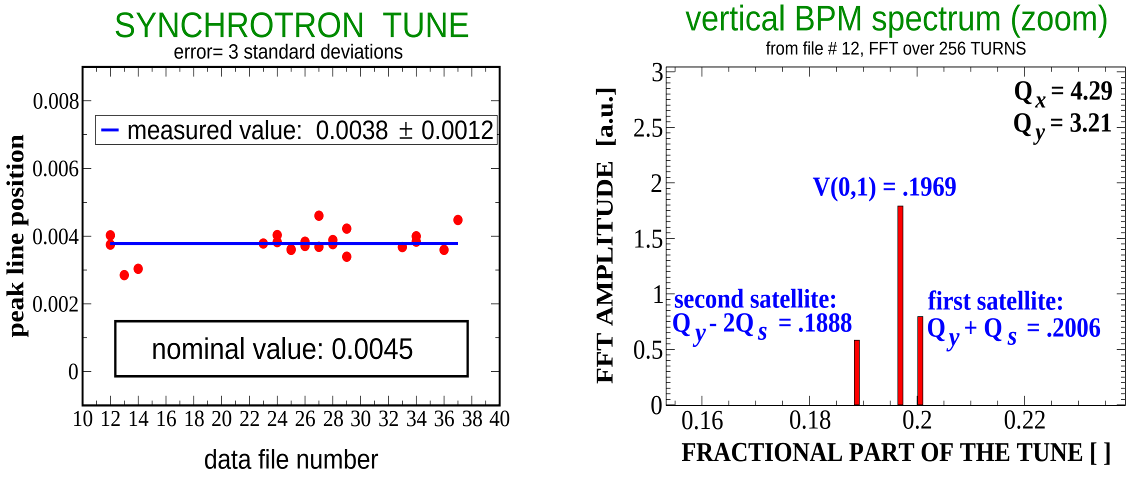

Figure 7.4: Measured synchrotron tune (left) and example of satellite lines excited by chromaticity (right).

---

[1] $\eta = 0.93696$, $h = 4$, $\hat{V} = 2$ kV, $Z = 47$, $A = 124$, $m_p = 1.67 \cdot 10^{-27}$kg, $\gamma = 1.0120$, $\beta = 0.15361$

7.3 Nonlinear chromaticity measurement

Particles with off momentum $\delta = (p - p_s)/(p_s)$, where p_s is the momentum of the synchronous particle, experience different focusing strengths and in turn different tunes. For a linear lattice the latter ones show a linear dependence on δ, whose coefficient Q' is called "natural chromaticity"

$$Q = Q_o + Q'\delta \ . \tag{7.8}$$

Any dependences on higher powers of δ are related to lattice nonlinearities. The underlying idea is that sextupolar (K_2) and decapolar (K_4) field components in the dipoles and octupolar components (K_3) inside the quadrupoles produce a linear, cubic and quadratic dependence of the tune on δ respectively. Measuring the chromaticity outside the linear region and fitting the data with a cubic polynomial provide information on the distributed multipolar components along the ring

$$Q_{x,y} = Q_{0,x,y} \underset{\underset{K_2}{\Uparrow}}{+} Q'_{x,y}\delta \underset{\underset{K_3}{\Uparrow}}{+} \frac{Q''_{x,y}}{2}\delta^2 + \underset{\underset{K_4}{\Uparrow}}{\frac{Q'''_{x,y}}{6}}\delta^3 \tag{7.9}$$

Once the cubic curve is inferred, the nonlinear model is constructed following the same procedure as in [36]. The main focusing quadrupoles are tuned to reproduce with MAD the $Q_{0,x,y}$. In the same way a sextupolar kick is introduced at the center or at the end of each dipole in order to reproduce the linear chromaticity $Q'_{x,y}$. Next an octupolar kick is added at each quadrupole to fit the quadratic terms $Q''_{x,y}$. Eventually decapolar kicks are inserted in the dipoles to reproduce the third order terms $Q'''_{x,y}$.

To check the quality of the model, the dependence of the tune on the kick amplitude I can be used. This dependence can be obtained imparting kicks with different amplitudes to the beam and measuring the tunes. In general a parabolic dependence

$$\nu = \nu_0 - \mu I^2 \tag{7.10}$$

is obtained. μ is a constant parameter to be inferred experimentally. On the other side, MAD tracking simulations using the new lattice can be run with the same kick strengths. The comparison between the two curves will establish the quality of the derived lattice model, e.g. $\mu_{MAD} \simeq \mu_{exp}$.

By definition chromaticity is inferred from measuring the tune $Q_{x,y}$ by varying the momentum deviation δ and keeping the magnetic lattice unchanged. The tune is measured as shown in the previous section offsetting the beam with a Q-kicker. The variation of δ is performed "by hand" changing the RF cavity frequency [32]. In practice this is done via the so-called "radial steering": a change of frequency corresponds to a change of energy which produces a closed orbit radius shift. The SIS control program allows the user to manipulate such radius keeping fixed the magnetic

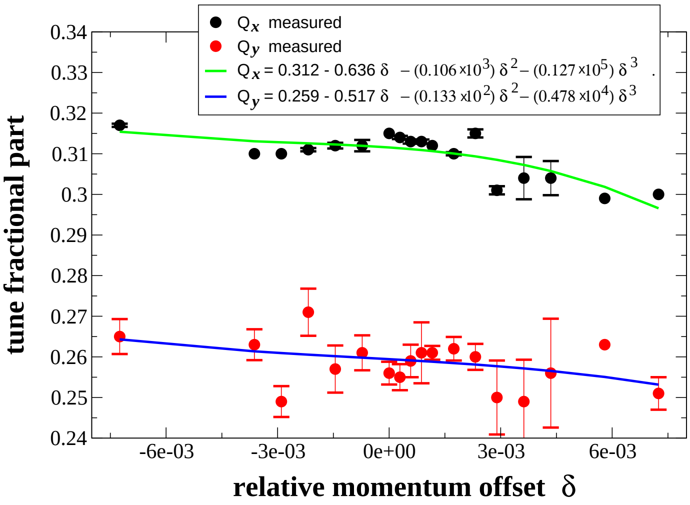

Figure 7.5: Measured horizontal and vertical tunes versus momentum offset (Error bars correspond to 1σ).

lattice. To a radial steering $\triangle R$ corresponds a momentum deviation, according to $\delta = (\triangle R)/(R\alpha_c)$, where R is the average machine radius ($R_{SIS} = 34.492$ m) and α_c is the momentum compaction (for the working point $Q_x = 4.29$ and $Q_y = 3.27$, $\alpha_{c,SIS} = 0.04$). During the measurement, for technical reasons the steering was limited to -1 cm $< \triangle R <$ 1 cm. Such a measurement was performed in 2003 and the results are shown in Fig. 7.5

Beam loss after kicking the beam was observed (see left plot of Fig. 7.6) and the impossibility of reducing the kicker strength prevented a better setup. This in turn drove a decoherence of the BPM signal over about 128 turns (see right plot of Fig. 7.6). The strong amplitude dependent detuning and the fast decoherence induced large fluctuations in the measured tunes. The limited radial steering range did not allow an explorations over a larger region of δ. All this resulted eventually in a poor fit quality and in the impossibility to infer a reliable nonlinear behavior (especially in the vertical plane), and to cross-check the results measuring the tunes at different Q-kicker strengths.

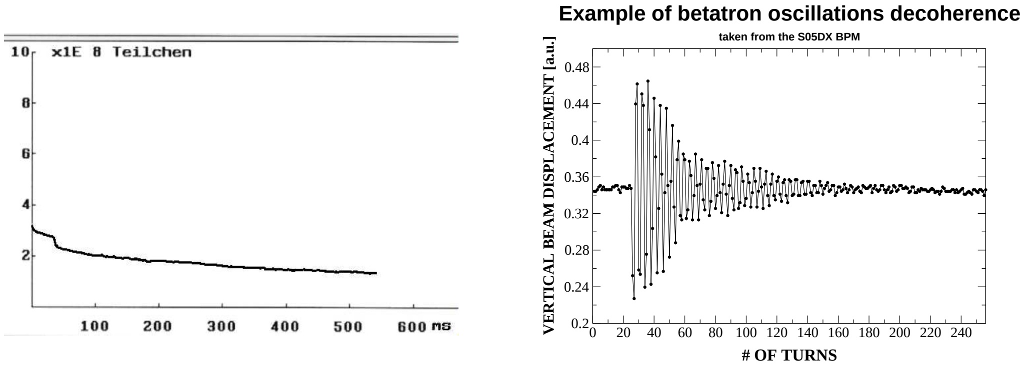

Figure 7.6: Left: Beam loss monitor (BLM) display with visible beam loss occurred after kicking the beam. Right: example of BPM signal with fast decoherence.

7.4 The SIS-18 residual gas profile monitor (RGM)

Residual Gas Monitors (RGM) provide a non-destructive beam profile measurement of circulating ion beam. The beam interacts with the residual gas (mainly composed of H_2) within the beam path and produces residual gas ions and electrons as schematically shown in Fig. 7.7. An electrostatic field $\mathbf{E_1}$ accelerates the ionization products (ions) towards a Micro Channel Plate (MCP). When the particles reach the MCP surface secondary electrons are produced and are accelerated into the channels by $\mathbf{E_2}$. Inside the channels they are multiplied by a factor of about 100. A wire array behind the MCP collects the secondary electrons and is connected to an adequate electronic device (current to voltage converter and adc).

Pictures of the RGM installed in the SIS-18 and commissioned during 2004 [37] by T. Giacomini and P. Forck are shown in Fig. 7.8. The duration of one measurement (one single beam profile) can be switched between 0.5 and 5 ms. At injection energy these times correspond to $\sim 10^2$ and $\sim 10^3$ turns, with the revolution time ~ 4.7 μs. Every 10 ms a new measurement starts. A turn-by-turn acquisition system is under development [38].

The dimensions of the MCPs are 100 mm x 30 mm and the active area is 100 mm x 26 mm. They are fixed in two sockets of glass ceramics and are fitted with two flat metal springs which are gold coated. An array of 64 wires with diameters of 1.5 mm and distances of 0.6 mm to each other is placed behind the MCPs. This wire array configuration determines the spatial resolution of 2.1 mm.

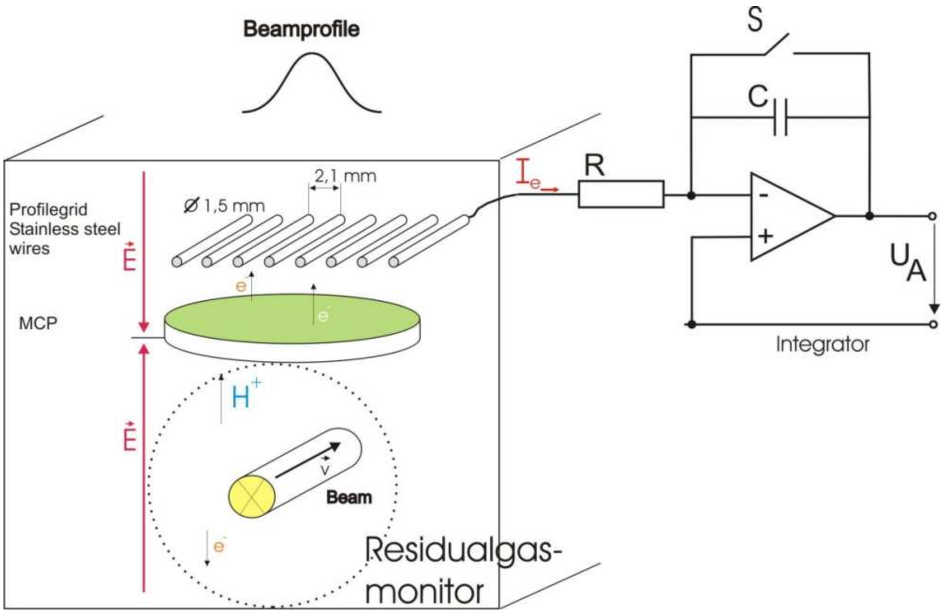

Figure 7.7: Schematic description of the residual gas ionization driven by the beam and of data acquisition (courtesy of T. Giacomini and P. Forck).

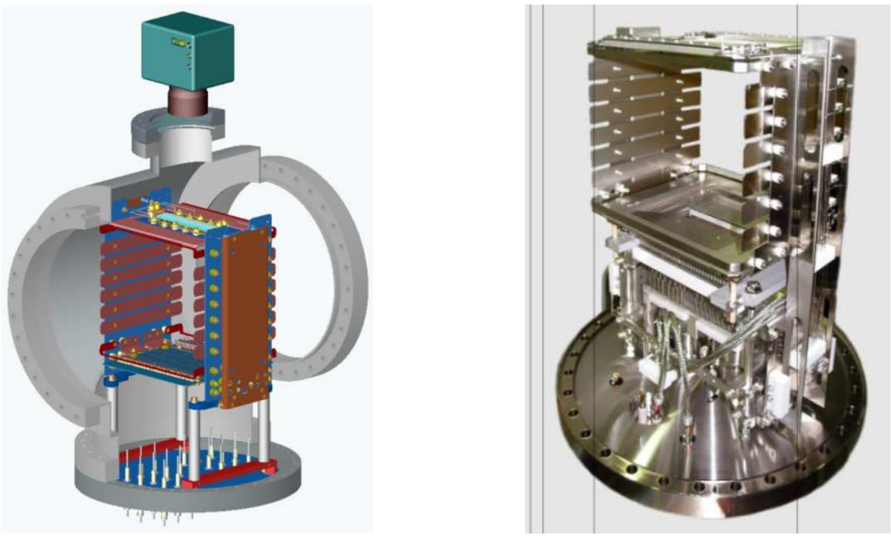

Figure 7.8: View of one of the two RGMs installed in the SIS-18: technical drawing (left) and picture (right) of the RGM installed inside the beam pipe. Note in the technical drawing the deuterium lamp on top of the box used for calibration (courtesy of T. Giacomini and P. Forck).

7.4.1 From RGM data to RMS emittance

A GUI software developed by T. Giacomini displays on-line and prints on file the ADC signals from the 64 wires of both planes. Data are acquired and stored every 10 ms. From the raw ADC data the HWHMs are inferred and the corresponding $\sigma_{x,y}$ are computed assuming a Gaussian profile via

$$\sigma_{x,y} = \frac{\mathrm{HWHM}_{x,y}}{2\ln(2)} \tag{7.11}$$

This assumption is motivated by the fact that the numerical computation of $\sigma_{x,y}$ directly from the ADC data are highly sensitive to tails far from the beam core and to calibration factors.

Transverse RMS emittances are inferred from the beam sizes according to

$$\epsilon_{x,y} = \frac{\sigma_{x,y}^2 - (D_{x,y}\delta)^2}{\beta_{x,y}} \tag{7.12}$$

where $D_{x,y}$ and $\beta_{x,y}$ are the dispersion and the beta functions respectively at the RGM location and δ is the momentum spread to be measured before. The optical functions are taken from the SIS-18 lattice model; their value for the triplet lattice at injection are listed in Tab. 7.2.

The RGM resolution of 2.1 mm corresponds to resolution in the measured emittance of 0.8 mm mrad.

horizontal RGM	vertical RGM
$D_x = 1.554$ m	$D_x = 1.77$ m
$D_y = 0$ m	$D_y = 0$ m
$\beta_x = 5.481$ m	$\beta_y = 7.767$ m

Table 7.2: Optical functions at the location of the RGM for the triplet lattice at injection energy.

Raw adc data out of the two arrays of 64 wires need to be corrected (namely divided) by calibration factors. A deuterium lamp (115 $\sim$ 400 nm spectral distribution) is placed above the **E**-field box outside the vacuum chamber (see left picture of Fig. 7.8) and used to infer the response of each wire to a homogeneous signal. This setting allows a periodic monitoring of RGM performances without need of dismounting the RGM from the beam line. An example of calibration factors measured before the measurement campaign of 2005 is shown in Fig. 7.9.

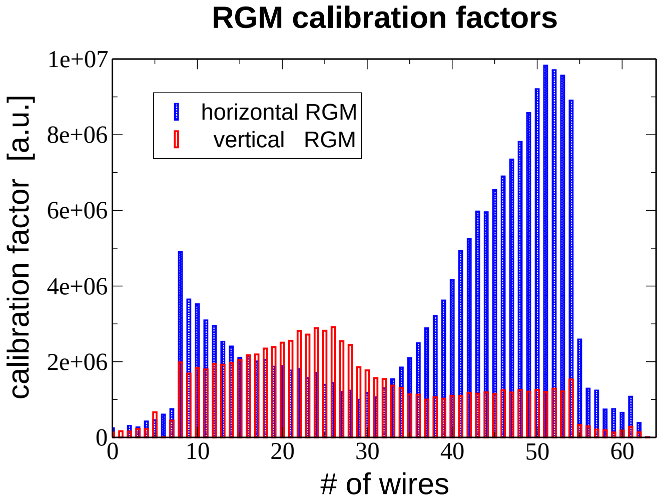

Figure 7.9: Calibration factors for both the horizontal and the vertical RGM measured at the beginning of 2005: raw adc data out of each wire must be divided by the corresponding factor (courtesy of T. Giacomini and P. Forck).

During the measurement campaign of March-May 2005 it was also observed that RGM data with peak values below 500 (in units of the adc file) were not suitable for analysis and they were rejected, as the noise level is of about 400. In this case large fluctuations when averaging over several data files were indeed observed, resulting in unreliable measurements. A solution to this problem is to increase the gain in the MCPs, which increases the flux of secondary electrons providing a higher RGM signal. Unfortunately this is not always possible: during May 2005, measurements at low current were carried out parasitically with a physics experiment at high intensity, whose beam passage was found to overload the MCP after the gain was optimized for a low current beam.

7.4.2 Measurement setup

Measurement of emittance transfer driven by betatron coupling in the SIS-18 requires a specific machine setup. Standard multi-turn injection makes the beam to fill the horizontal acceptance, which is larger than the vertical one by a factor four. The phase space rotation induced by betatron coupling hence induces beam losses as shown in Fig. 7.12. A beam injected with horizontal emittance much smaller than the vertical one prevents such losses and enhances the resolution of emittance transfer against hardware limitations and statistical fluctuations.

The first phase of the measurement carried out during 2005 was therefore the optimization of the injection. Beside a general optimization of the beam quality in the UNILAC, the variation of the emittance at injection was measured against the chopper window, i.e. the number of injection turns, as shown in Fig. 7.10. ϵ_{y0} remains practically constant, since we are painting the multi-turn injection in the horizontal phase space only. Injection in a single or few turns fulfills the requested condition $\epsilon_x < \epsilon_y$.

In all measurements the RF was turned off providing a coasting beam. The absence of acceleration makes the extraction focusing lattice to remain in the triplet mode. The tune sweeping for emittance exchange studies is performed selecting in the SIS-18 control room software SISMODI three pairs of Q-values $Q_{x,y}$ (start,

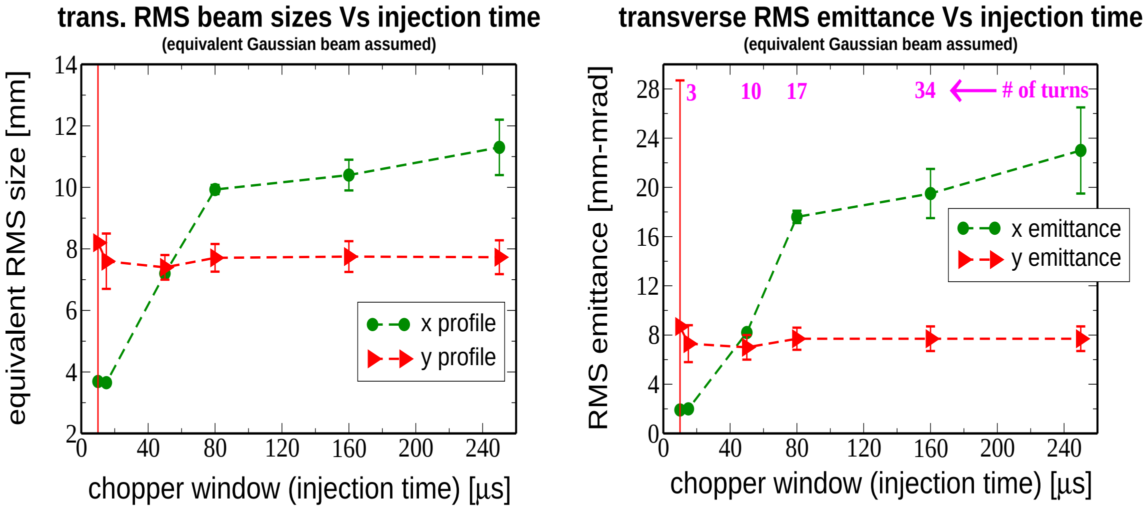

Figure 7.10: Measurement beam size (left) and RMS emittance (right) against chopper window after multi-turn injection for Carbon beam (February 8 2005). Error bars correspond to 1σ.

intermediate and final). The tune ramp between each pair is linear and the slope adjustable. The print out of the tune ramp against time $Q_{x,y}(t)$, together with the measured emittance variation during the machine cycle $\epsilon_{x,y}(t)$, makes it possible to plot and study the emittance exchange against the distance from the resonance, $\epsilon_{x,y}(\Delta)$, with Δ the difference between the fractional part of the tunes.

7.5 Measurement of emittance sharing

In May 2005 transverse RMS emittances were measured for different machine cycles scanning the region around the resonance condition $Q_x = Q_y$. Within the cycles the tunes were kept fixed. The RF cavity was turned off during the entire cycle, providing a coasting beam in few ms after injection. For a better integration of fast oscillations, the acquisition time for each beam profile was set to 5 ms, corresponding to $N \simeq 10^3$ turns. The main beam parameters are listed in Tab. 7.3.

Beam:	$^{86}\mathrm{Kr}^{34+}$
injected current:	~ 0.1 mA
injected # of particles:	$\sim 10^8$
energy:	11.3 MeV/u
RF Voltage:	0 kV
# of injection turns:	1
Q_x	4.26
Q_y	[3.29, 3.32]
tune shift at injection:	$\Delta Q_x, \Delta Q_y < 10^{-4}$
emittances at injection:	$\epsilon_{x0} \simeq 4.1$ $\epsilon_{y0} \simeq 8.3$ mm mrad

Table 7.3: Beam parameters during May 2-3 2005.

The results are shown in Fig. 7.11, where both horizontal and vertical emittances are plotted against the vertical tune. With $Q_x = 4.26$ fixed, this is equivalent to a plot against Δ, after subtracting the integer part. The resonance center is found to be at $\overline{Q}_x = 4.26$ and $\overline{Q}_y = 3.308$, instead of the expected $\overline{Q}_y = 3.26$. Practical reasons prevented the measurement in parallel of the real Q-values, and a cross-check of this deviation. An indirect confirmation of the shift in the tunes is anyway provided by beam loss measurement against a similar tune scan shown in the left plot of Fig. 7.12. A long multi-turn injection over several turns makes the beam to fill the full horizontal acceptance, the latter a factor four larger than the vertical one. Phase space rotation driven by betatron coupling makes the vertical emittance to exceed the corresponding acceptance, resulting in observable losses. Also in this case the resonance center (maximum loss), is compatible with the above numbers.

From the fit of the data curves with Eqs. (5.3)-(5.4) the resonance stop band width $|C|$ is inferred. The limited resolution indeed does not allow to deduce any asymmetry in the curve similar to the one shown in the right plot of Fig. 5.5. The observed coupling is

$$|C| = (2.5 \pm 0.9) \cdot 10^{-3} \tag{7.13}$$

Measuring the RMS emittances for about 1 hour at the same working point far from the resonance has shown a visible spread explaining the large error bars in Fig. 7.11, most probably related to fluctuations in the beam quality out of the injector.

Fit of data shown in Fig. 7.11 provides $\epsilon_{x0} \simeq 4.1$ mm mrad and $\epsilon_{y0} \simeq 8.3$. Inverting Eqs. (5.21)-(5.22) from the measured emittances, $|f_{1001}|$ against Δ is inferred and shown in the right plot of Fig. 7.12. Note that the definition of Δ given in Eq. (5.2) contains the fractional part of the tunes only.

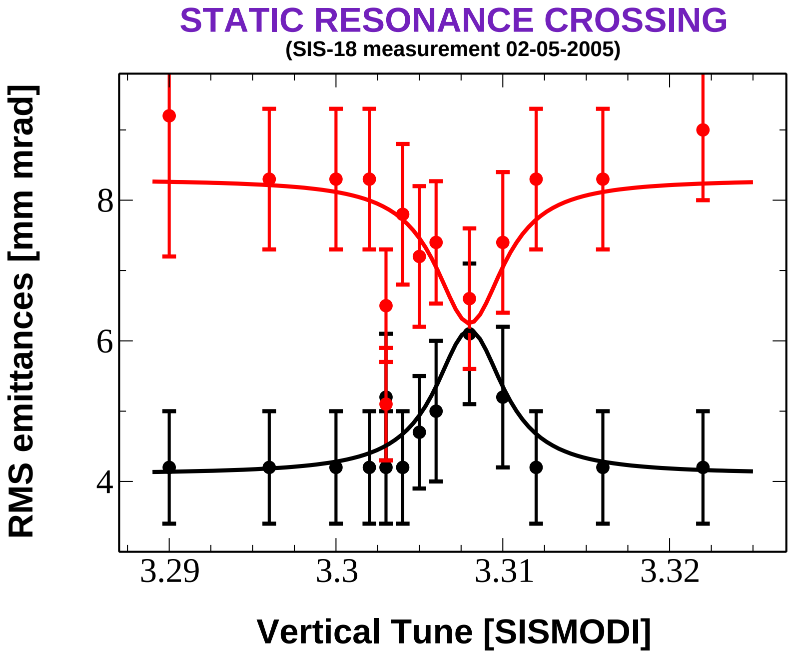

Figure 7.11: Measurement of emittance sharing in the SIS-18 driven by betatron coupling approaching the resonance condition $\Delta = 0$. The red points and curve correspond to the vertical emittance, the black to the horizontal. The continuous lines are obtained by fitting the data points with Eqs (5.3)-(5.4). The horizontal tune is fixed to 4.26 (Error bars correspond to 1σ).

7.6 Measurement of emittance exchange

In March 2005 a measurement campaign aiming at emittance exchange studies was carried out with a machine setup similar to the one described in Sec. 7.5. The exchange was in this case driven by sweeping adiabatically the vertical tune within the

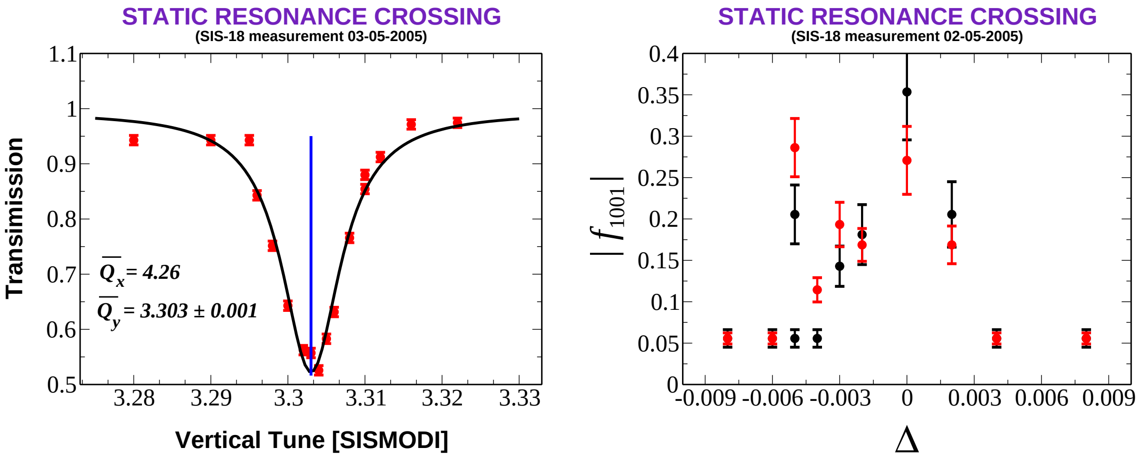

Figure 7.12: Left: beam loss measurement approaching the resonance condition $Q_x = Q_y$. The curve is obtain fitting the data with a Lorentzian function. The displayed Q-values (set in the control room software SISMODI) correspond to the inferred resonance center. Right: $|f_{1001}|$ inferred from emittance measurement against the distance from the resonance Δ (Error bars correspond to 1σ).

machine cycle. The combination of measured emittances and tune variation against time made it possible to study emittance transfer as function of Δ. The main beam parameters are listed in Tab. 7.4.

Beam:	$^{40}\mathrm{Ar}^{10+}$
injected current:	$\sim 50\ \mu$A
injected # of particles:	$\sim 1.5 \times 10^8$
energy:	11.3 MeV/u
RF Voltage:	0 kV
# of injection turns:	1
Q_x	$[4.25,\ 4.29]$
Q_y	$[3.29,\ 3.32]$
tune shift at injection:	$\Delta Q_x = 2 \times 10^{-4}\ \Delta Q_y = 4 \times 10^{-4}$
emittances at injection:	$\epsilon_{x0} \simeq 11.5\ \epsilon_{y0} \simeq 2.7$ mm mrad

Table 7.4: Beam parameters during March 17 2005.

In Fig. 7.13 an example of dynamical crossing in about 60 ms ($\sim 13 \times 10^3$ turns) is shown together with the emittance exchange curve. Large fluctuation in the vertical signal after crossing are due to a poor signal from the beam profile monitor: a weak gain in the multi-channel plate was set to attenuate the intense signal coming from a relative small beam size. After the exchange, the same charge extended over a large

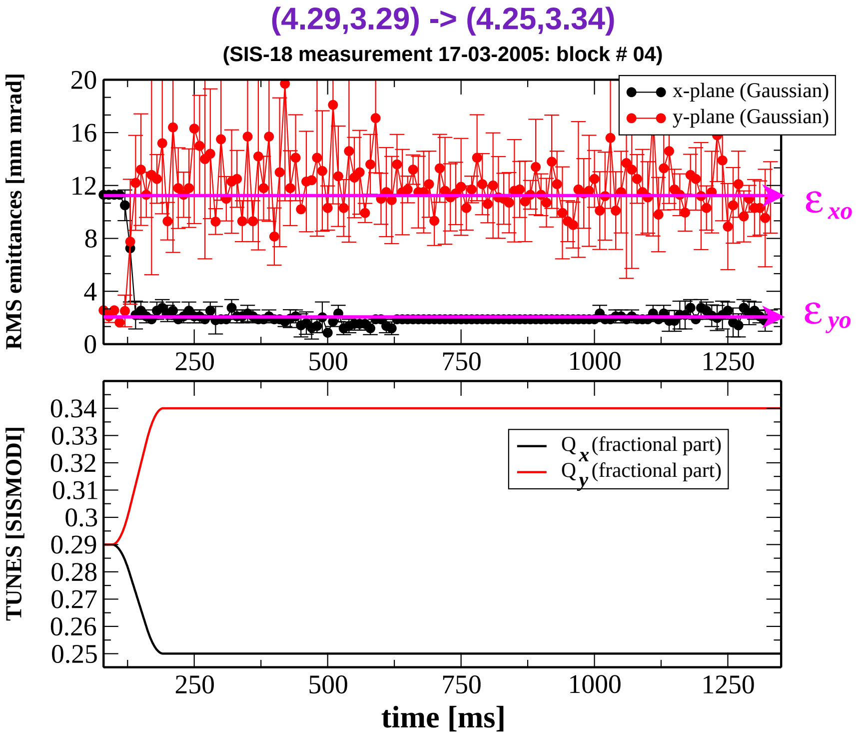

Figure 7.13: Example of emittance exchange and tune ramp against time. The resonance stop band is crossed in about 60 ms, corresponding approximately to 13×10^3 turns (Error bars correspond to 1σ).

region made the signal be lower and the multi-channel plate setting not optimized anymore. The absence of on-line analysis at that time prevented a better vertical resolution.

A double resonance crossing was also performed to verify the reversibility of the process. Both the tune ramp and the emittance exchange curve are shown in Fig. 7.14. As for the above case, large fluctuations appear in the vertical signal after the first crossing: small error bars after the second passage confirm that those fluctuations must be attributed to a not optimized reading rather than to a deterioration of the beam quality.

In both cases the resonance center is not found for equal fractional parts of the tune set in the control room software SISMODI. The center is found to be at $\overline{Q}_x = 4.27$ and $\overline{Q}_y = 3.295$, to be compared with the one found in Sec. 7.5 ($\overline{Q}_x = 4.26$, $\overline{Q}_y = 3.308$).

A repeated dynamical crossing was performed by moving the injection working point $(4.29, 3.29)$ to $(4.25, 3.25)$, which remains outside the stop band. From there the vertical tune was swept only crossing the resonance vertically from the bottom. Measurements were repeated for several final values of Q_y as shown in Fig. 7.15: on the left side the horizontal emittance is plotted against time together with the

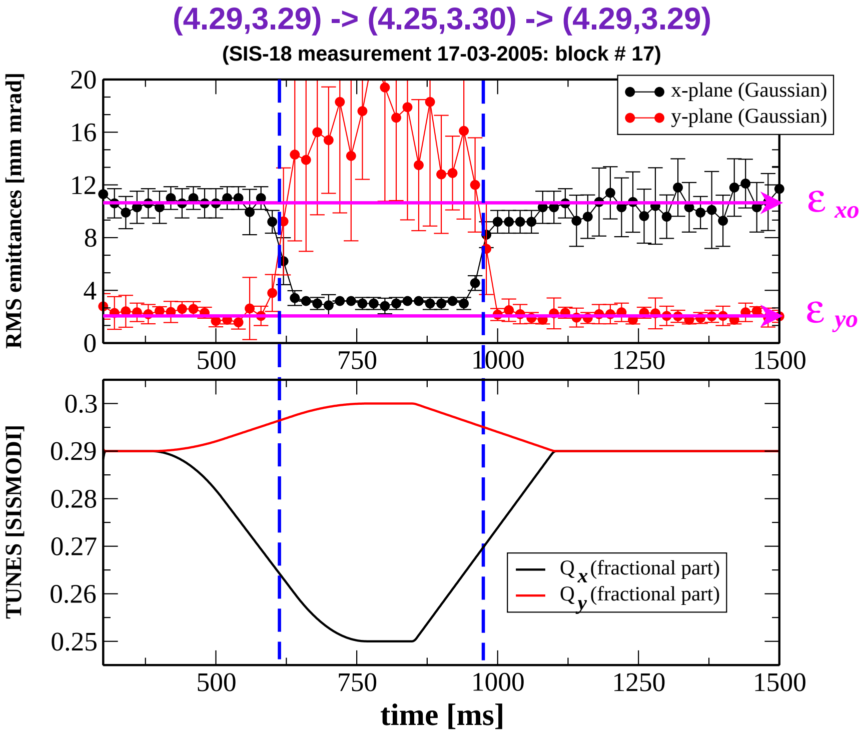

Figure 7.14: Example of double resonance crossing: tunes are initially swept from $(4.29, 3.29)$ to $(4.25, 3.30)$ in about 300 ms, to be eventually moved back to the initial values in about 250 ms. Note that the set Q-values are shifted with respect to the real ones. At the end of the dynamical crossing the initial emittances are restored (Error bars correspond to 1σ).

vertical tune ramp. Data from the vertical RGM were not suitable for analysis due to gain optimization problems. The resonance center, where $\epsilon_x = (\epsilon_{x0} + \epsilon_{y0})/2$, is found to be at $\overline{Q}_x = 4.25$ and $\overline{Q}_y = 3.289$.

Plotting the horizontal emittance against the vertical tune and fitting the curve with Eq. (6.1) provides the following value for the stop band width (averaged over the four data sets of Fig. 7.15)

$$|C| \quad = \quad (2.9 \pm 0.2) \cdot 10^{-3} \ , \tag{7.14}$$

consistent with the value inferred in Sec. 7.5. The main advantage of this method to measure $|C|$ with respect the one making use of the emittance sharing curve is that the latter one requires a time consuming scan over several machine cycles, whereas fitting the emittance exchange curve requires a single measurement. This in turn implies a better experimental resolution, as the measurement is less dependent on medium-term fluctuations ($\sim$ 1 hour) in the emittances of the beam out of the injector.

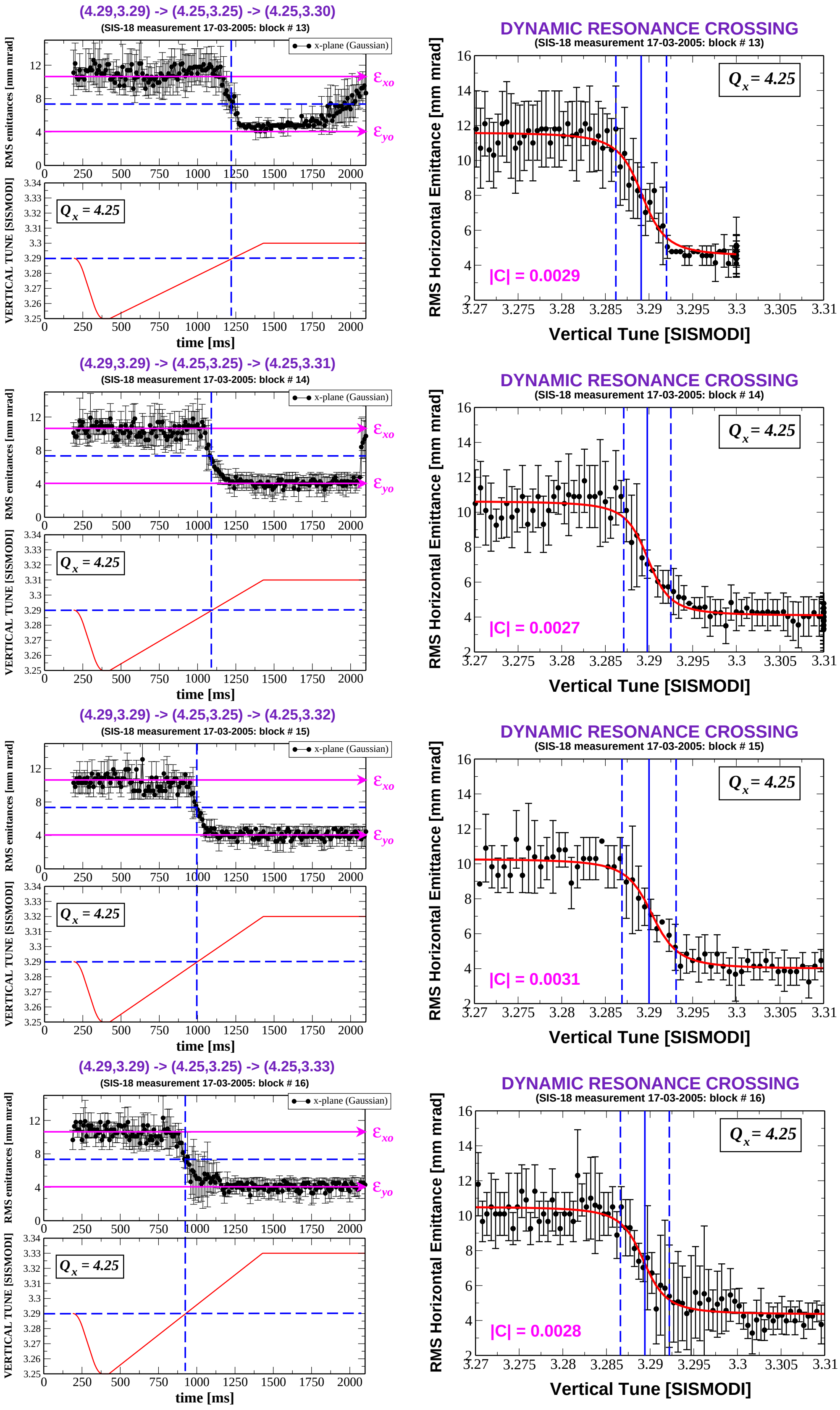

Figure 7.15: Left: the horizontal emittance exchange curve and tune ramp against time. Right: horizontal emittance exchange against the set value of Q_y ($Q_x = 4.25$ during the cycle) and superimposed fit of Eq. (6.1) (right). Error bars correspond to 1σ

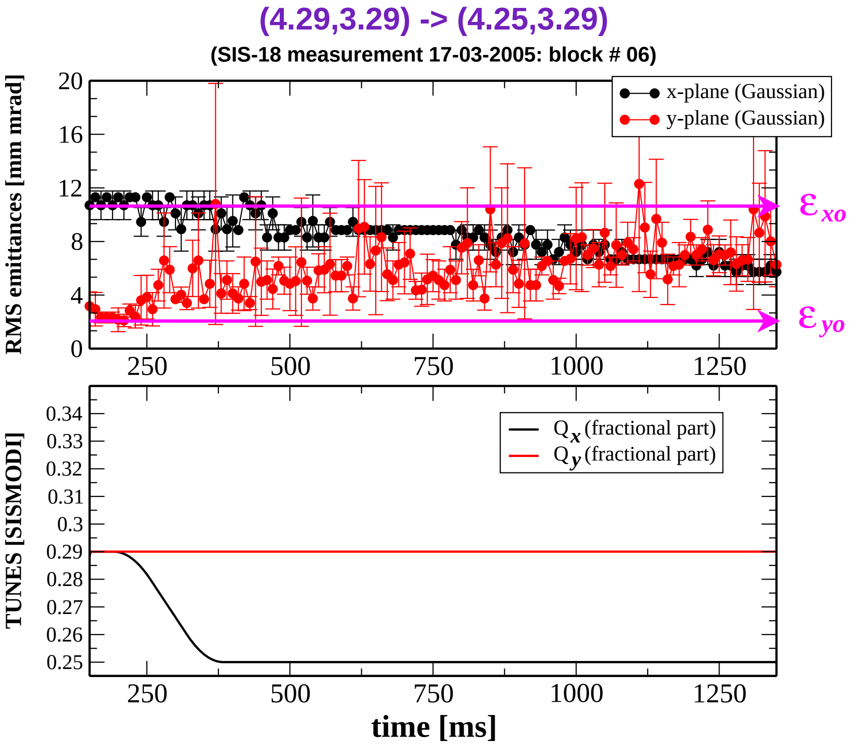

Figure 7.16: First evidence of emittance equilibration in the SIS-18 (at injection plateau) driven by betatron coupling and dynamical crossing of half stop band width (Error bars correspond to 1σ).

Future SIS-18 operations as booster for the planned SIS-100 requires emittance equilibration at extraction. Eqs. (6.1)-(6.2) guarantee that crossing adiabatically the resonance stop band, a working point $\Delta \simeq 0$ exists, where $|f_{1001}| \simeq \pi/8$ and the two transverse emittances are equal. Crossing half of the resonance stop band and fixing the final working point to the resonance center $\overline{Q}_x = 4.25$, $\overline{Q}_y = 3.289$ should provide in first approximation equal emittances. The first experimental evidence of this process in the SIS-18 is shown in Fig. 7.16: despite a poor resolution in the vertical signal, there is clear indication that final emittances get very close to each other. Further studies are anyway mandatory: besides the poor resolution in the vertical signal, it is not clear why the equilibration needs almost 1 s, whereas fast crossing in few tens of ms was observed to be enough to drive a full exchange, as shown in Fig. 7.13.

During the last block of measurement on May 2005 a dependence of the measured $|C|$ on the beam intensity was observed. For the same kind of crossing, different intensities and initial emittances (and hence different space-charge tune shifts) lead to two different emittance exchange curves. Differently from the measurement of

	case 1	case 2
Beam:	^{86}Kr^{34+}	^{86}Kr^{34+}
injected current (mA):	0.13 ± 0.01	0.10 ± 0.01
energy (MeV/u):	11.28	11.28
RF Voltage (kV):	0	0
Q_x	4.25	4.25
Q_y	$3.25 \rightarrow 3.32$	$3.25 \rightarrow 3.32$
tune shift at injection ($\times 10^{-3}$):	$x:\ 2.2 \pm 0.2\quad y:\ 1.4 \pm 0.1$	$x:\ 3.4 \pm 0.8\quad y:\ 1.3 \pm 0.1$
initial emittances (mm mrad):	$\epsilon_{x0} \simeq 4.4\ \epsilon_{y0} \simeq 12.8$	$\epsilon_{x0} \simeq 1.8\ \epsilon_{y0} \simeq 14.1$

Table 7.5: Beam parameters during May 1 2005.

March and April the injected beam had vertical emittance larger than the horizontal one. Beam parameters for both cases are listed in Tab. 7.5.

RGM data in the horizontal plane, despite the high reproducibility, did not show the expected exchange as in Fig. 7.14. It is not clear why ϵ_x remains almost unchanged. In Fig. 7.17 the vertical emittance curves for both cases are shown. Both the inferred stop band width $|C|$ and the resonance center, where the vertical emittance is half of the sum of the initial and final values, are listed in Tab. 7.6. For a given vertical space-charge tune shift ΔQ_y, the larger the horizontal tune shift ΔQ_x, the broader is the observable stop band width and the further away is $\overline{Q}_y$ from the resonance condition of the bare tunes. Technical problems and lack of beam time prevented any further systematic investigation on the dependence of $|C|$ on ΔQ_x. The impossibility of measuring on-line the tunes did not allow to cross-check the shift of the resonance condition. In Chapter 9 an attempt to explain such a dependence is presented.

	case 1	case 2
tune shift :	$\Delta Q_x = 0.0022$	$\Delta Q_x = 0.0034$
resonance center ($\overline{Q}_x = 4.25$):	$\overline{Q}_y = 3.277 \pm 0.003$	$\overline{Q}_y = 3.291 \pm 0.004$
$\lvert C\rvert$ (10^{-3}):	2.6 ± 0.1	3.9 ± 0.1

Table 7.6: Inferred resonance center and stop band width $|C|$ for both case 1 and case 2 of Tab. 7.5. $|C|$ is obtained fitting the emittance curve with Eqs. (6.1)-(6.2).

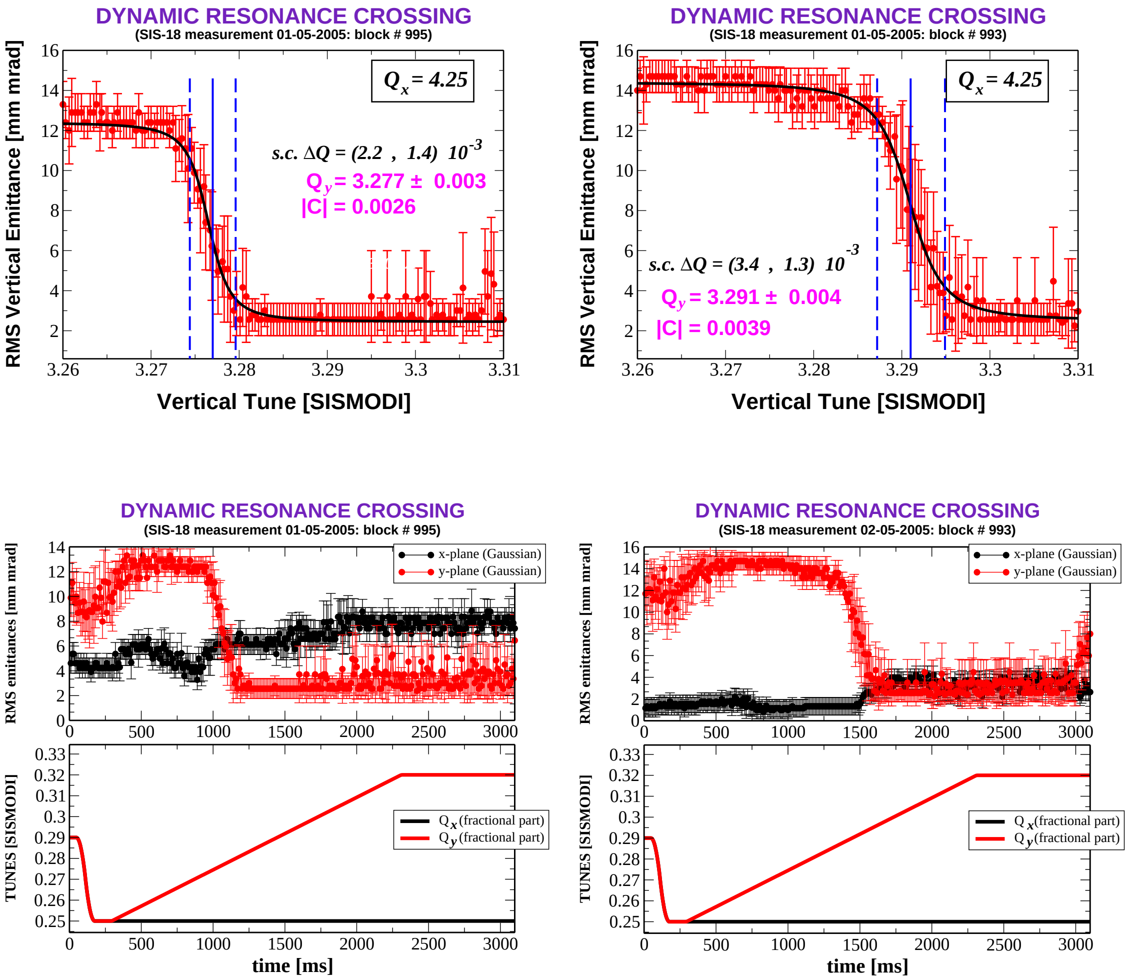

Figure 7.17: Emittance exchange curves during a dynamical crossing measured for different space-charge tune shift (Error bars correspond to 1σ): vertical emittance versus the nominal vertical tune (top) and time (bottom).

7.7 Betatron coupling resonance compensation in the SIS-18

In August 2005 for the first time the eight skew quadrupoles installed in the SIS-18 could have been powered. The compensation was carried out parasitically with a physics experiment at high intensity. For technical reasons it was not possible to acquire RGM data. The compensation therefore was carried using the injection efficiency to determine the best corrector setting. The beam was injected with a multi-turn injection over several turns, filling entirely the horizontal acceptance A_x. Close to the difference resonance $Q_x \simeq Q_y + 1$ uncompensated betatron coupling drives a rotation in the $x - y$ plane resulting in beam loss, as the vertical acceptance is smaller than the horizontal one (at injection energy $A_x = 200$ and $A_y = 50$ mm mrad). Betatron coupling is corrected when beam loss at $Q_x \simeq Q_y + 1$ is no longer

Q_y	S01KMQS	S02KMQS	S06KMQS	S07KMQS	S08KMQS	S12KMQS	$N_p \times 10^{10}$
3.355	**0**	**0**	**0**	**0**	**0**	**0**	$\mathbf{2.0 \pm 0.1}$
3.17	0	0	0	0	0	0	1.3 ± 0.1
3.17	0	5	0	0	5	0	1.4 ± 0.1
3.17	0	10	0	0	10	0	1.7 ± 0.1
3.17	0	12	0	0	12	0	1.7 ± 0.1
3.17	**0**	**15**	**0**	**0**	**15**	**0**	$\mathbf{2.0 \pm 0.1}$
3.17	0	10	-5	0	10	-5	0.5 ± 0.1
3.17	0	10	-2	0	10	-2	1.5 ± 0.1
3.17	0	10	2	0	10	2	1.6 ± 0.1
3.17	0	10	5	0	10	5	1.0 ± 0.1
3.17	2	10	0	2	10	0	1.7 ± 0.1
3.17	2	15	0	2	15	0	1.8 ± 0.1
3.17	5	15	0	5	15	0	1.9 ± 0.1
3.17	-5	15	0	-5	15	0	1.7 ± 0.1

Table 7.7: Number of particles after the multi-turn injection (4 ms) for different working point and strengths of the skew quadrupoles, whose units are the one of SISMODI (10^{-3} m^{-1}). $Q_x = 4.17$ during the measurement. S04KMQS and S10KMQS were not used.

observed.

The machine was setup and optimized for the main experiment with high intensity $^{14}N^{7+}$ beam. The injection was found to be optimized at $Q_x = 4.17$ and $Q_y = 3.355$ providing $\sim 10^{11}$ particles before the RF capture. For the compensation we proceeded as follows.

The intensity from UNILAC was reduced of a factor five in order to avoid space charge effects, obtaining

$$Q_x = 4.17, \quad Q_y = 3.355 \qquad \longrightarrow \qquad N_p = 2.0 \pm 0.1 \times 10^{10} \ .$$

The tune working point was moved close to the linear coupling resonance (see Fig. 7.18), obtaining a reduction of the injected beam of about 30%: [2]

$$Q_x = 4.17, \quad Q_y = 3.17 \qquad \longrightarrow \qquad N_p = 1.3 \pm 0.1 \times 10^{10} \ .$$

Skew quadrupoles were powered on and a heuristic scan of their strengths was performed aiming at minimizing this reduction (the scan is listed in Tab. 7.7). The entire 30% of losses was completely compensated by the following setting

$$\text{S02KMQS, S06KMQS} = 15 \times 10^{-3}\mathrm{m}^{-1} \qquad \longrightarrow \qquad N_p = 2.0 \pm 0.1 \times 10^{10} \ ,$$

with the other skew quadrupoles were turned off.

---

[2] Only the vertical tune was changed in order not to modify the injection scheme.

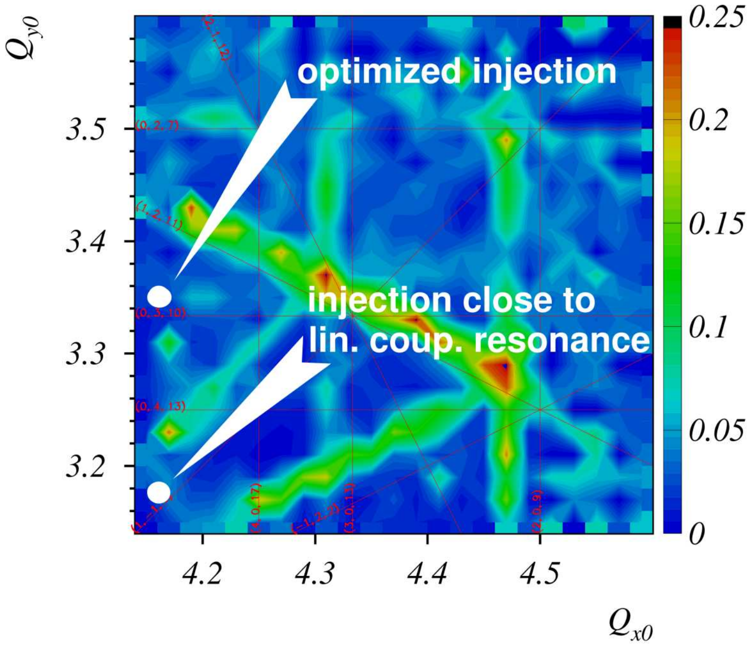

Figure 7.18: Picture showing the two working points used in the tune diagram: the upper spot corresponds to the injection point chosen for the main experiment, the lower one for linear coupling studies (Courtesy of G. Franchetti).

Chapter 8

Measuring and correcting betatron coupling

Measurement of $|C|$, also known in literature as ΔQ_{min}, is routinely performed in order to monitor and minimize betatron coupling by means of skew quadrupoles installed in the ring. For machine with split tunes (i.e. whose tunes are separated by at least one integer) the knowledge of $|C|$ is not enough to identify a priori the best corrector setting, and a scan of their strengths over several machine cycles is therefore necessary until a minimum is reached.

In this Chapter we present a new technique to infer from turn-by-turn multi-BPM data both the amplitude and phase of C and therefore a fast (single-cycle) correction scheme.

8.1 Betatron coupling correction

$|C|$ is usually inferred from tune measurement against Δ (closest-tune approach): the two eigen-tunes $Q_{h,v}$ get closer to each other approaching $\Delta \to 0$ until a minimum $\Delta_e \to \Delta Q_{min} = |C|$ is reached. Repeated tune measurements are therefore needed for different working points. In Sec. 7.5 and 7.6 alternative methods using beam profile monitors were illustrated. Other techniques such as first turn analysis and beam response after kick are described in [32].

None of the above technique provides any information on the phase of C. In [39] both amplitude and phase were measured observing the time evolution of the transverse beam profile after exciting the beam with a fast horizontal kick. In [40] the same measurement was carried out from turn-by-turn BPM data and a fit of the corresponding Poincaré map.

According to the definition of C given in Eq. (5.1) amplitude and phase are defined as follow

$$C = |C|e^{i\Theta} = -\frac{1}{2\pi}\oint ds\; j(s)\sqrt{\beta_x(s)\beta_y(s)}e^{-i(\phi_x(s)-\phi_y(s))+is/R\Delta} \;, \qquad (8.1)$$

In machine with unsplit tunes and working point close to the difference resonance $\phi_x(s) - \phi_y(s) \simeq 0$ along the entire ring. This results in $\Theta \simeq 0$ and a real C as sketched in Fig. 8.1. One family of corrector skew quadrupoles is therefore enough since its strength is always in phase with natural coupling. Note that this might not hold for colliders with unsplit tunes if local phase advances in the interaction regions differ largely from the phase advances in the arcs.

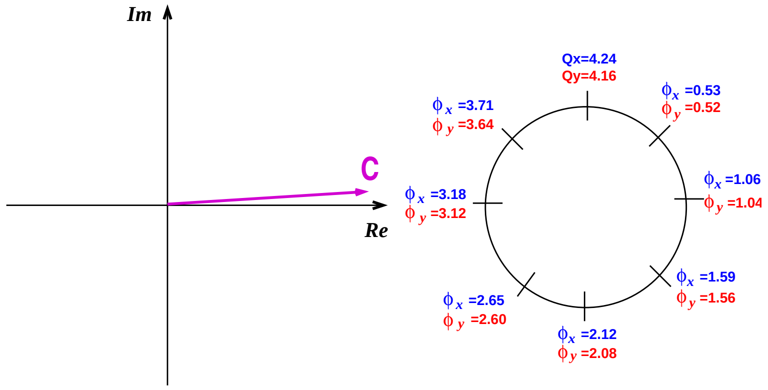

Figure 8.1: Sketch of C for a machine with unsplit tunes. On the right the betatron phases ϕ_x (blue) and ϕ_y (red) along the ring.

In machine with split tunes and working point close to the difference resonance $\phi_x(s) - \phi_y(s)$ varies from 0 to 2π along the ring, resulting in $\Theta \neq 0$ (see Fig. 8.2).

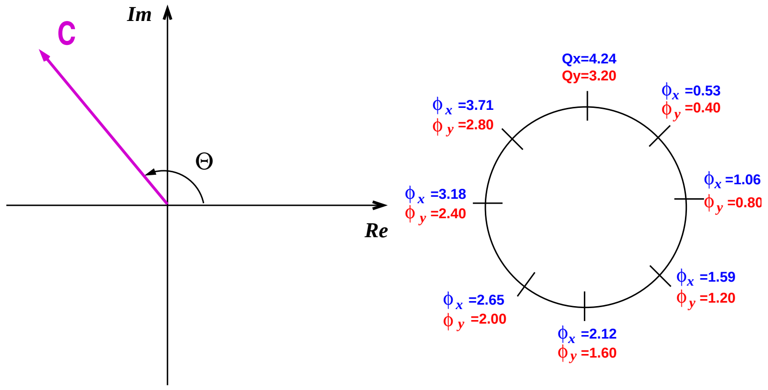

Figure 8.2: Sketch of C for a machine with split tunes. On the right the betatron phases ϕ_x (blue) and ϕ_y (red) along the ring.

The correction is in this case performed by means of at least two families of skew quadrupoles, each one them represented by a vector with phase Θ_{sq} given by

$$C_{sq} = |C_{sq}|e^{i\Theta_{sq}} = \frac{1}{2\pi} J_{sq} \sum_{w} \sqrt{\beta_x^w \beta_y^w} e^{-i(\phi_x^w - \phi_y^w)} \tag{8.2}$$

where the sum is over all the skew quadrupoles in the family, J_{sq} is the integrated strength (assuming a shared power supply), $\beta_{x,y}^w$ and $\phi_{x,y}^w$ are the Twiss functions at the skew quadrupole locations. If Θ is unknown a scan of the two families is necessary to drive an external coupling and minimize $C + C_{sq,1} + C_{sq,2}$. Measuring Θ the same goal is obtained without any scan by decomposing C on the directions $\Theta_{sq,1}$ and $\Theta_{sq,2}$ and making the families drive the opposite strengths as shown in Fig. 8.3.

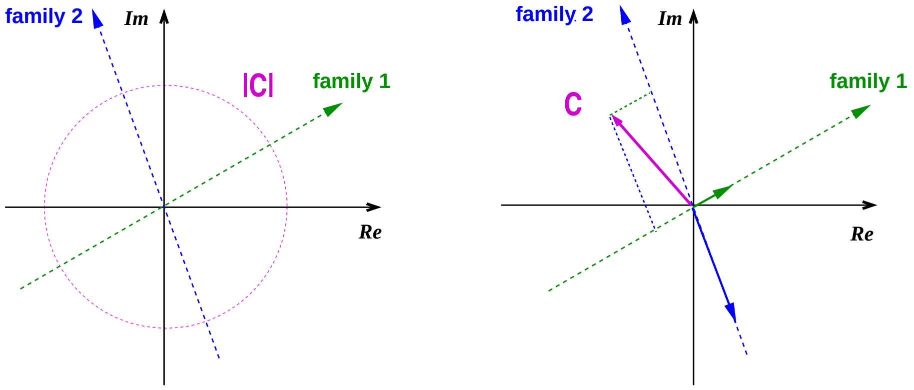

Figure 8.3: Left: complex plane with the measured $|C|$ and the directions of the two corrector families. Right: case with measurement of C, its decomposition along the two lines and corresponding correction setting.

In the following sections we illustrate a way to infer both $|C|$ and Θ from turn-by-turn multi-BPM data of a transversely excited beam.

8.2 From f_{1001} to $|C|$ (ΔQ_{min})

Eq. (5.26) suggests that $|C|$ can be measured with two separate measurements of both $|f_{1001}|$ (at any location) and $Q_{h,v}$. A Taylor expansion of $|C_0|$ around $\Delta = 0$ reads

$$4|f_{1001}\Delta_e| \simeq |C_0| \simeq |C| + C_o'\Delta, \qquad \text{for } |C| < \Delta << 1 \ . \tag{8.3}$$

the latter condition is required for replacing $\bar{f}_{1001}$ with f_{1001} in Eq. (5.26) (see Fig. 5.6). Two measurements of $|C_0|$ at two different working points (better if symmetric with respect to the resonance) are therefore enough to infer $|C|$ from a linear fit. In the left plot of Fig. 8.4 the inferred $|C|$ from two simulated measurements of $|f_{1001}|$ according to Eq. (8.3) is shown.

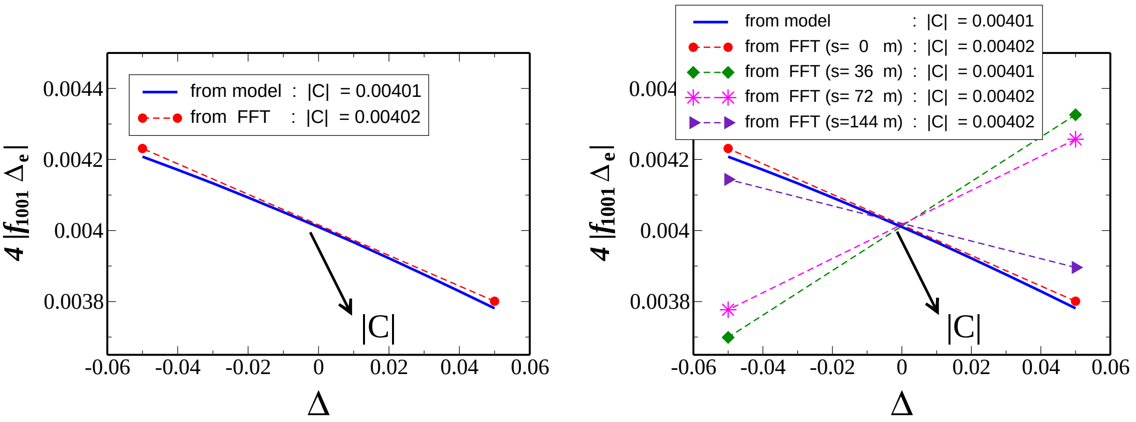

Figure 8.4: In the left plot an example of $|C|$ inferred from two simulated measurements of $|f_{1001}|$ at one location and Δ_e according to Eq. (8.3). In the right plot the measurement of $|f_{1001}|$ is performed at several locations and for each location Eq. (8.3) is applied. All the linear fits provide for $\Delta = 0$ almost the same expected value of $|C| = 4.01 \times 10^{-3}$. The average of $|C_0|$ in each measurement provides already a good estimation of $|C|$.

Variations of $|f_{1001}|$ along the ring result in different lines having nearly the same values at $\Delta = 0$ as shown in the right plot of Fig. 8.4: single-particle simulations of the SIS-18 with distributed skew quadrupole kicks along the ring are run for two working points. The picture indicates that a single measurement of $|f_{1001}|$ at different locations provides already a good estimation of $|C|$, namely $|C| \simeq \sum_w^N |C_0|/N$ and therefore

$$|C| \simeq 4|\Delta|\frac{1}{N}\sum_w^N |f_{1001}^w|, \qquad \text{for } |C| < \Delta << 1 \ , \tag{8.4}$$

where $\Delta = Q_x - Q_y$ is the difference of the bare tunes (fractional part), N is the number of available BPMs and the latter condition is required for making use of Eq. (8.3) and for substituting $\Delta_e \simeq \Delta$.

In simulations shown in the right plot of Fig. 8.4 the average of $|f_{1001}|$ and Eq. (8.4) gives $|C| = 4.03 \times 10^{-3}$ for $\Delta = -0.05$, $|C| = 4.00 \times 10^{-3}$ for $\Delta = 0.05$, whereas the real value is $|C| = 4.01 \times 10^{-3}$. The accuracy is about 0.5%. For an effective measurement the available BPMs should cover as much uniformly as possible the entire ring: regions with large coupling uncovered by BPMs would prevent the average from describing the global amount of coupling.

8.3 From f_{1001} to phase of C (Θ)

Eq. (4.2) applied to f_{1001} reads

$$\hat{h}_{w,1001} = f_{1001}^{(w)} e^{-i(\Delta\phi_x^{w,w-1} - \Delta\phi_y^{w,w-1})} - f_{1001}^{(w-1)} \ , \tag{8.5}$$

where $\Delta\phi_q^{w,w-1}$ are the phase advances between the $(w-1)^{-th}$ and the w^{-th} BPMs and $f_{1001}^{(w)}$ is the RDT measured at the w^{-th} BPM. The l.h.s. of the above equation is given by

$$\hat{h}_{w,1001} = \frac{1}{4}\sum_{\tau} J_{\tau,1}\sqrt{\beta_x^{\tau}\beta_y^{\tau}} e^{i(\Delta\phi_{\tau,x}^{w-1} - \Delta\phi_{\tau,y}^{w-1})} \ . \tag{8.6}$$

The sum runs over all the multipoles between the $(w-1)^{-th}$ and the w^{-th} BPMs and $\Delta\phi_{\tau,q}^{w-1}$ are the phase advances between those multipoles and the $(w-1)^{-th}$ BPM. $J_{\tau,1}$ are the integrated skew quadrupolar strengths. After some algebra, it can be shown that the global Hamiltonian term $h_{1001}^{(w)}$ at the w^{th} BPM introduced in Eq. (3.15) is related to the coupling strength $|C_0|$, defined in Eq. (5.24), by

$$h_{1001}^{(w)} = |h_{1001}^{(w)}| e^{ih_\phi^w} = -\frac{\pi}{2} C_0 e^{i(\phi_x^w - \phi_y^w)} \ . \tag{8.7}$$

h_ϕ^w and $\phi_{x,y}^w$ are the Hamiltonian term and the BPM phases respectively. Amplitude and phases therefore read

$$\begin{aligned} |h_{1001}^{(w)}| &= \frac{\pi}{2}|C_0| && (8.8)\\ h_\phi^w &= \pm\pi + \Theta_0 + (\phi_x^w - \phi_y^w) \ . && (8.9) \end{aligned}$$

The sign in of π can be chosen arbitrarily, since the difference between the two choices is 2π. From Eq. (3.15) we obtain

$$|f_{1001}^{(w)}| e^{iq^w} = \frac{|h_{1001}^{(w)}| e^{ih_\phi^w}}{1 - e^{2\pi i(Q_h - Q_v)}} \simeq \frac{|C_0|}{4|\Delta_e|} e^{i\left[-\pi + \Theta_0 + (\phi_x^w - \phi_y^w) + \mathrm{sgn}(\Delta_e)\frac{\pi}{2}\right]} \tag{8.10}$$

$$\Rightarrow \qquad \Theta_0 = q^w - (\phi_x^w - \phi_y^w) + \pi\left[1 - \mathrm{sgn}(\Delta_e)\frac{1}{2}\right] \ . \tag{8.11}$$

In absence of any coupling source between two BPMs $\hat{h}_{w,1001} = 0$ and, according to Eq. (8.5), the evolution of f_{1001} is a pure rotation whose angle is $\Delta\phi_x^{w,w-1} - \Delta\phi_y^{w,w-1}$. In this case the evolution of phase of $f_{1001}^{(w)}$ reads

$$q^w - q^{w-1} = \Delta\phi_x^{w,w-1} - \Delta\phi_y^{w,w-1} \qquad \text{for } \ \hat{h}_{w,1001} = 0 \ , \tag{8.12}$$

and the following quantity is invariant along regions free of coupling

$$q^w - (\phi_x^w - \phi_y^w) = \ \text{const.} \qquad \text{for } \ \hat{h}_{w,1001} = 0 \ . \tag{8.13}$$

From Eq. (8.11) we deduce that also Θ_0 is constant in region free of coupling, whereas exhibits jump in presence of a skew quadrupole kick. Θ_0 is observable, with both q and Δ_e measurable as shown in Sec. 5.6. $\phi^w_{x,y}$ are the betatron phase of the w^{-th} BPM and can be taken from the model.[1]

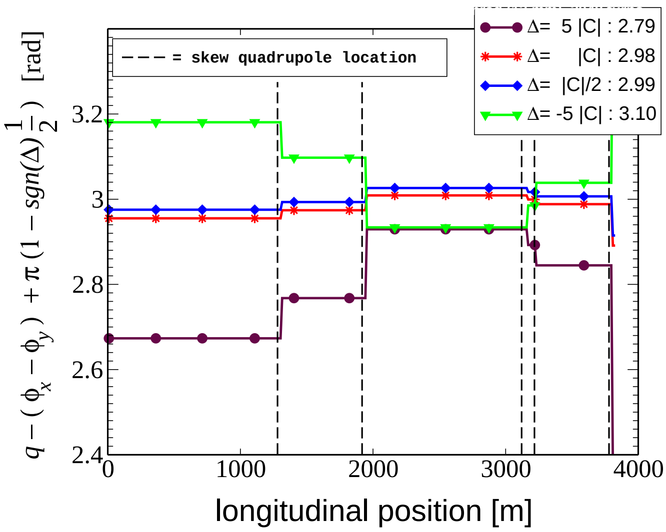

Figure 8.5: MADX tracking simulation of the RHIC Yellow ring at injection energy with betatron coupling $|C| = 0.01$: the quantity Θ_0 at the BPM locations is plotted for different working points, together with the location of skew quadrupolar kicks. In regions free of coupling it remains constant. Jumps become weaker approaching the resonance condition $\Delta = 0$. The betatron phases $\phi_{x,y}$ are taken from the MADX lattice model.

In Fig. 8.5 the variation along the RHIC Yellow ring (injection energy) of Θ_0 is plotted for a lattice with betatron coupling $|C| = 1\%$ and for different working points (outside, at the edge and inside the stop band $|C|$). For $\Delta > |C|$ jumps are visible in correspondence of skew quadrupolar kicks. They become less visible moving the working points towards the resonance $\Delta = 0$, where $\Theta_0 = \Theta$.

A Taylor expansion around $\Delta = 0$ similar to the one introduced in Eq. (8.3) can be performed

$$\Theta_0 = q^w - (\phi_x - \phi_y) + \pi\left[1 - \mathrm{sgn}(\Delta)\frac{1}{2}\right] \simeq \Theta + \Theta_0'\Delta \ , \qquad (8.14)$$

Two measurements taken at different working points in any location along the ring are therefore enough to infer unambiguously Θ. Note that the substitution $\mathrm{sgn}(\Delta_e) = \mathrm{sgn}(\Delta)$ made here is not an approximation, since the Δ and Δ_e change simultaneously sign.

---

[1] They can be also inferred from the BPM spectra after choosing one BPM as reference. The correction relies anyway on the Twiss function at the skew quadrupole locations as shown in Eq (8.2) which are taken from the model, not being observable in a straightforward and reasonably fast way.

A single measurement of Θ_0 along the ring for $|C| < \Delta << 1$ provides anyway a good estimation of Θ, resulting as

$$\Theta \simeq < \Theta_0 > = \frac{1}{N}\sum_{w}^{N}[q^w - (\phi_x^w - \phi_y^w)] + \pi\left[1 - \mathrm{sgn}(\Delta)\frac{1}{2}\right] \ + \ O(\Delta)\ , \tag{8.15}$$

where N is again the number of available BPMs, q^w is the phase of f_{1001} measured at the w-th BPM and the remainder is proportional to Δ. In Fig. 8.5 $\Theta = 3.0$ rad and Eq. (8.15) applied to $\Delta = \pm 0.05$ provides 2.8 and 3.1 respectively. The deviation from the correct value is $\approx 5\%$ as expected.

8.4 Measurement and correction of C in RHIC during 2005

Eq. (8.4) is applied to the RHIC BPM data of [14]. The inferred $|C|$ are compared with the one obtained applying the N-turn map algorithm described in [41]. The results listed in Tab. 8.1 are compatible. The standard deviation of $|f_{1001}|$ along the ring is used as error indicator. The use of several BPMs and the average make the formula robust against failure of few BPMs (isolated large jumps in upper plots of Fig. 8.6).

	date	$< \|f_{1001}\| >$	Δ_e	$\|C\|$ Eq. (8.4)	$\|C\|$ [41]
case 1	May 30	0.020 ± 0.008	0.013	0.0011 ± 0.0004	0.0016
case 2	May 30	0.049 ± 0.009	0.048	0.009 ± 0.001	0.010
case 3	June 8	0.025 ± 0.009	0.039	0.004 ± 0.001	0.0031
case 4	June 13	0.030 ± 0.009	0.041	0.0049 ± 0.001	0.0044
case 5	June 13	0.040 ± 0.010	0.030	0.0048 ± 0.001	0.0044
case 6	June 13	0.025 ± 0.008	0.045	0.0045 ± 0.001	0.0044

Table 8.1: $|C|$ of the RHIC “yellow” ring at injection energy from f_{1001} measurement during 2005 using Eq. (8.4) compared with the ones obtained with the N-turn map algorithm [41] (RHIC BPM data 2005, courtesy of R. Calaga).

During the measurement of May 30 and June 13 2005 BPM data were taken turning off the three families of corrector skew quadrupoles. The corresponding $|C|$ and Θ are therefore the amplitude and the phase respectively of the natural coupling complex vector C. In Fig. 8.6 the variation along the ring of $|f_{1001}|$ is shown. The measured coupling strengths are

$$|C| = (9.6 \pm 1.7) \times 10^{-3} \qquad \text{May 30} \tag{8.16}$$
$$|C| = (\ 16 \pm\ 1\ ) \times 10^{-3} \qquad \text{June 13} \tag{8.17}$$

The variation along the ring of $q - (\phi_x - \phi_y) + \frac{\pi}{2}$ is shown in Fig. 8.7 and the measured mean values according to Eq. (8.15) are

$$\Theta = (5.56 \pm 0.19)\ \text{rad} = (319 \pm 16)\ ^o \quad \text{May 30} \tag{8.18}$$
$$\Theta = (5.58 \pm 0.17)\ \text{rad} = (320 \pm 10)\ ^o \quad \text{June 13} \tag{8.19}$$

The standard deviation of $q - (\phi_x - \phi_y)$ along the ring is used to estimate the error. Despite the high reproducibility (the plotted data points have fluctuations smaller than 30%), few spikes appear due to faulty BPMs: their locations are indeed in correspondence of unrealistic large jumps in Fig. 8.6. Their contribution to the computation of Θ is anyway negligible thanks to their limited number.

In May 30 a scan using two independent skew quadrupoles (`SQ11C2Y` and `SQ01C2Y`) was performed to minimize $|C|$ (ΔQ_{min}). The measurement of the natural coupling was performed with trim values of

$$J_{1,\ \text{SQ01C2Y}} = 2 \times 10^{-4} \quad \text{m}^{-1} \qquad \text{trim value} \tag{8.20}$$
$$J_{1,\ \text{SQ11C2Y}} = 3 \times 10^{-4} \quad \text{m}^{-1} \qquad \text{trim value}\ . \tag{8.21}$$

The scan shown in Fig 8.8 provided the following best setting

$$J_{1,\ \text{SQ01C2Y}} \simeq 6 \times 10^{-4} \quad \text{m}^{-1} \qquad \text{best strength (scan)} \tag{8.22}$$
$$J_{1,\ \text{SQ11C2Y}} \simeq 7 \times 10^{-4} \quad \text{m}^{-1} \qquad \text{best strength (scan)}\ . \tag{8.23}$$

A similar result is obtained without any scan by just decomposing C on the axes defined by the skew quadrupoles, whose parameters are listed in Tab. 8.2. Their directions in the complex plane, defined by $e^{-i2\pi(\mu_x - \mu_y)}$ according to Eq. (8.2), are plotted in Fig. 8.9 together with C and its decomposition on the two axes. The gradients J_{sq} are obtained by C_{sq} using the model beta functions and inverting Eq. (8.2). Adding the trim values that were set while measuring C, the best corrector setting eventually reads

$$J_{1,\ \text{SQ01C2Y}} \simeq (5.2 \pm 1.9) \times 10^{-4} \quad \text{m}^{-1} \qquad \text{best strength (RDT)} \tag{8.24}$$
$$J_{1,\ \text{SQ11C2Y}} \simeq (6.3 \pm 1.9) \times 10^{-4} \quad \text{m}^{-1} \qquad \text{best strength (RDT)}\ . \tag{8.25}$$

Note that during the scan of each skew quadrupole, the other was was set to the trim value. The above setting therefore was actually never tried during the measurement. The error is inferred from the decompositions of the upper and lower values of both $|C|$ and Θ defined by their error bars.

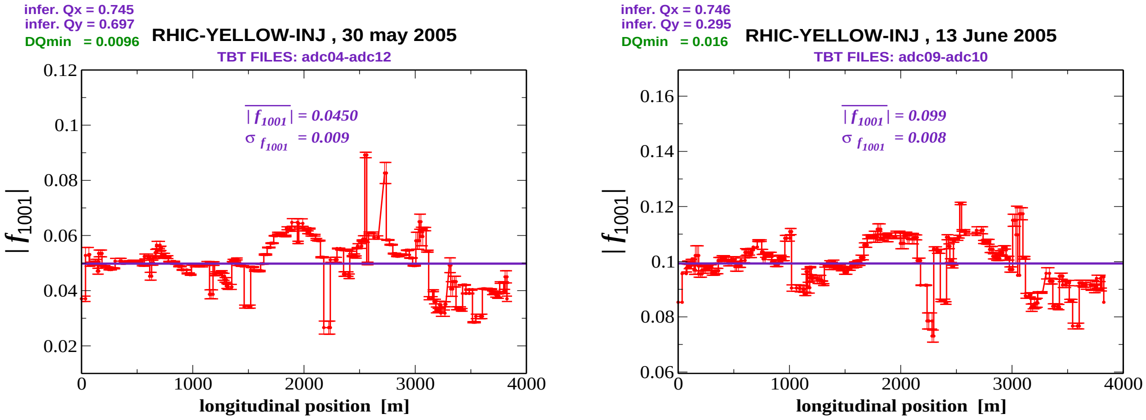

Figure 8.6: Variation along the "yellow" ring at injection of $|f_{1001}|$ driven by natural betatron coupling. In both cases the three families of corrector skew quadrupoles were turned off. (RHIC BPM data May 30 2005, courtesy of R. Calaga)

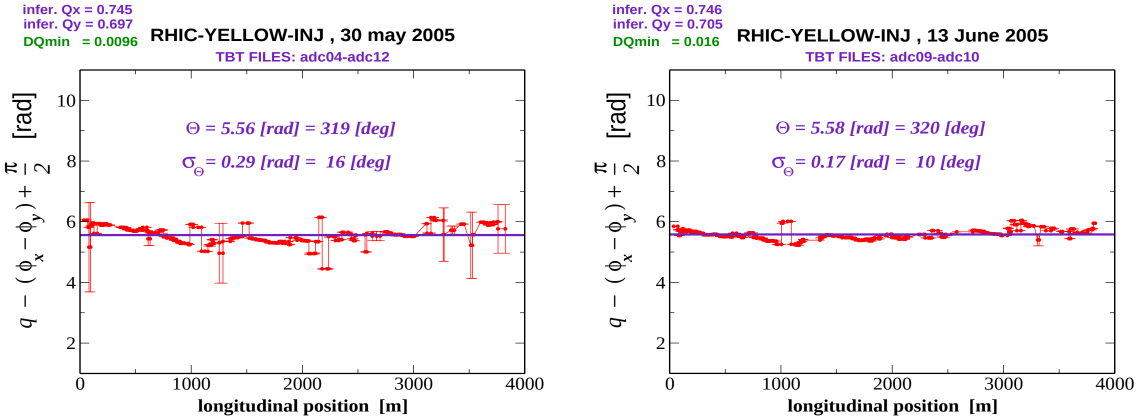

Figure 8.7: Measured variation along the "yellow" ring at injection of Θ_0 and corresponding averaged value Θ. The averaged is performed over 8 data files taken turning off all the corrector skew quadrupoles. Data points with fluctuation larger than 30% were rejected (RHIC BPM data May 30 2005, courtesy of R. Calaga).

skew quadrupole	location [m]	β_x [m]	β_y [m]	μ_x [2π]	μ_y [2π]	trim value [$\times 10^{-4}$ m^{-1}]
`SQ01C2Y`	1311.19	92.918	104.361	9.787	10.100	2
`SQ11C2Y`	1950.63	113.400	84.028	15.099	14.539	3

Table 8.2: Parameters of the two skew quadrupoles used to minimize $|C|$ (ΔQ_{min}).

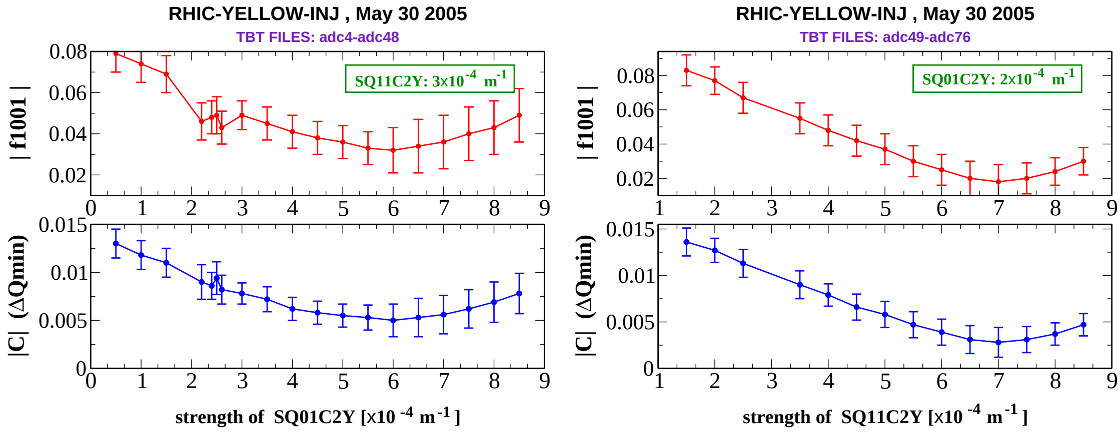

Figure 8.8: Scan of the skew quadrupoles SQ01C2Y (left)and SQ11C2Y (right) to minimize $|C|$ (ΔQ_{min}). During the scan of each quadrupole, the other one was set to the trim value (RHIC BPM data 2005, courtesy of R. Calaga).

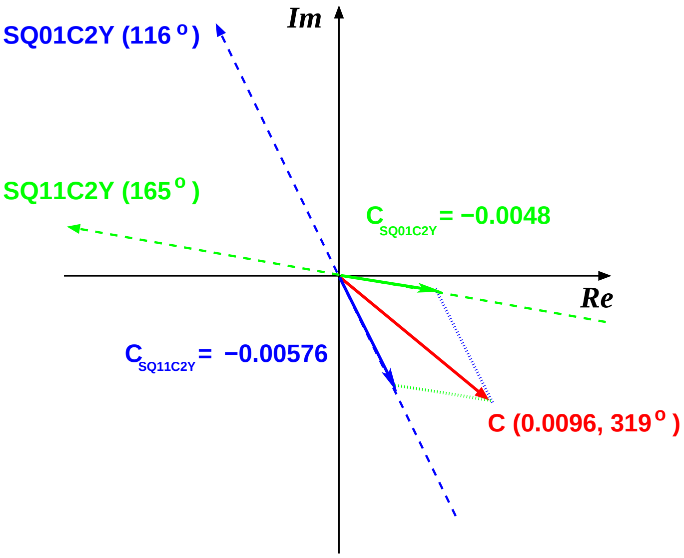

Figure 8.9: Sketch of the measured C decomposed on the axis defined by the two skew quadrupoles used for correction. The phase of C is measured, whereas the directions defined by the two skew quadrupoles are obtained using the model phase advances and Eq. (8.2).

Chapter 9

Space charge and emittance transfer

In the previous chapters we analyzed the emittance transfer driven by betatron coupling excited by tilted normal quadrupoles and skew quadrupoles. The emittance transfer is described in terms of the single particle motion, and the collective behavior is obtained averaging over the particle distribution.

The single particle nature of this effects results in linearly coupled Hill's equations and in a rotation of the beam in both the phase space and the configuration space x-y.

If space-charge effects need to be taken into account, the single particle description is not anymore sufficient because of the intrinsic coupling between forces acting on each particle and the RMS beam size.

Both in simulations [42, 43] and experiments carried out at the CERN Proton Synchrotron [44, 45] it was observed that in some cases, close to the difference resonance, space charge drives a similar emittance transfer, in the static as well as in the dynamic case, even in the absence of betatron coupling. A theoretical effort has being recently carried out at GSI by Franchetti and Hofmann aiming at describing these phenomena in terms of the "Montague octupolar resonance" [42, 47] and space-charge "self-skew" driven by a not upright beam distribution [43, 46, 48].

While undesirable emittance transfer driven by betatron coupling can be cured by using external skew quadrupoles to minimize the resonance stop band $|C|$, similar recipes for the exchange driven by space charge presently do not exist. A correct understanding of its mechanism is therefore mandatory to explore possible future countermeasures.

Despite some similarities between the emittance transfer driven by betatron coupling and space charge, some important differences (partially not yet understood in the literature) exist. Betatron linear coupling drives an almost symmetric emittance sharing and exchange independent from both the resonance crossing direction and the tune separation (integer difference between the betatron tunes). It has been observed that space-charge-driven emittance transfer is highly sensitive to both these aspects, namely

- PIC simulations show that the emittance exchange driven by space charge is not always reversible

- in machines with unsplit tunes space charge drives emittance transfer even without betatron coupling, whereas in machines with split tunes a nonzero, even if small, betatron coupling is necessary to lead the exchange
- if space charge is not negligible the emittance sharing curve exhibits a strong asymmetry around the resonance center
- the center of the space-charge resonance is always at $\Delta = 0$ in case of unsplit tunes, it is displaced in case of split tunes and the displacement is proportional to the Laslett tune shift
- if the tunes are unsplit, the dynamical crossing drives a symmetric curve and a complete exchange only if the crossing is executed in the *proper* direction; the emittance curve is asymmetric and the exchange partial if the crossing is performed in the opposite direction; on the resonance $\Delta = 0$ the emittance are always equal; for given RMS beam sizes, the stop band is proportional to the Laslett tune shift.
- if the tunes are split, the dynamical crossing is highly dependent on the direction and the ratio between the betatron coupling stop band $|C^{(b)}|$, defined in Eq. (5.1), and the tune shift; on the resonance the two emittances might not be equal
- in the case with unsplit tunes beam rotation, in the phase space as well in the configuration space x-y is not observed; the emittance transfer is connected with an *exchange of the RMS beam sizes*. Normally the sum of the RMS emittance is found preserved, although in some exceptional cases with transient behavior such a conservation is violated.

In this chapter space-charge effects on the emittance exchange crossing the difference resonance are numerically studied in oder to derive heuristic scaling laws for the stop band. The starting point in the case of machines with unsplit tunes and in the absence of betatron coupling is the stop band proposed in Ref. [49]

$$|\overline{C}^{(sc)}| = \frac{|\Delta Q_y|}{1+\dfrac{\sigma_{xo}}{\sigma_{yo}}} \qquad \Delta Q_y \simeq \frac{K_{sc}R^2}{2Q_{y0}\sigma_{yo}(\sigma_{xo}+\sigma_{yo})}\ , \tag{9.1}$$

where ΔQ_y is the *initial* Laslett tune shift, $\sigma_{xo,yo}$ are the initial RMS beam sizes, Q_{yo} is the bare vertical tune and $K_{sc} = qI/[2\pi\epsilon_0 m(\gamma\beta c)^3]$ is the space-charge perveance (I the current, q, m the charge and mass, β, γ the relativistic factors and ϵ_0 the dielectric constant). Multi-particle simulations with several initial conditions (beam current and RMS emittances) have been run in order to establish the range of validity of Eq. (9.1) and to infer correction factors.

In this chapter it is also shown why in machines with split tunes, in the smooth approximation, space charge cannot drive any emittance transfer. External nonzero betatron coupling is needed to initiate the exchange. Space charge here has the effect of introducing an emittance dependent detuning, through the Laslett tune shift: both the asymmetry in the emittance exchange curves and the enlargement of the observable stop band are described in term of the detuning. A scaling law for the ***observable*** stop band against the tune shift is inferred from multi-particle simulations.

9.1 Multi-particle PIC simulations

Multi-particle simulations, whose results are presented in this chapter, have been run using the MICROMAP libraries [50] with a self consistent 2D PIC Poisson solver described in Ref. [51, 52]. The reference particle is $^{238}\mathrm{U}^{+28}$ at 1.4 MeV/u and the beam is generated using a 4D Gaussian random generator. The reference lattice corresponds to the one of SIS-18 ($R = 34.492$ m) at the injection plateau and consists of 12 FDF periods. The nominal bare tunes are split, $Q_{x0} = 4.29$ and $Q_{y0} = 3.29$. Simulations with unsplit tunes have been run setting $Q_{x0} = 4.29$ and $Q_{y0} = 4.29$. Betatron coupling, when introduced, is driven by random skew quadrupole errors in the focusing quadrupoles. The beam simulated is coasting and the synchrotron motion, as well as any longitudinal coupling (chromaticity and dispersion), is not included.

The Poisson solver is based on a 2D FFT. Dirichlet boundary conditions can be imposed over a generic domain: in our simulations the boundaries are defined by a square of 10 cm side. The charge distribution is deposited onto 64 × 64 mesh points using the nearest grid point (NGP) algorithm. The number of tracked macro-particles is 5×10^4.

9.2 Case with unsplit tunes

In Ref. [49] it has been proposed that the emittance exchange driven by space charge while crossing dynamically the difference resonance (1,-1) can be fitted with equations borrowed from betatron coupling theory and envelope perturbation theory in presence of space charge,

$$\begin{aligned}
\epsilon_x &= \epsilon_{x0} + \frac{|\overline{C}^{(sc)}|^2}{\overline{\Delta}^2 + |\overline{C}^{(sc)}|^2 \pm \overline{\Delta}\sqrt{\overline{\Delta}^2 + |\overline{C}^{(sc)}|^2}} \frac{\epsilon_{y0} - \epsilon_{x0}}{2} && (9.2)\\
\epsilon_y &= \epsilon_{y0} - \frac{|\overline{C}^{(sc)}|^2}{\overline{\Delta}^2 + |\overline{C}^{(sc)}|^2 \pm \overline{\Delta}\sqrt{\overline{\Delta}^2 + |\overline{C}^{(sc)}|^2}} \frac{\epsilon_{y0} - \epsilon_{x0}}{2} \quad , && (9.3)
\end{aligned}$$

where $C^{(sc)}$ and $\overline{\Delta}$ are defined as follow

$$|\overline{C}^{(sc)}| = \frac{|\Delta Q_y|}{1 + \dfrac{\sigma_{xo}}{\sigma_{yo}}} \,, \qquad \overline{\Delta} = 2Q_{x0} - 2Q_{y0} \,. \tag{9.4}$$

In order to be consistent with the nomenclature used in the previous chapters we redefine both variables according to

$$|C^{(sc)}| = \frac{1}{2}\frac{|\Delta Q_y|}{1 + \dfrac{\sigma_{xo}}{\sigma_{yo}}} \,, \qquad \Delta = Q_{x0} - Q_{y0} \,. \tag{9.5}$$

The redefinition leaves the emittance exchange relations unchanged

$$\epsilon_x = \epsilon_{x0} + \frac{|C^{(sc)}|^2}{\Delta^2 + |C^{(sc)}|^2 \pm \Delta\sqrt{\Delta^2 + |C^{(sc)}|^2}} \frac{\epsilon_{y0} - \epsilon_{x0}}{2} \tag{9.6}$$

$$\epsilon_y = \epsilon_{y0} - \frac{|C^{(sc)}|^2}{\Delta^2 + |C^{(sc)}|^2 \pm \Delta\sqrt{\Delta^2 + |C^{(sc)}|^2}} \frac{\epsilon_{y0} - \epsilon_{x0}}{2} \tag{9.7}$$

The sign in the denominator depends on the crossing direction and the ration of the initial emittances according the following observations. In Fig. 9.1 two examples of crossings are shown. Multi-particle simulations have been run with a beam

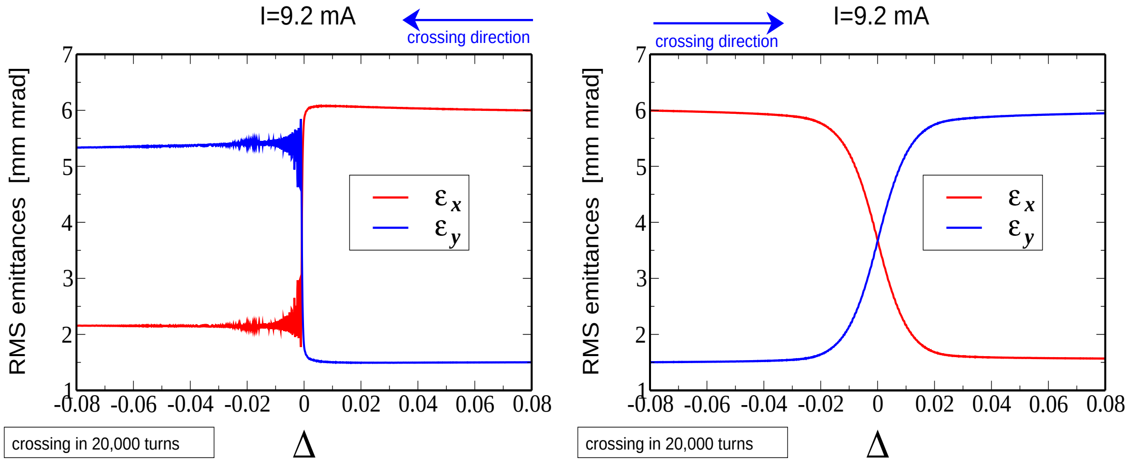

Figure 9.1: Multi-particle simulations of a Gaussian beam of initial RMS emittances $\epsilon_{x0} = 6$, $\epsilon_{y0} = 1.5$ mm mrad and current $I = 9.2$ mA. The resonance is crossed both *from below* (left) and *from above* (right), by fixing $Q_{x0} = 4.29$ and varying the bare vertical tune only.

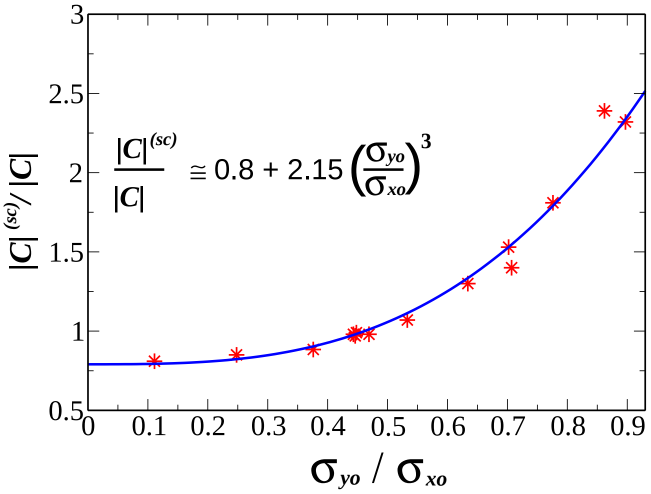

Figure 9.2: Ratio between the effective stop band computed numerically by multi-particle tracking, $|C|$, and the one defined by Eq. (9.5), $|C^{(sc)}|$, against the ratio between the two initial RMS beam sizes σ_{yo}/σ_{xo} (See Tab. 9.1). A polynomial fit is then superimposed.

of initial RMS emittances $\epsilon_{x0} = 6$, $\epsilon_{y0} = 1.5$ mm mrad and current $I = 9.2$ mA. The resonance is crossed at $Q_{x0} = Q_{y0} = 4.29$, by fixing $Q_{x0} = 4.29$ and varying the bare vertical tune only. No betatron coupling is introduced in the lattice. In the left plot the resonance is crossed starting *from below*, $\Delta > 0$, whereas in the right plot the starting point is $\Delta < 0$ and the resonance is crossed *from above*. Eqs. (9.6)-(9.7) can be applied to the second case only. If the initial emittances are such that $\epsilon_{x0} < \epsilon_{y0}$ the two conditions are inverted. Therefore the sign in the denominator is defined according to

$$\begin{cases} - & \text{if the crossing starts from } \Delta < 0 \text{ and } \quad \epsilon_{x0} > \epsilon_{y0} \\ + & \text{if the crossing starts from } \Delta > 0 \text{ and } \quad \epsilon_{x0} < \epsilon_{y0} \end{cases} \tag{9.8}$$

Multi-particle simulations have been run for various initial parameters, crossing the difference resonance *from above* ($\Delta < 0$) with initial emittances $\epsilon_{x0} > \epsilon_{y0}$. For each case the stop band defined in Eq. (9.5) is computed and compared with the one inferred superimposing Eqs. (9.6)-(9.7) to the emittance exchange curve obtained via tracking. The results are listed in Tab. 9.1. Eq. (9.5) predicts with very good agreement the resonance stop band if the initial beam sizes are such that $\sigma_{xo} \simeq 2\sigma_{yo}$. If $\sigma_{xo} >> \sigma_{yo}$ the stop band is slightly underestimated whereas it is largely overestimated if $\sigma_{xo} \simeq \sigma_{yo}$.

In Fig. 9.2 The ratio between the effective stop band computed via multi-particle tracking, $|C|$, and the one defined by Eq. (9.5), $|C^{(sc)}|$, is plotted against σ_{yo}/σ_{xo} (See Tab. 9.1). A polynomial fit is proposed to extend the range of applicability of $|C^{(sc)}|$ over $\sigma_{yo}/\sigma_{xo} \in [0.1, 0.9]$. Data of Tab. 9.1 are found to match Eqs. (9.6)-(9.7)

sim.	I mA	$(\epsilon_{x0},\ \epsilon_{y0})$ mm mrad	$(\sigma_{x0},\ \sigma_{y0})$ mm	initial tune shift $\lvert\Delta Q_x\rvert, \lvert\Delta Q_y\rvert$	$\lvert C^{(sc)}\rvert$ from Eq. (9.5)	$\lvert C\rvert$ from tracking
1	1.8	$(5, 1)$	$(6.34, 2.83)$	$0.009, 0.019$	0.0030	0.0031
2	1.8	$(5, 2.5)$	$(6.34, 4.48)$	$0.007, 0.010$	0.0021	0.0015
3	9.2	$(5, 1)$	$(6.34, 2.84)$	$0.043, 0.097$	0.0150	0.0152
4	9.2	$(5, 2)$	$(6.34, 4.02)$	$0.039, 0.061$	0.0118	0.0089
5	9.2	$(5, 3)$	$(6.34, 4.92)$	$0.035, 0.045$	0.0100	0.0054
6	9.2	$(5, 4)$	$(6.34, 5.69)$	$0.033, 0.037$	0.0088	0.0037
7	9.2	$(5, 4.6)$	$(6.34, 6.10)$	$0.032, 0.033$	0.0082	0.0018
8	18.4	$(5, 1)$	$(6.34, 2.81)$	$0.087, 0.196$	0.0300	0.0305
9	18.4	$(5, 2.5)$	$(6.34, 4.45)$	$0.074, 0.105$	0.0215	0.0141
10	20.0	$(9, 2)$	$(8.51, 3.99)$	$0.052, 0.110$	0.0175	0.0176
11	3.0	$(7, 2)$	$(7.50, 4.00)$	$0.010, 0.018$	0.0031	0.0028
12	10.0	$(4, 3.75)$	$(5.67, 5.47)$	$0.043, 0.045$	0.0110	0.0019
13	10.0	$(4, 3.00)$	$(5.67, 4.89)$	$0.046, 0.053$	0.0122	0.0051
14	15.0	$(7, 1.00)$	$(7.50, 2.82)$	$0.053, 0.141$	0.0191	0.0216
15	15.0	$(8, 0.50)$	$(8.02, 1.99)$	$0.051, 0.207$	0.0205	0.0242
16	15.0	$(8, 0.10)$	$(8.02, 0.89)$	$0.058, 0.540$	0.0250	0.0310

Table 9.1: Comparison between $|C^{(sc)}|$ defined in Eq. (9.5) and the one obtained from multi-particle simulations of the SIS-18 (FDF linear lattice without betatron coupling) and by fitting the emittance curves with Eqs. (9.6)-(9.7). The initial distribution is a 4D Gaussian and the resonance is crossed at $Q_{x0} = Q_{y0} = 4.29$ by keeping Q_{x0} fixed and sweeping the vertical tune only.

provided to use the following stop band width definition

$$|C| \simeq \frac{|C^{(sc)}|}{0.8 + \frac{Q}{2}\left(\frac{\sigma_{yo}}{\sigma_{xo}}\right)^3} = \frac{1}{2}\frac{|\Delta Q_y|}{1 + \frac{\sigma_{xo}}{\sigma_{yo}}} \frac{1}{0.8 + \frac{Q}{2}\left(\frac{\sigma_{yo}}{\sigma_{xo}}\right)^3}\ , \tag{9.9}$$

where $Q = 4.29$ is the center of the resonance in the above simulations.

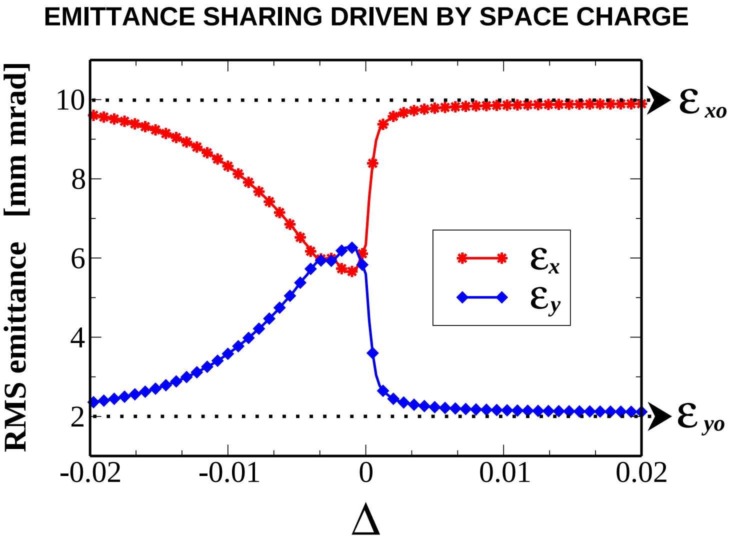

Figure 9.3: Sharing curve obtained from multi-particle simulation against Δ. For each working point the emittances are computed averaging over 500 turns the turn-by-turn values. The initial distribution is a Gaussian beam of initial RMS emittances $\epsilon_{x0} = 10$, $\epsilon_{y0} = 2.0$ mm mrad and current $I = 14.4$ mA.

In all the simulations, regardless on the crossing direction and the beam intensity (tune shift), the RMS emittances are found to be equal at $\Delta = 0$. This holds also in the static case as shown in Fig. 9.3: despite the asymmetry in the sharing curve, at $Q_{x0} = Q_{y0} = 4.29$ the averaged emittances are equal.

9.2.1 Suppressing the space charge driven emittance exchange

As shown in Chapter 8, betatron coupling can be corrected minimizing $|C^{(b)}|$ by means of skew quadrupoles families. A similar recipe does not apply to the space charge stop band $|C^{(sc)}|$ because of the different nature of the coupling: space charge deforms the shape of the distribution in the x-y space without driving any rotation (see Fig. 9.4), whereas skew quadrupoles preserve the elliptical shape and lead to a rotation (see Fig. 9.5).

Since the beam remains upright while crossing the Montague resonance one can think of normal quadrupoles to detune the machine and make the beam cross the resonance with an effective speed such to prevent any exchange and mismatch: a normal quadrupole (family) not belonging to the ones used for tuning the machine could be excited and its strength slowly varied to defocus the plane with larger envelope and focus the other one. The space-charge force acts in the opposite direction and the superposition of both might preserve the initial values as shown schematically in Fig. 9.6.

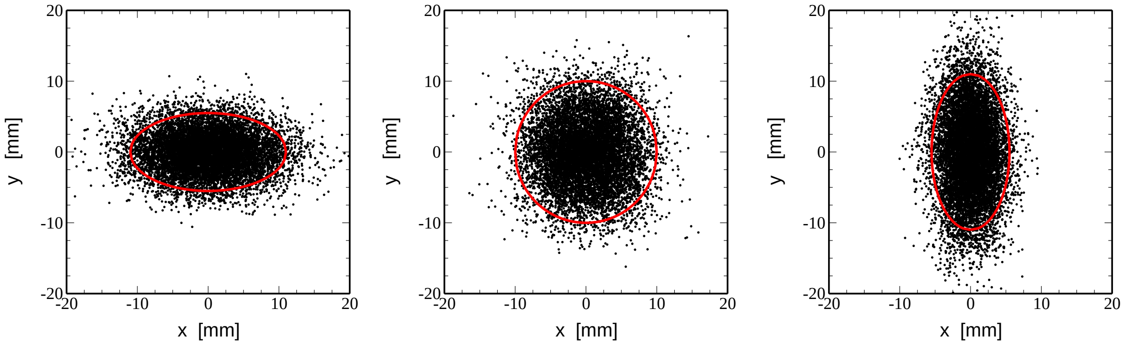

Figure 9.4: Transverse beam profile at the beginning of the resonance crossing $\Delta = -0.005$ (left), on the resonance $\Delta = 0$ (center), and at the end of the crossing $\Delta = 0.005$ (right). Multi-particle simulations without betatron coupling using a 4D Gaussian of initial emittances $\epsilon_{x0} = 10$, $\epsilon_{y0} = 2$ mm mrad and $I = 2.8$ mA, driving a stop band $|C^{(sc)}| = 0.008$.

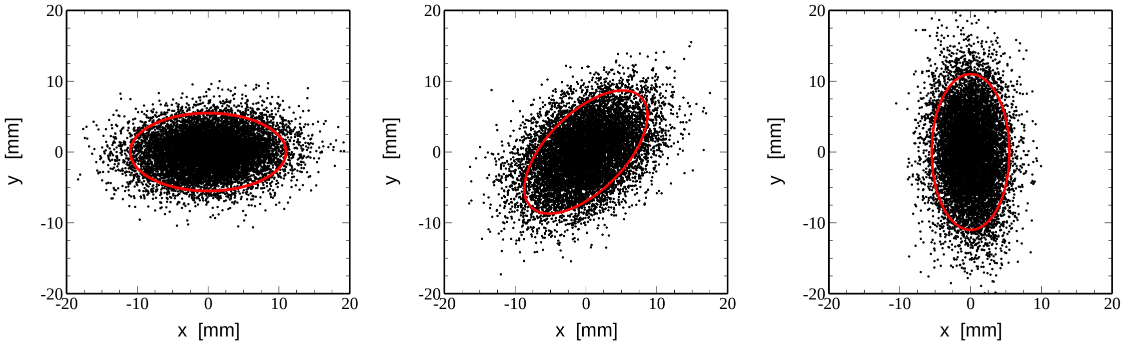

Figure 9.5: Transverse beam profile at the beginning of the resonance crossing $\Delta = -0.01$ (left), on the resonance $\Delta = 0$ (center), and at the end of the crossing $\Delta = 0.01$ (right). Multi-particle simulations at zero current with betatron coupling $|C^{(b)}| = 0.014$ using a 4D Gaussian of initial emittances $\epsilon_{x0} = 10$, $\epsilon_{y0} = 2$ mm mrad.

The main concern for using such a technique is that while turning off the normal quadrupole at the end of the crossing, the resonance is eventually hit. Therefore, optimized magnet ramps must be applied to avoid a fast emittance exchange and any induced mismatch due to a fast detuning at the rising and the fall edges of the ramp. The latter one must be fast and strong *enough* not to drive the exchange, but not *too* fast and strong in order to avoid mismatch and to be compatible with the performances of the power supplies.

Multi-particle simulations were run to investigate the efficiency of such a scheme. Dynamical crossings similar to the ones of Sec. 9 were performed while an additional normal quadrupole is powered and its integrated gradient varied turn by turn (N) according to

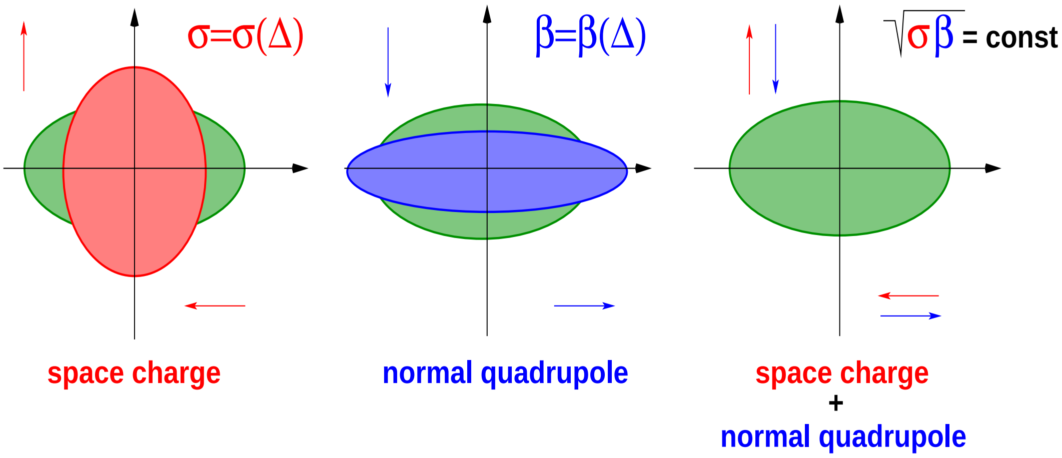

Figure 9.6: Sketch of the combined effect of space charge and additional normal quadrupole. An initial beam distribution (green ellipse) with large horizontal emittance is *squeezed* in x and *stretched* in y by space charge (left). An additional normal quadrupole defocusing in x and focusing in y has the opposite effect (center). The combination of the two deformations can preserve the initial envelopes and emittances (right).

$$K_1(N) = \overline{K}_1 \left[2\Theta(\Delta) - \mathrm{sign}(\Delta)\frac{N}{\overline{N}} \right]^p \ , \tag{9.10}$$

where $\overline{K}_1$ is the maximum (or minimum according to the magnet polarity) value of the gradient reached at resonance center, $\Theta(\Delta)$ is the step function ($\Theta(\Delta) = 0$ for $\Delta \leq 0$, $\Theta(\Delta) = 1$ for $\Delta > 0$), $\overline{N}$ is the total number of turns needed to cross the resonance, $\Delta = Q_x - Q_y$ is the distance from the resonance, and p is a free parameter. For given RMS emittances , $|C^{(sc)}|$ and dynamical crossing (i.e. $\overline{N}$) both $\overline{K}_1$ and p can be chosen to prevent or control the emittance exchange, in a way compatible with the power supplies (maximum deliverable gradient and magnet ramp).

In Fig. 9.7 simulated crossings in $\overline{N} = 2000$ turns with a beam current $I = 2.835$ mA, driving a stop band $|C^{(sc)}| = 0.0085$ are shown. In the left plot the normal quadrupole parameters are $\overline{K}_1 = -0.03$ m^{-1} and $p = 1/3$ leading to emittance equilibration at the end of the magnet ramp. In the center plot the case with $\overline{K}_1 = -0.04$ m^{-1} and $p = 1/3$ shows a partial exchange only, whereas in the right plot $\overline{K}_1 = -0.05$ m^{-1} and $p = 1/4$ prevent practically any emittance transfer.

In all cases the fast ramp does not induce any mismatch as shown in the bottom graphs of Fig. 9.7: the RMS beam sizes, as well as the RMS emittances, do not exhibit any growth after crossing the resonance and the magnet ramp; the skew momentum xy^{RMS} describing the beam titling remains in all cases close to zero.

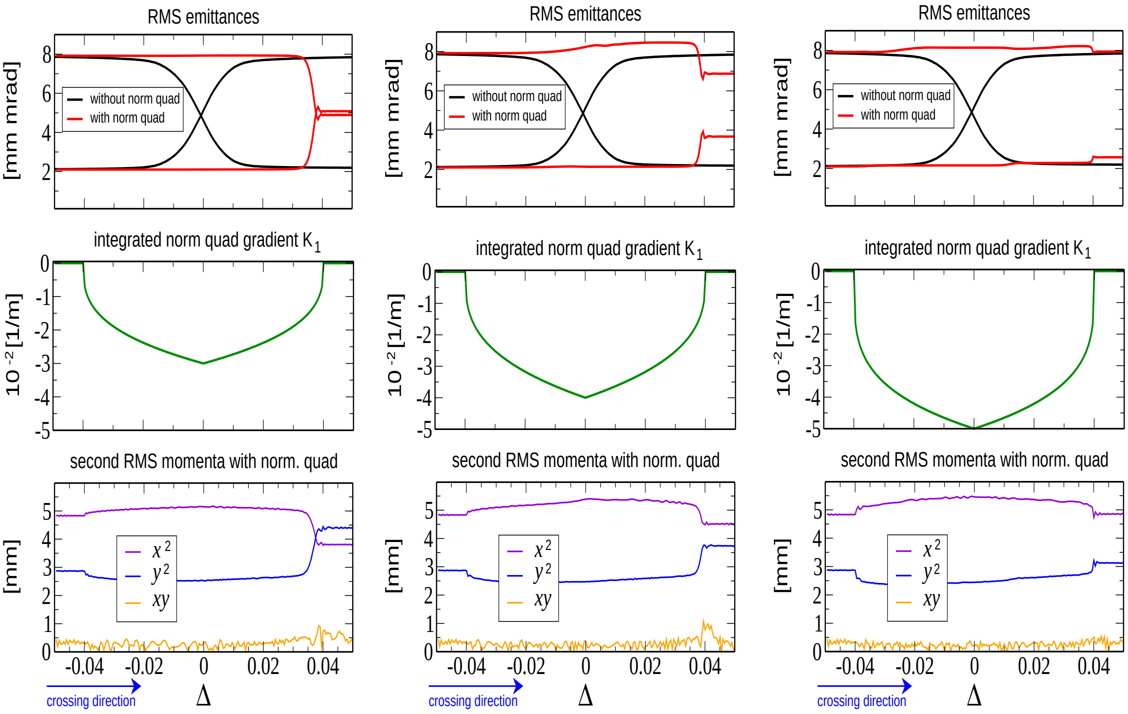

Figure 9.7: Multi-particle simulations of dynamical crossing of the space charge resonance ($|C^{(sc)}| = 0.0085$). Top: RMS emittance with (red curve) and without (black curve) the additional normal quadrupole. Center: variation of $\overline{K}_1$ while crossing. Bottom: second order RMS momenta $< x^2 >$, $< y^2 >$ and $< xy >$. Simulations have been run for different magnet ramps according to Eq. (9.10): $\overline{K}_1 = -0.03$ m^{-1} and $p = 1/3$ (left), $\overline{K}_1 = -0.04$ m^{-1} and $p = 1/3$ (center), $\overline{K}_1 = -0.05$ m^{-1} and $p = 1/4$ (right).

9.3 Case with split tunes

Split betatron tunes prevent space-charge to excite the difference resonance $(1, -1)$. This can be easily proven in the smooth approximation considering that potentials exciting the difference resonance are of the kind $V \propto (xy)^n$ for any n. The leading terms are skew quadrupoles, $V \propto xy$, and normal octupoles, $V \propto (xy)^2$. According to Sec. 3.4, the corresponding RDT are

$$\begin{cases} f_{1001} & \text{skew quadrupole potential} \quad V \propto xy \\ f_{2002} & \text{normal octupole potential} \quad V \propto (xy)^2 \end{cases} . \tag{9.11}$$

The other two excited RDTs are defined from the previous ones, since $f_{0110} = f^*_{1001}$ and $f_{0220} = f^*_{2002}$. According to Eq. (3.15) we can write

$$\begin{cases} f_{1001} = \dfrac{\sum\limits_w J_{w,1}\sqrt{\beta_x^w\beta_y^w}e^{i(\phi_{w,x}-\phi_{w,y})}}{4(1-e^{2\pi i(Q_h-Q_v)})} \\ f_{2002} = \dfrac{\sum\limits_w K_{w,3}\beta_x^w\beta_y^w e^{2i(\phi_{w,x}-\phi_{w,y})}}{64(1-e^{4\pi i(Q_h-Q_v)})} \end{cases}, \tag{9.12}$$

where $Q_{h,v}$ are the eigen-tunes (the depressed tunes in case of space charge), β and ϕ are the Twiss parameters, J_1 [m^{-1}] and K_3 [m^{-3}] are the integrated skew quadrupole and normal octupole strengths respectively. As the space-charge forces are smooth functions along the ring, the above summations can be replaced by integrals:

$$\begin{cases} f_{1001} = \dfrac{1}{4(1-e^{2\pi i(Q_h-Q_v)})}\oint J_1(s)\sqrt{\beta_x(s)\beta_y(s)}e^{i[\phi_x(s)-\phi_y(s)]}\,ds \\ f_{2002} = \dfrac{1}{64(1-e^{4\pi i(Q_h-Q_v)})}\oint K_3(s)\beta_x(s)\beta_y(s)e^{2i[\phi_x(s)-\phi_y(s)]}\,ds \end{cases}. \tag{9.13}$$

To simplify the computation of the above integrals, it can be assumed that both the coupling terms, $J_1(s)$ and $K_3(s)$, depend on fixed beam parameters only (ignoring acceleration) such as current, energy and beam size. In the smooth approximation the beam size can be approximated as constant along the ring, resulting in integrals dependent on the machine parameters only

$$\begin{cases} f_{1001} \simeq \dfrac{< J_1 > R}{4\sqrt{Q_{x0}Q_{y0}}(1-e^{2\pi i(Q_h-Q_v)})}\oint e^{i[\phi_x(s)-\phi_y(s)]}\,ds \\ f_{2002} \simeq \dfrac{< K_3 > R^2}{64 Q_{x0}Q_{y0}(1-e^{4\pi i(Q_h-Q_v)})}\oint e^{2i[\phi_x(s)-\phi_y(s)]}\,ds \end{cases}, \tag{9.14}$$

where $< J_1 >$ and $< K_3 >$ represent the averaged coupling strengths and we replaced $\beta_{x,y}(s) \rightarrow \overline{\beta}_{x,y} \simeq R/Q_{x0,y0}$, with R the machine radius and $Q_{x0,y0}$ the betatron bare tunes. The latter integrals are nonzero only if the tunes are unsplit, since close to the difference resonance $\phi_x(s) - \phi_y(s) \simeq 0$ along the ring and the integrals are equal to $2\pi R$. In case of split tunes the phase difference varies along the ring from 0 to $2\pi M$, M be the integer difference between the tunes (see Sec. 8.1 for $M = 1$). The integrals are hence equal to zero. In machines with split tunes therefore space charge alone cannot drive any emittance transfer, and betatron coupling, defined by the stop band

$$|C^{(b)}| \simeq \left| \frac{1}{2\pi}\sum_w J_{1,w}\sqrt{\beta_x^w\beta_y^w}e^{i(\phi_{w,x}-\phi_{w,y})} \right|, \tag{9.15}$$

is necessary. Note that betatron coupling, and hence $|C^{(b)}|$, are independent on the beam size, and space charge has the only effect (in first approximation) of introducing the tune shift in the envelope equations [53, 54]

$$\begin{cases} \sigma_x'' + \left[k_x(s) - \dfrac{1}{2}\dfrac{K_{sc}}{\sigma_x(\sigma_x+\sigma_y)}\right]\sigma_x - \dfrac{\epsilon_x^2(s)}{\sigma_x^3} = \displaystyle\sum_w J_{1,w}\ \delta(s-s_w)\ \sigma_y \\ \\ \sigma_y'' + \left[k_y(s) - \dfrac{1}{2}\dfrac{K_{sc}}{\sigma_x(\sigma_x+\sigma_y)}\right]\sigma_y - \dfrac{\epsilon_y^2(s)}{\sigma_y^3} = \displaystyle\sum_w J_{1,w}\ \delta(s-s_w)\ \sigma_x \end{cases}, \quad (9.16)$$

where $k_{x,y}$ are the normal quadrupole gradients, $J_{w,1}$ is the integrated strength of the w-th skew quadrupole, $\epsilon_{x,y}(s)$ are the RMS emittances and K_{sc} is the perveance defined in Eq. (9.1). The above equations hold for an up-right beam distribution ($< xy >= 0$) with ellipsoidal symmetry. Betatron coupling however leads to a beam rotation and a more rigorous description would require the generalized envelope equations derived by Chernin [48]. Envelope equations are more suitable to investigate space-charge effects with respect to single-particle equations since their constraints (up-right distribution with ellipsoidal symmetry) are more general, the Hill's equation requiring the knowledge of the single-particle forces.

Eqs. (9.16) are similar to the ones derived in case of pure betatron coupling. The only difference is in the collective nature, and in the presence in the l.h.s of the space-charge tune shift. The distance from the resonance is therefore represented by the difference of the depressed tunes

$$\Delta_d = Q_x - Q_y \quad \text{(fractional part)} \qquad \begin{cases} Q_x = \sqrt{Q_{x0} - \dfrac{1}{2}\dfrac{K_{sc}R^2}{\sigma_x(\sigma_x+\sigma_y)}} \\ \\ Q_y = \sqrt{Q_{y0} - \dfrac{1}{2}\dfrac{K_{sc}R^2}{\sigma_y(\sigma_x+\sigma_y)}} \end{cases}. \quad (9.17)$$

9.3.1 Emittance dependent detuning

Space charge couples tunes and RMS emittances through the perveance K_{sc} and the RMS beam sizes $\sigma_{x,y}$. For a KV distribution the tune does not depend on the particle position, resulting in a pure shift for the entire beam.

For a Gaussian beam a tune spread is also present, due to the dependence of the space-charge force on the particle position within the beam. Dealing with envelope equations, the concept of *RMS-equivalent beam* can be invoked, making possible to describe the evolution of the beam RMS size (and hence of the emittances) as function of the coherent tune shift only, provided to multiply the Laslett tune shift

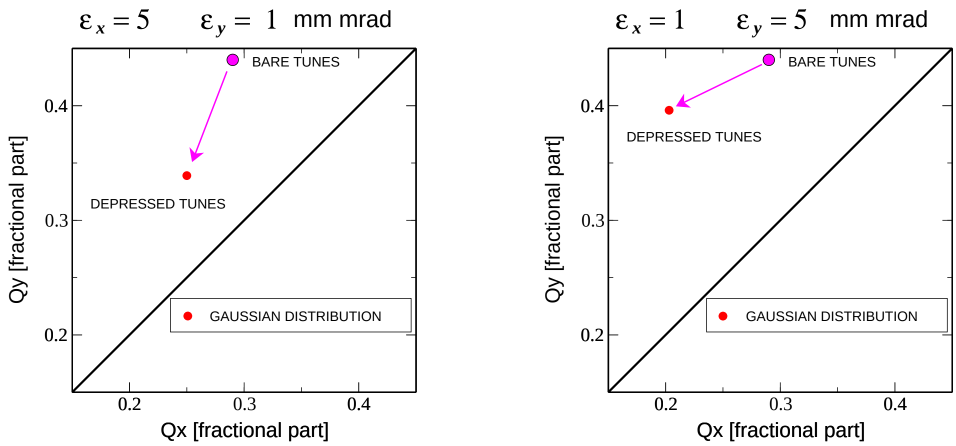

Figure 9.8: Depressed tune (Gaussian beam) computed for working point $Q_{x0} = 4.29$, $Q_{y0} = 3.44$ and beam current $I = 9.2$ mA ($K_{sc} = 1.8 \times 10^{-8}$) and different initial emittances: $\epsilon_{x0} = 1$, $\epsilon_{y0} = 5$ mm mrad (left), $\epsilon_{x0} = 1$, $\epsilon_{y0} = 5$ mm mrad (right).

by a factor two[1].

For given bare tunes $Q_{x0,y0}$ and space-charge perveance K_{sc}, different initial emittances result in different beam sizes and tune shifts according to

$$\sigma_x = \sqrt{\frac{\epsilon_x R}{Q_{x0}}} \,, \qquad \sigma_y = \sqrt{\frac{\epsilon_y R}{Q_{y0}}} \,, \tag{9.18}$$

$$Q_x(N, \epsilon_x, \epsilon_y, K_{sc}) = \sqrt{Q_{x0}^2 - \frac{R^2 K_{sc}}{\sigma_x(\sigma_x + \sigma_y)}} \tag{9.19}$$

$$Q_y(N, \epsilon_x, \epsilon_y, K_{sc}) = \sqrt{Q_{y0}^2 - \frac{R^2 K_{sc}}{\sigma_y(\sigma_x + \sigma_y)}} \quad . \tag{9.20}$$

In Fig 9.8 two examples are shown: the (Gaussian) depressed tunes are computed for $Q_{x0} = 4.29$, $Q_{y0} = 3.44$, $I = 9.2$ mA ($K_{sc} = 1.8 \times 10^{-8}$) and different initial emittances: $\epsilon_{x0} = 5$, $\epsilon_{y0} = 1$ mm mrad (left plot) and $\epsilon_{x0} = 1$, $\epsilon_{y0} = 5$ mm mrad (right plot). Any emittance exchange therefore results in different depressed tunes and, in turn, different distance from the resonance Δ.

9.3.2 Static case

In Chapter 5 it has been shown how for fixed bare tunes $Q_{x0,y0}$, i.e. fixed Δ, betatron coupling drives turn-by-turn RMS emittance oscillations. Emittance dependent

---

[1] The maximum tune shift at the beam center of a Gaussian beam RMS-equivalent to a KV distribution is indeed twice the tune shift defined in Eq. (9.17).

detuning makes Δ_d oscillate with the same frequency. The analysis performed in Chapter 5 is therefore not applicable, as Δ_d is time-dependent.

In Fig. 9.9 the sharing curves as computed by multi-particle simulations with betatron coupling $|C^{(b)}| = 0.01$ are shown for zero current (left) and $I = 7.2$ mA (right). The initial Laslett tunes shifts in the second case are $\Delta Q_x \simeq -0.1$, $\Delta Q_x \simeq -0.3$. The sum of the two emittances is preserved along the scan, although space charge makes the sharing be larger than in the case with betatron coupling only and leads to an asymmetric curve. The value of Δ for which the two averaged emittances are equal is displaced towards left. The displacement is found to be proportional to the Laslett tune shift.

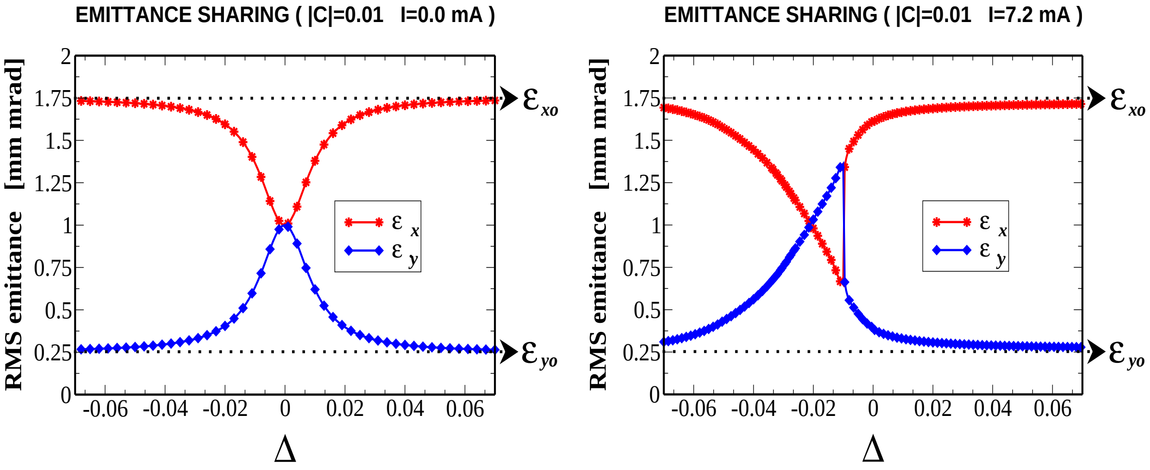

Figure 9.9: RMS emittances averaged over 500 turns for different working points scanning the resonance stop band and betatron linear coupling $|C^{(b)}| = 0.01$ induced by random skew quadrupolar errors in the normal quadrupoles. In case of zero current (left) the curve is rather symmetric and centered in $\Delta = 0$. The same simulation with a beam of $I = 7.2$ mA ($\Delta Q_x \simeq -0.1$, $\Delta Q_x \simeq -0.3$) generates a strongly asymmetric curve, whose *transition point* is displaced by 0.01.

9.3.3 Dynamic case

The same considerations on the asymmetry outlined in Sec. 9.2, namely the different behavior according to the crossing direction, apply also for the case with split tunes. Although the betatron coupling driving term and the resonance stop band, $|C^{(b)}|$, are independent on the beam current, it is observed that the emittance exchange curves strongly depend on the beam current. This is due to the emittance dependent detuning, $\Delta_d = \Delta_d(\epsilon_x, \epsilon_y, K_{sc})$, which makes the crossing speed to change while approaching the resonance. The detuning results in an *observable* stop band $|C^{(o)}|$, equal or larger than $|C^{(b)}|$, dependent on both betatron coupling and the Laslett tune shift.

Assuming initial emittances such that $\epsilon_{x0} > \epsilon_{y0}$, if the crossing starts from *below*, i.e. $Q_{x0} > Q_{y0}$ and $\Delta_0 > 0$, the depressed tunes approach the resonance *after* the bare tunes and the point where the two emittance are equal is displaced towards left

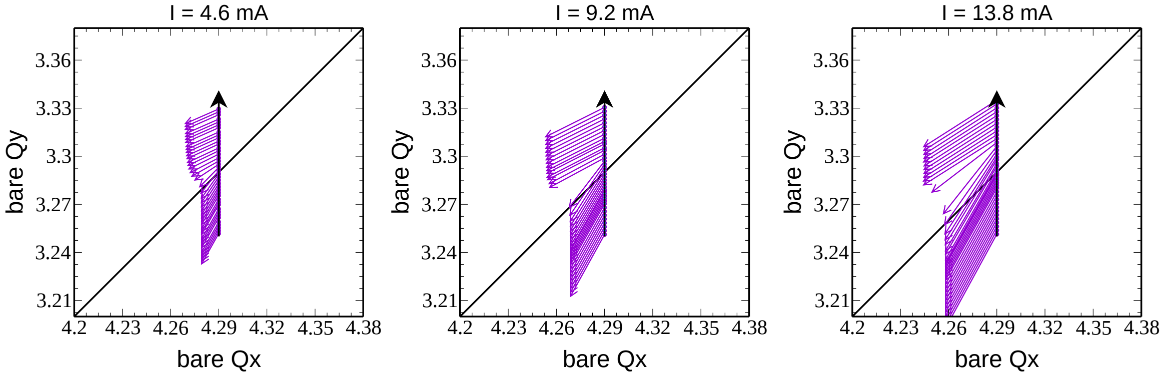

Figure 9.10: Variation of the tune shift while crossing *from below* a stop band of $|C^{(b)}| = 0.01$: the vertical bare tune (upper-right end of the arrow) is varied linearly, whereas the depressed tunes (bottom-left end of the arrow) cross the resonance faster because of the emittance dependent detuning. The tune shift is computed from RMS emittances obtained by multi-particle simulations at 4.6, 9.2 and 13.8 mA.

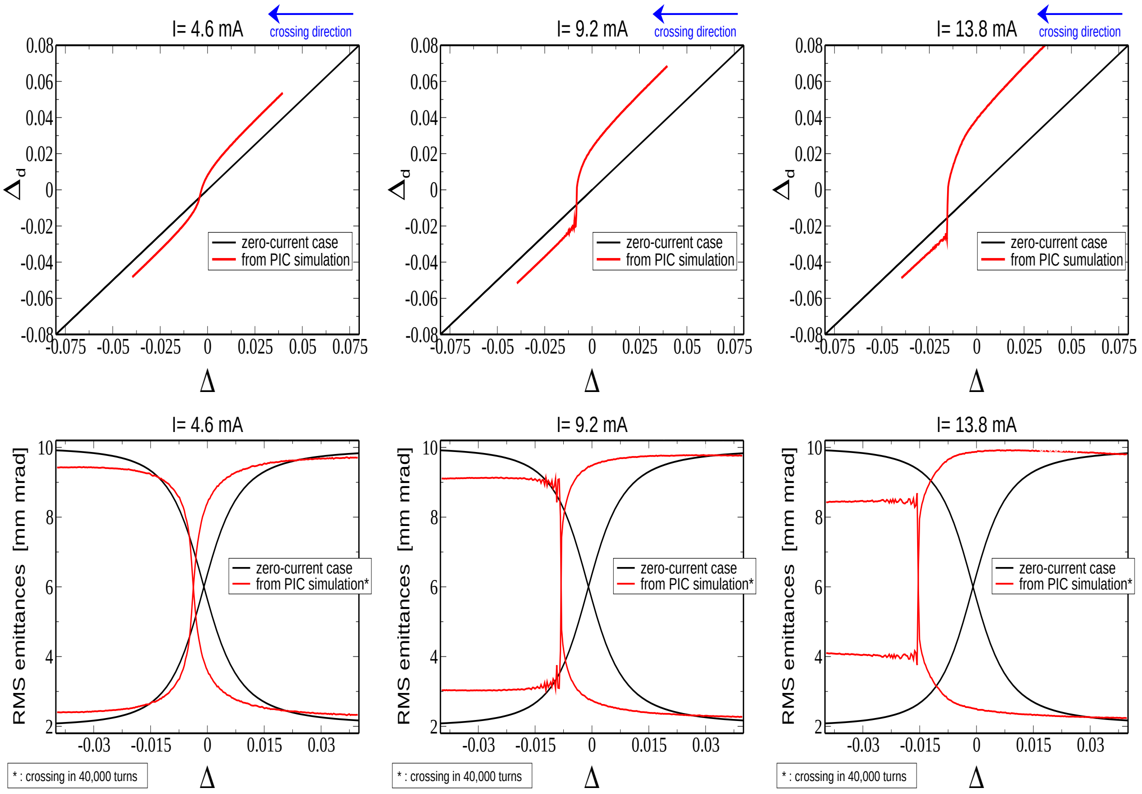

Figure 9.11: Distance from the resonance of the depressed tunes Δ_d versus Δ (upper) and RMS emittance exchange curve (bottom) crossing *from below* the same stop band of Fig. 9.10: multi-particle simulations at 4.6, 9.2 and 13.8 mA. The curves are compared with the case at zero current (black lines).

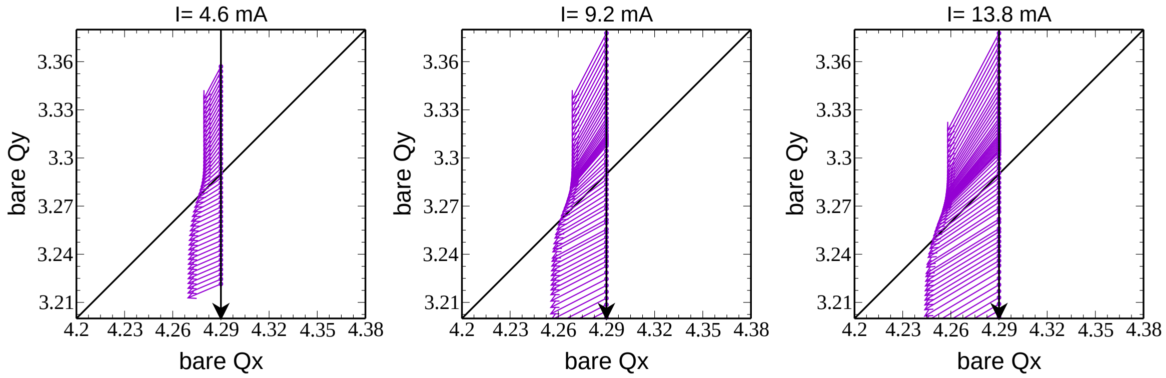

Figure 9.12: Variation of the tune shift while crossing *from above* a stop band of $|C^{(b)}| = 0.01$: the vertical bare tune (upper-right end of the arrow) is varied linearly, whereas the depressed tunes (bottom-left end of the arrow) cross the resonance faster because of the emittance dependent detuning. The tune shift is computed from RMS emittances obtained by multi-particle simulations at 4.6, 9.2 and 13.8 mA.

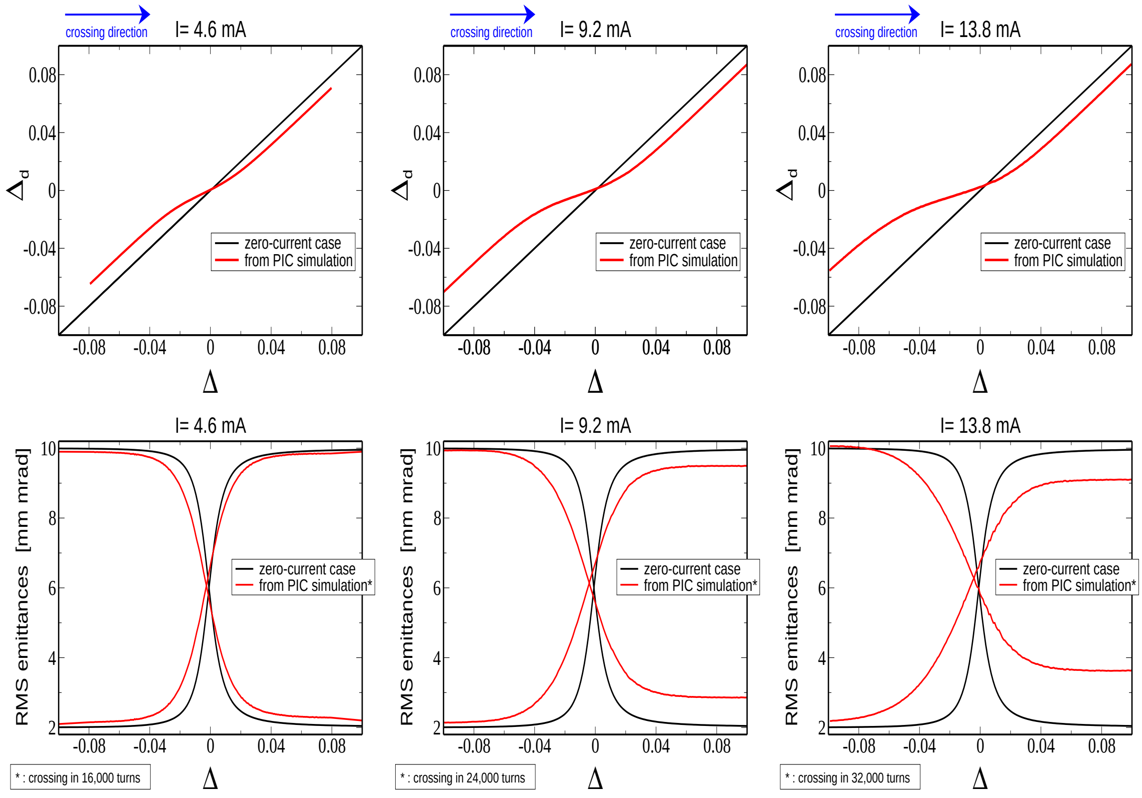

Figure 9.13: Distance from the resonance of the depressed tunes Δ_d versus Δ (upper) and RMS emittance exchange curve (bottom) crossing *from above* the same stop band of Fig. 9.12: multi-particle simulations at 4.6, 9.2 and 13.8 mA. The curves are compared with the case at zero current (black lines).

(see bottom plots of Fig. 9.11). The emittance exchange moves the necktie upwards (see Fig. 9.10). The crossing speed is therefore increased, which is the sum of the bare tune ramp and the emittance dependent detuning, as shown in the upper plots of Fig. 9.11. The larger the tune shift with respect to $|C^{(b)}|$ the faster is the crossing. For severe tune shift and weak betatron coupling, $|\Delta Q| >> |C^{(b)}|$, this might lead to a partial exchange and prevent the equilibration to happen, because the stop band is effectively crossed *too fast*.

If the crossing starts from *above*, i.e. $Q_{x0} < Q_{y0}$ and $\Delta_0 < 0$, the resonance is effectively approached by the depressed tunes *before* the bare tunes. As in the previous case the necktie moves upwards. The crossing speed is therefore reduced, the bare tune ramp and the emittance dependent detuning moving in opposite directions, as shown in Fig. 9.12 and in the upper plots of Fig. 9.13. The point where the two emittance are equal is therefore almost independent on the tune shift (see bottom plots of Fig. 9.13), since the depressed tunes need equal emittances to abandon the stop band . The larger the tune shift with respect to $|C^{(b)}|$ the slower is the effective crossing. This is the equivalent of the "snowplow" effect introduced in [43].

In the first case the adiabatic condition used to derive Eq. (6.1)-(6.2) cannot be invoked because of the large tune shift, although the sum of the two emittance is preserved. In the second case the same equations are still applicable under the condition that the bare tunes are replaced by the depressed ones. As the latter ones are dependent on the emittance themselves, coupled equations need to be solved self-consistently, namely

$$\begin{cases} \epsilon_x = \epsilon_{x0} + \dfrac{|C^{(b)}|^2}{\Delta_d^2 + |C^{(b)}|^2 \pm \Delta_d\sqrt{\Delta_d^2 + |C^{(b)}|^2}} \dfrac{\epsilon_{y0} - \epsilon_{x0}}{2} \\ \\ \epsilon_y = \epsilon_{y0} - \dfrac{|C^{(b)}|^2}{\Delta_d^2 + |C^{(b)}|^2 \pm \Delta_d\sqrt{\Delta_d^2 + |C^{(b)}|^2}} \dfrac{\epsilon_{y0} - \epsilon_{x0}}{2} \\ \\ \Delta_d = Q_x - Q_y \qquad \text{(fractional part)} \end{cases} \tag{9.21}$$

$$\begin{cases} \sigma_x = \sqrt{\dfrac{\epsilon_x R}{Q_{x0}}} \\ \\ \sigma_y = \sqrt{\dfrac{\epsilon_y R}{Q_{y0}}} \end{cases} \qquad \begin{cases} Q_x = \sqrt{Q_{x0}^2 - \dfrac{R^2\xi}{\sigma_x(\sigma_x + \sigma_y)}} \\ \\ Q_y = \sqrt{Q_{y0}^2 - \dfrac{R^2\xi}{\sigma_y(\sigma_x + \sigma_y)}} \end{cases} , \tag{9.22}$$

where the sign in the denominators of Eq. (9.21) is defined according to Eq. (9.8). Initial emittances, current (K_{sc}) and machine parameters (R and $Q_{x0,y0}$) are used to compute the depressed tunes $Q_{x,y}$ via Eq. (9.22). The corresponding Δ_d is then inserted in Eq. (9.21) to compute the new emittances. These are used together with

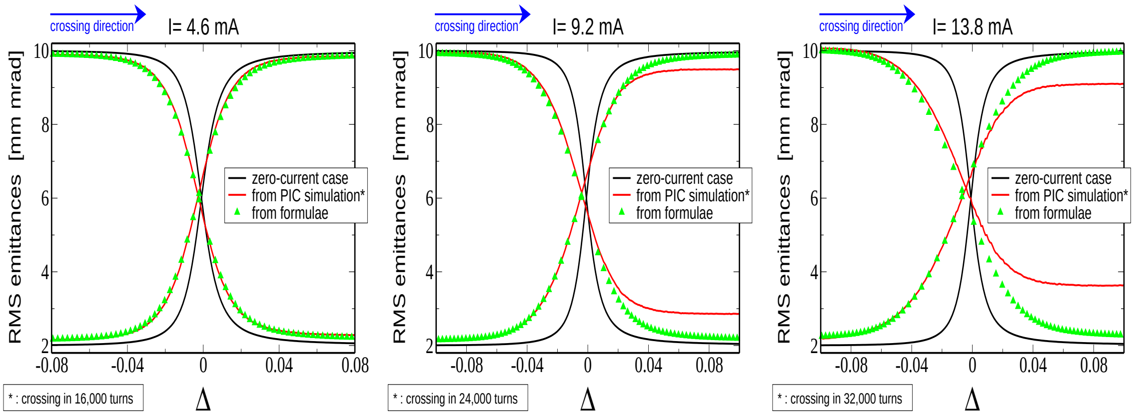

Figure 9.14: RMS emittance exchange curve crossing *from above* the same stop band of Fig. 9.12: the red lines are the results of multi-particle simulations at 4.6, 9.2 and 13.8 mA; the green triangles are the ones obtained solving the system (9.21)-(9.22) with the same initial conditions; both curves are compared with the case at zero current (black lines).

the new bare tunes to compute the updated Δ_d and the procedure repeated until the dynamical crossing (done as function of $Q_{x0,y0}$ or equivalently of Δ) is completed.

In Fig. 9.14 the results of the above system are compared with multi-particle simulations with betatron coupling $|C^{(b)}| = 0.01$, for different values of the current. The agreement is excellent before the equilibration, even for a case with a severe tune shift of $\Delta Q_x = -0.07$, $\Delta Q_y = -0.27$. After the equilibration the emittances appear not to exchange completely. The distance from the initial values is proportional to the beam current. Such limited exchange is not foreseen by Eqs. (9.21)-(9.22) and occurs even for very slow crossing over $\sim 10^5$ turns. It is not clear whether the reason of the partial exchange is physical (space charge self-skewing and mixing while crossing the resonance due to the beam rotation, high order effects) or numerical (discretization errors, loss of memory when using PIC solvers) or a combination of both. A cross-check with other codes implementing different algorithms, such as particle-particle solvers, has been not undertaken. A similar behavior was observed in simulations with initial KV distributions.

From the experimental point of view, system (9.21)-(9.22) is not suitable to infer $|C^{(b)}|$ because of the intrinsic dependence of Δ_d on the RMS emittances. For practical purpose it is more convenient to rewrite Eqs. (9.21)-(9.22) in terms of the distance from the resonance of the bare tunes $\Delta = Q_{x0} - Q_{y0}$ (fractional part), which is an independent quantity defined by the tune ramp only, and an *observable* stop band $|C^{(o)}|$, dependent on both betatron coupling and the space-charge tune shift.

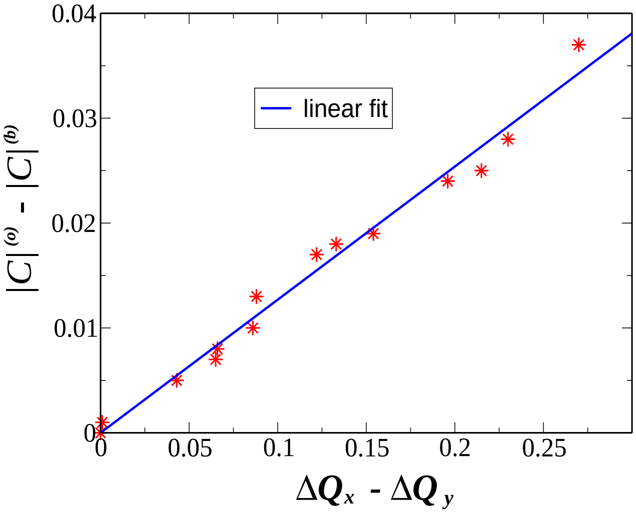

Figure 9.15: Difference between the observable stop band computed numerically by multi-particle tracking $|C^{(o)}|$ and the betatron coupling stop band $|C^{(b)}|$ against the difference between the initial tune Laslett tune shifts $\Delta Q_x - \Delta Q_y$ (See Tab. 9.2). A linear fit is superimposed.

$$\begin{cases} \Delta_d \rightarrow \Delta \ , \qquad |C^{(b)}| \rightarrow |C^{(o)}| \\ \epsilon_x = \epsilon_{x0} + \dfrac{|C^{(o)}|^2}{\Delta^2 + |C^{(o)}|^2 \pm \Delta\sqrt{\Delta^2 + |C^{(o)}|^2}} \dfrac{\epsilon_{y0} - \epsilon_{x0}}{2} \\ \epsilon_y = \epsilon_{y0} - \dfrac{|C^{(o)}|^2}{\Delta^2 + |C^{(o)}|^2 \pm \Delta\sqrt{\Delta^2 + |C^{(o)}|^2}} \dfrac{\epsilon_{y0} - \epsilon_{x0}}{2} \end{cases} . \tag{9.23}$$

Due to the intrinsic coupling, the analytical derivation of the relation between $|C^{(b)}|$ and $|C^{(o)}|$ might be a difficult task. Multi-particle simulations have been run with several initial beam parameters and various coupling strengths in order to infer a heuristic scaling law. For each simulation, the RMS emittances are plotted against Δ and Eqs. (9.23) are then superimposed to infer $|C^{(o)}|$. From the results listed in Tab. 9.2 and plotted in Fig. 9.15 it is found that $|C^{(o)}|$ increases linearly with the difference between the initial Laslett tune shifts $\Delta Q_x - \Delta Q_y$.[2] $|C^{(b)}|$ is represented by the offset, whereas the slope is inferred from the fit and does not appear to be dependent on neither $|C^{(b)}|$ nor the initial emittances

$$|C^{(o)}| \quad \simeq \quad |C^{(b)}| \mp \mathcal{A}(\Delta Q_x - \Delta Q_y) \qquad \text{with } |C^{(b)}| \neq 0 \ , \tag{9.24}$$

The sign must be consistent with the choice made in Eq. (9.23). From multi-particle

---

[2] The tune shifts are not constant while crossing the resonance because of the emittance dependent detuning. In order to derive a scaling law involving initial beam parameters only, this additional time dependence is ignored.

sim.	current [mA]	$(\epsilon_{x0},\ \epsilon_{y0})$ [mm mrad]	$\lvert C^{(b)}\rvert$	initial tune shift $\lvert\Delta Q_x\rvert, \lvert\Delta Q_y\rvert$	$\lvert C^{(o)}\rvert$ from tracking
1	0	$(2.5, 0.52)$	0.010	$0.0, 0.0$	0.010
2	4.8	$(2.5, 0.52)$	0.010	$0.043, 0.108$	0.017
3	9.6	$(2.5, 0.52)$	0.010	$0.087, 0.220$	0.028
4	13.8	$(2.5, 0.52)$	0.010	$0.125, 0.321$	0.034
5	5.0	$(2, 0.75)$	0.015	$0.051, 0.094$	0.020
6	30.0	$(2, 0.8)$	0.03	$0.309, 0.579$	0.067
7	14.0	$(2.75, 1.05)$	0.015	$0.103, 0.191$	0.028
8	6.5	$(1.3, 0.5)$	0.02	$0.101, 0.187$	0.030
9	4.8	$(2.5, 0.51)$	0.04	$0.043, 0.109$	0.048
10	20.0	$(5.0, 1.2)$	0.01	$0.088, 0.210$	0.027
11	25.0	$(4.5, 0.8)$	0.03	$0.130, 0.360$	0.058
12	10.0	$(1.4, 1.8)$	0.01	$0.107, 0.108$	0.011
13	15.0	$(0.5, 5.0)$	0.005	$0.235, 0.081$	0.024

Table 9.2: Comparison between the observable stop band $|C^{(o)}|$ predicted by Eq. (9.24) and the one inferred from multi-particle simulations plotting the emittance curves against Δ.

simulations crossing the resonance at $Q_{x0} = 1 + Q_{y0} = 4.29$, the slope is found to be $\mathcal{A} \simeq 0.13$.

Note that $|C^{(b)}|$ is automatically inferred from the emittance exchange curve in two cases only, namely the case with zero current and the case with equal initial horizontal and vertical tune shifts, regardless of the beam current. This is confirmed by simulations 1 and 12 of Tab. 9.2: the first one corresponding to the zero current case, the second to $I = 10$ mA, $\epsilon_{x0} = 1.4$ mm mrad and $\epsilon_{x0} = 1.8$ mmrad, generating almost the same tune shifts $\Delta Q_x = -0.107$, $\Delta Q_x = -0.108$. In the same table, simulations 1-11 were run crossing the resonance from $\Delta < 0$, with $\epsilon_{x0} > \epsilon_{y0}$; in simulations 12 and 13 the crossing is performed from $\Delta > 0$.

9.3.4 How to avoid overcompensation of betatron coupling

In Sec. 7.6 it has been reported how $|C^{(b)}|$ was measured in the SIS-18 by crossing dynamically the difference resonance and by measuring the emittance exchange curve. Fitting the latter one with Eq. (9.23) provides a direct measurement of $|C^{(b)}|$.

Nevertheless, the above discussion shows that this measurement is affected by space charge if the difference between the two initial Laslett tune shifts is comparable with the resonance stop band, $|\Delta Q_x - \Delta Q_y| \simeq |C^{(b)}|$. Repeated measurements of the *observable* stop band $|C^{(o)}|$ for at least two different beam intensities can be used to disentangle the two contributes, via Eq. (9.24). The tune shifts are computed from the measured beam size via Eqs. (9.17), knowing the beam parameters, i.e. K_{sc}. $|C^{(b)}|$ is inferred by plotting the observable stop band against $\Delta Q_x - \Delta Q_y$ and performing a linear fit.

This procedure is necessary in order not to overestimate (and hence overcompensate) of of betatron coupling, since external skew quadrupoles compensating $|C^{(o)}|$ instead of $|C^{(b)}|$ would leave a residual coupling $\propto |\Delta Q_x - \Delta Q_y|$.

Chapter 10

Conclusions

In this thesis a beam-based method has been developed to measure the strength and the polarity of corrector magnets (skew quadrupoles and sextupoles) in circular accelerators. The algorithm is based on the harmonic analysis (via FFT) of beam position monitor (BPM) data taken turn by turn from an accelerator in operation. It has been shown that, from the differences of the spectral line amplitudes between two consecutive BPMs, both the strength and the polarity of non-linear elements placed in between can be measured. The method has been successfully tested using existing BPM data from the SPS of CERN, since presently the SIS-18 is not equipped with the necessary hardware. The magnet strength of seven SPS extraction sextupoles was measured with a precision of about 10%. The polarities have been unambiguously measured. This method can be used to detect polarity errors and wrong power supply connections during machine commissioning, as well as for a continuous monitoring of the "nonlinearity budget" in superconducting machines.

A second beam-based method has been studied for a fast measurement and correction of betatron coupling driven by skew quadrupole field errors and tilted focusing quadrupoles. Traditional methods usually require a time-consuming scan of the corrector magnets in order to minimize the coupling stop band $|C|$. In this thesis it has been shown how the same correction can be performed in a single machine cycle from the harmonic analysis of multi-BPM data. The method has been successfully applied to RHIC. It has been shown that the stop band $|C|$ (also known in the American literature as ΔQ_{min}) measured in a single machine cycle with the new algorithm is compatible with the value obtained by traditional methods. The measurement of the resonance phase Θ defines automatically the best corrector setting, which was found in agreement with the one obtained with a traditional scan.

A third theoretical achievement is a new description of the betatron motion close to the difference resonance in presence of linear coupling. Compared to the matrix formalism the motion is parametrized as a function of the resonance driving term f_{1001} only (which is proven to be an observable), whereas making use of the matrix approach four parameters need to be measured. Formulae describing the exchange of RMS emittances when approaching the resonances have been already derived in the 70s in the smooth approximation. New formulae have been derived here making use of Lie algebra providing a better description of the emittance behavior. The emittance exchange curves are predicted by new formulae with excellent agreement with multi-particle simulations and the counter-intuitive emittance variation along the ring of the emittance is proven to be related to the variation of f_{1001}. A new way to decouple the equations of motion and explicit expressions for the individual single particle invariants have been found.

For the first time emittance exchange studies have been carried out in the SIS-18 of GSI. Transverse RMS emittances have been measured during 2005 from rest gas monitor (RGM) data. Crossing the linear coupling resonance, the transverse emittances exchange completely. It has been observed that this effect is reversible. Applications of this manipulation are: emittance equilibration under consideration for future operations of the SIS-18 as booster for the SIS-100; emittance transfer during multi-turn injection to improve the efficiency and to protect the injection septum in high intensity operations, by ***shifting*** part of the horizontal emittance into the vertical plane. The emittance exchange curves obtained experimentally have been compared with analytic formulae providing a fast measurement (in few machine cycles only) of the linear coupling stop band $|C|$. Technical problems prevented the use of the eight skew quadrupoles installed in the SIS-18 to compensate the linear coupling resonance. It has been observed that the emittance exchange curve is highly sensitive to the beam intensity. Multi-particle simulations with 2D PIC space-charge solver have been run to infer heuristic scaling laws able to quantify the observable stop band, to be used for the resonance compensation.

The analysis of BPM and RGM data has been performed making use of new software applications developed for this purpose. The ***bpm2rdt*** code for the harmonic analysis of BPM data has been written and tested with real data. The software reads the BPM turn-by-turn data and the Twiss parameters. Then it performs the FFT of these data, finds the peaks of the Fourier spectra and infers the RDT f_{jklm}, the strengths $\hat{h}_{jklm}$ and the local terms χ_{jklm}. All these observables are printed out together with the corresponding values of the model, computed from the nominal values of strengths and the Twiss parameters. From the FFT of dual-plane BPM data the linear optics (β functions and phase advances $\Delta\phi$) at the corresponding location is also inferred. From the measurement of f_{1000}, the linear coupling coefficient C (amplitude and phase) is also computed. The code has been tested by using existing SPS data and new RHIC data. For the on-line analysis of RGM data the ***rgm2emitt*** code has been written. The application reads in input the raw data files from the RGM and the beam loss monitor (BLM) respectively, the latter created by the RGM on-line software itself. From the RGM data the transverse beam sizes and emittances are inferred and used together with the BLM data to compute the tune shift during the machine cycle.

Acknowledgments

I would like to express my gratitude to the Accelerator Division of GSI and to the Institute of Applied Physics of the *J. W. Goethe* University of Frankfurt am Main for the financial support, and for giving me the opportunity to carry out this work.

I would like to thank Prof. Dr. Ingo Hofmann and Prof. Dr. Ulrich Ratzinger for their support, for making this work possible, and for the wide freedom that they conceded to me in the research activity.

Thanks to all the members of the HSSP group of GSI: our group meetings were highly educative and the discussions always useful.

Special thanks go to five people, five colleagues, five friends, to whom this thesis owes a lot.

Dr. Rogelio Tomás introduced me to the fascinating world of the resonance driving terms; he had the patience to reply to my daily emails. Despite the distance and the lack of opportunities to work closely together, he managed to collaborate and interact with me in the development of the main part of this work.

Dr. Rama Calaga shared with me and Rogelio the work on betatron coupling and mastered the acquisition of brand new BPM data from RHIC as soon as a new kind of possible measurement came out of our minds.

Dr. Giuliano Franchetti was a master of beam physics. He always found the time for answering an infinite number of questions of any kind. With him I had the longest and most useful discussions at the beginning of my studies. His numerical libraries MICROMAP have been a formidable tool for speeding up all the numerical studies. Without him, three years would have not been enough to carry out all the theoretical studies of this work.

Dr. Giovanni Rumolo followed from the beginning with interest and passion my work. His presence and experience in the GSI control room during the first measurements were of great help in suppressing the initial frustrations; furthermore, he had the patience to read every note, manuscript and paper that I wrote.

My gratitude to Peter Moritz will be eternal. Despite his important duties in the RF group of GSI, he found the time to setup and turn-by-turn BPM acquisition system by using a PC and a *toy* PCI card. He mastered all the electronics in the control room with an astonishing competence. I will never forget the day, in which he triggered a Q-kicker that was not responding to the timing generator, by plugging few meters of cables on a scope: this and other *miracles* were highly educative.

Special thanks go to other three young physicists of GSI, whose role was fundamental in the emittance exchange measurements. Tino Giacomini designed, installed and ran the residual gas monitor; he also updated the on-line software in order to provide me the largest amount of information in the easiest way. Dr. Andreas Redelbach was a key man for our experiment, operating the SIS-18 with competence and carrying to an extreme the possibilities of the control-room software SISMODI. Dr. Markus Kirk shared with me his office and his competence in the Schottky analysis. Tino, Andreas, Markus and Giuliano kindly participated to all the emittance exchange measurements.

My gratitude goes also to Dr. Wolfram Fischer and Dr. Thomas Roser for their support and interest in our betatron coupling studies in RHIC. They gave me the opportunity of visiting BNL and allowed me to use RHIC BPM data for this work.

Thanks to Dr. Frank Schmidt and Dr. Rogelio Tomás for giving me the possibility of using their BPM data of SPS.

Thanks to the group of Bologna, Prof. Giorgio Turchetti, Prof. Armando Bazzani and Dr. Carlo Benedetti for their interest in this work, their tutorials on the normal forms, and the useful discussions.

Special thanks to Prof. SY Lee, for his enthusiastic interest in this work and other manuscripts. I had the honor to discuss with him and to be introduced by him in several beam dynamics topics during his long stay at GSI.

Thanks to the SIS-18 machine coordinators and experts, Dr. Klaus Blasche, Dr. Peter Spiller, Bernhard Franczak, Dr. Petra Schütt and Dr. Udo Blell for giving me the opportunity of performing machine studies in the SIS-18 and for their technical support.

I am thankful to the friends of GSI who created a nice and cheerful atmosphere during the working time. In alphabetic order and without academic degree: Frederic Ameil, Ralph Bär, Maria Cristina Bellachioma, Magdalena Górska, Lars Groening, and Giovanni Rumolo.

A special mention deserve all the friends spread around Europe, for their friendship and their words of support in the most critical moments of the last years, and for helping me taking almost always the wisest decisions. The city of Frankfurt rendered Margherita, the personnel of the grocer's shops in Münchenerstraße and Santa Crispella the closest friends who had to deal with me and my moodiness.

Finally, I would like to spend a sentence for my parents who have been paying the highest price for the accomplishment of this work.

Zusammenfassung

Im Rahmen dieser Arbeit wurden drei Hauptaspekte untersucht, die die Strahlphysik von hadronischen Kreisbeschleunigern betreffen:

- Entwicklung einer neuen strahlbezogenen Methode für die Messung der Nichtlinearitäten und der Kopplung zwischen den Betatron-Schwingungen;
- Untersuchung des von der Betatron-Kopplung und Raumladung getriebenen Austauschs der transversalen Emittanzen
- Entwicklung einer schellen Technik für die Korrektur der Betatron-Kopplung und für die Kontrolle des transversalen Emittanz-Austauschs.

Messung der Nichtlinearitäten durch Strahllagemonitor vom SPS

Die hadronischen Kreisbeschleuniger SIS-100/SIS-300 des zukünftigen FAIR Projekts der GSI sind supraleitende Maschinen und werden Hochintensitätsstrahlen beschleunigen. Supraleitende Magneten sind dadurch bekannt, dass sie nichtlineare Felder bis zu einer höheren Größenordnung als normalleitende Magneten führen. Diese Tatsache liegt an der beschränkten Genauigkeit während der Verkabelung der Windungen und an dem nach jeder Energierampe verbleibenden Strom. Teilchen mit großen Schwingungsamplituden werden durch unkontrollierte nichtlineare Kräfte so beinflußt, dass keine stabilen Bahnen über beiliebig viele Umläufe mehr möglich sind (chaotische Dynamik). Solche Teilchen werden daher verloren. Die nichtlineare Teilchendynamik begrenzt den effektiven für die Teilchenbewegung nutzbaren Phasenraum, den man als *dynamische Apertur* bezeichnet. In Proton-hochenergiebeschleunigern sind sowhol das Strahlrohr als auch die dynamische Apertur größerer als die Strahlgröße. Das ist nicht der Fall deim SIS-100, wo Strahlgröße und Strahlrohr vergleichbar sind. Eine regelmäßige Kontrolle des “nonlinearity budget” ist daher notig, nicht nur um die erwartete Strahlqualität zu beschaffen, sondern auch um Strahlungsschäden und Quenchen der von dem Strahlverlust getriebene supraleitenden Magneten zu vermeiden.

Die Inbetriebnahme eines großen Beschleunigers kann im Falle von falschen magnetischen Polaritäten oder Netzgeräteanschlüssen eine langwierige Aufgabe werden. Seit Jahrzehnten wurden strahlbezogene Methoden für die Entdeckung von falschen Dipol- un Quadrupolstärken (Korrektur der Gleichgewichtsbahn und Messung der linearen Optik) entwickelt. Die modernste Messmethoden für Skew-Quadrupol- und Sextupolmagnete sind entweder zeitaufwendig oder beschränkt auf die Messung von allgemeinen Maschinenparametern (Amplitude abhängig Verstimmung, nichtlineare Chromatizität, Messung und Reduzierung des Kopplungskoeffizienten).

Thema des ersten Teils dieser Arbeit ist die Entwicklung einer schnellen strahlbezogenen Methode für die Kontrolle der Nichtlinearitäten des Kreisbeschleunigers entlang und für die Messung der Korrekturmagnetestärken.

Sobald der umlaufende Strahl mittels eines schnellen Dipolmagnetes schräg verschoben wird, regt er eine kohärente Betatron-Oszillation an, die nach jeder Umdrehung ("turn-by-turn") von einem Strahllagemonitor (BPM) gespeichert werden kann. Das Spektrum dieser Oszillation kann durch eine schnelle Fourier-Transformation (FFT) abgeleitet werden.

Im Falle einer ideal linearen Maschine mit nur Dipol- und Quadrupolfeldern besteht das Frequenzspecktrum nur aus der Spektrallinie entsprechend der Betatronfrequenz. In Anwesenheit von Nichtlinearfeldern enthält das Spektrum andere Sekundärlinien.

In den neunzigern Jahren wurde bewiesen, dass die Amplitude dieser Sekundärlinien direkt proportional zu der Summe von all den entlang dem Kreisbeschleuniger verteilten Nichtlinearkräften ist [15]. Vor kurzem wurde bewiesen, dass sich die Amplitude entlang des Kreisbeschleunigers ändert, und dass diese Änderung für die Lokalisierung der Nichtlinearitäten benutzt werden kann [1].

Im Rahmen dieser Arbeit wurde diese Methode aufgebessert, um die Stärken und die Polaritäten von nichtlinearen Korrekturmagneten durch die Benutzung von mehreren BPMs zu messen. Die Kräfte der Magnete zwischen zwei BPMs werden durch die Messung der Sekundärlinien und durch ihre Differenz abgeleitet.

Ein neues Computerprogramm für die Auswertung von BPM Daten durch diesen neuen Algorithmus wurde entwickelt und Daten des SPS des CERN angewendet. Stärken und Polaritäten von sieben Extraktionssextupolen wurden mit einer Auflösung von circa 10% gemessen. Das SIS-18 ist zur Zeit noch nicht mit der erforderlichen Hardware ausgerüstet.

Dieses Thema wurde in Zusammenarbeit mit Dr. Rogelio Tomás (CERN) hergestellt.

Beschreibung der linearen Kopplung durch die Resonanz-treibenden Terme

Supraleitende Quadrupolmagneten mit höhen Feldstärken leiten eine lineare Kopplung zwischen den beiden transversalen Ebenen ein, wegen Ungenauigkeiten in der Justierung der Magneten (Drehung) und wegen zusätzlicher Skew-Quadrupolfelder.

Die Kopplung wird gewöhnlich durch die Kopplungsmatrix [31] oder die Hamiltonsche Störungstheorie beschrieben. Letztere ist oft als weniger genau betrachtet, obwohl sie einen klareren physicalischen Einblick ermöglicht.

In dem zweiten Teil dieser Arbeit wurde die lineare Kopplung durch die Resonanztreibenden Terme (RDT) f_{1001} und f_{1010} beschrieben. Diese sind komplexe Zahlen, die mit den von Skew-Quadrupolfeld erregten Sekundärlinien verwandt (und daher messbar) sind. f_{1010} treibt die Summeresonanz $Q_x + Q_y = N$, wobei f_{1001} die Differenzresonanz $Q_x - Q_y = N$ verursacht. Da der Arbeitspunkt eines Kreisbeschleunigers oft in der Nähe der Differenzresonanz liegt, wurde hier f_{1001} besser erforscht.

Messung und Korrektur der Kopplung sowie der transversale Emittanz-austausch wurden vermittels der f_{1001} beschrieben. Dieses Thema wurde in Zusammenarbeit mit Dr. Rogelio Tomás (CERN), Dr. Rama Calaga (BNL) und Dr. Giuliano Franchetti (GSI) hergestellt.

Betatron-Kopplung getriebene Übertragung der transversalen Emittanzen

Die lineare Kopplung verändert die Emittanzverteilung zwischen beiden transversalen Ebenen und verursacht eine Drehung des Strahlprofils. In Hochstrom Schwerionen-Synchrotronen belegt der Strahl horizontal fast das ganze elliptische Strahlrohr bei niedrige oder mittlere Energie. Jede Drehung des Strahlprofils würde daher zu Strahlverlust führen. Andererseits steht es zur Debatte, das SIS-18 während des Boosterbetriebs für das SIS-100 mit gleichen transversalen Emittanzen zum flat top zu betreiben. Bei der Multi-turn-injektion während Hochstrombetrieb des SIS-18 ist auch eine teilweise Emittanzverteilung von der horizontalen Ebene zur der vertikalen vorgesehen, um das Injektionsseptum vor Strahlverlust zu schützen. Beide Bedienungen sind erhältlich durch eine kontrollierte Kopplung, die mit zusätzlichen Skew-Quadrupolen künstlich angetrieben werden kann.

Emittanzaustausch zwischen den transversalen Ebenen in Rahmen der Betatron-Kopplung wurde schon in den Siebzigern und Ende Neunziger Jahren im CERN untersucht [8, 28, 29, 30], und erfolgreich angewandt: Im PS booster wurde der Strahlverlust während der Multi-turn-injektion durch die Emittanzverteilung reduziert, wobei im SPS ein kompletter Emittanzaustausch ausgeführt wurde, um die Horizontale Emittanz in der vertikalen Ebene, die nicht von der Dispersion betroffen ist, mit höherer Auflösung zu messen. Gleichungen beschreibend die Verteilung und den Austausch der Emittanzen wurden von gekoppelten Einteilchenbewegungsgleichungen abgeleitet, dessen Lösung nur in der Glatt-Näherung, im Englischen “smooth approximation” genannt, mit gleichförmigen Skew-Quadrupolfeld gefunden werden kann. Die Emittanzübertragung wurde hauptsächlich in zwei verschiedenen Verfahren untersucht, nämlich die *statische Ann¨aherung an die Resonanz* [8, 28], die die Emittanzverteilung einführt, und die neu entwickelte *dynamische Kreuzung der Resonanz* [29, 30], die einen kompletten Emittanzaustausch einführt.

Die statische Annäherung an die Resonanz bezieht sich auf die Erforschung der Resonanz-Bandbreite in mehreren Maschinenzyklen. Nach jedem Maschinenzyklus wird der Arbeitspunkt verändert, und die Bandbreite in mehreren Zyklen gekreuzt.

Der Verteilungsbetrag hängt von der Resonanzstärke, mit $|C|$ bezeichnet, und der Distanz von der Resonanz, $\Delta = Q_x - Q_y - N$ ab, wobei N eine ganze Zahl und $Q_{x,y}$ die transversale Q-Werte, im Englischen "Tunes" genannt, sind. Auf der Resonanz ($\Delta = 0$) sind die zwei Emittanzen gleich. Die dynamische Kreuzung der Resonanz bezieht sich auf die Erkundung der Resonanz-Bandbreite in einem einzigen Maschinenzyklus, die Tunes langsam aufsteigend. Am Ende der Kreuzung werden die Emittanzen ausgetauscht.

In dieser Arbeit wurde der Formalismus der Resonanz-treibenden Terme (RDT) zusammen mit der Lie Algebra benutzt, um die die Emittanzübertragung beschreibenden Gleichungen aus den RDT f_{1001} zu folgern. Neue Formeln wurden abgeleitet, die die Verteilung und den Austausch, nach jeder Umdrehung ("turn-by-turn") sowie zeit-durchschnittlich, besser als die vorhandene Formeln beschreiben. Der Vorteil des neuen Formalismus liegt daran, dass keine Differentialgleichungen gelöst werden müssen, und keine Näherung über die Glättung des Magnetfeldes erforderlich ist. Die Benutzung des RDT Formalismus ermöglicht, nicht eingängige Phänomene zu erklären, die die vorhandene Formeln nicht vorehersagen: Wenn der Arbeitspunkt so ist, dass $\Delta << 1$, können sich die Emittanzen des Kreisbeschleunigers entlang ändern, und die Verteilungskurve nicht immer symmetrich bezüglich des Resonanz-Mittelpunktes $\Delta = 0$ ist.

Messung von Emittanzübertragung im SIS-18

Im Rahmen dieser Arbeit wurden zum ersten Mal experimentelle Untersuchungen von Emittanzübertragung im Schwerionen-Synchrotron SIS-18 durchgeführt. Transversale Emittanzen wurden 2005 durch Restgasmonitor Daten gemessen. Ein kompletter Emittanzaustausch wurde nach eiener dynamischen Kreuzung der Resonanz eingeführt. Es wurde auch geprüft, dass der Austausch umkehrbar ist. Nach einer unvollständigen Kreuzung wurden gleiche Emittanzen erhalten. Von der Verteilgungskurve, die nach einer statischen Annäherung an die Resonanz erzielt wurde, wurden die Amplitude der RDT f_{1001} gegen Δ und die Resonanz-stärke $|C|$ gemessen. Zum ersten Mal $|C|$ wurde auch durch die Austauschkurve gefolgert, die eine höhere Auflösung und eine schnellere Messung ermöglicht. Es wurde auch beobachtet, dass die Austauschkurve abhängig von der Strahlintensität ist.

Messung der Tunes und Chromatizität im SIS-18

Angaben über die allgemeine Nichtlinearität eines Kreisbeschleunigers können von Messungen der Tunes und Nichtlinear-Chromatizität abgeleitet werden. Teilchen mit Impulsabweichungen $\delta = (p - p_s)/(p_s)$, wobei p_s der Sollimpuls bezeichnet, erleben veränderte Quadrupolestärken und daher verschobene Betatron-Frequenzen (Tunes). In einer ideal linearen Struktur ist die Tune-Verschiebung eine Linearfunktion der δ, $Q = Q_o + Q'\delta$, wobei Q' die "natürliche" oder "lineare" Chromatizität ist. Jede Abhängigkeit von höheren Potenzen der δ ist auf die allgemeine Nichtlinearität zu beziehen. Sextupol- und Dekapolfelder innerhalb der Dipolmagnete und Oktupolfeldern innerhalb der Quadrupolmagnete treiben entsprechend eine lineare, kubische und quadratische Abhängigkeit an. Die Messung der Chromatizität außerhalb des Linearbereichs ermöglicht, nach der Anpassung eines kubischpolynomes ein allgemeines nichtlineares Modell der Struktur abzuleiten.

Die transversale Tunes wurden mit einer Auflösung von 10^{-4} gemessen, wobei der longitudinale Tune nur mit einer niedrigeren Auflösung von circa 30% gemessen wurde. Beide Messungen erfolgten mittels eines bei GSI von Peter Moritz aufgebauten experimentellen Erfassungssystem.

Das Abtasten der Impulsabweichung durch die Änderung des Sollbahnradius oder des Elektronenkühlerstroms ermöglicht die Messung der Chromatizität außerhalb des Linearbereichs. Im SIS-18 wurde die erste Methode benutzt. Der beschränkte verstellbare Bereich des Sollbahnradius verhinderte, ein zuverlässiges nichtlineares Modell des SIS-18 zu definieren.

Schnelle Messung und Korrektur der Kopplung im RHIC

Messungen der Amplitude des Kopplungskoeffizienten $|C|$ sind für seine Korrektur durch Skew-Quadrupolmagneten routinemäßig ausgeführt. Bei Kreisbeschleunigern mit transversalen Tunes, die von einer ganzen Zahl getrennt sind, wie z.B. beim PS und SPS am CERN, genügt es , nur die Amplitude $|C|$ zu messen, um die beste Einstellung der einzigen Familie von Skew-Quadrupolen zu bestimmen. Bei Kreisbeschleunigern mit Tunes, die von einer ganzen Zahl nicht getrennt sind, wie z.B. deim SIS-18 und RHIC, genügt die Amplitude $|C|$ nicht mehr und es sind mindestens zwei Familien von Skew-Quadrupolen nötig. Ohne die Kenntnis der Kopplungsphase ist eine zeitraubende Abtastung der zwei Skew-Quadrupolfelder für die Korrektur erforderlich.

In dieser Arbeit wurde eine neue Methode für die Messung sowohl der Amplitude $|C|$ als auch der Phase Θ des Kopplungskoeffizienten entwickelt, die nur einen einzigen Maschinenzyklus und keine Abtastung benötigt. Sowohl $|C|$ als auch Θ sind mit dem RDT f_{1001} verwandt, der in einem einzigen Maschinenzyklus durch Strahllagemonitoren-Daten messbar ist.

Die neue Techink wurde auf Strahllagemonitoren-Daten von RHIC von 2005 angewandt. Die durch die neuen Formeln abgeleiteten $|C|$ wurden mit denjenigen, die durch anderen Methoden [41] gemessen wurden, verglichen. Die Übereinstimmung zwischen den zwei Ergebnissen ist befriedigend. Am 30. Mai wurde eine übliche Abtastung mittels zwei unhabhängigen Skew-Quadrupolen für die Korrektur der Kopplung ausgeführt. Die beste Einstellung ist vergleichbar mit derjenigen, die durch die neuen Formeln nach einem einzigen Maschinenzyklus vorausgesehen wurde.

Raumladung getriebene Emittanzübertragung

In dem ersten Teil dieser Arbeit wurde die Emittanzübertragung in Rahmen der von Skew-Quadrupolfeldern getriebenen linearen Kopplung untersucht. Diese Art von Kopplung, die auch Betatron-Kopplung gennant ist, beeinflusst die Einteilchen-Dynamik. Die kollektiven Eigenschaften (Emittanzen) wurden von den Integralen über die Teilchen-Verteilung bestimmt. Die Einteilchennatur dieser Kopplung führt zu gekoppelten Hill'schen Differentialgleichungen und zu einer Drehung der Teilchen-Verteilung sowohl in den Phasenräumen als auch in der $x-y$ Ebene.

Wenn Raumladungskräfte berücksichtigt werden, genügt die Einteilchenbeschreibung nicht mehr, weil die Kräfte von den Strahlbreiten abhängig sind.

Sowohl in numerischen Berechnungen [42, 43] als auch in den beim PS am CERN ausgefürten Experimenten [44, 45] wurde beobachtet, dass Raumladung in einigen Fällen nahe an der Differenzen-Resonanz $\Delta = Q_x - Q_y - N << 1$ eine ähnliche Emittanzübertragung treibt. Das gilt für die statische Annäherung sowie für die dynamische Kreuzung, obwohl die Struktur exakt linear ist und keine Kopplung treibt.

Eine theoretische Anstrengung wurde bei der GSI von G. Franchetti und I. Hofmann durchgeführt, um die Emittanzübertragung von der Raumladung-Oktupol-Resonanz, die als Montague-Resonanz bekannt ist [42, 47], und die von Raumladung getriebenen "self-skew" [43, 46, 48] zu beschreiben.

Eine Unerwünschte Emittanzübertragung, die durch Betatron-Kopplung verursacht ist, kann mittels zusätzlichen Skew-Quadrupolen kontrolliert und kompensiert werden. Ähnliche Rezepte für die von der Raumladung getriebenen Übertragung existieren zurzeit nicht. Das inhaltsreiche Verständnis dieses Effekts ist erforderlich, um neue mögliche Gegenmaßnahmen zu untersuchen.

Obwohl einige Ähnlichkeiten zwischen den von Betatron-Kopplung und den von Raumladung getriebenen Emittanzübertragung bestehen, dauern manche wichtige Unterschiede fort, die in der Literatur noch nicht wohlverstanden sind. Betatron-Kopplung leitet symmetrische Verteilungs- und Austauchkurven ein, unabhängig von der Kreuzungsrichtung und der Abspaltung der Tunes. Es wurde beobachtet, dass die von der Raumladung getriebene Emittanzübertragung hoch empfindlich in beiden Hinsichten ist:

- Particle-In-Cell numerische Berechnungen zeigen, dass der von der Raumladung getriebenen Emittanzaustausch nicht immer umkehrbar ist.

- In Maschinen mit nicht getrennten Tunes leitet die Raumladung die Emittanzübertragung auch ohne Betatron-Kopplung ein, wobei in Maschinen mit getrennten Tunes eine nicht Null Betatron-Kopplung erforderlich ist, um den Austausch zu führen.

- Wenn die Raumladung nicht vernachlässigbar ist, stellt die Verteilungskurve eine stark Asymmetrie um $\Delta = 0$ dar.

- Das Zentrum der Raumladungresonanz liegt immer bei $\Delta = 0$ in Maschinen mit nicht getrennten Tunes, wobei es im Falle der getrennten Tunes verschoben wird und die Änderung proportional zu dem Laslett Tuneshift $\Delta Q_{x,y}$ ist.
- Im Falle der nicht getrennten Tunes leitet die dynamische Kreuzung der Resonanz eine symmetrische Emittanzkurve mit einem kompletten Austausch ein, nur wenn die Kreuzung in die *richtige* Richtung geführt ist. Die Kurve ist asymmetrisch und der Austausch unvollständig, wenn die Kreuzung in die andere Richtung geführt ist. Die Resonanz-Bandbreite ist linear proportional zu dem Laslett Tuneshift und von den Strahlbreiten abhängig.
- Im Falle der getrennten Tunes leitet die dynamische Kreuzung der Resonanz eine Kurve ein, die von der Betatron-Kopplung $|C|$ und dem Laslett Tuneshift abhängig ist. Bei $\Delta = 0$ können die Emittanzen nicht gleich sein.
- Im Falle der nicht getrennten Tunes ist keine Drehung der Teilchenverteilung sowohl in den Phasenräume als auch in der $x - y$ Ebene beobachtet worden.

In dem letzten Teil dieser Arbeit wurden die Raumladungseffekten auf die Emittanzübertragung mittels numerischen Berechnungen untersucht. Particle-In-Cell Computersimulationen wurden durchgeführt, um neue heuristische Skalierungsgesetzen für die Resonanz-Bandbreite anzuleiten.

Das erste Skalierungsgesetz gilt für Maschinen mit nicht getrennten Tunes in Abwesenheit von Betatron-Kopplung. Nahe an der Differenz-Resonanz treibt die Raumladung die folgende Bandbreite

$$|C| \simeq \frac{1}{2}\frac{|\Delta Q_y|}{1+\dfrac{\sigma_{xo}}{\sigma_{yo}}}\;\frac{1}{0.8+\dfrac{Q_{x0}}{2}\left(\dfrac{\sigma_{yo}}{\sigma_{xo}}\right)^3}\;,$$

wobei ΔQ_y der anfänglich Laslett Tuneshift, $\sigma_{xo,yo}$ die anfängliche Strahlbreiten, und $Q_{x0} = 4.29$ der horizontale Betatron-Tune sind.

Es wurde auch geprüft, dass Raumaldungskräfte in der “smooth approximation” keine Emittanzübertragung treiben dürfen. Eine zusätzliche Betatron-Kopplung ist nötig, um die Übertragung einzuleiten. Die Raumladung bringt hierbei eine emittanzabhängige Verstimmung durch den Laslett Tuneshift ein: Sowohl die Asymmetrie der Verteilungs- und Austauchkurve als auch die Vergrößerung der Resonanzbandbreite werden mittels der Verstimmung beschrieben. Das zweite Skalierungsgesetz gilt für Maschinen mit getrennten Tunes in Anwesenheit von Betatron-Kopplung und Raumladung. Es beschreibt die Vergrößerung der Bandbreite und lautet

$$|C^{(o)}| \;\simeq\; |C^{(b)}| + \mathcal{A}|\Delta Q_x - \Delta Q_y| \qquad \text{with } |C^{(b)}| \neq 0\;,$$

wobei $|C^{(o)}|$ die messbare vergrösste Bandbreite, $|C^{(b)}|$ die Bandbreite der Betatron-

Kopplung darstellen, $\Delta Q_{x,y}$ die anfänglich Laslett Tuneshifts sind, und $\mathcal{A}$ ein konstanter Parameter ist, der durch eine lineare Anpassung zu stimmen ist.

Am Ende der Arbeit wurde eine Maßnahme untersucht und numerisch getestet, die Normal-Quadrupolmagnete annimmt, um den von der Raumladung getriebenen Emittanzaustausch in Maschinen mit nicht getrennten Tunes zu unterdrücken.

Bibliography

[1] R. Tomás García, *Direct Measurement of Resonance Driving Terms in the Super Proton Synchrotron (SPS) of CERN using Beam Position Monitors*, PhD thesis, CERN-THESIS-2003-010 (2003).

[2] A. Franchi **et al.**, *A Method to Measure the Skew Quadrupole Strengths in the SIS-18 using Two BPMs* , Proceedings of EPAC 2004, Lucerne (2004), p. 1957.

[3] A. Franchi **et al.**, *First test of the new turn-by-turn BPM aquisition system*, GSI internal note, (unpublished). http://www-linux.gsi.de/∼franchi/WORKS/gsi_notes_bpm_2003.pdf

[4] A. Galatis **et al.**, *Digital Beam Position Measurement at GSI-SIS and CERN-PS*, Proceedings of DIPAC 2005, Lyon (2005), p. 184.

[5] P. Spiller **et al.**, *High Intensity Uranium Operation in SIS18*, Proceedings of EPAC 2004, Lucerne (2004), p. 1180.

[6] B. Hofmann **et al.**, *Design of A 352 MHz-Proton-RFQ for GSI*, Proceedings of LINAC 2004, Lübeck (2004), p. 620. Z. Li **et al.**, *Design of the R.T. CH-Cavity and Perspectives for a New GSI Proton Linac*, **ibidem**, p. 81. R. Tiede **et al.**, *KONUS Beam Dynamics Design of a 70 mA, 70 MeV Proton CH-DTL for GSI-SIS12*, **ibidem**, p. 60;

[7] M. M. kirk and P .Forck, *Experiment on slow resonant extraction*, GSI internal note, (unpublished).

[8] K. Schindl and P. van der Stok, *Increase of Betatron Stacking Efficiency via Linear Coupling in AG Proton Synchrotron ("Skew injection"). Application to the CERN PS Booster*, CERN/PS/BR 76-19 (1976).

[9] G.Franchetti and I. Hofmann, *Optimizing multiturn injection with space charge and linear coupling* Proceedings of EPAC 200, Vienna (2000), p. 1292.

[10] M. Hayes **et al.**, *Resonance Driving Terms Experiments in the SPS at 26 and 80 GeV during 2002*, Proceedings of EPAC 2002, Paris (2002), p. 1290.

[11] F. Schmidt, M. Hayes and R. Tomás, *Completion of the Sextupole Driving Terms Measurement at the SPS*, Proceedings of PAC 2003, Portland (2003), p. 2231.

[12] J. Klem **et al.**, *Multiturn Measurements at the CERN SPS*, Proceedings of EPAC 2000, Vienna (2000), p. 1576.

[13] M. Bai **et al.**, *RHIC AC Dipole Design and Construction*, Proceedings of PAC 2001, Chicago (2001), p. 3606.

[14] R. Calaga, **et al.**, *Measurement and Optimization of Local Coupling from RHIC BPM Data*, Proceedings of PAC 2005, Knoxville (2005), p. 3553.

[15] R. Bartolini and F. Schmidt, *Normal Form via Tracking or Beam Data*, Part. Accel. vol. **59** (1998), pp. 93-106.

[16] A. Bazzani, E. Todesco, G. Turchetti, G. Servizi, *A Normal Form Approach to the Theory of the Nonlinear Betatronic Motion*, CERN 94-02 (1994).

[17] A. Bazzani, A. Pisent, G. Turchetti *Normal forms for Hamiltonian maps and future applications to accelerators*, CERN report SPS 87/38(AMS) (1987).

[18] A. Bazzani, G. Turchetti, P. Mazzanti, G. Servizi *Normal forms for Hamiltonian maps and nonlinear effects in particle accelerators*, Il Nuovo Cimento B, vol. **102** (1988), pp. 51-80.

[19] G. Turchetti, *Beam stability analysis via normal forms and non perturbative methods* in "Non Linear Problems in Future Particle Accelerators", Ed. W. Scandale e G. Turchetti, World Scientific (1991).

[20] É. Forest **et al.**, *Normal Form Methods for Complicated Periodic Systems: a Comlpete Solution using Differential Algebra*, Particle Accelerators, vol. **24** (1989), pp. 91-113.

[21] M. Berz, E. Forest and J. Irwin, *Normal form methods for complicated periodic systems: a complete solution using differential algebra and lie operators*, Particle Accelerators , vol. **24** (1989), pp. 91-107.

[22] M. Berz, *High order computation and and normal form analysis of repetitive systems*, AIP conference proceedings, vol. **249** (1992), pp. 456-489.

[23] E. Forest, *Beam Dynamics: a new attitude and framework* Harwood Academic (1998) ISBN:90-5702-558-2(HC).

[24] É. Forest, *A Hamiltonian Free Description of Single Particle Dynamics for Hopelessly Complex Periodic Systems*, Journal of Mathematical Physics, vol. **31** (1990), pp. 1133-1144.

[25] Caussyn **et al.**, *Experimental Studies of Nonlinear Beam Dynamics*, Physical Review A, vol. **46** (1992), p. 7942.

[26] R. Calaga **et al.**, *Betatron Coupling: Merging Hamiltonian and Matrix Approach*, Physical Review ST-AB, vol. **8** (2005), p. 34001.

[27] R. Tomás García **et al.**, *Measurement of global and local resonance terms*, Physical Review ST-AB, vol. **8** (2005), p. 24001.

[28] G. Guignard, *Beam Blow-up and Luminosity reduction due to Linear Coupling*, CERN ISR-BOM/77-43 (1977).

[29] E. Métral, *Simple theory of Emittance Sharing and Exchange due to Linear Betatron Coupling*, CERN/PS 2001-066(AE), (2001).

[30] C. Carli **et al.**, *Emittance Exchange by Crossing a Coupling Resonance*, Proceedings of EPAC 2002, Paris (2002), p. 1157.

[31] D. Edwards and L. Teng, IEEE Transactions on Nuclear Science, vol. **20**, N. 3 (1973), pp. 885-888.

[32] N. Minty and F. Zimmermann, *Measurement and Control of Charged Particle Beams*, Springer, Berlin, 2003 (ISBN 3-540-44197-5).

[33] P. Castro García, PhD thesis, p.49, CERN-SL-96-070-BI (1996).

[34] M. A. Mariscotti, *A method for automatic identification of peaks in the presence of background and its application to spectrum analysis*, Nuclear Instruments and Methods, vol. **50** (1967), pp. 309-320.

[35] M. E. Angoletta **et al.**, Proceedings of EPAC 2002, Paris (2002), p. 1948.

[36] A. Arduini **et al.** *Modelling Nonlinear Optics in the CERN SPS*, Proceedings of EPAC 2002, Paris (2002), p. 1220; R. Cappi **et al.**, *Optics studies for the CERN proton synchrotron: linear and nonlinear modelling using beam based measurements*, Proceedings of PAC 2003, Portrland (2003), p. 2913.

[37] T. Giacomini **et al.**, *Development of Residual Gas Profile Monitors at GSI* , AIP conference proceedings, vol. **732** (2004), pp. 286-293.

[38] P. Forck **et al.**, *Development of a Permanent Magnet Residual Gas Profile Monitor With Fast Readout*, Proceedings of EPAC 2004, Lucerne (2004), p. 2724.

[39] P. F. Tavares **et al.**, *Measurement of the modulus and phase of the linear coupling coefficient by analysis of the transverse beam profile*, Physical Review ST-AB, vol. **1** (1998), p. 54001.

[40] J. Y. Liu **et al.**, *Determination of the linear coupling resonance strength using two-dimensional invariant tori*, Physical Review E, vol. **49** (1994), pp. 2347-2352.

[41] W. Fischer, *Robust linear coupling correction with N-turn maps*, Physical Review ST-AB, vol. **6** (2003), p. 62801.

[42] G. Franchetti **et al.**, *Simulation Aspects of the Code Benchmarking Based on the CERN-PS "Montague-resonance" Experiment*, AIP conference proceedings, vol. **773** (2005), pp. 169-171.

[43] G. Franchetti and I. Hofmann, *Collective Emittance Exchange with Linear Coupling Space Charge Forces and Linear Coupling*, Physical Review Letters, vol. **94** (2005), p. 194801.

[44] E. Métral **et al.**, *Space-charge Experiments at the CERN Proton Synchrotron*, AIP conference proceedings, vol. **773** (2005), pp. 122-126.

[45] E. Métral **et al.**, *Intensity dependent Emittance Transfer Studies at the CERN Proton Synchrotron*, proceedings of EPAC 2004, Lucerne (2004), p. 1894.

[46] M. Aslaninejad and I. Hofmann, *Effects of Space charge on Linear Coupling and Gradient Errors in High-intensity Rings*, Physical Review ST-AB, vol. **6** (2003), p. 124202.

[47] B. W. Montague, CERN Report No. 85 07 208 (unpublished).

[48] D. Chernin, *Evolution of RMS beam envelopes in transport systems with linear X-Y coupling*, Particle Accelerators **24** (1988), pp. 29-44.

[49] E. Métral, *Simple Analytical Computations of Intensity dependent Emittance Transfer*, CERN-AB-2003-001 (ABP).

[50] G. Franchetti, I. Hofmann, and G. Turchetti, AIP conference proceedings, vol. **448** (1998), p. 233.

[51] S. Rambaldi **et al.**, *Accuracy analysis of a spectral Poisson solver*, to be published on Nuclear Instruments and Methods A, special edition COULOMB'05 workshop, Senigallia (2005).

[52] G. Turchetti **et al.**, *3D solutions of the Poisson-Vlasov equations for a charged plasma and particle-core model in a line of FODO cells*, European Physics Journal C, vol. **30** (2003), pp. 279-290.

[53] F. J. Sacherer, *RMS envelope equations with space charge*, IEEE proceedings (1971), p. 1105.

[54] F. J. Sacherer, *Transverse space-charge effects in circular accelerators*, PhD thesis, UCRL-18454 (1968).

[55] D. Sagan and D. Rubin, *Linear analysis of coupled lattices*, Physical Review ST-AB, vol. **2** (1999), p. 74001.

[56] D. Sagan, *Betatron phase and coupling correction at the Cornell Electron/Positron Storage Ring*, Physical Review ST-AB, vol. **3** (200), p. 102801.

[57] R. Tomás, *Normal form of particle motion under the influence of an AC dipole*, Physical Review ST-AB, vol. **5** (2002), p. 54001.

[58] R. Bartolini **et al.**, *Tune evaluation in simulations and experiments* CERN SL/95-84 (AP) (1995).

Appendix A

From magnet strength to Hamiltonian coefficients

In this appendix we derive Eq. (3.11), starting from the Hamiltonian describing a multipole of order n

$$H^{(n)} = -\Re\Big\{\frac{(K_{n-1}+iJ_{n-1})}{n\,!}(x+iy)^n\Big\}\ . \tag{A.1}$$

According to the binomial theorem the Hamiltonian can be expanded in series as

$$H^{(n)} = -\Re\Big\{\sum_{p=0}^{n}\frac{(K_{n-1}+iJ_{n-1})}{(n-p)\,!\ p\,!}x^p(iy)^{n-p}\Big\}\ . \tag{A.2}$$

Defining $p = j + k$ and $n - p = l + m$ (note that $n = j + k + l + m$), the above equation reads

$$H^{(n)} = -\Re\Big\{\sum_{\substack{j\,+\,k\,=\,0\\ l\,+\,m\,=\,n\,-\,j\,-\,k}}^{n}\frac{(K_{n-1}+iJ_{n-1})}{(l+m)\,!\ (j+k)\,!}x^{j+k}(iy)^{l+m}\Big\}\ . \tag{A.3}$$

Introducing the complex Courant-Snyder coordinates $q = \frac{\sqrt{\beta_q}}{2}(h_{q,-}+h_{q,+})$, where $h_{q,\pm} = \sqrt{2J_q}e^{\mp i(\phi_q+\phi_{q,0})}$, we obtain

$$\begin{aligned} H^{(n)} &= -\Re\Big\{\sum_{\substack{j\,+\,k\\ l\,+\,m}}^{n}\frac{(K_{n-1}+iJ_{n-1})}{(l+m)\,!\ (j+k)\,!}\beta_x^{\frac{j+k}{2}}\beta_y^{\frac{l+m}{2}}\frac{i^{l+m}}{2^{j+k+l+m}}\ \times \\ &\qquad (h_{x,-}+h_{x,+})^{j+k}(h_{y,-}+h_{y,+})^{l+m}\Big\}\ . \end{aligned} \tag{A.4}$$

The binomial theorem can be invoked again to expand $(h_{q,-}+h_{q,+})$

$$\begin{aligned} H^{(n)} &= -\Re\Big\{\sum_{\substack{j\,+\,k\\ l\,+\,m}}^{n}\frac{(K_{n-1}+iJ_{n-1})}{(l+m)\,!\ (j+k)\,!}\beta_x^{\frac{j+k}{2}}\beta_y^{\frac{l+m}{2}}\frac{i^{l+m}}{2^{j+k+l+m}}\ \times \\ &\qquad \sum_{s=0}^{j+k}\sum_{t=0}^{l+m}\frac{(j+k)\,!\ (l+m)\,!}{(j+k-s)\,!\ (l+m-t)\,!\ s\,!\ t\,!}h_{x,-}^{s}h_{x,+}^{j+k-s}h_{y,-}^{t}h_{y,+}^{l+m-t}\Big\}\ . \end{aligned} \tag{A.5}$$

Renaming the mute the index $s \to j$ and $t \to l$ and simplifying the factorials the Hamiltonian reads

$$H^{(n)} = -\Re\{ \sum_{j,k,l,m=0}^{n=j+k+l+m} \frac{(K_{n-1} + iJ_{n-1})}{j\,!\,k\,!\,l\,!\,m\,!\,2^{j+k+l+m}} \beta_x^{\frac{j+k}{2}} \beta_y^{\frac{l+m}{2}} i^{l+m} h_{x,-}^{j} h_{x,+}^{k} h_{y,-}^{l} h_{y,+}^{m} \} \ . \tag{A.6}$$

It can be easily shown that the real part of the sum selects the normal terms K_{n-1} if the power of y (i.e. $l+m$) is even, whereas the skew terms J_{n-1} are selected when $l+m$ is odd. This selection can be expressed introducing a function Ω such as

$$\Omega(i) = \begin{cases} 1 & \text{if } i \text{ is even} \\ 0 & \text{if } i \text{ is odd} \end{cases} \tag{A.7}$$

which can be included in the Hamiltonian according to

$$\begin{aligned} H^{(n)} \quad = \quad & \sum_{j,k,l,m=0}^{n=j+k+l+m} -\frac{[K_{n-1}\Omega(l+m) + iJ_{n-1}\Omega(l+m+1)]}{j\,!\,k\,!\,l\,!\,m\,!\,2^{j+k+l+m}} \beta_x^{\frac{j+k}{2}} \beta_y^{\frac{l+m}{2}} i^{l+m} \quad \times \\ & h_{x,-}^{j} h_{x,+}^{k} h_{y,-}^{l} h_{y,+}^{m} \quad . \end{aligned} \tag{A.8}$$

From the above relation, Eq. (3.11) is derived.

Appendix B

Hamiltonian coefficients from RDT variation

In this appendix we provide an illustrative proof of Eq. (4.2). First we consider the case with only one magnet between two consecutive BPMs as sketched in Fig. B.1. At the end of this section the more general case with several magnets between two BPM's is outlined.

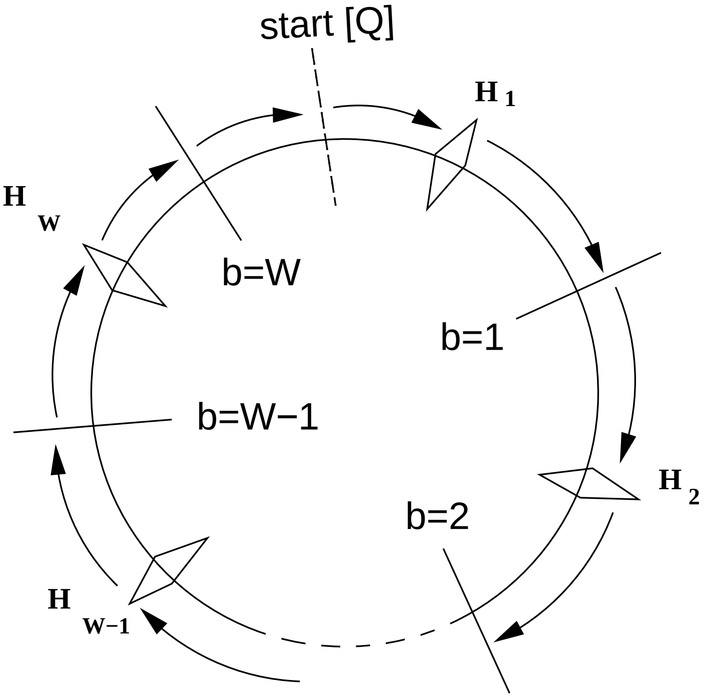

Figure B.1: Schematic view of a ring taking into account the distribution of BPMs and multipoles.

For sake of notation it is convenient to define some quantities as follow

$$
\begin{aligned}
\mathsf{B}_b &= i[(j-k)\phi_{b,x}^{BPM} + (l-m)\phi_{b,y}^{BPM}] \ , && \text{(B.1)}\\
\mathsf{W}_w &= i[(j-k)\phi_{w,x}^{M} + (l-m)\phi_{w,y}^{M}] \ , && \text{(B.2)}\\
\mathsf{Q} &= 2\pi i[(j-k)Q_x + (l-m)Q_y] \ , && \text{(B.3)}\\
h_{jklm}^{(b)} &= \sum_{w\leq b} h_{w,jklm} e^{\mathsf{B}_b-\mathsf{W}_w} + \sum_{w>b} h_{w,jklm} e^{\mathsf{B}_b-\mathsf{W}_w+\mathsf{Q}} \ . && \text{(B.4)}
\end{aligned}
$$

ϕ_w^M and $\phi_{b,q}^{BPM}$ are the betatron phases of the w-th magnet and the b-th BPM respectively, both calculated with respect to a starting point. Each time $b < w$ a factor Q must be added to take into account the *crossing* of this point. With the above nomenclature, Eq. (3.15) reads

$$
f_{jklm}^{(b)} = \frac{h_{jklm}^{(b)}}{1-e^{\mathsf{Q}}} \ , \tag{B.5}
$$

$h_{w,jklm}$ are inferred inverting the linear system (B.5). For sake of clarity, we show a case with $W = 3$ (the generalization to any number is straightforward) and omit the subscript $jklm$,

$$
\begin{aligned}
h^{(1)} &= e^{\mathsf{B}_1-\mathsf{W}_1}h_1 + e^{\mathsf{B}_1-\mathsf{W}_2+\mathsf{Q}}h_2 + e^{\mathsf{B}_1-\mathsf{W}_3+\mathsf{Q}}h_3\\
h^{(2)} &= e^{\mathsf{B}_2-\mathsf{W}_1}h_1 + e^{\mathsf{B}_2-\mathsf{W}_2}\quad h_2 + e^{\mathsf{B}_2-\mathsf{W}_3+\mathsf{Q}}h_3\\
h^{(3)} &= e^{\mathsf{B}_3-\mathsf{W}_1}h_1 + e^{\mathsf{B}_3-\mathsf{W}_2}\quad h_2 + e^{\mathsf{B}_3-\mathsf{W}_3}\quad h_3 \ .
\end{aligned}
$$

In the matrix notation the system reads $\vec{H} = \mathbf{A}\vec{h}$,

$$
\begin{pmatrix} h^{(1)} \\ h^{(2)} \\ h^{(3)} \end{pmatrix} = \begin{pmatrix} e^{\mathsf{B}_1-\mathsf{W}_1} & e^{\mathsf{B}_1-\mathsf{W}_2+\mathsf{Q}} & e^{\mathsf{B}_1-\mathsf{W}_3+\mathsf{Q}} \\ e^{\mathsf{B}_2-\mathsf{W}_1} & e^{\mathsf{B}_2-\mathsf{W}_2} & e^{\mathsf{B}_2-\mathsf{W}_3+\mathsf{Q}} \\ e^{\mathsf{B}_3-\mathsf{W}_1} & e^{\mathsf{B}_3-\mathsf{W}_2} & e^{\mathsf{B}_3-\mathsf{W}_3} \end{pmatrix} \begin{pmatrix} h_1 \\ h_2 \\ h_3 \end{pmatrix} \ .
$$

$\mathbf{A}$ can be factorized as $\mathbf{A} = \mathbf{A_1 A_2}$,

$$
\mathbf{A} = \begin{pmatrix} e^{\mathsf{B}_1} & 0 & 0 \\ 0 & e^{\mathsf{B}_2} & 0 \\ 0 & 0 & e^{\mathsf{B}_3} \end{pmatrix} \begin{pmatrix} e^{-\mathsf{W}_1} & e^{-\mathsf{W}_2+\mathsf{Q}} & e^{-\mathsf{W}_3+\mathsf{Q}} \\ e^{-\mathsf{W}_1} & e^{-\mathsf{W}_2} & e^{-\mathsf{W}_3+\mathsf{Q}} \\ e^{-\mathsf{W}_1} & e^{-\mathsf{W}_2} & e^{-\mathsf{W}_3} \end{pmatrix} \ .
$$

$\mathbf{A_2}$ is inverted according to $\mathbf{A_2} = (\mathbf{A_3 A_4})^{-1}$,

$$
\mathbf{A_2} = \left[\begin{pmatrix} e^{\mathsf{W}_1} & 0 & -e^{\mathsf{W}_1+\mathsf{Q}} \\ -e^{\mathsf{W}_2} & e^{\mathsf{W}_2} & 0 \\ 0 & -e^{\mathsf{W}_3} & e^{\mathsf{W}_3} \end{pmatrix} \begin{pmatrix} \frac{1}{1-e^{\mathsf{Q}}} & 0 & 0 \\ 0 & \frac{1}{1-e^{\mathsf{Q}}} & 0 \\ 0 & 0 & \frac{1}{1-e^{\mathsf{Q}}} \end{pmatrix} \right]^{-1} .
$$

The linear system and its inverse eventually read

$$
\vec{H} = \mathbf{A_1}(\mathbf{A_3 A_4})^{-1}\vec{h} \qquad \rightarrow \qquad \vec{h} = \mathbf{A_3 A_4 A_1^{-1}}\vec{H} \ ,
$$

providing the solution

$$
\begin{pmatrix} h_1 \\ h_2 \\ h_3 \end{pmatrix} = \frac{1}{1-e^{\mathsf{Q}}} \begin{pmatrix} e^{\mathsf{W}_1}(h^{(1)}e^{-\mathsf{B}_1} - h^{(3)}e^{\mathsf{Q}-\mathsf{B}_3}) \\ e^{\mathsf{W}_2}(h^{(2)}e^{-\mathsf{B}_2} - h^{(1)}e^{-\mathsf{B}_1}) \\ e^{\mathsf{W}_3}(h^{(3)}e^{-\mathsf{B}_3} - h^{(2)}e^{-\mathsf{B}_2}) \end{pmatrix} \ .
$$

From Eq. (B.5) we obtain

$$\begin{pmatrix} h_1 \\ h_2 \\ h_3 \end{pmatrix} = \begin{pmatrix} e^{\mathsf{W}_1}\left(f^{(1)}e^{-\mathsf{B}_1} - f^{(3)}e^{\mathsf{Q}-\mathsf{B}_3}\right) \\ e^{\mathsf{W}_2}\left(f^{(2)}e^{-\mathsf{B}_2} - f^{(1)}e^{-\mathsf{B}_1}\right) \\ e^{\mathsf{W}_3}\left(f^{(3)}e^{-\mathsf{B}_3} - f^{(2)}e^{-\mathsf{B}_2}\right) \end{pmatrix} .$$

The general expression for the above equations reads

$$\begin{aligned} h_w &= e^{\mathsf{W}_w}\left(f^{(w)}e^{-\mathsf{B}_w} - f^{(w-1)}e^{-\mathsf{B}_{w-1}}\right), \text{ for } 2 \leq w \leq W \\ h_1 &= e^{\mathsf{W}_1}\left(f^{(1)}e^{-\mathsf{B}_1} - f^{(W)}e^{\mathsf{Q}-\mathsf{B}_W}\right) . \end{aligned} \tag{B.6}$$

Reinserting the index $jklm$ and making explicit W_w, B_w and Q we obtain

$$h_{w,jklm}e^{-i[(j-k)\Delta\phi_x^{wb}+(l-m)\Delta\phi_y^{wb}]} = f_{jklm}^{(w)}e^{-i[(j-k)\Delta\phi_x^{w,w-1}+(l-m)\Delta\phi_y^{w,w-1}]} - f^{(w-1)}, \tag{B.7}$$

where $\Delta\phi_q^{wb}$ are the phase advances between the w-th magnet and the $w-1$-th BPM and $\Delta\phi_q^{w,w-1}$ the phase advances between the two consecutive BPMs.
The most general case with T sources between two consecutive BPMs introduces a modification in the l.s.h. of the above equation, namely the replacement of the single Hamiltonian coefficient with a sum of all the contributes

$$h_{w,jklm}e^{-i[(j-k)\Delta\phi_x^{wb}+(l-m)\Delta\phi_y^{wb}]} \longrightarrow \hat{h}_{w,jklm} \tag{B.8}$$

where

$$\hat{h}_{w,jklm} = \sum_{\tau=1}^{T} h_{\tau,jklm}e^{i[(j-k)\Delta\phi_{\tau,x}^{w-1}+(l-m)\Delta\phi_{\tau,y}^{w-1}]} . \tag{B.9}$$

The sum is over all the T multipoles between the $(w-1)$-th and the w-th BPMs and $\Delta\phi_{\tau,q}^{w-1}$ are the phase advances between those multipoles and the $w-1$-th BPM (see Fig. B.2).

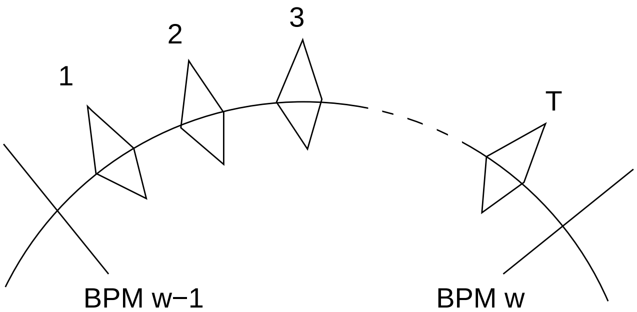

Figure B.2: Schematic view of a section of the ring when several multipoles are placed between two BPMs.

B.1 The shadow effect

Eq. (B.7) shows how the amplitudes of the RDT at two BPMs change only if there are multipoles in between. From the difference between the two RDT the total strength of the multipoles in between $\hat{h}_{w,jklm}$ can be therefore inferred.

Nevertheless even if the amplitudes of the RDT change *only* in presence of nonlinear magnet in between, it is not true that the latter ones make *always* the RDT change. Indeed exist particular lattice configurations which can make the method fail. We consider for example the case with two nonlinear magnets. The numerator in the r.s.h. of Eq. (B.5) reads

$$\begin{aligned} h^{(1)} &= e^{\mathsf{B}_1-\mathsf{W}_1}h_1 + e^{\mathsf{B}_1-\mathsf{W}_2+\mathsf{Q}}h_2 \\ h^{(2)} &= e^{\mathsf{B}_2-\mathsf{W}_1}h_1 + e^{\mathsf{B}_2-\mathsf{W}_2}\quad h_2 \ . \end{aligned}$$

The amplitudes of both equations are

$$\begin{aligned} |h^{(1)}| &= |h_1 + e^{\mathsf{W}_1-\mathsf{W}_2+\mathsf{Q}}h_2| = |h_2||\frac{h_1}{h_2} + e^{\mathsf{W}_1-\mathsf{W}_2+\mathsf{Q}}| \\ |h^{(2)}| &= |h_1 + e^{\mathsf{W}_1-\mathsf{W}_2}\quad h_2| = |h_2||\frac{h_1}{h_2} + e^{\mathsf{W}_1-\mathsf{W}_2}| \ . \end{aligned}$$

According to Eq. (B.5)

$$\frac{|f^{(1)}|}{|f^{(2)}|} = \frac{|h^{(1)}|}{|h^{(2)}|} = \frac{|\frac{h_1}{h_2} + e^{\mathsf{W}_1-\mathsf{W}_2+\mathsf{Q}}|}{|\frac{h_1}{h_2} + e^{\mathsf{W}_1-\mathsf{W}_2}|} \ . \tag{B.10}$$

We recall that the ratio $\frac{h_1}{h_2}$ is real. If $\mathsf{W}_1 - \mathsf{W}_2 + \mathsf{Q} = \pm(\mathsf{W}_1 - \mathsf{W}_2)$ the RDT at location 1 and 2 have the same amplitudes (for any values of the strengths) and the formula (B.6) cannot be applied, since it is not possible anymore to localize the magnets, being the jumps not anymore observable. The above condition is satisfied whether either $\mathsf{Q} = 0$ (integer resonance condition) or

$$\begin{aligned} \mathsf{Q} &= -2(\mathsf{W}_1 - \mathsf{W}_2) \qquad\qquad \text{(B.11)} \\ (j-k)(\phi^M_{1,x} - \phi^M_{2,x} + \pi Q_x) &= (m-l)(\phi^M_{1,y} - \phi^M_{2,y} + \pi Q_y) \end{aligned}$$

This is a condition between the betatron phases of the magnets and the tunes. Two pairs of skew quadrupoles, one of skew sextupoles and three of normal sextupoles installed in the GSI SIS-18 satisfy such a relation.

B.2 RDT close to a resonance

In proximity of a resonance $\mathsf{Q} = 2\pi i[(j-k)Q_x + (l-m)Q_y] \to 0$, the RDT's defined in Eqs. (3.15) and (B.5) diverge. Nevertheless it is possible to manipulate the denominator constructing a quasiresonant normal form that allows this limit and reproduce the nonresonant case outside the stop-band [16]. In any case, the denominator remains invariant along the ring. The second sum in Eq. (B.4)

$$h^{(b)}_{jklm} = \sum_{w\leq b} h_{w,jklm} e^{\mathsf{B}_b - \mathsf{W}_w} + \sum_{w>b} h_{w,jklm} e^{\mathsf{B}_b - \mathsf{W}_w + \mathsf{Q}} \tag{B.12}$$

drives the variation along the ring of $|h^{(b)}_{jklm}|$ and therefore of $|f_{jklm}|$. Close to a resonance $\mathsf{Q} \rightarrow 0$ and the above expression reads

$$h^{(b)}_{jklm} = \sum_{w} h_{w,jklm} e^{\mathsf{B}_b - \mathsf{W}_w} + O(\mathsf{Q}) \tag{B.13}$$

where now the sum is over all multipoles along the ring and the reminder proportional to Q. The variation of $h^{(b)}_{jklm}$ and therefore of f_{jklm} becomes a pure rotation making the amplitudes be invariant.

B.3 beta functions at the multipoles

If one relies on the nominal strengths of either skew quadrupoles or sextupoles, the computation of $|h_{jklm}|$ from the measured f_{jklm} provides a direct way to infer the beta function at their location if only one magnet is placed between two consecutive BPMs. In this case indeed Eq. (4.4) can be applied yielding

$$\begin{aligned}
\beta_{w,x} &= \left(48\left|\frac{h_{w,3000}}{K_{w,2}}\right|\right)^{2/3} && \text{for normal sextupoles} && \text{(B.14)}\\
\beta_{w,y} &= \left(16\left|\frac{h_{w,1020}}{K_{w,2}}\right|\right)\sqrt{\beta_{w,x}} && \text{for normal sextupoles} && \text{(B.15)}\\
\sqrt{\beta_{w,x}\beta_{w,y}} &= \left(4\left|\frac{h_{w,1001}}{J_{w,1}}\right|\right)^{2} && \text{for skew quadrupoles} && \text{(B.16)}
\end{aligned}$$

Therefore the beta functions at the sextupoles can be unambigously inferred measuring $|h_{jklm}|$ for several values of the sextupole strengths K_2 and fitting Eqs. (B.14) and (B.15). Ss far as the skew quadurpoles are concerned only an indirect check on their product can be performed.

Appendix C

Lie series and RDT close to the (1,-1) resonance

From Eqs. (3.18) and (3.19) the turn-by-turn normalized particle positions and momenta at a location s of a coupled lattice are described as follows,

$$\begin{aligned} \hat{x} - i\hat{p}_x &= \sqrt{2I_x}e^{i\psi_x} - 2if_{1001}\sqrt{2I_y}e^{i\psi_y} \\ &\quad -2if_{1010}\sqrt{2I_y}e^{-i\psi_y} \ , \end{aligned} \tag{C.1}$$

$$\begin{aligned} \hat{y} - i\hat{p}_y &= \sqrt{2I_y}e^{i\psi_y} - 2if^*_{1001}\sqrt{2I_x}e^{i\psi_x} \\ &\quad -2if_{1010}\sqrt{2I_x}e^{-i\psi_x} \ , \end{aligned} \tag{C.2}$$

where $I_{x,y}$ are the horizontal and the vertical invariants, $\psi_{x,y}$ are the phases of the oscillations which can be expressed as function of the tunes $Q_{x,y}$, the turn number N and the initial phases $\phi_{x0,y0}$ as $\psi_{x,y} = 2\pi Q_{x,y}N + \phi_{x0,y0}$.

Eqs. (C.1)-(C.2) provide a truncated expansion of $h_{q,-}$ for a lattice in presence betatron coupling driving the sum (1,1) and difference (1,-1) resonance. The normal form tranformation introduced in Sec.3.3 is nonresonant. Tune working point is here assumed to be close enough to the difference resonance, i.e. $\Delta << 1$, to neglect the sum RDT f_{1010}.

Under these assumptions it is anyway possible to construct a quasiresonant normal form transformation [16] and a closed Lie expansion of the complex Courant-Snyder coordinates $h_x = \hat{x} - i\hat{p}_x$ [15]

$$h_x = e^{:F:}\zeta^-_x = \sum_{n=0}^{\infty}\frac{D^n_F\zeta^-_x}{n!} = \zeta^-_x + [F,\zeta^-_x] + \frac{1}{2!}[F,[F,\zeta^-_x]] \ + \ldots, \tag{C.3}$$

where $\zeta^- = \sqrt{2I}e^{\psi}$ are the normal form coordinates; $D_F\zeta^-_x = [F,\zeta^-]$ denotes the Poisson brackets ; $F = f_{1001}\zeta^+_x\zeta^-_y + f^*_{1001}\zeta^-_x\zeta^+_y$ is the generating function for the normal form transformation and f_{1001} is now a quasiresonant RDT. An expression of f_{1001}, approximated up to the first order, reads

$$\bar{f}^{(b)}_{1001} = \frac{\sum\limits_{w} J_{w,1}\sqrt{\beta_x^w \beta_y^w}\, e^{i(\Delta\phi^b_{w,x}-\Delta\phi^b_{w,y})}}{4(1-e^{2\pi i(Q_h-Q_v)})}\ . \tag{C.4}$$

The difference between the above definition and the one given in Eq. (3.15) is in that here the eigen tunes Q_h, Q_v appear instead of the bare tunes Q_x, Q_y. The substitution makes the quasiresonant f_{1001} not to diverge for $\Delta \to 0$. Outside the resonance stop-band the two expression are equivalent.

The Possion brackets can be explicited with a recursive relation (note that $[\zeta_q^+, \zeta_q^-] = -2i$, all other combinations provide zero):

$$\begin{aligned}
D^1_F\zeta_x^- &= [F,\zeta_x^-] = [f_{1001}\zeta_x^+\zeta_y^-, \zeta_x^-] = -2if_{1001}\zeta_y^- \\
D^2_F\zeta_x^- &= [F,[F,\zeta_x^-]] = [F, D^1_F\zeta_x^-] = (-2if_{1001})(-2if^*_{1001})\zeta_x^- \\
D^3_F\zeta_x^- &= [F,[F,[F,\zeta_x^-]]] = [F, D^2_F\zeta_x^-] = (-2if_{1001})^2(-2if^*_{1001})\zeta_y^- \\
&\ \vdots
\end{aligned}$$

$$D^{2n}_F\zeta_x^- = (-1)^n|2f_{1001}|^{2n}\zeta_x^- \tag{C.5}$$

$$D^{2n+1}_F\zeta_x^- = (-1)^{n+1}|2f_{1001}|^{2n}2if_{1001}\zeta_y^- \tag{C.6}$$

Manipulating the r.s.h. in the latter relation yields

$$|f_{1001}|^{2n}f_{1001} = |f_{1001}|^{2n+1}\frac{|f_{1001}|}{{f_{1001}}^*}\ .$$

It is convenient to make explicit the abosulte value and the phase of f_{1001} as follow

$$f_{1001} = fe^{iq}\ . \tag{C.7}$$

Some algebra in Eqs. (C.5)-(C.6) yields

$$\begin{aligned}
D^{2n}_F\zeta_x^- &= (-1)^n(2f)^{2n}\zeta_x^- \\
D^{2n+1}_F\zeta_x^- &= -ie^{iq}(-1)^n(2f)^{2n+1}\zeta_y^-\ .
\end{aligned}$$

The Lie series (C.3) therefore reads

$$h_x = \sum_{n=0}^{\infty}(-1)^n\frac{(2f)^{2n}}{2n!}\zeta_x^- - ie^{iq}(-1)^n\frac{(2f)^{2n+1}}{(2n+1)!}\zeta_y^-\ .$$

The summations in the above r.s.h. are the Taylor expansions of $\cos 2f$ and $\sin 2f$ respectively, providing

$$h_x = \cos 2f\zeta_x^- - ie^{iq}\sin 2f\zeta_y^- \tag{C.8}$$

$$h_y = \cos 2f\zeta_y^- - ie^{-iq}\sin 2f\zeta_x^-\ , \tag{C.9}$$

where the expression for h_y has been obtained with a similar derivation. Making explicit ζ, the following turn-by-turn relations are obtained

$$\begin{aligned} h_x(N) &= \cos 2f\sqrt{2I_x}e^{i(2\pi NQ_h+\psi_{x0})} - ie^{iq}\sin 2f\sqrt{2I_y}e^{i(2\pi NQ_v+\psi_{y0})} && \text{(C.10)} \\ h_y(N) &= \cos 2f\sqrt{2I_y}e^{i(2\pi NQ_v+\psi_{y0})} - ie^{-iq}\sin 2f\sqrt{2I_x}e^{i(2\pi NQ_h+\psi_{x0})} \ , && \text{(C.11)} \end{aligned}$$

where N is the turn number, $\psi_{x0,y0}$ are the initial particle phases in normal form.

Appendix D

Betatron coupling: equivalence of RDT and matrix approaches

Betatron coupling is usually analyzed using either the matrix formalism or the Hamiltonian perturbation theory. The latter is regarded as being less exact but providing better physical insight. In this chapter direct relations are derived between the two formalisms. This makes possible the interpretation of the matrix approach in terms of resonances, as well as use results of both formalisms indistinctly. An approach to measure the coupling matrix and its determinant from turn-by-turn data is presented together with results from measurement at the Relativisti Heavy Ion Collider (RHIC) of BNL.

D.1 Resonance driving term formalism

From Eqs. (3.18) and (3.19) the turn-by-turn normalized particle positions and momenta at a location s of a weakly coupled lattice are described as follows,

$$\begin{aligned}\hat{x} - i\hat{p}_x &= \sqrt{2I_x}e^{i\psi_x} - 2if_{1001}\sqrt{2I_y}e^{i\psi_y} \\ &\quad -2if_{1010}\sqrt{2I_y}e^{-i\psi_y} \ , \qquad \text{(D.1)}\\ \hat{y} - i\hat{p}_y &= \sqrt{2I_y}e^{i\psi_y} - 2if^*_{1001}\sqrt{2I_x}e^{i\psi_x} \\ &\quad -2if_{1010}\sqrt{2I_x}e^{-i\psi_x} \ , \qquad \text{(D.2)}\end{aligned}$$

where $I_{x,y}$ are the horizontal and the vertical invariants, $\psi_{x,y}$ are the phases of the oscillations which can be expressed as function of the tunes $Q_{x,y}$, the turn number N and the initial phases $\phi_{x0,y0}$ as $\psi_{x,y} = 2\pi Q_{x,y}N + \phi_{x0,y0}$. The RDT f_{1001} and f_{1010} are proportional to the Hamiltonian terms and drive the difference and the sum resonances respectively. These terms are functions of the uncoupled lattice parameters at the location of both the coupling elements and the observation point b given by

$$f^{(b)}_{\substack{1001\\1010}} = \frac{\sum\limits_{w} J_{w,1}\sqrt{\beta^w_x\beta^w_y}\,e^{i(\Delta\phi^b_{w,x}\mp\Delta\phi^b_{w,y})}}{4(1-e^{2\pi i(Q_x\mp Q_y)})} \tag{D.3}$$

where $J_{l,1}$ is the w^{th} integrated skew quadrupole strength, $\beta^w_{x,y}$ are the Twiss functions at the location of the w^{th} skew quadrupole, $\Delta\phi^b_w$ are the phase advances between the observation point *b* and the w^{th} skew quadrupole and $Q_{x,y}$ are the horizontal and vertical tunes.

D.2 Matrix formalism

In the matrix approach, the coupled motion [31] is parametrized by factoring the one turn matrix into block diagonal normal mode form by means of the similarity transformation given by the symplectic 4×4 matrix $\mathbf{V}$, of the form

$$\mathbf{V} = \begin{pmatrix} \gamma\mathbf{I} & \mathbf{C} \\ -\mathbf{C}^{+} & \gamma\mathbf{I} \end{pmatrix} , \tag{D.4}$$

where $\mathbf{I}$ is the 2×2 identity matrix, and $\mathbf{C}$ is the 2×2 coupling matrix requiring $|\mathbf{C}| + \gamma^2 = 1$. By means of another similarity transformation the β dependence is normalized out of $\mathbf{C}$,

$$\overline{\mathbf{C}} = \mathbf{G_a}\mathbf{C}\mathbf{G_b^{-1}} \tag{D.5}$$

where $\mathbf{G_{a,b}} = \begin{bmatrix} \frac{1}{\sqrt{\beta_{a,b}}} & 0 \\ \frac{\alpha_{a,b}}{\sqrt{\beta_{a,b}}} & \sqrt{\beta_{a,b}} \end{bmatrix}$ are the normalization matrices for the *a* and *b* modes defined in [55]. Note that $|\overline{\mathbf{C}}| = |\mathbf{C}|$.

The normalized motion in the horizontal and vertical planes is given by [55]

$$\begin{pmatrix} \hat{x} \\ \hat{p}_x \\ \hat{x} \\ \hat{p}_y \end{pmatrix} = \begin{pmatrix} \gamma & 0 & \overline{C}_{11} & \overline{C}_{12} \\ 0 & \gamma & \overline{C}_{21} & \overline{C}_{22} \\ -\overline{C}_{22} & \overline{C}_{12} & \gamma & 0 \\ \overline{C}_{21} & -\overline{C}_{11} & 0 & \gamma \end{pmatrix} \begin{pmatrix} A_x\cos\psi_x \\ A_x\sin\psi_x \\ A_y\cos\psi_y \\ A_y\sin\psi_y \end{pmatrix} \tag{D.6}$$

Using the above expressions for normalized positions and momenta, the complex Courant-Snyder variables are given by

$$\begin{aligned} \hat{x} - i\hat{p}_x &= \gamma A_x e^{i\psi_x} + \frac{A_y}{2}\Big((\overline{C}_{11} - i\overline{C}_{12} - i\overline{C}_{21} - \overline{C}_{22})e^{-i\psi_y} && \text{(D.7)} \\ &\qquad +(\overline{C}_{11} + i\overline{C}_{12} - i\overline{C}_{21} + \overline{C}_{22})e^{i\psi_y}\Big) , \\ \hat{y} - i\hat{p}_y &= \gamma A_y e^{i\psi_y} + \frac{A_x}{2}\Big((\overline{C}_{11} - i\overline{C}_{12} - i\overline{C}_{21} - \overline{C}_{22})e^{-i\psi_x} && \text{(D.8)} \\ &\qquad +(-\overline{C}_{11} + i\overline{C}_{12} - i\overline{C}_{21} - \overline{C}_{22})e^{i\psi_x}\Big) . \end{aligned}$$

Note that the convention for momenta used in Hamiltonian theory described in [15] is the negative of that used in matrix formalism described in [56].

D.3 Relating the $\overline{\mathrm{C}}$ matrix and the RDT's

The relation to the Hamiltonian formalism can now be established by directly comparing Eqs. (D.1) and (D.2) to Eqs. (D.7) and (D.8), obtaining

$$\begin{aligned} f_{1001} &= \frac{1}{4\gamma}(\overline{C}_{12} - \overline{C}_{21} + i\overline{C}_{11} + i\overline{C}_{22}) \ , \qquad \text{(D.9)} \\ f_{1010} &= \frac{1}{4\gamma}(\overline{C}_{12} + \overline{C}_{21} + i\overline{C}_{11} - i\overline{C}_{22}) \ , \qquad \text{(D.10)} \end{aligned}$$

or, equivalently expressing $\overline{\mathbf{C}}$ as function of the generating terms,

$$\begin{aligned} \frac{1}{2\gamma}\overline{C}_{\substack{12\\21}} &= \Re\{f_{1010} \pm f_{1001}\} \ , \qquad \text{(D.11)} \\ \frac{1}{2\gamma}\overline{C}_{\substack{11\\22}} &= \Im\{f_{1001} \pm f_{1010}\} \ , \qquad \text{(D.12)} \end{aligned}$$

where $\Re$ and $\Im$ stand for real and imaginary parts respectively. The determinant of $\overline{\mathbf{C}}$ can also be related to the resonance terms as

$$\frac{|\overline{\mathbf{C}}|}{4\gamma^2} = |f_{1001}|^2 - |f_{1010}|^2 \ , \qquad \text{(D.13)}$$

and using $|\overline{\mathbf{C}}| + \gamma^2 = 1$ yields,

$$\begin{aligned} |\overline{\mathbf{C}}| &= 1 - \frac{1}{1 + 4(|f_{1001}|^2 - |f_{1010}|^2)} \ , \qquad \text{(D.14)} \\ \gamma^2 &= \frac{1}{1 + 4(|f_{1001}|^2 - |f_{1010}|^2)} \qquad \text{(D.15)} \end{aligned}$$

These expressions have a direct interpretation: if $|\overline{\mathbf{C}}|$ is positive the difference resonance (f_{1001}) dominates, and if it is negative the sum resonance (f_{1010}) dominates. From these expressions it is also observed that a null $|\overline{\mathbf{C}}|$ does not imply null coupling, but $|f_{1001}| = |f_{1010}|$. If $|f_{1010}|^2 > \frac{1}{4} + |f_{1001|}$, then $\gamma^2 < 0$ and the particle motion is unstable (see discussion in [55] after Eq. (12)).

As shown in [1] and reported in Sec. B.2 the relative longitudinal variations of the generating terms become smaller as the tunes approach the resonance. On the resonance, the amplitude of the generating term becomes invariant around the ring. Thus, by virtue of Eq. (D.13), the determinant of $\overline{\mathbf{C}}$ also tends to be invariant around the ring as the tunes approach the resonance.

To better understand the behavior of the above quantities in presence of localized coupling source, single particle simulations were run using the RHIC yellow lattice. In Fig. D.1 the elements of $\overline{\mathbf{C}}$ are plotted together with the location of skew quadrupole kicks and $|\overline{\mathbf{C}}|/\gamma^2$. In regions free of coupling the firsts show a slow modulation, whereas $|\overline{\mathbf{C}}|/\gamma^2$ remain constant in a way similar to the RDT's. In presence of coupling they both exibit large jumps.

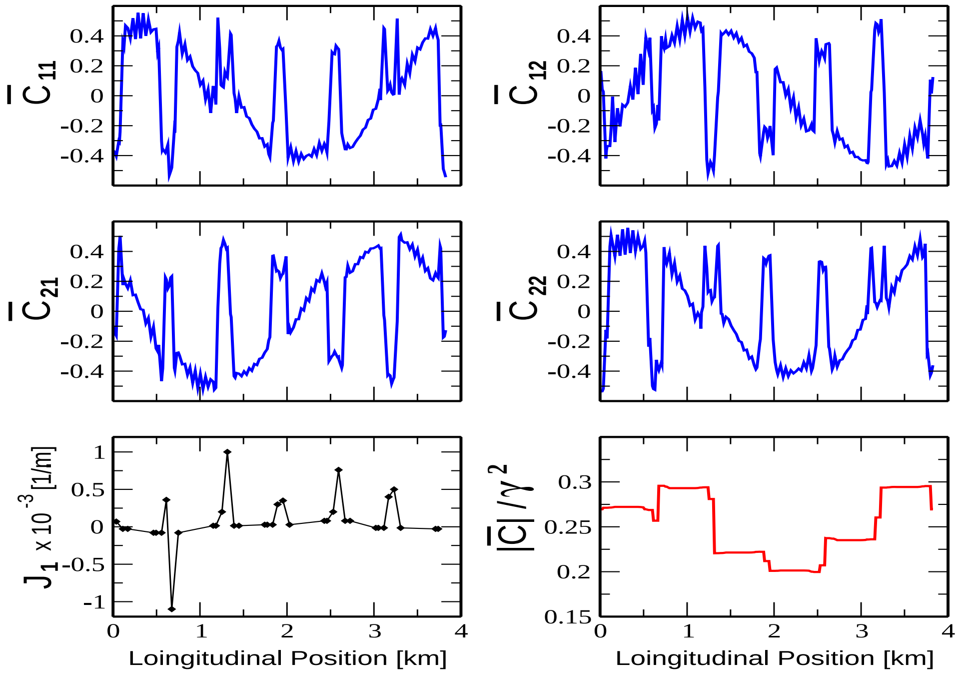

Figure D.1: Single particle simulations of the RHIC "yellow" lattice: the elements of $\overline{\mathbf{C}}$ are plotted (upper four windows) together with the location of skew quadrupole kicks (bottom left) and $|\overline{\mathbf{C}}|/\gamma^2$ (bottom right).

D.4 $\overline{\mathbf{C}}$ matrix and skew quadrupole strengths

Eq. (4.2) was derived to obtain multi-polar strengths from the RDT. Skew quadrupolar strengths can now be equivalently obtained from the measurement of the $\overline{\mathbf{C}}$ matrix by use of the above relations.

We assume that only one skew quadrupole of integrated strength $J_{w,1}$ exists between the two BPMs where the $\overline{\mathbf{C}}$ matrices have been measured. Under this assumption we can make use of Eq. (4.2)

$$J_{w,1} = \frac{4e^{i(\phi_x^{skew\ w}+\phi_y^{skew\ w})}}{\sqrt{\beta_x^w \beta_y^w}}\left(f_{1001}^{(w)}e^{i(\phi_x^w+\phi_y^w)} - f_{1001}^{(w-1)}e^{i(\phi_x^{w-1}+\phi_y^{w-1})}\right) , \qquad \text{(D.16)}$$

where $\beta_{x,y}^w$ and $\phi_{x,y}^{skew\ w}$ are the Twiss functions at the location of the skew quadrupole, $\phi_{x,y}^w$ and $\phi_{x,y}^{w-1}$ are the betatron phases at the w^{th} and $(w-1)^{th}$ BPMs respectively and $f_{1001}^{(w)}$ and $f_{1001}^{(w-1)}$ are the corresponding RDT. These terms are given by Eq. (D.9) as a function of the measured $\overline{\mathbf{C}}$ matrix. f_{1010} can also be used leading to a similar equation. It is also possible to relate the change of the determinant of $\overline{\mathbf{C}}$ to the strength of the skew quadrupole. By manipulating the above expressions,

$$J_{w,1} = \left(\frac{|\overline{\mathbf{C}}^{(w)}|}{\gamma^{(w)2}} - \frac{|\overline{\mathbf{C}}^{(w-1)}|}{\gamma^{(w-1)2}} \right) \frac{1}{\chi_w \sqrt{\beta_x^w \beta_y^w}} \,, \tag{D.17}$$

where χ is given by

$$\begin{aligned} \chi_w &= \frac{1}{\gamma^{(w)}} \Big(\cos\delta\phi_x \cos\delta\phi_y \overline{C}_{21}^{(w)} - \sin\delta\phi_x \sin\delta\phi_y \overline{C}_{12}^{(w)} \\ &\quad + \sin\delta\phi_x \cos\delta\phi_y \overline{C}_{22}^{(w)} - \cos\delta\phi_x \sin\delta\phi_y \overline{C}_{11}^{(w)} \Big) \,, \end{aligned} \tag{D.18}$$

where $\delta\phi_{x,y} = \phi_{x,y}^{skew\ w} - \phi_{x,y}^{w}$ are the phase advances between the skew quadrupole and the second location of observation.

D.5 Measurement of $|\overline{\mathrm{C}}|/\gamma^2$ in RHIC during 2005

As shown in Eq. (D.17) the variation of $|\overline{\mathrm{C}}|/\gamma^2$ is directly related to the coupling sources placed between two observation point. Moreover its measurement requires the knoledge of $|f_{1001}|$ and $|f_{1010}|$ only, whereas the computation fo the matrix element requires the additional measurement of their phases.

Beam experiments were performed during the 2005 polarized proton run of RHIC at BNL to measure the coupling RDT f_{1001} [14]. Turn-by-turn BPM data where acquired at injection energy for both rings, yellow and blue. Global coupling was initially corrected using the skew quadrupole families to minimize the tune split ΔQ_{min}. Coherent betatron oscillations in both transverse planes were driven using two ac dipoles: the normal form procedure under such a periodic beam excitation

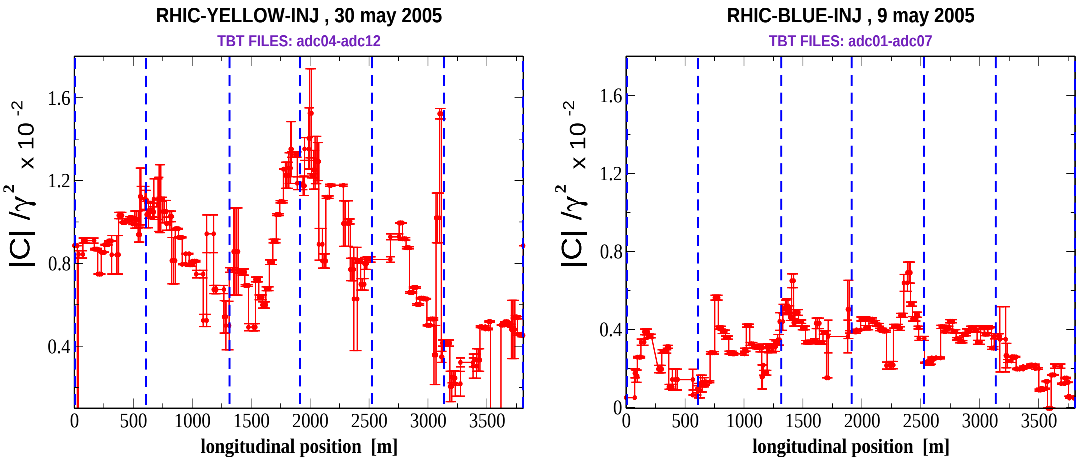

Figure D.2: Measured variation along the ring of $|\overline{\mathrm{C}}|/\gamma^2$ in the yellow ring (left) as well as in the blue ring (right). Vertical dashed lines denote the interaction regions (IR's) (RHIC BPM data 2005, courtesy of R. Calaga).

is described in [57]. The BPM data analysis is in first approximation, for a driving oscillation close to the betatron tune, the same as for a transversely kicked beam.

Although globally decoupled, $|\overline{\mathbf{C}}|/\gamma^2$ in the yellow ring shows significant relative variations in the ring indicating uncorrected local skew quadrupole sources in the arc regions. The blue ring looks relatively flat and therefore globally well decoupled (jumps are visible in the interaction reagion only).

Appendix E

Software for the analysis of turn-by-turn BPM data

bpm2rdt reads BPM files containing the turn-by-turn (TBT) data of a transversely excited beam. From the betatron oscillations, the resonance driving terms (RDT) excited by linear coupling (skew quadrupoles) and first order nonlinearities (normal sextupoles) are inferred. The code needs also an external file containing the optics at the BPM's (a MAD-X Twiss table). If in the same file also the Twiss parameter of skew quadrupoles and normal sextupoles are written, the codes tries to compute both their strengths and polarities, under the assumption the these elements are the sources of coupling/nonlinearities.

Editing the Input File

An example of **bpm2rdt** input file `bpm2rdt_input` is:

```
! ******** bpm2rdt INPUT FILE: 11 DECEMBER 2004 ********
!
! WARNING: DO NOT CHANGE THE ORDER OF THE INPUT PARAMETERS
! WARNING: UP TO 1000 COMMENTED LINES ARE ALLOWED. THE LINE
!          IS COMMENTED WHEN STARTS WITH a !. DO NOT PUT
!          OTHER CHARACTERS, BECAUSE NO FURTHER CHECK IS
!          PERFORMED
! *********************************************************

! # of turns (power of 2) =================================
1024

! TBT BPM DATA FILE (in  ./EXPERIMENTAL_FILES) ============
top-05.data.rama

! twiss MADX file (in  ./EXPERIMENTAL_FILES)     ==========
! Twiss functions at the BPMs and the multipoles ==========
```

```
top-02.twiss

! BPM twiss values from on-line/SVD file       ============
! (in  ./EXPERIMENTAL_FILES) if you type NONE, ============
! it means that the optics at the BPMs is      ============
! taken from the previous MADX file            ============
top-05.twiss.rama
!none

! estimated X and Y tunes to be found from FFT  ===========
28.246
29.217

! .true. use only dual BPM, .false. use all BPMs ==========
.true.

! expected spectrum peaks to search =======================
20
```

ITEMS DESCRIPTION

- **item # 1:** # of turns recorded in the BPM TBT file
- **item # 2:** BPM TBT file name, to be placed in the `./EXPERIMENTAL_FILES` directory
- **item # 3:** twiss MAD-X file containing the Twiss functions at both the BPM's and the multipoles, and the magnet strengths of the latter ones from the model, to be located in `./EXPERIMENTAL_FILES` directory. To generate it add in your MAD-X input file the following lines:

```
select, flag=twiss, clear;
select, flag=twiss, class=HMONITOR ,column=name,     s, betx, mux, bety, muy, k2l, k1sl;
select, flag=twiss, class=VMONITOR ,column=name,     s, betx, mux, bety, muy, k2l, k1sl;
select, flag=twiss, class=SEXTUPOLE ,column=name,    s, betx, mux, bety, muy, k2l, k1sl;
select, flag=twiss, pattern="B2M05C3Y" ,column=name, s, betx, mux, bety, muy, k2l, k1sl;
select, flag=twiss, pattern="^SQ*" ,column=name,     s, betx, mux, bety, muy, k2l, k1sl;
select, flag=twiss, class=MULTIPOLE ,column=name,    s, betx, mux, bety, muy, k2l, k1sl;
twiss,table=twiss,file=top-02.twiss;
twiss,save;
```

- **item # 4:** if this item is different from `NONE` or `none` , it is considered as an on-line model file containing the Twiss functions at the BPM, to be located in `./EXPERIMENTAL_FILES` directory. The format is the following (each line corresponds to one BPM)
  - name
  - location [m]

- β_x [m]
- β_x [m]
- ϕ_x [units of 2π]
- ϕ_y [units of 2π]

An example:

```
g6-bx   8.326374  34.83935797  31.833034695 0.22395109 0.21069863
yi6-b1 25.023783 306.23090546 271.211432935 0.24979144 0.23944553
yi6-b3 36.899612 620.13844556 199.177101845 0.25501097 0.24499780
. . .
```

- **items # 5:** estimated tunes Q_h, Q_v (in case of linear coupling) or ν_x, ν_y (in case of nonlinear detuning driven by sextupoles). These numbers drive the peak search routine to detect the tune and the secondary lines in the BPM spectra. The correctness of these numbers can be checked in the output file `fft.dat` , where for each BPM, the detected spectral lines are listed (first column) together with their amplitude (second col.) and phase (third col.). The detected tune lines should be the one with largest amplitudes. Notice that a wrong guess might drive wrong RDT computations, specially if the two tunes are exchanged. An example of `fft.dat`:

```
 *******   SPECTRUM  AT THE BPM #  1  ***********
x harmonic (# 1) =   0.246004    0.134455E-03   -0.44683
x harmonic (# 2) =   0.217005    0.478461E-05    1.14855
x harmonic (# 3) =   0.754004    0.359196E-04   -1.04088
. . .
y harmonic (# 1) =   0.216997    0.621436E-04    1.41147
y harmonic (# 2) =   0.246025    0.646516E-05    1.76046
y harmonic (# 3) =   0.782996    0.150994E-04    2.91047
. . .
```

- **item # 7:** Logic flag to select the kind of BPM to be used for the analysis: `.true.` selects dual-plane BPM's only, `.false.` makes all BPMs be used.

- **item # 6:** # of peaks/harmonics to search in the BPM spectra: for clean BPM data, ten harmonics should be in principle enough, but the more noisy are the data the higher number of harmonics to be searched you need.

Output Files

The output files can be divided in three groups

1. measured and model RDT files
2. measured and model strengths files
3. “diagnostic” files

Measured and Model RDT Files

To this group belong:

- `fJKLMm.dat`: it contains the absolute value of RDT f_{jklm} from the model (Twiss file) against longitudinal position and BPM number (to the first order approximation, i.e. for large values it might not correspond to the real value). Format: BPM position [m], $|f_{jklm}|$ [depends on $jklm$], BPM number

```
 0  0.0518917888 0
25  0.0518917888 1
25  0.0304226093 1
73  0.0304226093 2
73  0.0486926585 2
. . .
```

  The file has a "step-wise" format, i.e. the value of $|f_{jklm}|$ at the i-th BPM is repeated at the next BPM to show vertical jumps.

- `fJKLMe.dat`: it contains the measured absolute value of RDT f_{jklm}. Format and structure as for the above model file.

- `zfJKLM.dat`: it contains the measured RDT f_{jklm} against longitudinal position. Format (for f_{1001} from `zf1001.dat`):

```
# s[m]      Re{f1001}    Im{f1001}    |f1001|   phi{f1001}
25.0238  -0.100217E-1  0.287245E-1  0.30422E-1   1.906483
73.1987  -0.151963E-1 -0.462606E-1  0.48692E-1  -1.888185
. . .
```

- `cgam_matrix.dat`: it contains the measured coupling matrix $\bar{C}$ and γ against longitudinal position. They are computed from the measured f_{1001} and f_{1010}. Format:

```
# s[m]   barC11   barC12   barC21   barC22  gamma  |C|/gamma2
25.023  0.01664 -0.00437  0.03567  0.09815  0.999  0.0017930
73.198 -0.01350 -0.09459 -0.03377 -0.17160  1.000 -0.0087734
. . .
```

- `cgamma.dat`: it contains the measured determinant of the coupling matrix $|\bar{C}|/\gamma^2$ against longitudinal position in a "step-wise" format similar to `fJKLMe.dat`.

Measured and Model Strength Files

To this group belong:

- `strengths-f1001.dat` and `strengths-Cmatrix.dat`: they contain the reconstructed skew quadrupole strengths according to the measured RDT f_{1001},

f_{1010} and $|\bar{C}|/\gamma^2$ and the MAD-X Twiss file that provides the optical parameters at the skew quadrupoles. Only values corresponding to individual skew quadrupoles between two consecutive BPM's (according to the MAD-X file) are displayed. If several skew quadrupoles are instead present, the complex Hamiltonian coefficients contained in the `hamiltonian_fft.dat` file must be considered. If the momentum reconstruction is suspected of error (due to the presence of nonlinearities between two BPM's) an exclamation mark is printed out. Format:

```
#=====================================================
# If from the twiss file, several skew quads are
# between two BPMs, the correspondig 'strength' is
# not displayed here: see file hamiltonian_fft.dat
#
#
# BPM location   gradient   gradient   gradient
#       [m]       f1001      f1010        MADX
  3      113.    0.1271E-1  0.1324E-8 -0.6690E-03  !
  8      752.    0.9875E-2  0.8654E-2  0.3530E-03
 13     1205.    0.3588E-2  0.1179E-1  0.2800E-03  !
 16     1391.    0.5358E-8  0.2535E-1  0.2800E-03  !
. . .
```

- `strengths-f3000.dat`: contains the sextupolar strength inferred from the RDT f_{3000} and f_{1200}. The above remarks hold for this file.
- `hamiltonian_model.dat` and `hamiltonian_fft.dat`: they contain the Hamiltonian coefficients $\hat{h}_{jklm}$ and the corresponding RDT f_{jklm} along the ring, from the model and measurement respectively. Format:

```
***** j k l m =  1 0 0 1 ******* FROM MODEL/REC. FORMULA
BPM#  BPM-pos  |h_jklm| phase_h_jklm   |f_jklm|  phase_f_jklm
  1      25    0.04731    -0.24822     0.37635     1.9964
  2      73    0.0000      0.0000      0.37635    -1.6234
. . .
***** j k l m =  1 2 0 0 ******* FROM MODEL/REC. FORMULA
BPM#  BPM-pos  |h_jklm| phase_h_jklm   |f_jklm|  phase_f_jklm
  1      25    18.443     -1.5046      11.686      1.4312
  2      73     0.314     -3.1306      11.636     -1.3395
. . .
```

- `chi_from_model.dat` and `chi_from_fft.dat`: they contain the observable χ_{jklm} along the ring, from the model and measurement respectively. Format:

```
***** ROGELIO's CHI ***** FROM MODEL/FFT (HORIZONTAL!)
```

```
BPM#  BPM-pos   |chi_1010| phase_chi_1010 |chi_1020| . . .
  1     25       0.0000      0.0000       0.0000     . . .
. . .
```

“Diagnostic” Files

- **Model MAD-X optics:** `optics_bpm_model.dat`, `optics_nsext_model.dat`, `optics_skewq_model.dat`: they contain the optical functions of BPM’s, normal sextupoles and skew quadrupoles respectively as read from the MADX Twiss file (ignore $\alpha_{x,y}$).
- **Optics from FFT:** `optics_bpm_fft.dat`: if only dual plane BPM’s are used, the codes computes the optical functions from the BPM TBT data and they are printed in this file.
- **BPM measured spectra:**
  - `fft.dat` contains all the detected lines (both vertical and horizontal according to the corresponding BPM).
  - `lines.dat` shows the correspondence between the detected secondary and their physical name (H(0,1), V(1,-2) …)
  - `lines_chi.dat` shows the correspondence between the detected spectral lines of the observable χ_{jklm} and their physical name.
  - `spectrum_ampli.dat` lists the amplitudes of all detected spectral lines at each BPM.
  - `spectrum_phase.dat` lists the phases of all detected spectral lines at each BPM.
  - `spectrum_ampli_chi.dat`lists the amplitudes of the detected lines corresponding to the observable χ_{jklm}.
- **Various:**
  - `exspec_jump.dat` lists the positions of the expected jumps according to the MADX Twiss file.
  - `topology_bpm.dat` lists all the used BPM’s: name, location and plane (ignore last column).
  - `skew_quad.dat` and `norm_sext.dat` group the measured RDT excited by skew quadrupoles and normal sextupoles respectively (old format).
  - **to be ignored:** `peaks_o.dat` and `skew_sext.dat`.

Code Structure

The main directory (`bpm2rdt-x10`) contains:

- `bpm2rdt.f`: the main source code in FORTRAN77 (the author loves FORTRAN). Under Linux it is compiled running

  ```
  g77 -O2 bpm2rdt.f -o bpm2rdt
  ```

- `bpm2rdt_input`: input file described above.
- `clean`: script to remove all previous *.dat files (DANGEROUS)
- `INCLUDE`: this directory contains all the include files linked in the main source code (a detailed description would take some time and is postponed to the future)
- `EXPERIMENTAL_FILES`: this directory contains the BPM TBT, the MADX and on-line model files
- `TEST`: this directory contains other directories whose files where used to benchmark the code (against the code used i n [1])
- `MANUAL`: is the directory with the .tex source of this documentation and a draft note (a candidate paper maybe) where the algorithm implemented is explained and results from SPS data analysis are shown

Acknowledgments

The implemented FFT routine is a modified version of the routine developed at the Bologna University by Armando Bazzani *et al.* [58]. The routine has been speeded up including a peak search routine in order to avoid a repetitive FFT computation. Thomas Beier is the author of this routine, originally written for gamma spectroscopy in atomic physics [34]. Giuliano Franchetti contributed with his MIMAC tracking and optics engine in testing the software.

Curriculum Vitae of the Author

1. PERSONAL DATA

Family name: Franchi
Name: Andrea
Marital Status: Single
Nationality: Italian
Place of birth: Teramo (Italy)
Date of birth: January 16 1978

2. EDUCATION

- March 2002: Master degree (Laurea) in physics in the University of Bologna: thesis on halo formation studies in high intensity linacs. Co-supervisors Profs. Giorgio Turchetti e Armando Bazzani, Dr. Andrea Pisent (LNL-INFN); grade: 110/110 *cum laude*.
- June 2004: US Particle Accelerator School in Madison, Wisconsin: 2-weeks course on ”Beam control and manipulation” held by Michiko Minty and Frank Zimmermann; grade “A”.
- September 2001: CERN school in Seville, intermediate course.
- June 2001: US Particle Accelerator School in Boulder, Colorado: 2-weeks course on ”Linear Accelerators” held by Thomas Wangler and James Billen; grade “A”.
- July 1996: High school (Scientific Lyceum) in Nereto (Teramo): Grade 60/60 .

3. PRESENT PROFESSIONAL STATUS

Institute: GSI Darmstadt
Address: Plackstrasse 1 D-6429, Darmstadt, Germany
Telephon: +49 6159 71 2411
Fax: +49 6159 71 2985
E-mail: a.franchi@gsi.de
Position: wissenschaftliche Hilfskraft

4. PROFESSIONAL EXPERIENCE

Place: GSI, Darmstadt, Germany.
period: from March 1 2003
Subjects: PhD thesis measurement and studies of nonlinearities and linear coupling in high intensity hadron circular accelerators

Place: BNL, Uptown, New York, USA.
period: Scientific visitor December 5-13 2004
Subjects: Measurement of linear coupling and nonlinearities in the Relativistic Heavy Ion Collider (RHIC).

Place: LNL-INFN, Legnaro, Italy.
period: Technical student from January 1 to August 30 2002
Subjects: Development of the 3D PIC code HALODYN for space-charge simulations of high intensity hadron linacs, applied to the TRASCO ISCL proton linac.

5. RESEARCH ACTIVITY

Development of algorithm and software to measure nonlinearities in synchrotron using beam position monitors (BPM) data. Technique applied successfully to existing SPS data where both the strengths and polarities of the extraction sextupoles have been measured.

Studies on betatron linear coupling using normal forms and the resonance driving terms (RDT) description. Development of an algorithm to infer the complex linear coupling coefficient C (amplitude and phase) in a single machine cycle using BPM data. Technique applied successfully to RHIC data.

Studies on emittance exchange driven by betatron coupling and space charge. Measurement of emittance exchange and equilibration in the SIS-18. Development of a technique to control the amount of space-charge driven emittance exchange using normal quadrupoles.

Upgrade of the 3D PIC parallel code ***HALODYN*** for the study of space-charge effects in high intensity linacs.

Spoke-person of the sub-task on *code benchmarking* of the working package 5 in the framework of the European network HIPPI (***High intensity Pulsed Proton Injectors***).

Coordinator of measurements carried out at GSI in the SIS-18 concerning linear and nonlinear optics, multi-turn injection optimization, emittance exchange and correction of linear coupling.

6. CONGRESSES AND WORKSHOPS

- “ICFA workshop HB2004” (member of the local organizing committee)
- “EPAC04”, Lucern, Switzerland, June 2004
- “LINAC02“, Kyoungju, Korea, 2002

7. LANGUAGES

- Italian: Mother tongue
- English: Good
- German: Mittelstufe

8. COMPUTING

- Linux as favorite operating system
- Programming languages: fortran (advanced); C/C++(basic)
- Experience with parallel programming using MPI
- Experience in running numerical code for particle tracking and design of hadron linacs: HALODYN, IMPACT, PARMILA, SUPERFISH, DYNAMION, PARTRAN, PATH
- Experience in running numerical code for particle tracking in circular accelerators: MAD, MICROMAP

9. SCIENTIFIC PUBLICATIONS

Journals (refereed):

1. R. Tomás, M. Bai, R. Calaga, W. Fischer, A. Franchi and G. Rumolo, “Measurement of global and local resonance terms”, Phys. Rev. ST Accel. and Beams **8**, issue 2, 024001 (2005).

2. R. Calaga, R. Tomás and A. Franchi, “Betatron coupling: Merging the Hamiltonian and Matrix approaches”, Phys. Rev. ST Accel. and Beams **8**, 034001 (2005).

3. S. Rambaldi, G. Turchetti, C. Benedetti, F. Mattioli, A. Franchi, ”Accuracy analysis of a spectral Poisson solver”,, accepted by NIM-A, special edition COULOMB’05 workshop, Senigallia Italy, 2005.

Conference and Workshop Proceedings:

1. A. Franchi, R. Duperier, G. Franchetti, F. Gerigk, L. Groening, I. Hofmann, A. Orzhekhovskaya, A. Sauer, D. Uriot, S. Yaramyschev, ”Benchmarking linac code for the HIPPI project”, proceedings of ICFA-HB04 workshop, Bensheim, Germany, 2005
2. R. Calaga, S. Abeytunge, M. Bai, W. Fischer, R. Tomás, A. Franchi, “Measurement and Optimization of Local Coupling from RHIC BPM Data” proceeding of PAC05, Knoxville, Tennessee, USA, 2005
3. Rogelio Tomás, Mei Bai, Wolfram Fischer, Andrea Franchi, Giovanni Rumolo, ”Measurement of Multipole Strengths from RHIC BPM Data”, proceedings of EPAC04, Luzern, Switzerland, 2004
4. A. Franchi, R. Tomas, T. Beier, M. Kirk, P. Moritz, G. Rumolo, ”A Method to Measure the Skew Quadrupole Stregths in the SIS-18 Using Two BPMs” , proceedings of EPAC04 , Luzern, Switzerland, 2004
5. G. Turchetti, A. Bazzani, C. Benedetti, A. Franchi, S. Rambaldi, ”Accuracy Analysis of a 2D and 3D Poisson-Vlasov PIC Solver and Estimates of the Collisional Effects in Space Charge Dynamics” , proceedings of ICAP02, East Lansing, USA, 2002
6. A. Franchi M. Comunian, A. Pisent, G. Turchetti, S. Rambaldi, A. Bazzani, ”HALODYN: A 3D Poisson-Vlasov Code to Simulate The Space Charge Effects in the High Intensity TRASCO Linac” , proceedings of LINAC02, Kyoungju, Korea, 2002

Laboratory or Institute Internal Reports:

1. ”Measurement of emittance exchange driven by betatron linear coupling in the SIS-18”, GSI March-May 2005
2. ”Report on the visit at BNL December 5-13, 2004”, BNL-GSI January 2005
3. ”First test of the new turn-by-turn BPM aquisition system”, GSI November 2003
4. ”Chromaticity measurement (attempt of) in the GSI SIS-18”, GSI August 2003
5. ”HALODYN documentation and user manual”, LNL-Univerista’ di Bologna, July 2002